Master's thesis

NTNU
Norwegian University of Science and Technology
Faculty of Engineering
Department of Marine Technology

Rikke Olsen Fredheim

Tower design for very large floating wind turbines

Master's thesis in Marine Technology
Supervisor: Erin Bachynski-Polić, Jørgen Amdahl and Zhaolong Yu
June 2022

NTNU
Norwegian University of
Science and Technology

Rikke Olsen Fredheim

Tower design for very large floating wind turbines

Master's thesis in Marine Technology
Supervisor: Erin Bachynski-Polić, Jørgen Amdahl and Zhaolong Yu
June 2022

Norwegian University of Science and Technology
Faculty of Engineering
Department of Marine Technology

NTNU

Kunnskap for en bedre verden

To mom and dad, for always supporting me.

NTNU Trondheim
Norwegian University of Science and Technology *Faculty of Engineering*
Department of Marine Technology

PROJECT THESIS IN MARINE TECHNOLOGY

SPRING 2022
for

Stud. Tech. Rikke Olsen Fredheim

Tower design for very large floating wind turbines
Tårndesign for store flytende havvindturbiner

The price of electricity produced by offshore wind turbines has decreased drastically in recent years, in part through increased rotor size, which allows a single installation to capture more energy – thus reducing overall costs for foundations, installation, and maintenance. The same trend is expected for floating offshore wind turbines, where 15 MW reference designs are already becoming available. As the rotor size increases, the relative importance of different loads may also change: for example, gravitational loads become more important for blade design, and wind loads tend to become more important than wave loads. The structure as a whole is expected to become heavier, with longer natural periods in the flexible modes, moving these closer to important excitation from waves. The longer tower will interact with the flexible hull, flexible blades, and control system in new ways.
In the project work in Fall 2021, a literature study was carried out, and hydrodynamic models for two 25 MW semi-submersible wind turbine designs were developed.
The thesis work to be carried out in Spring 2022 includes:

1. As needed, extend the literature review into wave and wind statistical description (spectra), floating offshore wind turbine dynamics, fatigue and ultimate strength, upscaling of floating wind turbines, and relevant guidelines and standards, also related to buckling. Include a survey of wind turbine control for floating wind turbines.
2. Develop a numerical model in SIMA for the selected 25MW Upscale baseline wind turbine (v0, either the center column or side column design) with a rigid body model of the hull, flexible model of the theoretically upscaled tower, and flexible rotor model.
3. Carry out decay tests, constant wind tests, and tests in regular waves and characterize the tower natural frequencies and mode shapes and the 1P and 3P frequencies.
4. Evaluate the tower design with respect to buckling criteria.
5. Define a set of simplified environmental conditions for fatigue screening (for example based on the LIFES50+ data), and carry out fatigue analysis of the tower.
6. Examine the trends in the tower natural frequency, mode shapes, and fatigue damage for design modifications such as changing thickness and diameter in different parts of the tower.
7. If time permits, make use of the simplified 2D beam python model from PhD candidate Serageldin Abdelmoteleb (or an equivalent model in matlab or abaqus) to study trends with respect to scaling, tower design, and floater design.
8. Conclusions and recommendations for further work.

The work scope may prove to be larger than initially anticipated. Subject to approval from the supervisors, topics may be deleted from the list above or reduced in extent.

In the project report, the candidate shall present her personal contribution to the resolution of problems within the scope of the project work

Theories and conclusions should be based on mathematical derivations and/or logic reasoning identifying the various steps in the deduction.

The candidate should utilise the existing possibilities for obtaining relevant literature.

Project report format
The project report should be organised in a rational manner to give a clear exposition of results, assessments, and conclusions. The text should be brief and to the point, with a clear language. Telegraphic language should be avoided.

The report shall contain the following elements: A text defining the scope, preface, list of contents, summary, main body of thesis, conclusions with recommendations for further work, list of symbols and acronyms, references and (optional) appendices. All figures, tables and equations shall be numerated.

The supervisors may require that the candidate, in an early stage of the work, presents a written plan for the completion of the work.

The original contribution of the candidate and material taken from other sources shall be clearly defined. Work from other sources shall be properly referenced using an acknowledged referencing system.

The report shall be submitted in electronic format (.pdf):
- Signed by the candidate
- The text defining the scope shall be included (this document)
- Drawings and/or computer models that are not suited to be part of the report in terms of appendices shall be provided on separate (.zip) files.

Ownership
NTNU has according to the present rules the ownership of the project reports. Any use of the report has to be approved by NTNU (or external partner when this applies). The department has the right to use the report as if the work was carried out by a NTNU employee, if nothing else has been agreed in advance.

Thesis supervisors:

Prof. Erin Bachynski-Polić, NTNU, erin.bachynski@ntnu.no
Prof. Jørgen Amdahl, NTNU, Jorgen.amdahl@ntnu.no
Assoc. Prof. Zhaolong Yu, NTNU, zhaolong.yu@ntnu.no

Deadline: As decided on the web, June 2022

Trondheim, January 2022

Erin Bachynski-Polić

Preface

This report presents my master thesis written at the department of Marine Technology, at the Norwegian University of Science and Technology. It concludes my Master in Science within the spesialization Marine Constructions, completed during spring 2022. It builds on a preparatory project carried out during fall 2021, and it reflects the growing industry interest in offshore wind.

I want to thank my supervisor Erin Bachynski-Polić for great guidance through our weekly meetings. Both through the preparatory project and through the first part of the master thesis up until her maternity leave. Her dedication and extensive knowledge has been of great inspiration to me. Thank you to Jørgen Amdahl for taking over as my supervisor and providing great advice and exceptional expertise. A special thanks also goes out to PhD candidate Serag Eldin Abdelmoteleb for providing me with upscaled designs, relevant files, as well as always going above and beyond to help me. Lastly I would like to thank my friends and family for all their support during my Master's degree.

Rikke Olsen Fredheim

Trondheim, 10.06.2022

Abstract

A Floating Offshore Wind Turbine (FOWT) can exploit abundant wind potential in deeper waters and be a valuable source of renewable and clean energy. For FOWTs to become cost-efficient, the structures are required to increase in size. When upscaling, the importance of loads and responses may change. Coupled aero-hydro-servo-elastic simulations are required to better understand the complex dynamic behavior. This thesis explores the upscaling of a FOWT. It evaluates the results of coupled analyses and examines the trends in natural periods, mode shapes, and fatigue damage for tower modifications.

A literature study is conducted on aerodynamics, hydrodynamics, and FOWT dynamics to explain the baseline of coupled simulations. Different types of upscaling methods are examined. For upscaling of the turbine, the self-weight becomes a limiting factor, as it scales with the radius cubed. Geometric upscaling of floaters is not necessarily the best option, and typically a parametric study is carried out to optimize the design. Large turbines are seen to have excitation frequencies that move towards the wave frequency area, creating possible challenges of resonance. Other challenges for upscaling include manufacturing, transportation, testing, and installation facilities, as well as the fact that the human scale remains unchanged.

The numerical model of a 25 MW FOWT is successfully upscaled based on the INO WINDMOOR 12 MW platform and the IEA 15 MW UMaine VolturnUS-S tower and turbine. The model is created in sima and coupled aero-hydro-servo-elastic analyses are conducted. The upscaled design is stable and operational during initial testing. The 25 MW turbine is found to have a rated wind speed of 11 m/s, a maximum thrust force of 3 MN, and a mean generator power of 26 MN. It is further found that the 1P frequency band is located in the wave frequency range, which is one of the big challenges for large FOWTs. Decay tests without wind, with rated wind, and above-rated wind, confirms correct coupled behavior of the FOWT. The wind turbine tower is in the stiff-stiff range, and simplified buckling checks show that the upscaled tower design is stable in terms of global buckling. Regular wave tests confirm the natural period found from decay. A fatigue analysis is conducted based on environmental conditions from the LIFES50+ EU-funded project. The fatigue analysis shows that the geometric upscale of the turbine tower experience fatigue failure before 20 years.

Two alternative tower designs, designs 2 and 3, are created to examine the trends in tower natural frequency, mode shapes, and fatigue damage. The changes are limited to changing diameter and thickness, while all other parameters are kept constant. For both designs, there is little effect on natural periods for global motions, due to low weight differences. The natural period for tower bending is decreased as the diameter and thickness modifications make the tower stiffer. This is again seen for mode shapes, where the bending is less profound for the stiffer tower designs.

Design 2 has a larger diameter and decreased thickness. The increased diameter results in a much better fatigue capacity and fatigue damage distribution. However, the tower still experiences failure from fatigue before 20 years. For design 3, the diameter is increased further, but the thickness is not altered. The diameter is changed according to the relationship between diameter, stress, and fatigue damage. Design 3 has the best fatigue resistance of the three designs. The fatigue damage is constant along 3/4 of the tower length, just above $D = 1$. Though improved, the fatigue damage is still > 1, so design 3 of the turbine tower also experiences failure. In addition, due to the increased diameter, the tower is also exposed to local buckling.

Through this thesis, it is shown that when upscaling, a strict geometric upscaling is not the best option. It is however a good starting point for design modifications. Designs 1 and 3 have approximately the same amount of steel, but a different distribution of it and hence a significant difference in fatigue resistance. A smarter distribution of the steel has proven to give a better utilization of the material, without causing large influences on other coupled aspects of the system. It seems likely that if several design modifications were implemented, it would be possible to end up with a 25 MW tower design that can withstand 20 years without experiencing fatigue or local buckling.

Sammendrag

Flytende havvind kan utnytte vindpotensial på dypere vann og være en verdifull kilde til fornybar og ren energi. For at disse vindturbinene skal bli kostnadseffektive, er det nødvendig å oppskalere. Ved oppskalering kan viktigheten av belastninger og respons endres. Koblede aero-hydro-servo-elastiske simuleringer er nødvendig for bedre å forstå den komplekse dynamiske oppførselen. Denne masteroppgaven utforsker oppskalering av en flytende vindturbin. Den evaluerer resultatene av koblede analyser, og undersøker endring i naturlig periode, svingeform og utmattelsesskader ved ulike tårnmodifikasjoner.

En litteraturstudie utføres innen aerodynamikk, hydrodynamikk og flytende vindturbin-dynamikk, for å forklare koblede simuleringer. Ulike typer oppskaleringsmetoder undersøkes. For oppskalering av turbinen blir egenvekten en begrensende faktor, da den skaleres med radius i tredje. Geometrisk oppskalering av flytere er ikke nødvendigvis det beste alternativet, og typisk utføres en parametrisk studie for å optimalisere designet. Store turbiner er sett å ha eksitasjonsfrekvenser som beveger seg mot bølgefrekvensområdet, og skaper mulige utfordringer med resonans. Andre utfordringer for oppskalering inkluderer produksjon, transport, testing og installasjonsfasiliteter, samt det faktum at den menneskelige skalaen forblir uendret.

Den numeriske modellen av en 25 MW vindturbin er vellykket oppskalert basert på INO WINDMOOR 12 MW-plattformen og IEA 15 MW UMaine VolturnUS-S-tårnet og -turbinen. Modellen lages i sima og koblede aero-hydro-servo-elastiske analyser utføres. Det oppskalerte designet er stabilt og operativt under innledende testing. 25 MW turbinen har en nominell vindhastighet på 11 m/s, en maksimal skyvekraft på 3 MN og en gjennomsnittlig generatoreffekt på 26 MN. Det er videre funnet at 1P frekvensbåndet ligger i bølgefrekvensområdet, som har vist seg å være en av hovedutfordringene til store flytende vindturbiner. Fri bevegelsestester uten vind, med nominell vind og høyere enn nominell vind, bekrefter korrekt koblet oppførsel av vindturbinen. Vindturbintårnet viser seg å være i stiv-stiv området, og forenklede knekkingskontroller viser at det oppskalerte tårndesignet er stabilt når det gjelder global knekking. Regulære bølgetester bekrefter den naturlige perioden funnet fra fri bevegelsestest. Det gjennomføres en utmattelsesanalyse basert på miljøforhold fra det EU-finansierte prosjektet LIFES50+. Utmattelsesanalysen viser at den geometriske oppskaleringen av turbintårnet opplever utmattingssvikt før det har gått 20 år.

To alternative tårndesign, design 2 og 3, er laget for å undersøke trendene i tårnets egenfrekvens, svingeform, og tretthetsskader. Endringene er begrenset til endring av diameter og tykkelse, mens alle andre parametere holdes konstante. For begge utformingene er det liten effekt på naturlige perioder for globale bevegelser, grunnet lave vektforskjeller. Den naturlige perioden for tårnbøying reduseres ettersom diameter- og tykkelsesmodifikasjonene gjør tårnet stivere. Det samme sees for svingeform, der bøyningen er mindre for de stivere tårndesignene.

Design 2 har større diameter og redusert tykkelse. Den økte diameteren gir en mye bedre utmattingskapasitet og utmattelsesskadefordeling. Imidlertid opplever tårnet fortsatt svikt fra tretthet før 20 år. For design 3 økes diameteren ytterligere, men tykkelsen endres ikke. Diameteren endres i henhold til forholdet mellom diameter, spenning og utmattelsesskader. Design 3 har den beste tretthetsmotstanden av de tre designene. Tretthetsskaden er konstant langs 3/4 av tårnlengden, like over $D = 1$. Selv om det er forbedret, er tretthetsskaden fortsatt > 1, så design 3 av turbintårnet opplever også svikt fra utmatting. I tillegg, på grunn av den økte diameteren, kan tårnet også være utsatt for lokal knekking.

Gjennom denne oppgaven vises det at ved oppskalering er en full geometrisk oppskalering ikke det beste alternativet. Det er imidlertid et godt utgangspunkt for designmodifikasjoner. Design 1 og 3 har omtrent samme mengde stål, men en annen fordeling av det og dermed en betydelig forskjell i utmattingsmotstand. En smartere fordeling av stålet viser seg å gi en bedre utnyttelse av materialet, uten å gi store påvirkninger på andre koblede aspekter av systemet. Mye tyder på at dersom flere designmodifikasjoner blir gjennomført, ville det være mulig å ende opp med et 25 MW tårndesign som tåler 20 år uten å oppleve utmatting eller lokal knekking.

Contents

List of Figures

List of Tables

Acronyms

ABS	American Burau of Shipping.
ALS	Accidental Limit State.
BEM	Blade Element Momentum.
COB	Center of Buoyancy.
COG	Center of Gravity.
DLF	Dynamic Load Factor.
DNV	Det Norske Veritas.
DOF	Degree of Freedom.
FEM	Finite Element Method.
FLS	Fatigue Limit State.
FOWT	Floating Offshore Wind Turbine.
GDW	Generalized Dynamic Wake.
GW	Gigawatt.
IEA	International Energy Agency.
IEC	International Electrotechnical Commission.
ITTC	International Towing Tank Conference.
MWh	Megawatt Hour.
NREL	National Renewable Energy Laboratory.
RAO	Response Amplitude Operator.
RPM	Rotations per Minute.
SLS	Service Limit State.
SWL	Still Water Line.
TLP	Tension Leg Platform.
ULS	Ultimate Limit State.
UMaine	University of Maine.
VSVP	Variable Speed Variable Pitch.
WEO	World Energy Outlook.

Nomenclature

g	Acceleration of gravity.
A	Area.
A_γ	Normalizing factor.
A_{kj}	Added mass coefficient.
B_{kj}	Damping coefficient.
B_n	Number of blades on wind turbine.
C_D	Drag coefficient.
C_L	Lift coefficient.
C_M	Mass coefficient.
C_P	Power coefficient.
C_T	Thrust coefficient.
C_n	Coefficient normal to rotorplane.
D_c	Characteristic cumulative damage.
E_{kin}	Kinetic energy.
F_D	Drag force.
F_L	Lift force.
F_T	Thrust force.
F_p	Prandtl's tip loss factor.
I_{wp}	Moment of inertia about water plane.
M	Bending moment.
M_a	Mass.
N_{ax}	Key identification of the SN-curve.
OD	Equivalent diameter of a line with constant cross section along its length.
P	Power.
P_0	Load history.
P_E	Euler Load.
P_a	Available power in wind.
Q_T	Torque.
R	Radius.
R_{amp}	Amplitude.
Re	Reynolds number.
$S(\omega)$	Wave spectrum.
S_J	The JONSWAP spectrum.
S_{PM}	The Pierson-Moskowitz spectrum.
S_{max}	Maximum stress in a cycle.
S_{min}	Minimum stress in a cycle.
S_m	Mean stress in a cycle.
TI	Turbulence intensity.
U_r	Ursell number.
V_{rel}	Relative velocity.
ΔS	Mean stress in a cycle.
Ω	Angular velocity.
α	Angle.
β	Frequency ratio.
δ	Displacement.
$\dot{m}$	Mass flux.
ϵ	Strain.
ϵ_j	Random phase angle.
γ	Non-dimensional peak shape parameter.
γ_F	Load factor.
γ_m	Material factor.
λ	Wave length.
λ_{TSP}	Tip Speed Ratio.
λ_r	Local speed ratio.
μ	Viscosity.

∇	Fluid volume.
ν	Poisson's ratio.
ω	Circular frequency.
ω_0	Natural frequency.
ω_a	Angular velocity.
ϕ	Velocity potential.
ϕ_p	Angle between the plane of rotation and the relative velocity.
ρ	Density of water.
ρ_{air}	Density of air.
ρ_s	Density of steel.
σ	Stress.
σ_b	Bending stress.
σ_d	Standard deviation.
σ_r	Solidity rate.
σ_s	Spectral width parameter.
$\mathbf{V}$	Velocity vector.
θ	Phase angle.
ξ_d	Damping ratio.
ζ	Wave elevation.
ζ_a	Wave amplitude.
a	Axial induction factor.
a'	Angular induction factor.
a_f	Axial load.
c	Damping.
c_{cr}	Critical damping.
c_l	Local chord length.
f	Frequency.
f_R	Excitation frequency.
f_y	Yield stress limit.
h	Water depth.
k	Stiffness.
k_t	Thickness component.
k_w	Wave number.
m	Mass.
m_w	The Wöhlner exponent.
n_i	Number of cycles.
p	Pressure.
p_0	Atmospheric pressure.
p_N	Force normal to rotorplane.
p_T	Force tangential to rotorplane.
q	Applied load.
r	Radius.
r_c	Curvature of streamlines.
r_p	Radial position of the control volume.
t	Time.
t_{ref}	Reference thickness.
t_t	Tower wall thickness.
u	Velocity.
u_H	Homogeneous solution.
u_P	Particular solution.
u_m	Maximum velocity.
v	Wind velocity.
v_0	Wind velocity upstream of wind turbine.
v_1	Wind velocity downstream of wind turbine.
v_A	Velocity at rotor disk.

1 Background

Energy systems worldwide need to transition to renewable and clean energy sources to avoid fueling climate change. Upscaling electricity from renewable sources is crucial in making the decarbonization of the energy system happen. One source of renewable energy is floating offshore wind turbines (FOWT)s. However, the cost of these is still high. In order to reduce the cost, the FOWTs must increase in size.

1.1 Offshore wind

Oceans occupy a large portion of the world. These oceans have the potential of providing an abundant supply of renewable energy, in terms of a wind resource which is generally higher and sometimes smoother than on land. Placing wind turbines offshore allows for the harvest of this energy. It also results in less sight and sound pollution compared to land turbines, and hence less dissatisfaction among the population. These are all contributing factors to the increasing trend seen in the offshore wind industry.

The International Energy Agency (IEA) performed an analysis of offshore wind for the 2019 World Energy Outlook (WEO) with emphasis on technical potential, continued evolution, and its role in the energy systems now and in the future (IEA, 2019a). From this analysis, the wind capacity is seen to have increased from 3 Gigawatt (GW) in 2010, to 23 GW in 2018. The annual deployment increased by nearly 20 % each year. By mid-2019 there were over 5500 offshore turbines connected to a grid in 17 countries (IEA, 2019a). In the 2019 Energy transition outlook by Det Norske Veritas (DNV), it is forecast that in 2050, 63% of the world's electricity will be generated from variable renewable sources (DNV, 2019). Figure 1.1 shows the world's electricity generation, and it is clear that the proportion of offshore wind is anticipated to increase.

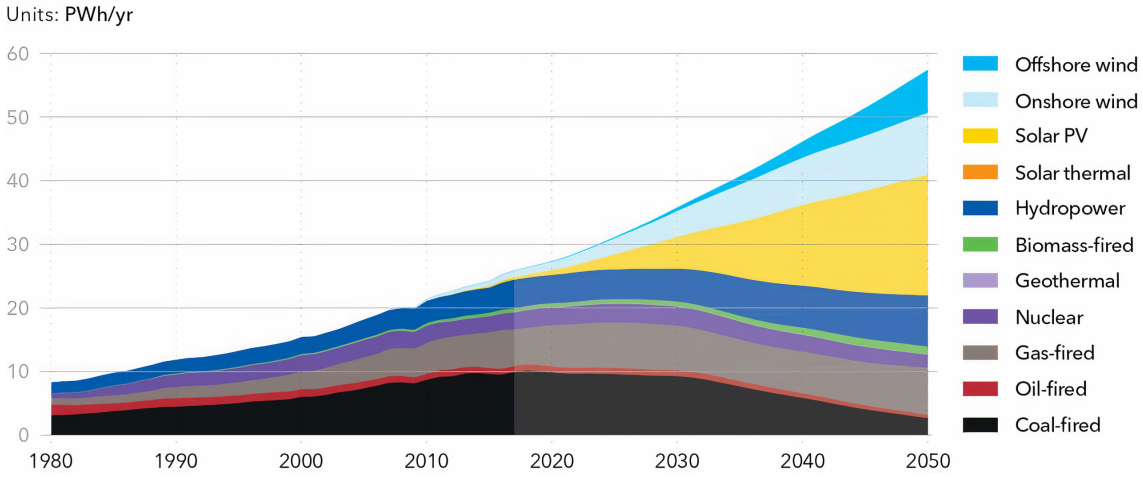

Figure 1.1: World electricity generation by power station type (DNV, 2019).

Despite the impact of COVID-19, 6.1 GW of offshore wind was commissioned worldwide in 2020. With the new installations, the total offshore wind capacity has passed 35 GW and is now representing 4.8% of global cumulative wind capacity (GWEC, 2021). Offshore wind turbines with fixed foundations still make up most of this total capacity. Bottom-fixed turbines are routinely deployed in water depths of around 40-60 m, and at up to 80 km distance from shore (IRENA, 2019b). Installation of bottom fixed turbines at water depths of more than 60 m is not economically profitable. The technological developments of floating wind turbine foundations are hence a key factor in the continued growth of the offshore wind industry.

1.2 Floating offshore wind turbines

The three dominant floating support structure classifications are semi-submersible, spar, and Tension Leg Platform (TLP), as shown in Figure 1.2 (Atcheson and Garrad, 2016). Compared to fixed turbines, floating wind turbines give access to at least four times as much ocean surface space (DNV, 2021c). Industry experts estimate that by 2050, based on the pace of development, floating wind farms could cover around 5-15% of the global offshore wind installed capacity (IRENA, 2019a). The first commercial-scale floating wind farm was Equinor's Hywind Scotland, which was commissioned in 2017 with a capacity of 30 MW (IRENA, 2019b). Since then there have been installed several floating wind parks, including the 30 MW WindFloat Atlantic in Portugal and the 48 MW Kincardine in Scotland (IEA, 2019b). Hywind Scotland achieved the highest average capacity factor of all offshore wind farms in the UK (DNV, 2021c). This indicates that floating wind turbines can perform just as well, or even better, than bottom-fixed. The interest is hence increasing and Equinor is currently developing Hywind Tampen, an offshore wind park 140 km outside the coast of Norway, with a water depth of 260-300 m. It will have a capacity of 88 MW and is expected to be in operation by the third quarter of 2022 (Equinor, 2021b). Equinor also received approval in 2019 to build a 200 MW project off the coast of the Canary Islands (IEA, 2019b). It will entail an investment of more than 860 million euros and could start operation in 2024 (Radowitz and Snieckus, 2019).

Figure 1.2: Different types of floating foundations, from left to right: spar, semi-submersible, TLP. Illustration by Joshua Bauer, National Renewable Energy Laboratory (Joshua Bauser, 2020).

The main challenge with FOWTs is the cost. The first floating wind farms have seen a levelized cost of energy four times that of bottom fixed wind, exceeding 200 USD/Megawatt Hour (MWh) (DNV, 2021c). Much of the reason is linked to the small size of the first floating wind farms and the immaturity of the technology. Rapid technology development, supply chain efficiencies, and logistical synergies in closely linked markets in Europe are bringing down the costs (IRENA, 2019b). In addition, offshore wind turbines are increasing in size to reduce the levelized cost of energy. Instead of redesigning the structure, upscaling the existing floating substructure can

improve the efficiency of the design process (Leimeister et al., 2016). Though the structure itself is not necessarily made cheaper by upscaling, replacing several smaller turbines with one large one means fewer wind turbines to fabricate, transport, and maintain.

1.3 The upscaling trend

The first offshore wind farm was inaugurated in 1991 at Vindeby off the coast of Denmark. The wind farm consisted of 11 wind turbines with a tip height of 54 m and an installed capacity of 450 kW per turbine (Open Ocean, 2017). The maximum output of turbines has since been raised through an increase in turbine size in terms of tip height and swept area. In 2010, commercially available wind turbines reached a capacity of 3 MW. The 3 MW wind turbines have a tip height of just over 100 m, which is an increase of almost double in 10 years. Technology innovation has since accelerated the development, and in 2017 there were 8 MW wind turbines with tip-heights of more than 200 m (IEA, 2019a). Figure 1.3 shows the evolution of offshore wind turbines from the 1991 Vindeby wind farm to the 8 MW 2017 Burbo Bank Extension Offshore Wind Farm in Liverpool Bay. The rotor diameter is seen to be 164 m for the 8 MW turbine, which compared to the 35 m diameter of the Vindeby turbine is a 369% increase in 16 years.

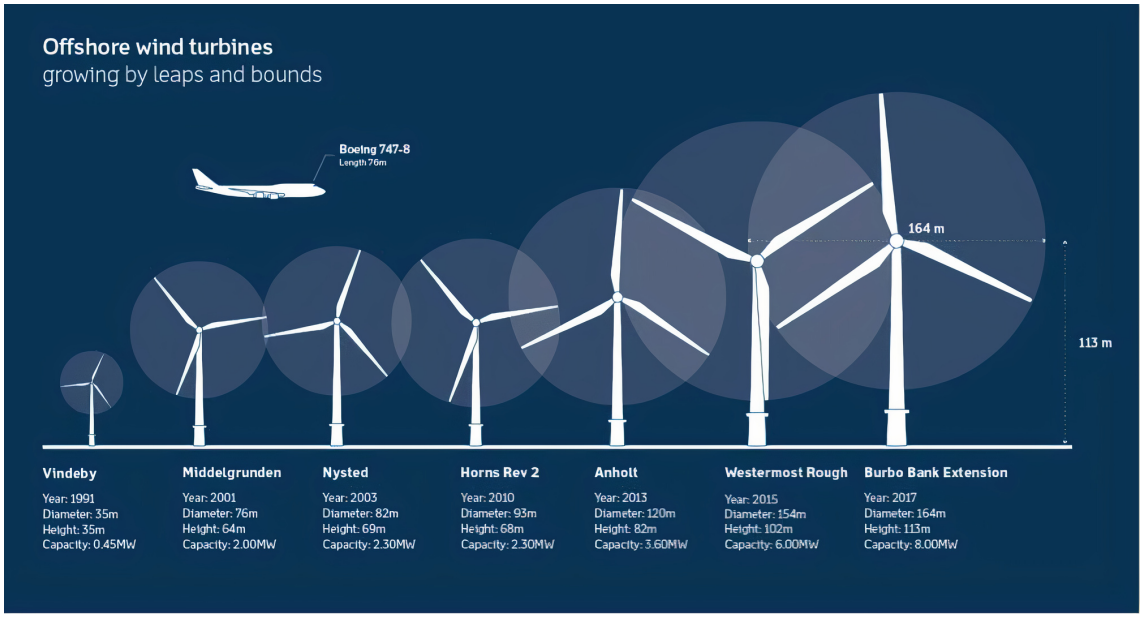

Figure 1.3: Evolution of wind turbines (Open Ocean, 2017).

In 2019 a 12 MW turbine was under development with an expected tip height of 260 m (IEA, 2019a). Further, the Danish wind turbine company Vestas has announced a 15 MW turbine which, in February 2021, had the highest wind turbine rating in the world. It will be first tested in 2022, with scheduled production in 2024. There is also the GE Haliade X-13, which is scheduled to be installed in the UK's Dogger Bank offshore wind project in the North Sea (Hanley, 2021). A subsidiary of Norwegian renewable energy company Zephyr has unveiled plans for a 1GW-plus offshore wind farm off Sweden, which would possibly feature turbines with power ratings up to 20 MW (Craig Richard, 2021). Scale is key to cost reduction, both of the wind turbine itself, the supply chain, and the infrastructure (DNV, 2021c). The effect is seen by, for example, Equinor's 40% reduction in investment cost per MW for Hywind Tampen compared to Hywind Scotland (Equinor, 2021a). Hywind Tampen consists of 11 turbines on 8 MW each, while Hywind Scotland consists of 5 turbines on 6 MW each.

As the FOWTs are becoming larger, the need for understanding the dynamic behavior of such systems is emphasized. For land-based wind turbines, it is necessary to account for the coupled dynamics of the rotating turbine, the elasticity of structural elements, the aerodynamics, and the

turbine control system. Put a wind turbine on a floating structure and it becomes necessary to account for incident waves, current, mooring dynamics, and global motions of the substructure (A. Robertson et al., 2014). All these factors testify to a high degree of complexity, even for small-scale turbines. As the wind turbine towers become higher, there may also be new interactions between the motion of the flexible tower, the flexible blades, the platform, and the control system. Further, as the FOWTs are upscaled the relative importance of the dynamic loads may change, and responses of the system might give rise to new challenges that put today's knowledge to the test. It is necessary with more information about how large FOWTs behave, what problems arise and how these problems can be mitigated.

1.4 Objective and structure of the report

The objective of this master thesis is to upscale a FOWT to support a 25 MW turbine, evaluate the tower design, and examine the trends in the tower's natural frequency, mode shapes, and fatigue damage for design modifications. The master thesis is a continuation of a project report written during the fall of 2021. The project report consisted of a literature study into wave and wind statistical description (spectra), FOWT dynamics, fatigue and ultimate strength, upscaling of FOWTs, and relevant guidelines and standards. It also included the upscaling and validation of two reference FOWT sub-structures.

In this master thesis, the literature study is expanded. The complete literature study is hence a combination of work completed during both the project thesis and master thesis. Following the literature study, the numerical model is finalized. Out of the two platforms upscaled in the project, one is chosen for further analyses. The selected platform is equipped with an upscaled tower, turbine and mooring system.

Evaluating the FOWT tower design requires coupled aero-hydro-servo-elastic analyses. This is accomplished through using the DNV Sesam software. To understand the various contributions to the analyses, Section 2, 3 and 4 contains a review of the theory that steps through the fundamental aspects relevant to aerodynamics, hydrodynamics, FOWT dynamics, and wind turbine control in a coupled analysis. Section 5 outlines the upscaling methods, relevant guidelines and the necessary software. The reference wind turbines are then presented and upscaled in Section 6. Section 7 contains the results from the coupled analyses on the upscaled design. Section 8 discusses two design modifications, and Section 9 presents conclusion and recommendations for future work.

2 Wind and aerodynamics

As can be deduced by the name, the wind is a very central part of wind turbines. This section outlines how the wind is described and explains the fundamental aerodynamic concepts behind how a wind turbine operates. The computation of wind force acting on the rotor is explained using the Blade Element Momentum (BEM) method and necessary corrections.

2.1 Description of wind

Manwell, McGowan and Rogers (2010) give the four atmospheric forces in a simplified model of the mechanics of the atmosphere's wind motion. These are the pressure force, the Coriolis force from the earth's rotation, the inertial force from large-scale circular motion, and the frictional force at the earth's surface. The pressure forces are driven by the spatial variation in heat transfer to the earth's atmosphere, due to the sun unevenly heating up the earth.

2.1.1 Spatial variations

The variation in atmospheric pressure causes air to flow from a high-pressure area to a low-pressure area. The resulting circulation of the atmosphere is influenced by the effects of the rotation of the earth, while seasonal variations in the distribution of solar energy give rise to variations in circulation (Manwell, McGowan and Rogers, 2010). These large spatial variations are of importance when assessing suitable locations for wind turbines. Figure 2.1 shows the wind velocity along the shore, and it is seen to be higher in the north and south where the temperature variations typically are higher than along equator. Areas where wind velocity is shown to be high, e.g. outside Scotland, are one of the locations where there are already several offshore wind turbines installed.

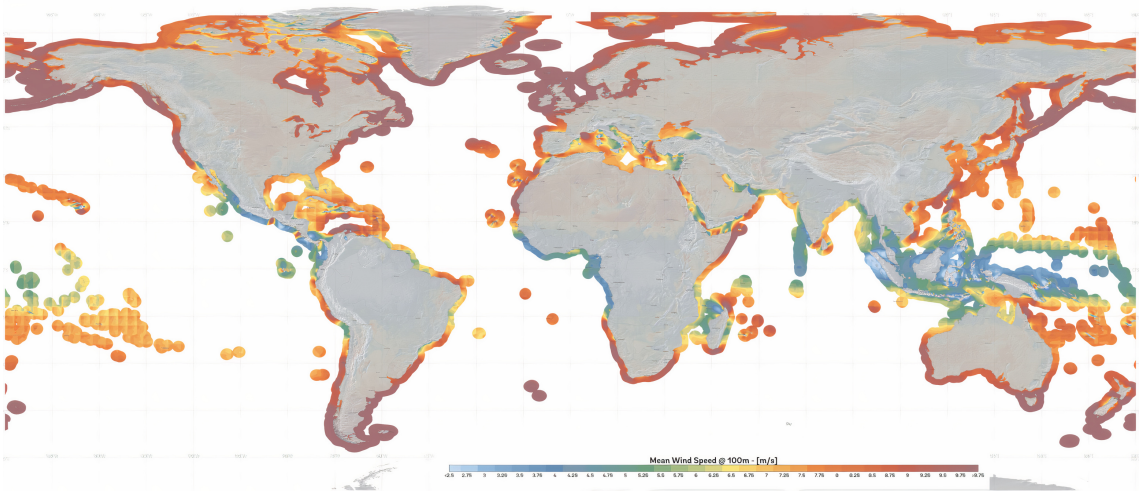

Figure 2.1: Wind velocity offshore (Global.Wind.Atlas, 2021).

In addition to these **global** spatial variations, wind turbines experience **local** spatial variations. The local spatial variations are more important than the global variations in regard to the load variations experienced by the wind turbine. Figure 2.2 shows a momentary representation of a typical wind speed distribution. The profile is called the vertical profile of the wind speed or vertical wind shear (Manwell, McGowan and Rogers, 2010). The actual wind speed profile shows the spatial variation of the wind, which will subsequently lead to spatial variations in the loads. The mean profile also gives an impression of how the wind speed increases with height. As wind turbines are becoming larger, the turbine will reach areas of higher wind speeds and hence increased loads with more spatial variance.

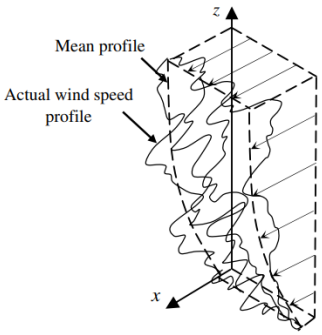

Figure 2.2: Wind speed profile (Tempel, 2006).

In addition to variations in space, there are also variations in time. Time variations can be divided into inter-annual, annual, diurnal, and short-term. Short-term variations include turbulence and gusts and are usually time intervals less than 10 minutes.

2.1.2 Turbulence

In the lower 2 km of the atmospheric boundary layer, the earth influences the wind speed due to friction with the earth's surface (Tempel, 2006). The surface roughness length for the calm open sea and the blown sea is 0.20 mm and 0.50 mm respectively. In comparison, forests and woodlands have a roughness length of 500 mm, while centers of cities with tall buildings have a surface roughness length of 3000 mm (Manwell, McGowan and Rogers, 2010). Rough terrain gives higher turbulence intensity. The turbulence intensity, TI, is defined in Equation 2.1 as the standard deviation, σ_d, of the time-varying wind speed divided by the mean wind speed, v. It is given in percentage and represents how strongly the wind varies with time,

$$TI = \frac{\sigma_d}{v}. \tag{2.1}$$

Turbulence can have a significant impact on the design and performance of the individual wind turbine (Burton et al., 2011). The significance is increasing along with the increase in turbine size, as there may be little spatial coherence in wind gusts and turbulence (Nybø et al., 2020). Devinant, Laverne and Hureau (2002) showed that the aerodynamic properties of the turbine have a strong dependence on the turbulence intensity. Further, Barthelmie and Jensen (2010) concluded on energy absorption also being strongly dependent on the turbulence intensity. It is thus important to include the turbulence in aero-hydro-servo-elastic analyses for FOWTs. This can be accomplished using TurbSim, which is a stochastic, full-field, turbulence simulator. It allows for the simulations of advanced turbine design with simulated inflow turbulence environments (Kelley and B. J. Jonkman, 2007).

2.1.3 Wind spectrum

The variety of frequencies, amplitudes, and phases in the turbulent wind can be described by a wind spectrum (Manwell, McGowan and Rogers, 2010). Two spectra commonly used to describe the spectrum of the longitudinal component of the turbulence are the Kaimal and the von Karman spectra (Burton et al., 2011).

The von Karman gives a good description of turbulence in wind tunnels, while the Kaimal may give a better fit to empirical observations of atmospheric turbulence (Burton et al., 2011). For standard wind turbine classes, the random wind velocity field for the turbulence models shall, according to the International Electrotechnical Commission (IEC) standard, satisfy the Kaimal model. IEC Kaimal turbulent wind spectrum is shown in Figure 2.3 for two different turbulence intensities. The frequency, f, is given as $1/T$ hertz, where T is the period.

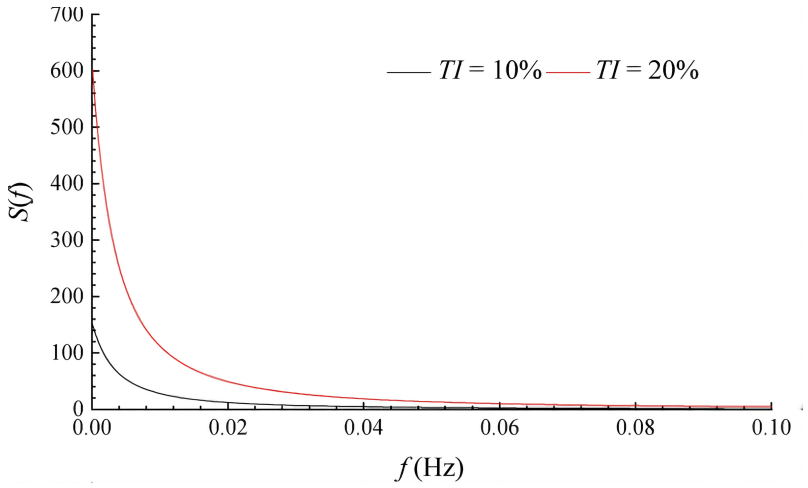

Figure 2.3: IEC Kaimal spectrum for turbulent wind (Li et al., 2019).

From Figure 2.3, the spectrum can be seen to increase significantly for a higher turbulence intensity. This consequently induces higher loads on the wind turbine. As an alternative to the Kaimal model, the Mann model may be applied (ACP, 2021). The Mann model is based on the spectral tensor for atmospheric surface-layer turbulence at high wind speed (Mann, 1998). In short, the models are different in terms of the spatial distribution of the turbulence (Eliassen and Bachynski, 2017).

The Kaimal and Mann models are challenged by the increase in rotor size where the spatial and temporal distribution of the wind field is becoming increasingly important. The difference in coherence has consequences for the global loads on the wind turbines (Myrtvedt, Nybø and Nielsen, 2020). In addition, the floating wind turbines are seen to be more sensitive to the choice of turbulence model than the fixed turbines. For example, the Mann model can be seen to induce more yaw movement, while the Kaimal can induce more surge and pitch (Bachynski and Eliassen, 2018). The variance in loads imposed by the choice of turbulence model is hence important when considering very large floating wind turbines.

2.2 One-dimensional momentum theory

Upon placing the wind turbine in a turbulent wind inflow, the wind force acting on the rotor is typically computed using the Blade Element Momentum (BEM) method. Before introducing BEM, it is useful to introduce the one-dimensional momentum theory. One-dimensional momentum theory is a simplified method used to calculate how much power can be extracted from an ideal turbine, the thrust on an ideal rotor, and the effect of that rotor on the local flow.

2.2.1 Available wind power

Wind turbines extract available power from the wind by slowing down the wind velocity. As wind passes the wind turbine, a thrust force, F_T, acts on the wind and lowers the wind velocity from v_0 to v_1. As the wind velocity changes, the kinetic energy, E_{kin}, changes. Some of this energy is converted to mechanical energy by the wind turbine shaft. The mechanical energy is then converted to electricity by the wind turbine generator (Hansen, 2008). The available power in wind, P_a, is given by

$$P_a = \frac{\Delta E_{kin}}{\Delta t} = \dot{m}(v_0^2 - v_1^2) \tag{2.2}$$

where t is time and $\dot{m}$ is the mass flux given by

$$\dot{m} = \rho_{air} A(x) v(x). \tag{2.3}$$

ρ_{air} is the density of air, A is the rotor swept area and v is the wind velocity (Hansen, 2008). However, not all this available power can be extracted by the wind turbine, this is explained through the actuator disk method.

2.2.2 Actuator disk method

By assuming that the air surrounding the turbine is not affected by the presence of the turbine, a boundary can be drawn between the unaffected air and the air which passes through the rotor. This boundary can be extended upstream and downstream, giving shape to a stream tube with a circular cross-section. It is assumed that there is no flow through the stream tube boundary. It is further assumed that the flow is homogeneous, incompressible, and steady-state, with no friction drag and no rotational velocity component in the wake. The turbine is included as an actuator disc assumed to have infinite blades and uniform distribution of thrust (Hansen, 2008).

The presence of the turbine causes the wind to slow down from v_0 ahead of the disk, to v_A at the actuator disk, and v_1 in the wake. The situation is illustrated in Figure 2.4. Upstream of the rotor, and far downstream of the rotor, the pressure is assumed to be the same, i.e., equal to atmospheric pressure, p_0.

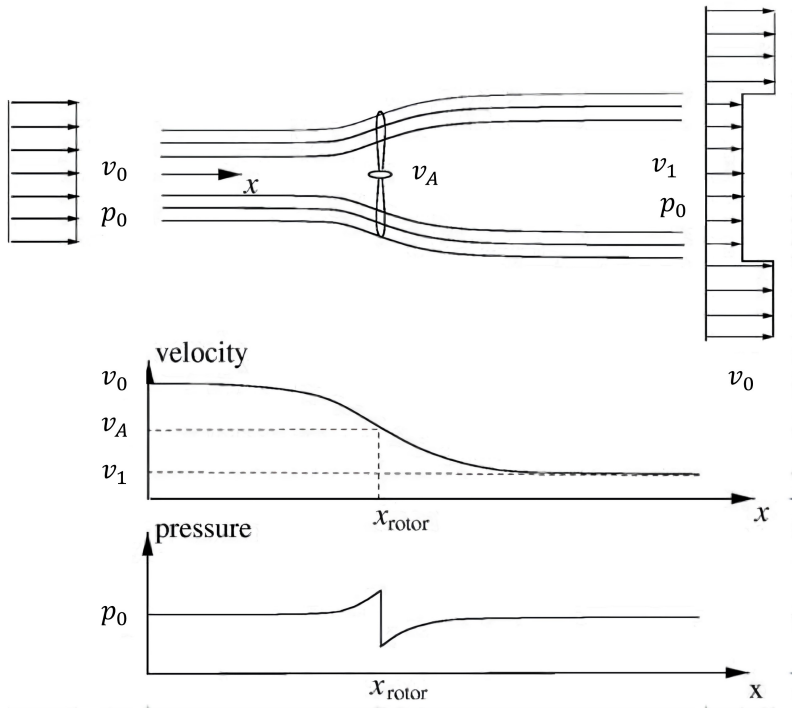

Figure 2.4: Change in velocity and pressure past the rotor (based on (Hansen, 2008) but amended notations).

The stream tube boundary expands because the air is slowing down without being compressed. As the wind has not yet reached the turbine, no work has been done. However, since the wind velocity is lowering, the pressure increases to absorb the decrease in kinetic energy. As the wind passes the rotor, work is done and there is a drop in pressure, Δp. Downstream of the rotor, both the velocity and pressure are hence lower than at the inlet. To achieve equilibrium, the pressure increases back to atmospheric pressure, resulting in a further lowering of the wind speed (Burton et al., 2011). The necessary thrust force F_T, due to the change in pressure, p, is given by

$$F_T = \Delta p A. \tag{2.4}$$

With Bernoulli's equation, the change in pressure Δp can be expressed as

$$\Delta p = \frac{1}{2}\rho_{air}(v_0^2 - v_1^2). \tag{2.5}$$

By using the simplified assumption of an ideal rotor, along with the conservation of mass, the equation for thrust can be changed to

$$F_T = \rho_{air} v_A A(v_0^2 - v_1^2) \tag{2.6}$$

where v_A is the velocity at the rotor disk. By replacing the thrust with the pressure difference in Equation 2.4, and by utilizing Δp as in Equation 2.23, v_A can be calculated as

$$v_A = \frac{1}{2}(v_0^2 - v_1^2). \tag{2.7}$$

As the flow has been assumed frictionless, the internal energy will not change from inlet to outlet, except for the power converted by the wind turbine shaft (Hansen, 2008). If considering the volume drawn by the stream tube boundary as a control volume, the power P is given by

$$P_w = \dot{m}\left(\frac{1}{2}v_0^2 + \frac{p_o}{\rho_{air}} - \frac{1}{2}v_1^2 - \frac{p_o}{\rho_{air}}\right), \tag{2.8}$$

substituting for the mass flux it becomes

$$P_w = \frac{1}{2}\rho_{air} v_A A(v_0^2 - v_1^2). \tag{2.9}$$

The relationship between the velocity at the rotor and the upstream velocity can be described by the dimensionless axial induction factor a (Mendes et al., 2020), given by

$$a = \frac{v_0 - v_A}{v_0}. \tag{2.10}$$

By using the axial induction factor, the velocity at the rotor can be expressed as

$$v_A = (1 - a)v_0. \tag{2.11}$$

Equation 2.7 and 2.11 can be combined to give an expression for the downstream velocity

$$v_1 = (1 - 2a)v_0. \tag{2.12}$$

Equation 2.12 can be introduced into Equation 2.9 for power, and Equation 2.6 for thrust,

$$P_w = 2\rho_{air} v_0^3 a(1 - a)^2 A \tag{2.13}$$

and

$$F_T = 2\rho_{air} v_0^2 a(1 - a)A. \tag{2.14}$$

A power coefficient, C_P, describes how much of the wind power the turbine can convert to usable power. The power coefficient can be used to non-dimensionalize the power, using the available power in wind, Equation 2.2, i.e.

$$C_P = \frac{P}{\frac{1}{2}\rho_{air} v_0^3 A}. \tag{2.15}$$

The same approach can be used to define a thrust coefficient, C_T,

$$C_T = \frac{T}{\frac{1}{2}\rho_{air} v_0^2 A}. \tag{2.16}$$

Expressed in terms of the axial induction factor, C_T and C_P becomes

$$C_P = 4a(1-a)^2 \tag{2.17}$$

and

$$C_T = 4a(1-a). \tag{2.18}$$

To find the maximum power coefficient the equation is differentiated

$$\frac{dC_P}{da} = 4(1-a)(1-3a). \tag{2.19}$$

The maximum value of C_P occurs when Equation 2.19 is equal to 0, which happens when $a = 1/3$. Hence the maximum C_P is

$$C_{P_{max}} = 16/27 = 0.593 \tag{2.20}$$

$0.593 = 59.3\%$ is known as the **Lanchester-Betz limit** (Burton et al., 2011) and is the theoretical maximum a wind turbine can extract from the available power in the wind.

2.2.3 Wake rotation

So far the air has been assumed to have no rotational velocity component in the wake. In reality, there will be some rotation caused by the torque exerted by the rotating blades. The torque will be equal to the rate of change of the angular momentum of the air passing through the rotor. Since the turbine is then giving kinetic energy to the wake, a rotating turbine cannot achieve the hypothetical Betz limit (Bachynski-Polic, 2021a). As the wind passes the rotor, the air rotates in the opposite direction of which the rotor travels. Therefore, there will be air particles in the wake which will have a velocity component tangential to the rotation, in addition to an axial component. The change in tangential velocity is expressed by an angular induction factor a'. To allow variations of both components, one can consider an annular ring of the rotor disk with radius r and radial width dr. The rotor disc comprises a multiplicity of annular rings which are assumed to act independently (Burton et al., 2011).

An angular induction factor a', is introduced, given by

$$a' = \frac{\omega_a}{2\Omega} \tag{2.21}$$

where ω_a is the angular velocity imparted to the free stream and Ω is the angular velocity of the rotor. It requires some algebra which is not shown here, but by using the angular induction factor, the thrust, power, and torque, Q_T, can be expressed in terms of one annular ring:

$$\mathrm{d}F_T = \frac{1}{2}\rho_{air}\Omega^2 4a'\left(1+a'\right) r^2 2\pi r \ \mathrm{d}r \tag{2.22}$$

$$\mathrm{d}P_w = \frac{1}{2}\rho v_0^3 A\left[8a'(1-a)\right]\frac{\lambda_r^3}{\lambda_{TSR}^2}d\lambda_r. \tag{2.23}$$

$$\mathrm{d}Q_T = 4a'(1-a)\frac{1}{2}\rho_{air}v_0\Omega r^2 2\pi r\ \mathrm{d}r \tag{2.24}$$

λ_{TSP} is the tip speed ratio and λ_r is the local speed ratio given by

$$\lambda_{TSP} = \frac{\Omega R}{v_0} \tag{2.25}$$

and

$$\lambda_r = \frac{\lambda_{TPR} r}{R} \tag{2.26}$$

where R is rotor radius. The coefficient for the maximum power becomes

$$C_P = \frac{8}{\lambda_{TSR}^2}\int_0^{\lambda_{TSR}} a'(1-a)\lambda_r^3 d\lambda_r. \tag{2.27}$$

It can be shown mathematically that to maximize the power coefficient, a' should be

$$a' = \frac{1-3a}{4a-1}. \tag{2.28}$$

2.2.4 Lift and drag forces

The actuator disc is now replaced by actual wind turbine blades. Most wind turbines consist of three wind turbine blades attached to a hub. The cross-section of turbine blades has the shape of an airfoil, as illustrated in Figure 2.5. Aerodynamic performance is decided by the width and length of the blade (Manwell, McGowan and Rogers, 2010). The curve of the airfoil causes the streamlines to curve. From fluid mechanics, it is known that a pressure gradient is necessary to curve the streamlines (Hansen, 2008). It is given by

$$\frac{\partial p}{\partial r} = \frac{\rho_{air} v_w^2}{r_c} \tag{2.29}$$

where r_c is the curvature of the streamlines. The pressure gradient acts like the centripetal force, causing a lower pressure on the convex side, and a higher on the concave side (Manwell, McGowan and Rogers, 2010). The result is the lift and drag force. The lift force is perpendicular to the velocity and is caused by the difference in pressure. The drag force is parallel to the velocity and is due to both viscous friction forces and unequal pressure on the airfoil surface (Manwell, McGowan and Rogers, 2010). Lift and drag forces are shown in relation to an airfoil in Figure 2.5, denoted L and D respectively.

There is only lift if there is rotation in the flow. Rotation in flow can either be caused by geometry, like in the case of an airfoil, or it can be caused by rotation, i.e. the Magnus effect. For a thin symmetric airfoil, the lift coefficient, C_L, is equal to $2\pi\alpha$. Where α is the angle as indicated in Figure 2.5. By adding camber (curvature), the foil is no longer symmetric and the lift coefficient will be non-zero at zero angle of attack.

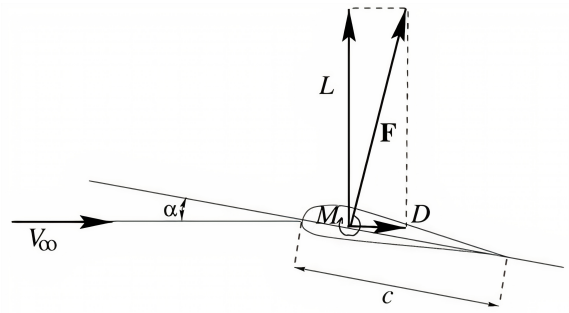

Figure 2.5: Drag and lift force (Hansen, 2008).

2.3 Blade Element Momentum theory

The Blade Element Momentum method couples the momentum theory with the shape of the blades and the local aerodynamic effects.

2.3.1 Method

In the BEM method, the stream tube illustrated in Figure 2.4 is discretized into annular elements with height dr. For these elements, it is assumed that there is no radial dependency and that the force from blades on the flow is constant in each annular element (Hansen, 2008).

The thrust and torque from an annular ring can be expressed based on momentum theory:

$$dF_T = 4\pi r \rho_{air} v_0^2 a(1-a)dr \tag{2.30}$$

and

$$dQ_w = 4\pi r^3 \rho_{air} v_0 \Omega (1-a) a' dr. \tag{2.31}$$

Lift is perpendicular to the velocity, while drag is parallel to the velocity. This velocity is the relative velocity, V_{rel}, and includes the incoming wind, the velocity of the blade due to rotor rotation, the induced axial velocity, and the induced tangential velocity (Bachynski-Polic, 2021a). The lift and drag force are projected into p_N and p_T:

$$p_N = F_L \cos\phi_p + F_D \sin\phi_p \tag{2.32}$$

and

$$p_T = F_L \sin\phi_p + F_D \cos\phi_p \tag{2.33}$$

where F_L and F_D are the lift and drag force, illustrated in Figure 2.6. ϕ_p is the angle between the plane of rotation and the relative velocity.

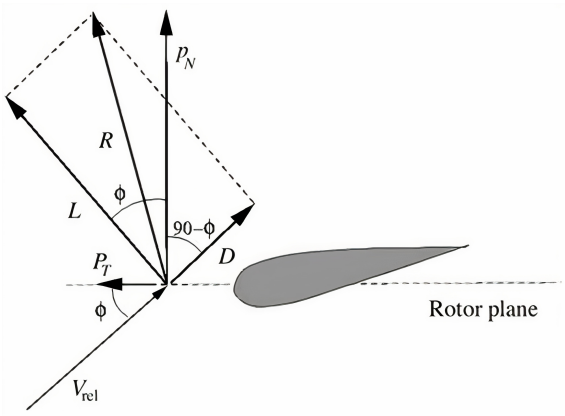

Figure 2.6: Loads on the blade (Hansen, 2008).

Based on Equation 2.32 and 2.33, the normal coefficient, C_n, and tangential coefficient, C_T, can be expressed as

$$C_n = \frac{p_N}{\frac{1}{2}\rho_{air} V_{rel}^2 c} \tag{2.34}$$

and

$$C_t = \frac{p_T}{\frac{1}{2}\rho_{air} V_{rel}^2 c_l} \tag{2.35}$$

where c_l is chord length. A solidity, σ_r, is defined as the area which is covered by the blades in the control volume, given by

$$\sigma_r = \frac{c_l B_n}{2\pi r_p}. \tag{2.36}$$

B_n is the number of blades and r_p is the radial position of the control volume. As p_N and p_T are forces per length, and by using Equation 2.34 and 2.35, the thrust and torque can be expressed as

$$dF_T = \frac{1}{2}\rho_{air} B_n \frac{v_0^2 (1-a)^2}{\sin^2(\phi_p)} c_l C_n dr \tag{2.37}$$

and

$$dQ_T = \frac{1}{2}\rho_{air} B_n \frac{v_0 (1-a)\omega_a r\,(1+a')}{\sin(\phi_p)\cos(\phi_p)} c_l C_t r dr \tag{2.38}$$

If the equations for thrust and torque are equalized and combined with the solidity, the expression for the axial induction factor and angular induction factor can be derived to be

$$a = \frac{1}{\frac{4\sin^2(\phi_p)}{\sigma_r C_n} + 1} \tag{2.39}$$

and

$$a' = \frac{1}{\frac{4sin(\phi_p)cos(\phi_p)}{\sigma_r C_t} - 1}. \tag{2.40}$$

a and a' are unknowns in Equation 2.39 and 2.40. However, ϕ_p, C_n and C_t depend on a and a'. Hence, the solution process becomes iterative.

2.3.2 Corrections

Some corrections are necessary when applying BEM theory. These are implemented in simulations when using most software and are briefly mentioned in the following.

Prandtl's Tip Loss factor
When applying BEM theory it is assumed that there is an infinite number of blades. Prandtl's tip loss factor corrects this assumption. When moving from an infinite number of blades, to a finite number of blades, the vortex system in the wake will change (Hansen, 2008). This is because the air tends to flow around the tip, i.e. it follows the pressure gradient, from the lower to upper side (Bachynski-Polic, 2021a). How the correction factor is derived is not included here, but the resulting correction factor, F_p, is given by

$$F_p = \frac{2}{\pi}\cos^{-1}[\exp(-\frac{B_n}{2}\frac{R-r}{r\sin(\phi_p)}] \tag{2.41}$$

where R is now the total radius of the rotor while r is the local radius (Hansen, 2008).

Glauert correction
The one-dimensional momentum theory becomes invalid once the axial induction factor is greater than approximately 0.4. The Glaubert correction factor is an empirical relation between the axial induction factor and the thrust coefficient for these cases (Hansen, 2008), given by:

$$C_T = \begin{cases} 4a(1-a)F_p & a \leq \frac{1}{3} \\ 4a\left(1-\frac{1}{4}(5-3a)a\right)F_p & a > \frac{1}{3} \end{cases} \tag{2.42}$$

Dynamic wake
Due to shedding and downstream convection of vorticity, there is a time lag in induced velocities. This time lag is called the "dynamic wake effect". Stig Øye proposed a filter for the induced velocities consisting of first-order differential equations (Hansen, 2008). Dynamic wake can also be found using the Generalized Dynamic Wake (GDW) method, which is an acceleration potential method (Bachynski-Polic, 2021a). The dynamic wake method is widely used as an alternative to BEM. However, it is not elaborated on here because it is not implemented in the current analyses.

Dynamic stall
The drag and lift coefficients used as input for the BEM method have a value for each angle of attack and can be described as static lift and drag curves (Bachynski-Polic, 2021a). However, the flow around the blade is constantly changing due to wind shear, yaw/tilt misalignment, the blade passing the tower, and turbulence in the wind. These disturbances have an impact on the angle of attack, hence the coefficients do not follow the static values 100%. The effect on the loads depends on the state of the boundary layer. For wind turbines, the most important one is when the boundary layer starts separation at the trailing edge and gradually increases upstream at increasing angles of attack, called dynamic stall. If a dynamic model is not used, flap-wise vibrations may be computed in analysis, even though non-existent on the real turbine. It is thus recommended to apply a dynamic stall model for the lift (Hansen, 2008).

Skewed wake
The last correction included is the correction for the skewed wake. If the rotor is yawed, a blade pointing downstream is deeper into the wake than a blade pointing upstream. Hence, the upstream blade sees a higher wind and thus experiences higher loads compared to the downstream blade. This will in turn produce a beneficial yawing moment, which tries to turn the rotor more into the wind, enhancing yaw stability. The distribution of the induced velocity is described by the yaw model. If this model is not included, the BEM method will not be able to predict the restoring moment in yaw (Hansen, 2008).

3 Hydrodynamics

The wind turbine is placed on a floating substructure, making hydrodynamics an important part of the coupled dynamic behavior. This section introduces wave motion and wave loads through linear wave theory. It further outlines the description of waves and wave load calculations using Morison's equation. Lastly, it briefly introduces non-liner waves.

3.1 Linear wave theory

The first component necessary for simulating the interaction of a body in the ocean is a basic understanding of linear wave theory. The fundamentals are outlined in the following, based on the work by Faltinsen (1990). Relevant terms are shown for a cosine wave in Figure 3.1.

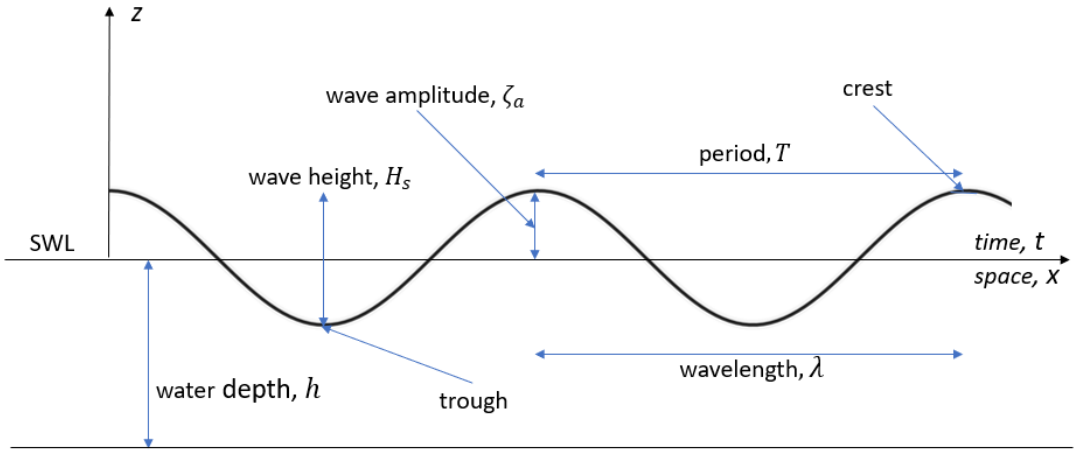

Figure 3.1: Relevant terms shown for a cosine wave.

3.1.1 Assumptions

The basic assumptions for seawater is that the fluid is **inviscid** and **incompressible**, and that the flow is **irrotational**. The velocity of the fluid is noted by the velocity vector, $\mathbf{V}\ (x, y, z, y, t) = (u, v, w)$. The velocity vector describes the velocity at a time, t, at a point **x=(x, y, z)** in a Cartesian coordinate system fixed in space (Faltinsen, 1990).

Inviscid fluid means that it has zero viscosity and no viscous stress, i.e., the viscosity, μ, $= 0$. **irrotational** flow means that locally the flow does not rotate and the vorticity is zero:

$$\nabla \times V = 0. \tag{3.1}$$

For an **incompressible** fluid the fluid volume, ∇, does not change. This means that $\nabla \cdot \mathbf{V} = 0$. The Laplace equation, given by

$$\frac{\partial^2 \phi}{\partial x^2} + \frac{\partial^2 \phi}{\partial y^2} + \frac{\partial^2 \phi}{\partial z^2} = 0, \tag{3.2}$$

is hence satisfied (Faltinsen, 1990). The consequences of these assumptions are that the potential flow theory is valid and the velocity vector of the fluid can be described using a velocity potential

ϕ (Faltinsen, 1990). The fluid evolution can hence be fully described by the velocity and pressure fields at a time and point in space. This can be expressed as

$$\mathbf{V} = \nabla\phi = \mathbf{i}\frac{\partial\phi}{\partial x} + \mathbf{j}\frac{\partial\phi}{\partial y} + \mathbf{k}\frac{\partial\phi}{\partial z}. \tag{3.3}$$

If the z-axis is assumed vertical and positive upwards, the pressure can be expressed as

$$p - p_0 = -\rho g z - \rho\frac{\partial\phi}{\partial t} - \frac{1}{2}\rho|\nabla\phi|^2 \tag{3.4}$$

where ρ is the density of water, g is the gravity acceleration, and z is the location along the z-axis ($z = 0$ at the free surface). The first part of the expression is the static pressure, while the two last parts are the dynamic linear and quadratic pressure.

3.1.2 Boundary conditions

The kinematic boundary conditions for a fixed body in a moving fluid is that of impermeability:

$$\frac{\partial\phi}{\partial n} = 0, \tag{3.5}$$

meaning that no fluid penetrates the body surface. $\partial/\partial n$ denotes the differentiation along the normal to the body surface, defined positive into the fluid (Faltinsen, 1990).

The next boundary condition is the free-surface kinematic condition. With this boundary condition is it assumed that a fluid particle on the free surface will stay on the free surface. The free surface is defined by

$$z = \zeta(x, y, y), \tag{3.6}$$

where ζ is the wave elevation. The function F can then be defined as

$$F(x, y, z, t) = z - \zeta(x, y, y) = 0. \tag{3.7}$$

The free-surface kinematic condition implies that Equation 3.7 is always satisfied, along with the assumption that the substantial derivative of the function is equal to zero. The boundary condition then becomes

$$\frac{\partial\zeta}{\partial t} + \frac{\partial\phi}{\partial x}\frac{\partial\zeta}{\partial x} + \frac{\partial\phi}{\partial y}\frac{\partial\zeta}{\partial y} - \frac{\partial\phi}{\partial z} = 0 \tag{3.8}$$

on $z = \zeta(x, y, y)$ (Faltinsen, 1990).

3.1.3 Dynamic free-surface condition

The dynamic free-surface condition states that the pressure on the surface is equal to the atmospheric pressure, p_0, expressed as

$$g\zeta + \frac{\partial\phi}{\partial t} + \frac{1}{2}\left(\left(\frac{\partial\phi}{\partial x}\right)^2 + \left(\frac{\partial\phi}{\partial y}\right)^2 + \left(\frac{\partial\phi}{\partial z}\right)^2\right) = 0. \tag{3.9}$$

Both of the free-surface conditions are non-linear. However, it is possible to linearize through a perturbation method, simplifying the problem. The linearization depends on the forward speed and current. By setting them both to zero and assuming small wave amplitude relative to wavelength and body dimensions, the free-surface position $z = \zeta(x, y, y)$, can be transferred to the mean free-surface at $z = 0$ by Taylor expansion (Faltinsen, 1990). Linearized, Equation 3.8 and 3.9 becomes

$$\frac{\partial \zeta}{\partial t} = \frac{\partial \phi}{\partial z} \quad \text{on} \quad z = 0 \tag{3.10}$$

$$g\zeta + \frac{\partial \phi}{\partial t} = 0 \quad \text{on} \quad z = 0 \tag{3.11}$$

and combined they become:

$$\frac{\partial^2 \phi}{\partial t^2} + g\frac{\partial \phi}{\partial z} = 0 \quad \text{on} \quad z = 0. \tag{3.12}$$

Equation 3.12 can be rewritten when the velocity potential is oscillating harmonically in time with circular frequency ω (Faltinsen, 1990)

$$-\omega^2 \phi + g\frac{\partial \phi}{\partial z} = 0 \quad \text{on} \quad z = 0. \tag{3.13}$$

3.1.4 Linearized wave theory

When assuming an infinite horizontal extent of the free surface, along with a horizontal sea bottom, linear wave theory can be derived. The free surface condition can be combined with the Laplace equation and sea bottom condition, which gives

$$\frac{\partial \phi}{\partial z} = 0 \quad \text{on} \quad z = -h, \tag{3.14}$$

where h is the water depth. The velocity potential can be expressed as

$$\phi = \mathrm{e}^{k_w x}(A\cos(k_w x) + B\sin(k_w x))\cos(\omega t + \alpha) \tag{3.15}$$

which will satisfy the Laplace equation. A, B, and α are arbitrary constants and k_w is the wave number. However, for the velocity potential to be representing propagating waves, space and time variations must be combined. The properties of regular sinusoidal propagating waves, as per linear wave theory, can be described through the equations listed in Table 3.1, for deep water. Deep water implies that the water depth is larger than half the wavelength, $h > \frac{1}{2}\lambda$. Where λ is given as the third equation from the top in Table 3.1. For deep water, the phase of the waves is hardly influenced by the depth (Faltinsen, 1990).

That the waves are linear means that the measure of nonlinearities is small. A perfect linear wave has equally large troughs and crests, while second-order solutions give the waves sharper crests and more shallow troughs. Regular linear waves are far from how ocean waves appear in reality, but they are useful in describing more general waves (Greco, 2019).

3.2 Ocean waves

The ocean is composed of waves of many different parameters. The sea surface can not be described on a single wave basis, but must rather be treated as stochastic. The statistical properties of waves may be found through frequency and probability domains. Wave heights of deep-water waves follow

Table 3.1: Equations for linear wave theory for infinite water depth.

Velocity potential	$\phi = \frac{g\zeta_a}{\omega} e^{k_w z} \cos(\omega t - k_w x)$
Wave number	$\frac{\omega^2}{g} = k_w$
Wavelength	$\lambda = \frac{g}{2\pi} T^2$
Wave profile	$\zeta = \zeta_a \sin(\omega t - k_w x)$
Dynamic pressure	$p = \rho g \zeta_a e^{k_w z} \sin(\omega t - k_w x)$
Velocity x-component	$u_x = \omega \zeta_a e^{k_w z} \sin(\omega t - k_w x)$
Velocity z-component	$u_z = \omega \zeta_a e^{k_w z} \cos(\omega t - k_w x)$
Acceleration x-component	$\dot{u}_x = \omega^2 \zeta_a e^{k_w z} \cos(\omega t - k_w x)$
Acceleration z-component	$\dot{u}_z = \omega^2 \zeta_a e^{k_w z} \cos(\omega t - k_w x)$

a Gaussian distribution. Shallow-water waves do not, but can still be described with a theoretical probabilistic distribution (Benitz, Lackner and Schmidt, 2015).

3.2.1 Response in irregular sea

Sea surface waves can be described by a combination of free-surface regular linear waves with different amplitudes, frequencies and phase angles. The resulting waves are then called irregular waves. The sum of the responses can be formulated as

$$\sum_{j=1}^{N} \zeta_{a,j} \left| H\left(\omega_j\right) \right| \sin\left(\omega_j t + \delta\left(\omega_j\right) + \epsilon_j\right) \tag{3.16}$$

where $|H(\omega_j)|$ is the transfer function. The transfer function describes the response amplitude per unit wave amplitude (Faltinsen, 1990). For the floating substructure, the relative importance of the response will depend on the natural period of the different modes of motion. In order to know at which periods or frequencies the waves have the most amount of energy, it is convenient with a way to describe the waves.

3.2.2 Statistical description of waves

By summarizing a large number of wave components, the wave elevation of a long-crested irregular sea propagating along the positive x-axis can be expressed as

$$\zeta = \sum_{j=1}^{N} = \zeta_{a,j} \sin(\omega_j t - k_{n,j} x + \epsilon_j) \tag{3.17}$$

where ϵ_j is the random phase angle of the wave component of number j. The phase angles are distributed between 0 and 2π and constant with time. Similarly to the wind spectrum, wave amplitude ζ_a can be expressed by using a wave spectrum $S(\omega)$

$$\frac{1}{2}\zeta_{a,j}^2 = S(\omega_j)\Delta\omega_j \tag{3.18}$$

where $\Delta\omega_j$ is a constant difference between successive frequencies (Faltinsen, 1990). It is hence possible to study the response of a marine structure to irregular waves as the sum of the response

to regular waves (Greco, 2019). Figure 3.2 shows how the frequency domain representation of the waves by a wave spectrum is related to the time domain solution. The wave shown previously in Figure 3.1 showed wave propagation reliant on time. In frequency domain however, the wave is described in terms of frequency. As mentioned for the wind spectra, frequency is given as $f = 1/T$.

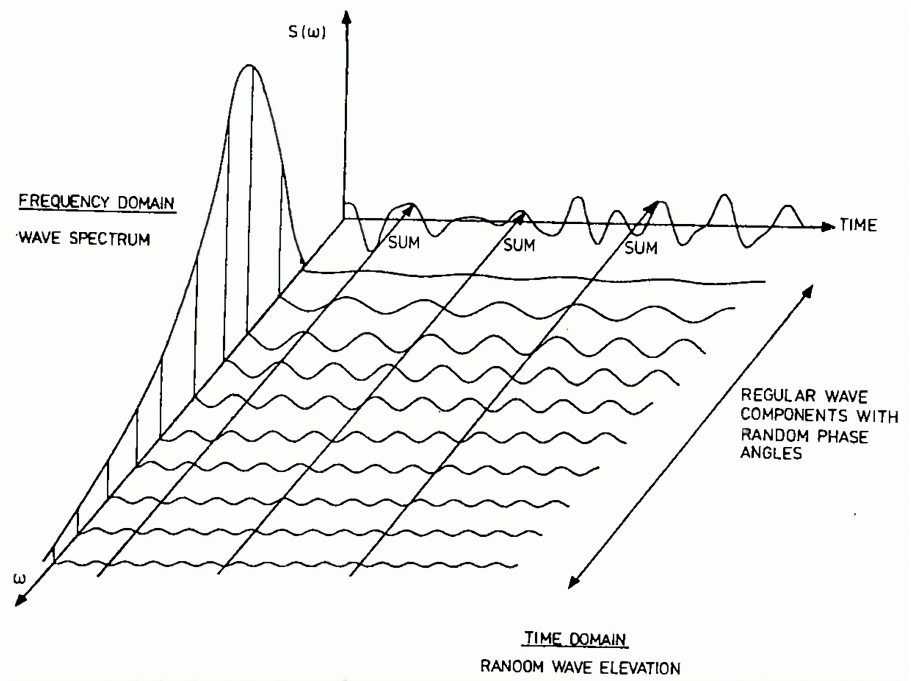

Figure 3.2: The connection between a frequency domain and time domain representation of waves in a long-crested short-term sea state (Faltinsen, 1990).

3.2.3 Wave spectra

When using the wave spectrum, it is assumed that the sea can be described as a stationary random process. The sea state is characterized by the *significant wave height* H_s and the *peak period* T_p, for it to be stationary the wave height and period are assumed constant. The sea surface can be assumed stationary for a duration of 20 minutes to a duration of 3 to 6 hours (DNV, 2014). This is referred to as a short-term description.

The International Towing Tank Conference (ITTC) recommends a modified Pierson-Moskowitz spectrum for fully-developed sea and a JONSWAP spectrum for limited fetch (Greco, 2019). The two-wave spectra are shown in Figure 3.3. In open sea areas, moderate and low sea states are often composed of both wind sea and swell. For these scenarios, DNV recommends a two-peak spectrum that can be used to account for both wind and swell, i.e., the OchiHubble spectrum or the Torsethaugen spectrum (DNV, 2014).

The Pierson-Moskowitz spectrum S_{PM}, is given by

$$S_{PM}(\omega) = \frac{5}{16} \cdot H_S^2 \omega_p^4 \cdot \omega^{-5} \exp\left(-\frac{5}{4}\left(\frac{\omega}{\omega_p}\right)^{-4}\right) \tag{3.19}$$

where $\omega_p = 2\pi/Tp$ is the angular peak frequency (DNV, 2014). The JONSWAP spectrum, S_J, is given by

$$S_J(\omega) = A_\gamma S_{PM}(\omega)\gamma^{\exp\left(-0.5\left(\frac{\omega-\omega_p}{\sigma_s \omega_p}\right)^2\right)} \tag{3.20}$$

where A_γ is a normalizing factor, S_{PM} is the Pierson-Moskowitz spectrum, γ is a non-dimensional peak shape parameter and σ_s is a spectral width parameter. The JONSWAP spectrum is assumed reasonable for $3.6 < T_p/\sqrt{H_s} < 5$.

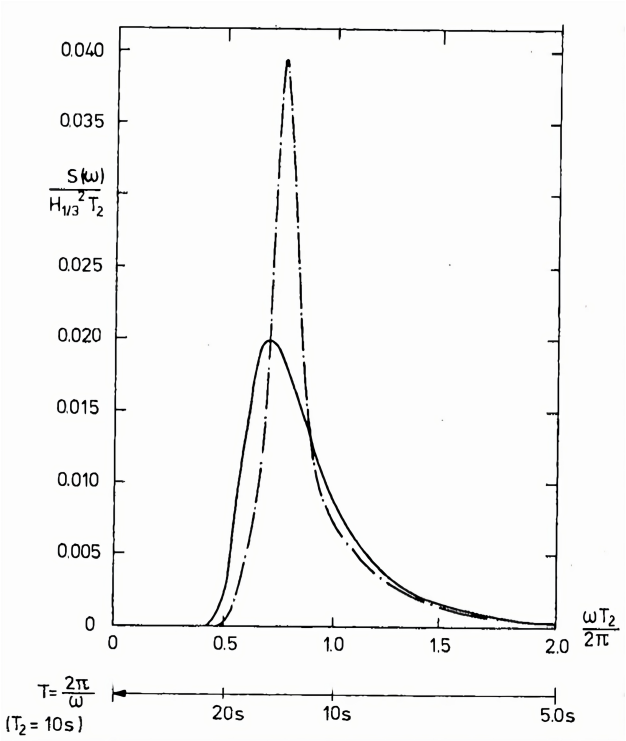

Figure 3.3: Modified Pierson Moskowitz spectrum (-) and JONSWAP spectrum (-.-) (Faltinsen, 1990).

Different sea states can alternate, and after one short-term sea state, another can occur. The re-occurrence of a certain sea state depends on the probability. A larger probability means that the sea state can be expected to occur longer. It is hence possible to sum up the short-term predictions, weighted by the probability, and get the long-term prediction(Greco, 2019).

3.3 Wave-body interaction

Motions can be divided into wave-frequency motion, high-frequency motion, slow-drift motion, and mean drift (Faltinsen, 1990). The degrees of freedom (DOF)s of the FOWT are defined in the inertial reference frame and the oscillatory translations and rotational motions are defined as surge, sway, heave, roll, pitch, and yaw (Greco, 2019), illustrated in Figure 3.4.

The translations are noted in terms of η_j where j is the mode number. The motion, at any point on the body, can hence be expressed as

$$\begin{aligned} s = &(\eta_1 + z\eta_5 - y\eta_6)\,\mathbf{i} + (\eta_2 - z\eta_4 + x\eta_6)\,\mathbf{j} \\ &+ (\eta_3 + y\eta_4 - x\eta_5)\,\mathbf{k}. \end{aligned} \tag{3.21}$$

where **i**, **j** and **k** are unit vectors along the x-, y- and z-axis, respectively.

3.3.1 Static loads

The most basic load case on a floating structure is on the body at rest. The structure will then experience a hydrostatic pressure acting normal to the wet surface. The forces in the vertical

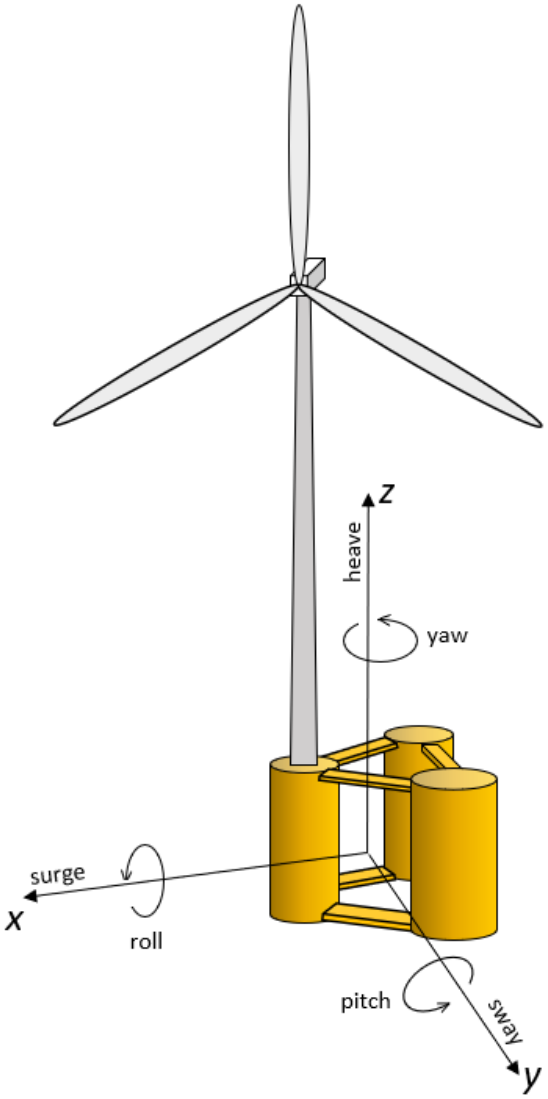

Figure 3.4: Cartesian coordinate system with translational and rotational motions.

direction are balanced by the gravitational force which acts on the mass of the structure, In the case of static equilibrium the buoyancy force equals the gravitational force,

$$F^{buoyancy} = F^{weight} \tag{3.22}$$

The hydrostatic loads are obtained by integrating the pressure along the wet surface of the body. For a linear problem the quadratic velocity term in Equation 3.4, Bernoulli's equation, and the pressure is hence given by

$$p = \underbrace{-\rho \frac{\partial \phi}{\partial t}}_{\text{dynamic= } P_D} - \underbrace{\rho g z}_{\text{hydrostatic}} . \tag{3.23}$$

For the body at rest, the dynamic part of the expression will be zero.

Static loads also include loads from currents. Currents can alter the shape and size of the waves. Current is generally assumed to be time-invariant and approximated by a mean value. The current induces pressure distributions on marine structures, which generate drag forces in the direction of

the flow (A. Robertson et al., 2014). The pressure distribution is not necessarily symmetric about the structure due to vortex shedding.

3.3.2 Dynamic loads

As the results in irregular sea can be obtained by superimposing results from regular wave components, it is sufficient to consider a structure in incident regular sinusoidal waves of small wave steepness. For the following theory, it is assumed a steady-state condition. Hence, the linear dynamic motions and loads on the structure are assumed to be harmonically oscillating with the same frequency as the wave loads which excite the structure (Faltinsen, 1990). The total hydrodynamic force on a floating structure is given by three separate contributions.

$$F^{Hydrodynamics} = F^{Hydrostatics} + F^{Diffraction} + F^{Radiation}. \tag{3.24}$$

Now, the hydrostatic forces include loads due to the changes in the water plane area, i.e. changes in pressure distribution over a wet surface. The pressure distribution is determined from Equation 3.23. The latter parts of the equations are the **diffraction** and **radiation** problems.

Diffraction is when the structure is fixed and there are incident waves. The loads are *wave excitation loads*, composed of Froude-Kriloff and diffraction forces and moments (Faltinsen, 1990).

Radiation is when the structure is forced to oscillate with the wave excitation frequency, with no incident waves. As the body moves, waves are generated (radiated), and the body is subjected to hydrodynamic loads identified as *added mass*, *damping*, and *restoring* terms (Greco, 2019). The restoring terms are connected with the hydrostatic pressure, while added-mass and damping terms are connected with the dynamic pressure caused by the body motions, given by

$$F_k = -A_{kj}\frac{\mathrm{d}^2\eta_j}{\mathrm{d}t^2} - B_{kj}\frac{\mathrm{d}\eta_j}{\mathrm{d}t} \tag{3.25}$$

A_{kj} and B_{kj} are the added mass and damping coefficients. The indexes j and k represent the six DOFs. Unequal indexes ($j \neq k$) express a coupling between DOFs, so motion in j, affects motion in k. The added mass and damping depend on the body form, frequency of oscillation, and forward speed (Faltinsen, 1990). Added mass is described in terms of the fluid displaced by the moving body. The mass of the structure does not change, but it experiences a change in inertia per unit mass (Benitz, Lackner and Schmidt, 2015). The damping of the structure is connected with the wave energy radiated from the body. It is linked to the amplitude squared of far-field waves generated by the body as it oscillates (Greco, 2019).

The character of the wave-body interactions depends significantly on the size of the body. Typically size distinction is done by looking at the size of the structure, the wavelength and the wave amplitude ζ_a. The wave-size ratio, along with the Keulegan-Carpenter (KC) number and Reynolds number is important in assessing the validity of different methods of wave load calculations (Benitz, Lackner and Schmidt, 2015). Reynolds number is given by

$$Re = \frac{uD}{\mu} \tag{3.26}$$

and describes whether the fluid flows laminarly or turbulently. The Keulegan-Carpenter number is given by

$$KC = \frac{u_m}{D} \tag{3.27}$$

and compares the drag coefficient to inertial forces.u is flow velocity, u_m is maximum flow velocity, D is diameter and μ is viscosity. An approximate mapping of the different load regions is shown in Figure 3.5.

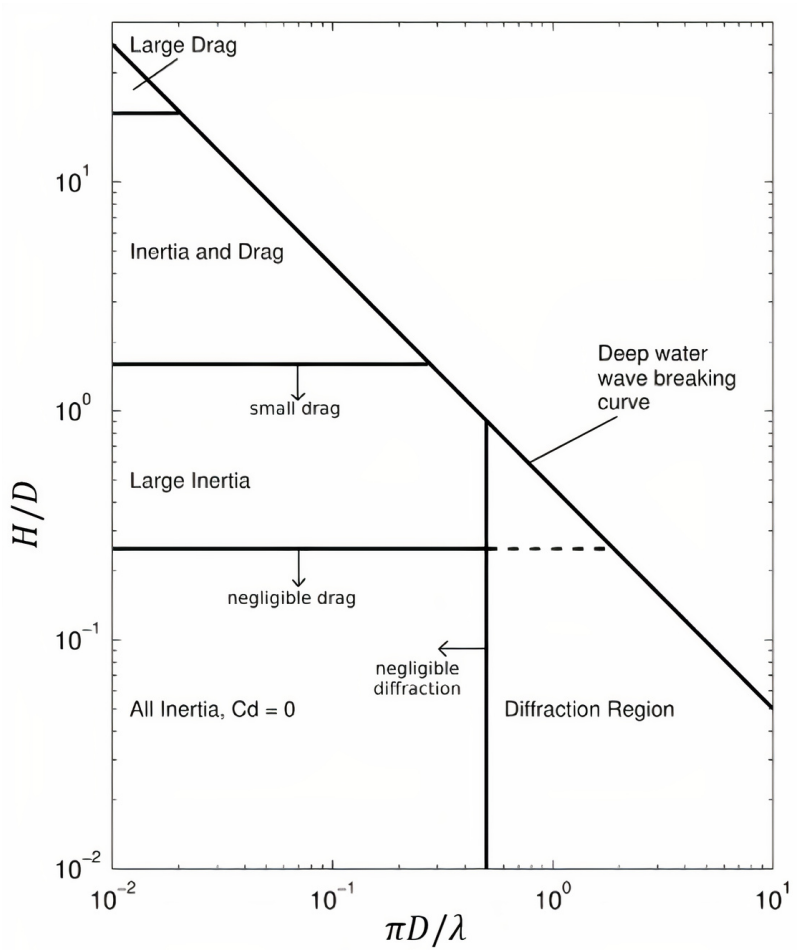

Figure 3.5: Classification of structures and limits of applicability adapted from Chakrabarti (2005).

Typically, wave loads on a floating platform fall into one of two categories. In the case of cross-sections small relative to wavelength, $D/\ \lambda < 0.05$, free surface effects are not as significant as the oscillatory drag due to separation (Newman, 1992). In this case, Morison's equation is used.

3.3.3 Morison's equation

Morison's equation is an empirically derived hydrodynamic loading model. It captures excitation from waves, added mass effects, and viscous forces (A. Robertson et al., 2014). Morison's equation consists of two terms representing the drag and inertial forces of the body. The equation is expressed as

$$F = \rho C_m V \dot{u} + \frac{1}{2}\rho C_d A u|u| \tag{3.28}$$

where C_M and C_D are the mass and drag coefficients, which have to be empirically determined and depend on several parameters. Morison's equation can be adjusted to account for the current and/or moving body. Morison is also applicable for wind loads, where ρ would then be the density for wind.

When the size of the structure is increasing, wave diffraction and radiations become more significant. Viscous effects are of less importance due to a reduced KC number. It is hence appropriate to assume potential flow and to account for free-surface effects (Newman, 1992). For simulations using a combined-theory approach, the potential-flow solution is used to model the radiation and

diffraction loads while Morison's equation is used to model the viscous drag loads (A. Robertson et al., 2014).

3.3.4 Cancellation effect

An important effect relevant for a semi-submersible FOWT is the cancellation effect. If looking at the motion in heave, the main contribution to the vertical excitation force F_3 comes from the pressure force acting on the pontoons. If the wavelength is equal to the length of the pontoon, i.e., a wave crest is present at one end and a wave through at the other end, the force will act in opposite directions and cancellation occurs, as illustrated in Figure 3.6.

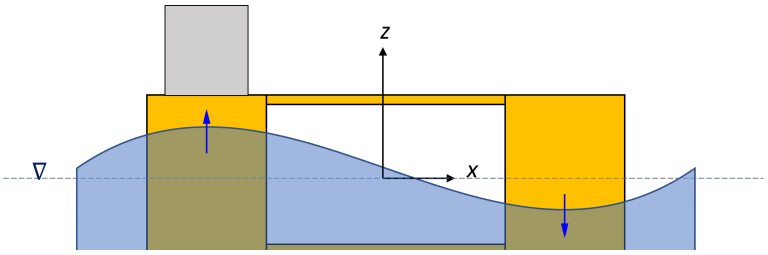

Figure 3.6: Cancellation of heave motion of FOWT sub-structure.

3.4 Non-linear waves

If the waves become to steep, or the water becomes to shallow, the linear wave theory, as described in the previous sections, is no longer valid. The wave spectrum no longer provides complete statistical and physical description of the waves. A "real" nonlinear wave is compared to a cosine wave in Figure 3.7.

For linear wave theory, the wave-induced motions and load amplitudes are linearly proportional to the wave amplitude ζ_a. To a large extent, linear theory can describe the wave-induced motions and loads on a semi-submersible. However, non-linear effects are important when severe sea states are considered, and when describing the horizontal motions of a moored structure (Faltinsen, 1990). FOWT will be deployed in increasingly deeper water so the nonlinearity of waves due to shallow water becomes less prominent. Nevertheless, the FOWT will be moored. Hence, a brief overview of non-linear effects are included.

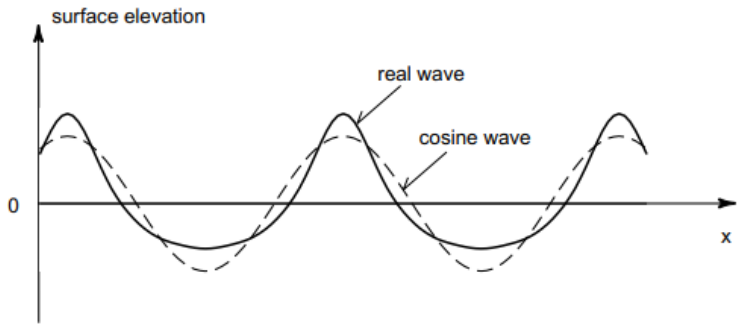

Figure 3.7: Nonlinear wave compared to a linear cosine wave (Brorsen, 2007).

The degree of wave non-linearity can be described by the Ursell number U_r

$$U_r = \frac{\text{steepness}}{(\text{ relative depth })^3} = \frac{H/\lambda}{(h/\lambda)^3} = \frac{H\lambda^2}{h^3}. \tag{3.29}$$

Classical nonlinear wave theories typically assume each wave as one wave in a train of periodic but not harmonic waves. Each with a constant shape, amplitude and length. An overview of the applicability of nonlinear wave theories is given in Figure 3.8. Stokes and Deans theory are typically used for steep waves with U_r<10, while the cnoidal theory is used for shallow water with U_r>26 (Holthuijsen, 2007).

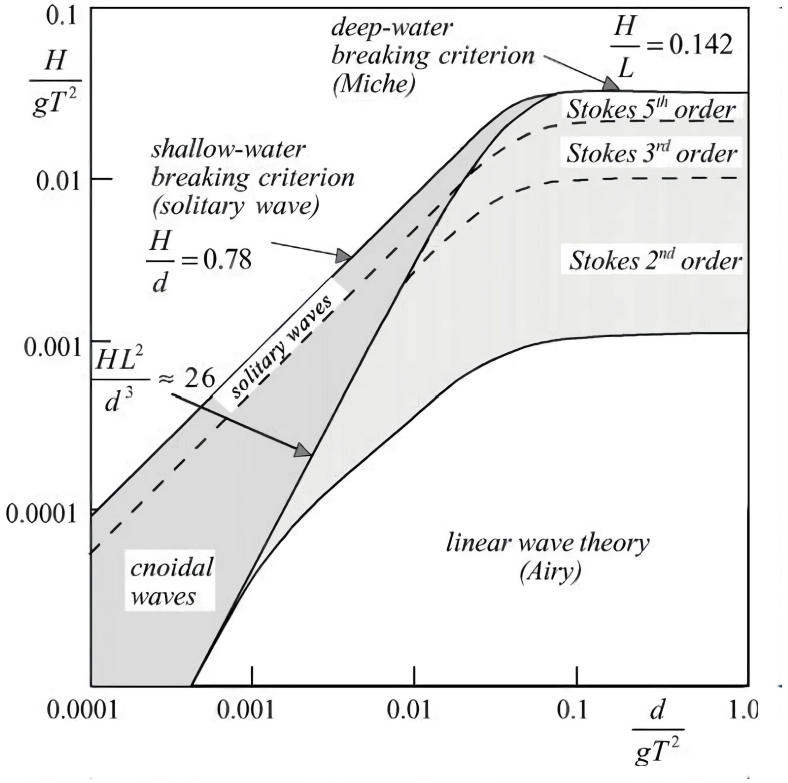

Figure 3.8: Applicability of wave theories (Holthuijsen, 2007).

In Stokes theory, the non-linearities are approximated by adding corrections to the harmonic wave profile. The corrections typically results in steeper crests and wider troughs than for regular waves. The second order Stokes theory provides an extra harmonic wave written with the wave steepness raised to the power of two (hence second-order). Using linear theory, the nonlinear euation are solved for an extra wave with nonlinear boundary conditions (Holthuijsen, 2007), given as

$$\eta(x,t) = a\cos(\omega t - k_w x) + ka^2 \frac{\cosh(k_w d)}{4\sinh^3(kd)}[2+\cosh(2k_w d)]\cos[2(\omega t - k_w x)]. \tag{3.30}$$

The first term on the right-hand side is the Airy wave of the linear wave theory and the second term is the second order correction. This practice is expanded by adding more corrections for the higher order corrections of Stokes theory (Holthuijsen, 2007). The software used later on for the coupled analyses relies on Stokes for irregular wave calculations.

4 FOWT dynamics

For a platform moving in waves with a flexible tower equipped with a rotating turbine, there is a complex interrelation in the dynamic behavior of the system. As introduced in the past two sections, the wind turbine experiences aerodynamic forces from the wind, while the platform experiences hydrodynamic loads from the waves. These external loads also cause displacements and oscillations in the FOWT system.

For the rigid platform body, the whole body oscillates without individual members experiencing bending. The motion is coupled with the control system of the wind turbine. The flexible tower can bend and vibrate in response to the external loads. The vibration of the tower can be excited by the frequency of the turbine rotor speed. Structural dynamics aims at assessing the integrity and reliability of the structure against the varying loads over the targeted lifetime (Voutsinas, 2010). The structural dynamics for a FOWT is outlined in this section through platform body oscillations, wind turbine control system, the behavior of a flexible tower modeled as an Euler-Bernoulli beam, and lastly tower limit states in terms of tower buckling and fatigue.

4.1 Body oscillations

Due to the external forces experienced by the FOWT, the body starts moving. As it moves, internal forces in terms of elastic energy develop trying to bring the system back to the original position. Upon reaching equilibrium, the energy is converted to kinetic energy and the body continues to move in the opposite direction. The kinetic energy is then again converted to strain or elastic energy which coerces the system back to equilibrium. The motion can be repeated indefinitely through this energy exchange (Chandrasekaran, 2015).

Motion that repeats itself after an interval of time is called vibration. The time it takes to complete one cycle is the *time period*, and the number of cycles per unit time is the *frequency*. These terms were introduced in Section 3, as it is the same concept as for a regular sinusoidal wave. For a system exposed to an initial displacement without any external forces, the resulting free vibrations oscillate with the *natural frequency*. If an external force is applied with the same frequency as the natural, the amplitude of vibration becomes extensively large, i.e. resonance occurs (Chandrasekaran, 2015).

Oscillation, natural frequency, and resonance can in a simplified manner be expressed through a single Degree of Freedom (DOF) mass-spring-damper system, like the one illustrated in Figure 4.1. A one DOF system can then be expanded to a multi-body system where the equation of motion is written on matrix form.

4.1.1 One degree-of-freedom system

The characteristics of the one DOF system are given by the mass m, a spring element representing the stiffness k, the damping element c, and the external force P(t) causing a displacement u(t). The energy of the system is stored by the mass as kinetic energy and by the spring as potential energy (Chandrasekaran, 2015). Equilibrium between the external force, internal restoration force, and damping force can be found through Newton's second law of motion. The equation is known as the **equation of motion** and is, for a one DOF system, given by

$$m\ddot{u} + c\dot{u} + ku = P(t). \tag{4.1}$$

The time-dependent displacement u(t), i.e. the response of the system is given by

$$u(t) = u_H(t) + u_p(t). \tag{4.2}$$

where u_H is the contribution from the homogeneous solution which is found by setting P(t) equal to

zero, and u_P is the contribution from the particular solution. In the situation illustrated in Figure 4.1, the mass is resting on a surface, meaning that the system is not influenced by a constant external force like gravity (Larsen and Bachynski, 1990). This non-deformed state is taken as a reference for the explanation of the equation of motion problem divided into free oscillation and forced oscillation.

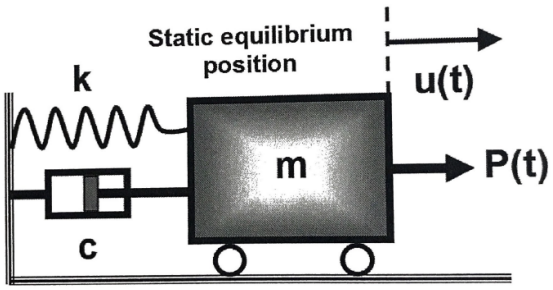

Figure 4.1: Illustration of one DOF system (Larsen and Bachynski, 1990).

4.1.2 Free oscillation

Free oscillation is when the system vibrates due to an initial displacement given to the body but in the absence of any persistent external forces. For this vibrating system, one of two things will happen. 1) there is no damping and the kinetic and potential energy exchange is kept constant, keeping the system vibrating to the end of time. 2) Damping is present and vibration will eventually diminish and the system comes to a stop. The damping is hence the resistance of the body to the motion of vibration (Chandrasekaran, 2015). For an offshore structure, the water is an important source of damping. When the system vibrates in a viscous medium, like water, the damping is called viscous damping. In real life, there will always be some form of damping. Hence, $c \neq 0$.

For free oscillation, the force P(t) is equal to zero. Equation 4.1 thus becomes

$$m\ddot{u} + c\dot{u} + ku = 0. \tag{4.3}$$

The characteristic solution for non-trivial solutions is given by

$$s = \omega_0(-\frac{c}{2m\omega_0} \pm \sqrt{(\frac{c}{2m\omega_0})^2 - 1}) \tag{4.4}$$

where s is a complex constant and ω_0 is the natural frequency defined by

$$\omega_0 = \sqrt{\frac{k}{m}} rad/s. \tag{4.5}$$

Equation 4.4 has three different types of solutions, based on the type of damping. The damping types are **sub-critical damping**, **critical damping** and **supercritical damping** (Larsen and Bachynski, 1990) (also called under-damped, critically damped and over-damped (Chandrasekaran, 2015)).

With damping equal to critical damping there will be no oscillation. Critical damping, c_{cr}, is given by

$$c_{cr} = 2\sqrt{mk} = 2m\omega_0. \tag{4.6}$$

In practice, marine structures will not have damping equal to critical damping. However, the critical damping is useful as it is used in the damping ratio ξ_d:

$$\xi_d = \frac{c}{c_{cr}} = \frac{c}{2m\omega_0}. \tag{4.7}$$

Supercritical and sub-critical damping are subsequently defined in terms of the damping ratio. For $\xi_d > 1$ the damping is supercritical, and the system expresses a strongly damped motion without oscillation. For $\xi_d < 1$ the damping is sub-critical, which is the most common for real structures (Larsen and Bachynski, 1990). For a damped system, the natural frequency ω_0 becomes the damped natural frequency ω_d, given by

$$\omega_d = \omega_0\sqrt{1-\xi_d^2} \tag{4.8}$$

Following the damped natural frequency, the damped natural period is given by

$$T_d = \frac{2\pi}{\omega_d}. \tag{4.9}$$

The damped natural period is also shown in Figure 4.2 which illustrates free oscillation for a sub-critically damped system. The initial displacement (in the figure termed using capital U), is seen to initiate an oscillatory motion which then decays towards zero. The decaying is due to the damping present in the system. The displacement solution for the system is given by

$$u(t) = e^{-\xi_d\omega_d t}(A\sin(\omega_d t) + B\cos(\omega_d t)) \tag{4.10}$$

where A and B are constants that can be found when the initial conditions are known (Larsen and Bachynski, 1990). The term $Re^{-\xi_d\omega_d t}$ in Figure 4.2 is the real part of $e^{-\xi_d\omega_d t}$.

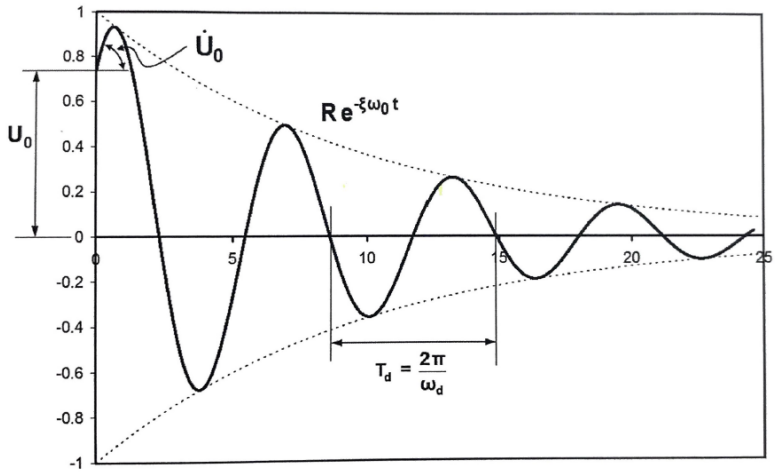

Figure 4.2: Free oscillation of the sub-critically damped system (Larsen and Bachynski, 1990).

4.1.3 Forced oscillation with simple harmonic load

When subjected to a harmonically varying load, P_0 and circular frequency ω, the equation of motion is given as

$$m\ddot{u} + c\dot{u} + ku = P_0\sin(\omega t). \tag{4.11}$$

As recalled from Equation 4.2, the homogeneous part of the solution, u_H, was found when $P(t) = 0$. For the case of forced oscillation, $P(t) \neq 0$ and the particular solution, u_p, is given by

$$u_p = C_1 \sin(\omega t) + C_2 \cos(\omega t) \tag{4.12}$$

where C_1 and C_2 are constants. If u_p is inserted into Equation 4.11, the following two equations are found

$$\begin{aligned} -m\omega^2 C_1 - c\omega C_2 + kC_1 &= P_0 \\ -m\omega^2 C_2 - c\omega C_1 + kC_2 &= 0. \end{aligned} \tag{4.13}$$

Solved for the integration constants, it becomes

$$\begin{aligned} C_1 &= \frac{P_0}{k} \frac{1-\beta^2}{((1-\beta^2)^2 + (2\xi_d)\beta)^2} \\ C_2 &= \frac{P_0}{k} \frac{2\xi_d \beta}{((1-\beta^2)^2 + (2\xi_d)\beta)^2} \end{aligned} \tag{4.14}$$

where β is the frequency ratio given by

$$\beta = \frac{\omega}{\omega_0}. \tag{4.15}$$

The particular solution is then

$$u_p = \frac{P_0}{k} \frac{1}{(1-\beta^2)^2 + (2\xi_d\beta)^2} [(1-\beta^2)\sin\omega t - 2\xi_d\beta\cos\omega t]. \tag{4.16}$$

The homogeneous solution will die out after some time, due to the exponential term in Equation 4.14 (Larsen and Bachynski, 1990). The harmonic response can hence be simplified to

$$u_p = R_{amp} \sin(\omega t - \theta) \tag{4.17}$$

where R_{amp} is the amplitude of the response given by

$$R_{amp} = (C_1^2 + C_2^2)^{\frac{1}{2}} = \frac{P_0}{k} \frac{1}{[(1-\beta^2)^2 + (2\xi_d\beta)^2]^{\frac{1}{2}}}. \tag{4.18}$$

The phase angle, θ, by which the response lags behind the applied loading is given by

$$\theta = \arctan(-\frac{C_2}{C_1}) = \arctan(\frac{2\xi_d\beta}{1-\beta^2}). \tag{4.19}$$

θ ranges between 0 and 180 degrees. The ratio of the resultant harmonic response amplitude to the static displacement is called the dynamic load factor Dynamic Load Factor (DLF) and is given as

$$DLF = |\frac{u_{maks}}{u_{st}}| = \frac{1}{[(1-\beta^2)^2 + (2\xi_d\beta)^2]^{\frac{1}{2}}}. \tag{4.20}$$

If the enforced frequency approaches the natural frequency for $\beta \to 1$, then the maximum response will increase, i.e., resonance occurs. For the floating semi-submersible, the natural period of the different modes of motion will determine the relative importance of the response. Near resonance,

the FOWT will have the largest motion amplitude. If any of the DOFs have natural periods in the wave-frequency range, then it can be excited as a wave-frequency motion. For very large motions, nonlinear effects may also become important and excite high-and/or low-frequency motions. Nonlinear effects are the only contribution to motion excitation if the natural period of the marine unit is outside the wave-frequency range and in a steady-state condition (Greco, 2019).

Depending on the site, ocean waves typically contain first-order energy in the range of 3 to 30 s (ABS, 2020). The semi-submersibles upscaled in this master are both column stabilized. This design is characterized by having natural periods outside the range of energetic wave periods. However, the wave frequency motions of the platform may be significant, especially in extreme environmental conditions (ABS, 2020).

For a semi-submersible wind turbine, low-frequency motions can be of importance as the natural period is higher. With both waves and wind, non-linear effects cause slow drift and mean motions. The slow drift motion arises from resonance oscillations. For a moored structure, such as the wind turbine, it occurs in surge, sway, and yaw (Faltinsen, 1990).

4.1.4 Natural period of the platform body

As seen from the derivation of the equation for damped natural frequency, Equation 4.8, the natural period depend on the restoring and mass contributions. Natural periods of typical FOWTs are shown in Table 4.1. The relevant type for the upscaled 25 MW platform is the semi-submersible type.

Table 4.1: Representative natural periods for FOWT substructure (ABS, 2020).

Motion	**Natural periods [s]**		
	Spar-Type	Semi-Submersible-Type	TLP-Type
Surge	>40	>40	>40
Sway	>40	>40	>40
Heave	20-50	17-40	<5
Roll	25-60	25-50	<5
Pitch	25-60	25-50	<5
Yaw	>3	>3	>3

The semi-submersible receives damping from the surrounding fluid either in the form of viscous damping or wave radiation damping. Surge, sway, and yaw are typically dominated by viscous damping, while heave, roll, and pitch are dominated by linear damping from wave radiation (Faltinsen, 1990). The restoring force of the system is due to both equilibrium between weight and buoyancy, as well as the restoring force of the mooring system. Restoring forces are kept approximately constant for later design modifications of the turbine tower. Changes in natural periods of the semi-submersible will hence mostly rely on potential weight difference. Changing the mass contribution will affect the draft of the FOWT, the Center of Gravity (COG), and the Center of Buoyancy (COB). Making a floating body lighter will cause a smaller draft and shift the COG and COB. A smaller draft means less fluid to displace, typically resulting in shorter natural periods for surge and sway. For rotational translations like roll and pitch, removing weight at a distance from the platform will lower the total COG and subsequently increases the natural period for roll and pitch.

The natural period of the FOWT system can also be found through decay tests. The natural period is then found by determining the average period between oscillation peaks of the body moving freely after initiating movement. A decay test without wind could look similar to the decaying oscillation in Figure 4.2. The key note here is "without wind", as natural periods for the platform are reliant on whether or not the wind turbine is operational, and at what wind speed it is operating. Especially surge and pitch show variations in decay periods when subjected to different incident wind velocities (Carlos Eduardo S. Souza and Bachynski, 2019). To illustrate, Figure 4.3 show surge and pitch for a three-column semi-submersible concept known as the OC4semi, as defined by Robertson et al. (2014).

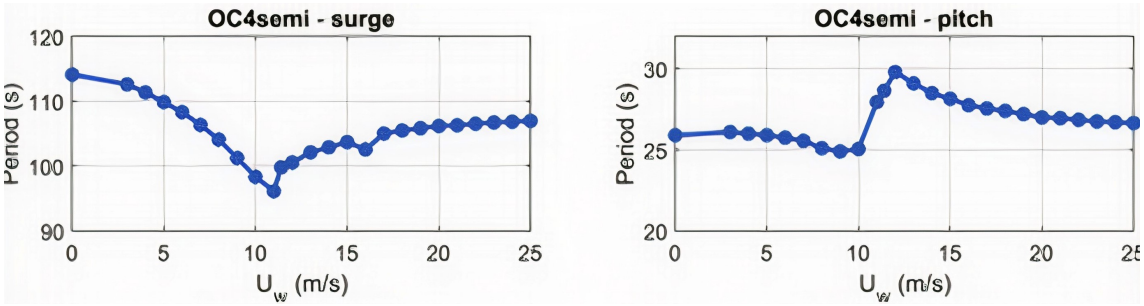

Figure 4.3: Surge and pitch decay with increasing wind speed (Carlos Eduardo S. Souza and Bachynski, 2019).

Surge motion shows a decreasing natural period for increasing wind velocities up until a wind velocity of 11 m/s, after which it starts increasing moderately. Pitch is roughly constant until 5 m/s before it starts decreasing, suddenly increasing, and then decreasing again. In the research paper from which Figure 4.3 is referenced, Carlos Eduardo S. Souza and Bachynski (2019) found that period variations in surge were dominated by the mooring system nonlinearities, as the wind displaces the platform, straightening mooring lines. They further found that pitch was affected by the relative phase between the nacelle velocity and the thrust induced in the rotor, leading to an "apparent inertia/damping" effect. The large differences in natural period at around 11 m/s is hence due to this being the *rated* wind speed, where the thrust force is at a maximum and the wind turbine control system acts to limit loads on the turbine. For a FOWT with an operating turbine, it is important with an accurate estimation of natural periods to ensure proper tuning of the turbine control system. This in turn ensures a fair prediction of the rigid-body response to linear loads (Carlos Eduardo S. Souza and Bachynski, 2019).

4.2 Wind turbine control system

The control system creates a coupled interaction between the hull motions and the control system (ABS, 2020). As the wind turbines are increasing in size, the control system plays an increasingly important role in the response of the system. Optimizing the control system has been found to reduce motion and loads on the system (J. M. Jonkman, 2008).

4.2.1 Operating strategies

Control systems of wind turbines are typically divided into three parts: (1) wind farm controller, (2) supervisory controller, and (3) dynamic controller (Manwell, McGowan and Rogers, 2010). The first one controls several wind turbines in a wind farm. The supervisory controller controls operation and sequences for each turbine, for example, startup and shut-down. Dynamic control controls the various subsystems of the turbines, like pitch control or generator torque. In terms of reaction time, the supervisory control tends to be slow in comparison to the operational controller, except in cases of fault detection. It is the quick reactions of the generator torque and the blade pitch controller which will influence the FOWT dynamics the most.

Most wind turbines today operate with Variable Speed Variable Pitch (VSVP). As implied by the name, these turbines can rotate at various speeds and the blade pitch can be altered. This allows for higher aerodynamic efficiency and the ability to better control the aerodynamic loads. The strategy of a VSVP turbine is illustrated in Figure 4.4 and shows the mean rotor speed, the generator torque, generator power, and blade pitch angle as a function of wind speed. The different regions describe different stages of the operational controller (Bachynski-Polić, 2021).

- **Region 1.** The wind speed is too low for the wind turbine to start rotating, and no power is extracted.

- **Region 2.** The wind turbine has started rotating and is trying to extract as much power as possible. The rotor speed is increasing approximately linearly with wind speed, the generator torque increases quadratically, while generator torque increases approximately cubically.
- **Region 3.** The turbine has reached the rated wind speed and is now operating at a constant mean rotor speed, with a constant mean power extraction and torque.
- **Region 4.** The wind speed is too high for the turbine to operate safely. The blades are fully pitched and there is no power being extracted.

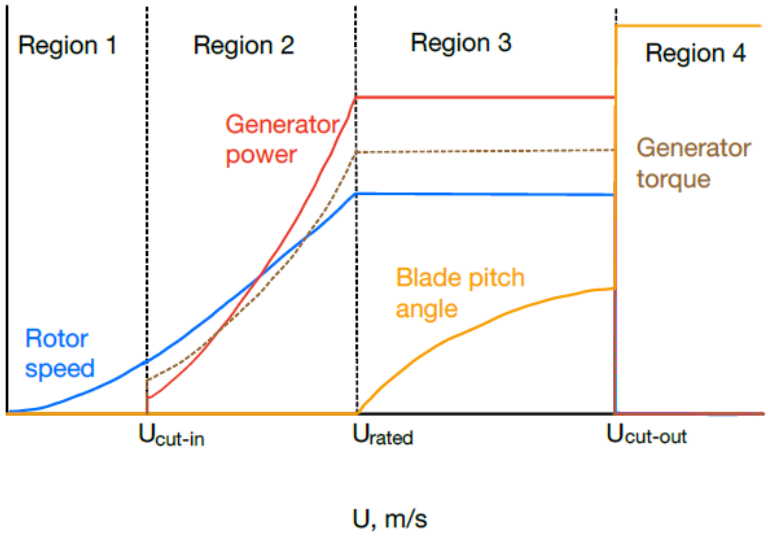

Figure 4.4: VSVP operational strategy (Bachynski-Polić, 2021).

At **below-rated** wind speed, the torque controller typically has full responsibility for the turbine operation. The goal is to maximize power output, i.e. maximizing the aerodynamic power coefficient C_p from Equation 2.15. C_p is typically maximum at a specific tip speed ratio, hence the controller tries to maintain an approximately constant tip speed ratio (Bachynski-Polić, 2021).

When reaching **above-rated** wind speed, both the torque control and pitch control are active and attempt to keep the rotor speed from exceeding the rated rotor speed. The generator torque is either adjusted to try and maintain constant power or kept constant as long as rotor speed is above or equal to the rated wind speed. The latter is the most common strategy for FOWT (Bachynski-Polić, 2021).

4.2.2 Negative feedback

The control system of a fixed wind turbine does not understand the motions of a floating wind turbine. Pitch control in combination with aerodynamics and FOWT motion can result in negative feedback (J. M. Jonkman, 2008).

The pitch controller changes the pitch angle of the blades to regulate the rotating speed of the wind turbine. If the rotor speed exceeds the rated rotor speed the pitch angle is increased, hence lowering the rotor torque. A FOWT will experience motion. If the nacelle moves forward, the wind speed is experienced as increasing. The controller hence pitches the blades, resulting in a reduction in rotor thrust which further causes the nacelle to move forward (Veen, Couchman and Bowyer, 2012). This is not a common problem for bottom fixed turbines due to the different natural periods governing the structure. Bottom fixed wind turbines typically have the longest natural period in the range of 3-5 seconds (Bachynski-Polić, 2021). For a controller with a control period of 10 s, the controller has no time to react. A floating platform has much longer natural periods, as shown

in Table 4.1. Hence, the controller has time to react and negative damping can occur. The same occurs in reverse when the nacelle moves backward.

4.2.3 Negative feedback mitigation

There are several ways to try and mitigate the negative damping. The ones mentioned here are detuning the controller, applying a notch filter, and including nacelle velocity feedback.

1. Detuning the controller
This strategy implies making the controller slower than the platform dynamics. So for a platform with a 30 s natural period in pitch, the controller can be tuned to 34 s. The downside is that the controller becomes very slow, hence power fluctuations may become large. Detuning is frequently used in academic studies but is typically not an accepted approach in real-life (Bachynski-Polić, 2021).

2. Applying notch filter
By applying a notch filter the resonant platform motions can be removed from the measured shaft speed. Ideally, the filter would only remove frequency content in that specified range. It is however difficult to implement, as the pitch period can change with wind speed, as previously shown in Figure 4.3, and the notch has to be placed perfectly. It must also not introduce large delays (Bachynski-Polić, 2021).

3. Including nacelle velocity feedback
This method is accomplished by equipping the turbine with additional sensors and providing the turbine with information about the nacelle velocity. This velocity can be multiplied by some gain and added to the blade pitch angle, or used to vary the target rotor speed (Bachynski-Polić, 2021).

4.2.4 1P and 3P

The rotation of the wind turbine also gives rise to the 1P and 3P frequencies. 1P represents the frequency in which the rotor completes one whole rotation. As seen from Figure 4.4, a VSVP turbine has a varying rotational speed. The 1P will span from the lowest rotation speed to the highest rotational speed. It is hence the most variation in region 2, before reaching rated wind speed. The 1P is found by measuring the turbine Rotations per Minute (RPM), and dividing it by 60 s to get the frequency. 3P frequency is the rotor blade passing frequency, for a three-bladed rotor (Tempel, 2006). The 3P frequency is found by dividing the 1P frequency by 3.

As the blades rotate, the turbine tower experiences a sudden drop in wind pressure, when shielded by the wind turbine blade. The frequency at which the 1P and 3P operate at are typically much higher than natural frequencies in global platform motions and create little risk of resonance. However, natural periods of tower bending are typically closer to the 1P and 3P regions. The resonance between tower bending and the rotational frequencies can create large vibrations motions. This is of concern for the tower, which is a flexible body.

4.3 Vibration of flexible wind turbine tower

When considering flexible bodies, the equilibrium equation of the system not only depends on time but also on a spatial variable. The wind turbine tower is to be modeled as a flexible beam following the Euler-Bernoulli beam theory. Displacement of elastic beams can be determined by solving corresponding differential equations.

A beam is defined as a structure where one of the dimensions is significantly larger than the two others (O. A. Bauchau, 2009). With the wind turbine tower modeled as a beam, the solid mechanics theory of beams provides a measure to analyze the structure. Several beam theories exist, but here the Euler-Bernoulli beam theory is emphasized as it is the beam theory used in SIMA.

The Bernoulli beam theory is a technical theory of elastic beams. An important aspect of upscaling FOWTs is that the towers become so large that it is no longer reasonable to assume that it behaves as a rigid beam. It is hence necessary to look at the tower as a flexible beam that will experience bending. For Bernoulli beam theory, both statics and kinematics are included. This means both internal forces and loads, as well as displacements and deformations, as illustrated in Figure 4.5. The Bernoulli beam theory also considers the effect of the beam's mechanical behavior and support conditions. For a simply supported beam, the six internal forces are the axial force N, the shear forces Q_y and Q_z, the bending moments M_y and M_z, and the torsional moment M_x.

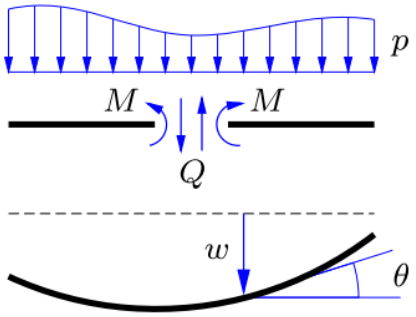

Figure 4.5: Static and kinematic in Bernoulli beam theory (Krenk and Høgsberg, 2013).

A few fundamental assumptions need to be in place for the Euler-Bernoulli beam theory to be valid. The first one regards in-plane displacements and states that the cross-section of the beam is infinitely rigid in its own plane. This means that even though the beam can deform, there is no deformation in the plane of the cross-section. For out-of-plane deformations, the cross-section is assumed to remain plane and normal to the deformed axis of the beam (O. A. Bauchau, 2009). For homogeneous beams for which the length is 10 to 20 times longer than the cross-sectional length, the shear fraction is typically disregarded (Öchsner, 2021). Other beam theories, like the Timoshenko beam, take shear forces into account.

4.3.1 Time-varying loads

A beam carrying a distributed load q is illustrated in Figure 4.6 (q is noted p). The normal force is not shown in the figure, but the results are similar to those of the shear force (Krenk and Høgsberg, 2013).

The partial differential equations for the shear force distribution and the moment distribution are obtained by considering the equilibrium of a slice of the beam (Krenk and Høgsberg, 2013). The equations for shear force and moment are hence given as

$$\frac{\partial Q}{\partial x} = -q(x) \tag{4.21}$$

and

$$\frac{\partial M}{\partial x} = Q(x). \tag{4.22}$$

By combining them it can be shown that the second derivative of the moment is given by

$$\frac{d^2 M}{dx^2} = -q(x). \tag{4.23}$$

As a flexible beam is exposed to these static loads, the beam may bend. In homogeneous bending, the beam is experiencing moments of equal magnitude but opposite orientation. The cross-section

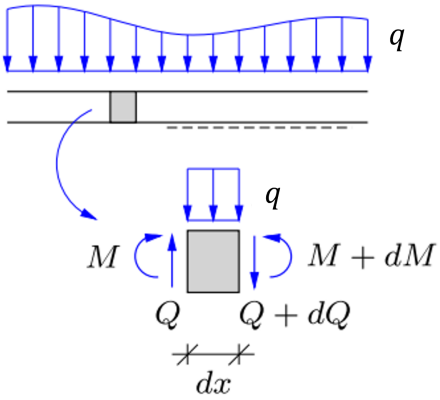

Figure 4.6: Beam with distributed load (Krenk and Høgsberg, 2013).

of the beam remains orthogonal to the beam axis in the deformed state. In non-homogeneous bending the cross-section is inclined due to the moment along the beam, generating a shear force. However, this deviation is often small (Krenk and Høgsberg, 2013). Figure 4.7 show a homogeneous beam bending. It will experience a compression on the upper side and an extension on the lower side. s denotes the arc length, which follows the axis taken as the intersection of the neutral plane and the plane of symmetry. Equilibrium here implies that the internal moment is equal to the imposed moment for any value along s. The internal moment is the same for each cross-section and hence the beam bends into a circle with center C and radius R, as shown in Figure 4.7.

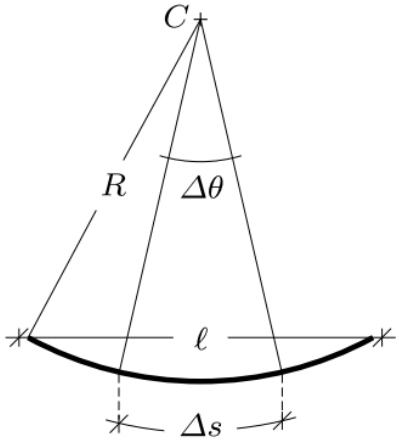

Figure 4.7: Beam bent into a circle with center C and radius R (Krenk and Høgsberg, 2013).

The deformation of the bending can be described by a curvature, denoted by kappa, κ:

$$\kappa = \frac{1}{R} = \frac{\Delta\theta}{\Delta s} \tag{4.24}$$

$\Delta\theta$ is the angle between two cross-sections. If the initial length of the beam is δs, then after deformation, the length will be

$$\Delta s_* = (R + z)\Delta\theta = (R + z)\kappa\Delta s \tag{4.25}$$

The elongation corresponds to the normal strain, ϵ, given by

$$\varepsilon = \frac{\Delta s_* - \Delta s}{\Delta s} = \kappa z. \tag{4.26}$$

Hence, the normal strain is proportional to the curvature and to the distance from the neutral axis (Krenk and Høgsberg, 2013). For linear elastic material, the normal stress is given by

$$\sigma = E\varepsilon = E\kappa z \tag{4.27}$$

where E is the modulus of elasticity. Only pure bending is included, hence there is no normal force

$$N = \int_A \sigma dA = \kappa \int_A E z dA = 0. \tag{4.28}$$

The bending moment generated by the normal stress σ, is determined by

$$M = \int_A z\sigma dA = \kappa \int_A z^2 E dA. \tag{4.29}$$

In Bernoulli beam theory it is assumed that the shear force does not directly contribute to the deformation of the beam. There is hence proportionality between the curvature and bending moment, shown by

$$M = EI\kappa \tag{4.30}$$

where EI is the bending stiffness of the beam, consisting of the modulus of elasticity and the moment of inertia, I. For a pipe cross-section, the moment of inertia is given by

$$I = \frac{\pi D^4 - (D-2t)^4}{64}. \tag{4.31}$$

κ can also be expressed as the rate of change of the angle of the tangent with respect to a fixed direction. The curvature is then defined by

$$\kappa(s) = \frac{1}{R(s)} = \lim_{\Delta s \to 0} \frac{\Delta\theta}{\Delta s} = \frac{d\theta}{ds} \tag{4.32}$$

If the change of the angle θ is assumed small it is possible to use a linearized curvature, which is the case in linear beam theory. θ is defined by the following relationship

$$\sin(\theta) = -\frac{dw}{ds}. \tag{4.33}$$

$w(x)$ is the transverse displacement and represents the kinematics of the Bernoulli beam. κ can be expressed in terms of this displacement,

$$\kappa = \frac{d\theta}{ds} = -\frac{1}{\cos(\theta)} \frac{d^2 w}{ds^2}. \tag{4.34}$$

The linearized expressions for θ and κ are then given by

$$\theta \simeq -\frac{dw(x)}{dx}, \quad \kappa \simeq \frac{d\theta(x)}{dx} \simeq -\frac{d^2 w(x)}{dx^2}. \tag{4.35}$$

4.3.2 Time and spatial varying loads

When considering flexible bodies, the equilibrium equation of the system not only depends on time, but also on the spatial variable. The solution is similar to that of static problems, but the inertia force must now be accounted for according to d'Alembert's principle (Larsen and Bachynski, 1990). The beam is still presumed to deform according to Bernoulli beam theory:

$$\sin(\alpha) \approx \alpha \approx \frac{dv}{dx}, \qquad \cos(\alpha) \approx 1, \qquad ds \approx dx \tag{4.36}$$

α is the angle as defined in Figure 4.8, which shows the cross-sectional forces.

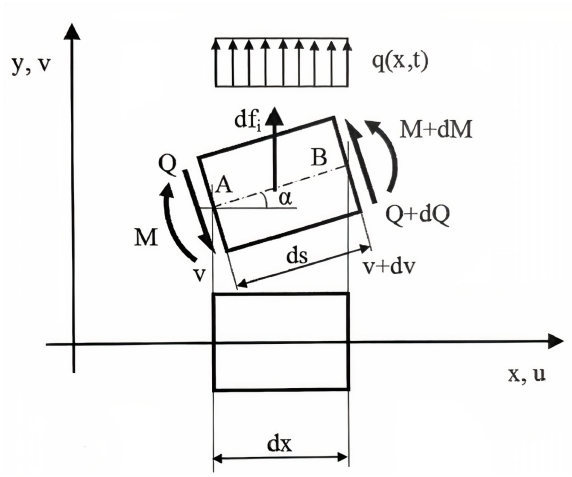

Figure 4.8: Equilibrium of infinitesimal beam element (Larsen and Bachynski, 1990).

When including the inertia force, the force equilibrium in the cross-sectional direction gives

$$q(x,t)dx - Q + (Q + \frac{\partial Q}{\partial x}) - m\ddot{v}dx = 0. \tag{4.37}$$

q is the applied load, which is now dependent on both spatial variable x, as well as time t. The partial derivative of the shear force is given a

$$\frac{\partial Q}{\partial x} = -q(x,t) + m\ddot{v} \tag{4.38}$$

By enforcing equilibrium in the moment M about the point B, as seen in Figure 4.8, the moment equation becomes

$$-M + Q\ \mathrm{d}x - q(x,t)\mathrm{d}x\frac{\mathrm{d}x}{2} + m\ddot{v}\ \mathrm{d}x\frac{\mathrm{d}x}{2} + \left(M + \frac{\partial M}{\partial x}\ \mathrm{d}x\right) = 0 \tag{4.39}$$

which then gives the shear force as

$$Q = -\frac{\partial M}{\partial x}. \tag{4.40}$$

This is the same expression as Equation 4.22 for the static case. When dx goes to zero, the terms proportional to $(\mathrm{d}dx)^2$ will disappear. By differentiating Equation 4.40 and inserting in Equation 4.38

$$\frac{\partial^2 M}{\partial x^2} + m\ddot{v} = q(x,t). \tag{4.41}$$

The moment can still be expressed by the curvature, same as for the static case in Equation 4.23, ie.,

$$M = EI(x)\frac{\partial^2 v}{\partial x^2} \tag{4.42}$$

By inserting for M in Equation 4.41, the differential equation for the beam is hence found as

$$\frac{\partial^2}{\partial x^2}\left(EI(x)\frac{\partial^2 v}{\partial x^2}\right) + m\ddot{v} = q(x,t) \tag{4.43}$$

which, for constant stiffness can be simplified as

$$\frac{\partial^4 v}{\partial x^4} + \frac{m}{EI}\ddot{v} = \frac{q(x,t)}{EI}. \tag{4.44}$$

Equation 4.44 is similar to the static equation, except for the inertia term. For free vibration, the load term vanishes, and Equation 4.44 becomes

$$\frac{\partial^4 v}{\partial x^4} + \frac{m}{EI}\frac{\partial^2 v}{\partial t^2}. \tag{4.45}$$

The most common way to solve the differential equation in the case of free oscillations is to separate the variables into a time-dependent factor and a spatial factor. This mean a time function, $\phi_b(x)$, and shape function, $Y(t)$, respectively (Larsen and Bachynski, 1990).

$$v(x,t) = \phi_b(x)Y(t). \tag{4.46}$$

Inserting these separate variables into Equation 4.45 gives

$$\frac{EI}{m}\frac{\phi_{b,xxxx}(x)}{\phi_b(x)} = -\frac{\ddot{Y}(t)}{Y(t)} = \omega^2 \tag{4.47}$$

The comma as index denotes derivation with respect to the subsequent indices. The term to the left of the equal sign in Equation 4.47 is only dependent on the spatial part x, while the right terms only depend on time. These two terms must be equal, but as they are functions of different variables the only possibility is that they are both constant, i.e., independent of x and t (Larsen and Bachynski, 1990). The constant is called ω^2. Equation 4.47 can hence be split onto two new harmonic differential equations:

$$\ddot{Y} + \omega^2 Y = 0 \tag{4.48}$$

and

$$\phi_{b,xxxx} - \frac{m}{EI}\omega^2\phi_b = 0. \tag{4.49}$$

By introducing the constant a_b, Equation 4.49 can be expressed as

$$a_b^4 = \frac{m}{EI}\omega^2 \tag{4.50}$$

which gives

$$\phi_{b,xxxx} - a^4\phi_b = 0 \tag{4.51}$$

The equation is supposed to have the following form

$$\phi_b(x) = Ce^{sx}. \tag{4.52}$$

Insertion into Equation 4.52 yields

$$(s^4 - a_b^4)Ce^{sx} = 0. \tag{4.53}$$

The polynomial has the following roots (Larsen and Bachynski, 1990):

$$s_1 = ia, \quad s_2 = -ia, \quad s_3 = a, \quad s_4 = -a \tag{4.54}$$

so the solution can be expressed by

$$\phi_b(x) = C_1\sin(ax) + C_2\cos(ax) + C_3\sinh(ax) + C_4\cosh(ax). \tag{4.55}$$

C_1, C_2, C_3, and C_4 are free integration constant, a is an unknown parameter which depends on angular frequency ω. The constants can be computed from the boundary conditions. It is hence possible to determine ω and express three of the C-constants in terms of the fourth. The fourth constant is then determined using initial conditions. The initial conditions make it possible to determine the products $C \cdot A$ and $C \cdot B$, which enables the determination of the complete solution (Larsen and Bachynski, 1990).

The eigenfrequency for a beam with a constant cross-section can be expressed as

$$\omega_0 = \bar{\omega_o}\sqrt{\frac{EI}{ml^4}} \tag{4.56}$$

Assuming the beam has a constant cross-section. $\bar{\omega_0}$ is a table value depending on the boundary conditions (Larsen and Bachynski, 1990). The boundary conditions at the beam ends can be specified for displacements, rotations, moments, or shear forces.

4.3.3 Boundary conditions

Boundary conditions are needed to secure the structure in space and make it possible to solve differential equations describing the displacements. In Bernoulli beam theory the beam is either statically determinate or statically indeterminate. For statically determinate, the support conditions allow for the calculation of internal forces without reference to the kinematics of the beam. For statically indeterminate beams there are more than two kinematic support conditions and it is necessary to use the kinematic variables (Krenk and Høgsberg, 2013).

In terms of support conditions, FOWTs differ from a bottom-fixed wind turbine. When modeling wind turbines, a bottom-fixed wind turbine is secured against the motion in the vertical and horizontal directions, as well as against rotation. This is not the case for a FOWT which can move in all six DOFs. The mooring will ensure that the platform does not drift off, but it will not restrict all motion. Hence, the tower beam is not technically fixed, nor is it completely free. The floating platform will allow some rotation which will decrease the amount of moment resisted at the tower base, compared to a fixed wind turbine. However, the tower will still experience bending illustrated in Figure 4.9. During computational analysis, the system is provided with hydrostatic stiffness along with mooring stiffness.

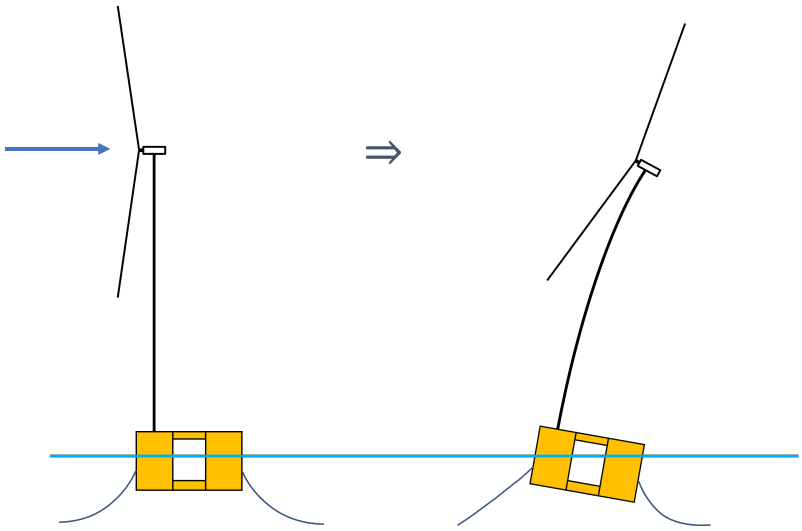

Figure 4.9: Illustration of FOWT with applied load.

4.3.4 Tower bending and rotational frequencies

As the turbine is rotating, it gives rise to two potential excitation frequencies, 1P and 3P. When designing the tower, it is important to avoid natural frequencies around the excitation frequencies to avoid resonance (Manwell, McGowan and Rogers, 2010).

As the tower is required to be outside these frequencies, it leaves three possible frequency intervals, illustrated in Figure 4.10. A stiff tower with a frequency higher than 3P, a soft-stiff tower with a frequency between 1P and 3P, and lastly a soft tower with a natural frequency lower than 1P (Tempel, 2006). As introduced previously, the tower can be modeled as a beam with a top mass and structural dynamics represented by a mass-spring-damper system. The spring stiffness and damping are noted by the bending flexibility and damping coefficient (Tempel, 2006). The first natural frequency is hence given by

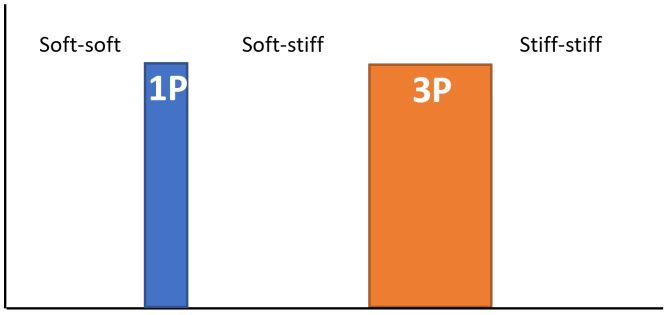

Figure 4.10: Frequency intervals for a three-bladed wind turbine with variable speed (adapted from(Tempel, 2006)).

$$f_1 \cong \frac{D}{L^2}\sqrt{\frac{E}{104(a^* + 0.227)\rho_s}} \tag{4.57}$$

where D is the average diameter of the rotor, ρ_s is the density of steel and L is the length of the tower. a^* is given by

$$a^* = \frac{M_a}{\rho_c \pi D t L} \tag{4.58}$$

where M_a is the mass and t_t is the tower thickness. As the tower has to support an increasingly

large rotor, there is a direct influence on the soft to stiff approach. The rotational frequency is given by

$$f_{1P} = \frac{\lambda u_w}{\pi D_R}. \tag{4.59}$$

Resonance motion can induce large motions which can affect the structural integrity of the turbine tower to keep the tower from violating limit states.

4.4 Limit states

When developing a preliminary model for analysis, the tower is checked for preliminary sizing under different environmental loads. This is typically achieved through the limit state method, which is the method enforced by the European and Norwegian authorities (Chakrabarti, 2005). A limit state is a condition beyond which a structure or structural component will no longer satisfy the design requirements (DNV, 2021a). In the limit state method, partial factors are applied to the loads and to the characteristic resistance of the elements. The limit state method includes the following limit states:

- Ultimate Limit State (ULS), corresponding to an ultimate event considering the structural resistance.
- Fatigue Limit State (FLS), corresponds to the possibility of failure under cyclic loads.
- Accidental Limit State (ALS), the structure shall not collapse under accidental loads.
- Service Limit State (SLS), criteria for normal use or durability.

For the purpose of this master thesis, the limit states considered are ULS in terms of buckling, and FLS in terms of fatigue. The design considerations are based on the partial safety method, which obtains the target safety value by applying load and resistance factors (DNV, 2021a).

4.4.1 Buckling

When the wind turbine tower is exposed to axially compressive loads and/or external forces, buckling can occur. The first type of buckling is global buckling, which does not involve local deformation of the cross-section, and which can be analyzed using methods for beams. The second form of buckling is shell buckling, where local deformation of the cross-section is key.

The RNA will represent a large weight inducing a compressive axial load on the tower. For a large compressing force, the effective stiffness of the structure may become reduced (Krenk and Høgsberg, 2013). Following Bernoulli beam theory, the tower is assumed to initially be straight with an applied compressive axial load $P = -N > 0$. The shortening of the tower due to the compressive axial load is neglected. If the tower experiences a load sufficiently large, the tower may experience a buckled shape. This load is known as the Euler load P_E, and is given by

$$P_E = EI_z(\frac{\pi}{l})^2. \tag{4.60}$$

The z subscript specifies the moment of inertia about the z-axis. The problem takes on the shape of an eigenvalue problem and the associated load is found as an eigenvalue (Krenk and Høgsberg, 2013). The equilibrium equation of the system is given by

$$\frac{d^4w}{dx^4} + \frac{P}{EI_z}\frac{d^2w}{dx^2} = 0. \tag{4.61}$$

P/EI_z can be denoted by a parameter k_e

$$k_e^2 = \frac{P}{EI_z} \tag{4.62}$$

with dimension [length^{-1}]. The normalized differential equation becomes

$$\frac{d^4w}{dx^4} + k_e^2 \frac{d^2w}{dx^2} = 0. \tag{4.63}$$

The general solution for the 4'th order differential equation is

$$w(x) = C_1 + C_2 k_e x + C_3 \cos(kx) + C_4 \sin(k_e x). \tag{4.64}$$

x represents the coordinate along the beam and only appears in the non-dimensional combination $k_e x$ (Krenk and Høgsberg, 2013). The moment is given by

$$\frac{M(x)}{EI_z} = -\frac{d^2w}{dx^2} = C_3 k^2 \cos(kx) + C_4 k^2 \sin(kx) \tag{4.65}$$

and the shear force is given by

$$\frac{Q(x)}{EI_z} = -\frac{d^3w}{dx^3} - k^2 \frac{dw}{dx} = -C_2 k^3. \tag{4.66}$$

The solution of the equations is affected by the choice of boundary conditions. In the case of the Euler column, the boundary conditions are

$$w(0) = w(\ell) = 0, \quad M(0) = M(\ell) = 0. \tag{4.67}$$

The differential equation, Equation 4.63, and the boundary conditions, Equation 4.67, are both homogeneous. The solution to the deformation $w(x)$ is hence zero except for values of k_e that permits a nontrivial solution (Krenk and Høgsberg, 2013). These particular values of k_e are noted k_n, and they are the eigenvalues. Corresponding to each of the eigenvalues is an eigenfunction $\omega_n(x)$, that describes the buckled shape of the column, called buckling modes.

The loads and corresponding buckling modes are given by

$$\left.\begin{array}{l} P_n = n^2 \left(\frac{\pi}{\ell}\right)^2 EI_z \\ w_n(x) = C_n \sin\left(n\pi \frac{x}{\ell}\right) \end{array}\right\} \quad n = 1, 2, 3, \cdots \tag{4.68}$$

The displacements and rotations due to displacement gradients are assumed small. No distinction is hence made between the length increments ds along the deformed beam and the projected length of the initial beam axis. This is an approximation. Further, a description of the development after instability occurs requires a non-linear theory (Krenk and Høgsberg, 2013). For the purpose of this master, only simplified buckling checks are conducted and non-linear theory is hence not elaborated on.

The buckling modes depend on the choice of boundary conditions. As mentioned previously, the tower can in reality be said to be neither free nor fixed. However, for global buckling checks, the platform is assumed rigid and hence the tower is assumed fixed at tower base and free at tower top. When applying the weight of the RNA as a point load, the situation is hence as illustrated in Figure 4.11

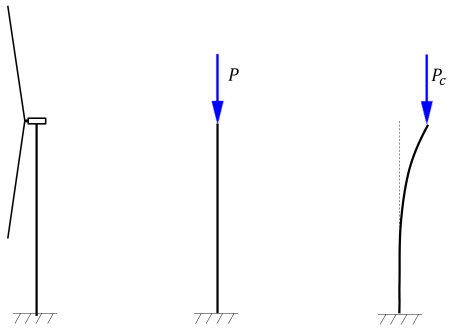

Figure 4.11: Buckling of built-in column.

The load P_c denoted in Figure 4.11 represents the critical load corresponding to instability, given by

$$P_c = k_c^2 EI_z. \tag{4.69}$$

k_c is the value corresponding to the critical load. k_c differs from k_e in the Euler load, Equation 4.62, as it depends on an effective column length l_e, which is the length between the inflection points (Krenk and Høgsberg, 2013).

$$P_c = (\frac{\pi}{l_e})^2 EI_z \tag{4.70}$$

The buckling modes are based on the symmetric buckling modes of a simply supported Euler column. By extending the actual column symmetrically below the fixed support, the respective length of the total column becomes $2l$. This is represented as the situation furthest to the left in Figure 4.12.

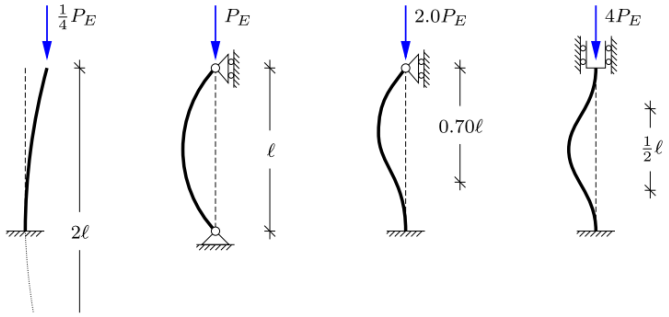

Figure 4.12: Buckling modes (Krenk and Høgsberg, 2013).

The buckling modes shown in Figure 4.12 are the result of axial loading, which in the case of the FOWT stems from the weight of the RNA. In operational conditions, the tower will also be exposed to a bending moment due to the thrust force acting at the tower top. There will also be bending moments from the wind acting on the tower. The moment at tower base is calculated by requesting moment equilibrium. If considering a scenario of only thrust force then the moment at tower base is given by force times arm, i.e.

$$M = T \cdot l \tag{4.71}$$

where l is the length of the tower. This moment creates bending stresses, σ_b, at tower base, given by

$$\sigma_b = \frac{M}{W}. \tag{4.72}$$

W is the moment resistance, which for the tower cross-section is given by

$$W = (\frac{\pi}{32D})D^4 - d^4 \tag{4.73}$$

D and d are the outer and inner diameter respectively. For the structure to be safe from failure the bending stress is required to be lower than the yield stress divided by the material factor, f_y/γ_m.

In addition, the shift of the tower top under loading gives rise to a moment arm for the RNA weight. As illustrated in Figure 4.13, the tower will experience a horizontal displacement of the tower top when exposed to a thrust force.

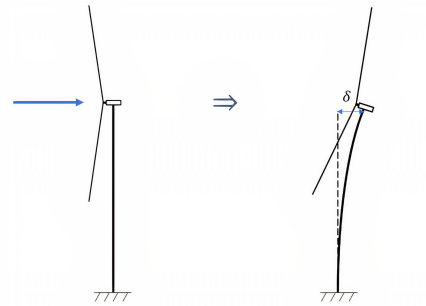

Figure 4.13: Illustration of a bottom-fixed wind turbine tower bending.

The tower top displacement, δ, can be calculated by

$$\delta = \frac{PL^3}{3EI} \tag{4.74}$$

The buckling of the tower will also be influenced by imperfections. Imperfections introduced during manufacture, storage, transportation, and installation can affect the buckling and ultimate strength of the structural components (ABS, 2004). These imperfections are typically implicit incorporated in the buckling and ultimate strength formulations.

As mentioned in Section 2, the wind is not a constant value. In terms of ULS it is useful to check buckling under maximum load. However, fatigue is typically the design-limiting factor for wind-turbine towers.

4.4.2 Fatigue

A FOWT is by default subjected to loads from wind and waves which both vary in time. The changes in stress cause a deterioration of the material and an initiation of cracks which can eventually lead to the material breaking. This gradual damage done to the material as a result of the varying stress is known as fatigue (Tempel, 2006).

A load variation following a sinusoidal function is shown in Figure 4.14. The parameters used to describe the cycle are the maximum stress S_{max}, minimum stress S_{min}, and mean stress S_m, often also noted by ΔS.

Fatigue data is usually presented through an SN diagram where the nominal stress range is plotted against cycles to failure. Marine structures typically experience fatigue stresses in the high-cycle range, which encompass lives from 10^5 to 10^7. For this range, SN data tend to follow a log-linear relationship commonly referred to as the SN curve (Berge and Aas, 2017). The SN curve is usually based on fatigue tests in the laboratory (DNV, 2021a). In DNV-ST-0126, it is specified that the characteristic S-N relationship may be taken as

$$\log_{10} N = \log_{10} a - m \log_{10} \left(\Delta\sigma \cdot \left(\frac{t}{t_{\text{ref}}} \right)^{k_t} \right) \tag{4.75}$$

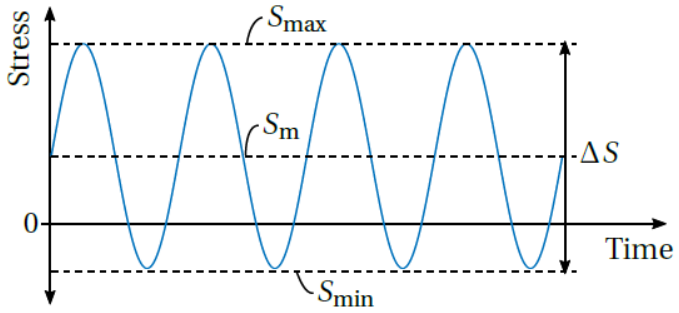

Figure 4.14: Fatigue load history with notation (Berge and Aas, 2017).

where

N = number of cycles

N_{ax} = key identification of the SN-curve (identified as the intercept of the SN-curve with the N-axis in a log-log depicition).

m_w = the Wöhlner exponent (identified as the negative inverse slope of the SN-curve in a log-log depicition).

$\Delta\sigma$ = stress range at subject detail.

t_{ref} = reference thickness and k is thickness exponent (= 25 mm for welded connections).

t = actual thickness through which the potential fatigue crack will grow.

k_t = thickness component.

Predicting the fatigue life may be based on calculations of the cumulative fatigue damage under the assumption of linearly cumulative damage, utilizing Miner's rule (DNV, 2021a). For cumulative damage analysis, the stress-time history is broken down into individual cycles which are then summed up to a distribution of stress ranges. The individual stress cycles can be counted using the Rainflow counting method. The method is named from a comparison of the flow of rain running down a roof. The principle of the method is to rotate the loading history 90 degrees such that the load time history resembles a pagoda roof. The rain starts at each successive extremum point and drips down the roofs until it either:(a) falls opposite a larger maximum or smaller minimum, (b) meets a previous flow falling from above, or (c) falls below the roof. Each cycle is identified by pairing up the same counted reversals (Lee, Barkey and Kang, 2011).

For each load cycle, the basic assumption in the Miner summation is that the damage to the structure is given by

$$D = \frac{1}{N} \tag{4.76}$$

leading to the failure criterion of

$$D = 1. \tag{4.77}$$

Summing up over several stress ranges with a number of cycles n_i, the characteristic cumulative damage, D_c is expressed as

$$D_c = \sum_{i=1}^{k} \frac{n_i}{N_i}. \tag{4.78}$$

For dynamic analyses, the resulting loads on the FOWT are given as axial loads and bending moments. The resulting stress in the tower is calculated by

$$\sigma = \frac{N_{\text{ax}}}{A} + \frac{M_y}{I_y} r \cdot \sin(\theta) + \frac{M_z}{I_z} r \cdot \cos(\theta) \tag{4.79}$$

where a_f is the axial load, A is the cross-sectional area, M_y and M_z are the moment around y and z, same as I_y and I_z are moment of inertia around y and z. θ is the angle of the fatigue location. Using Rainflow counting and Miners summation, the fatigue damage for the duration of the simulation is found. The long term fatigue is found by combining the short-term fatigue damage with the probability of occurrence for the associated environmental conditions for the desired time. In the case of a one-hour simulation, the 20-year fatigue damage is found by multiplying 20 years by 365.25 days and 24 hours. the 0.25 days are included to account for leap years.

When conducting a fatigue analysis consisting of several environmental conditions, each condition will have a probability of occurrence. The sum of the probabilities equals 1. Through the Miners sum principle, the damage is summarized for all conditions. If D $>$ 1, the structure experiences fatigue.

Resonance is most likely to implicate a considerable amount of fatigue being quite rapidly accumulated in members and joints (DNV, 2021a). It should be noted, that exposure to seawater may have a detrimental effect on structural durability. Corrosion can reduce the cross-section of steel components. For offshore structures, corrosion allowance should be taken into account by decreasing the nominal wall thickness in fatigue limit state analyses (DNV, 2021a). This is not accounted for here.

5 Methodology of upscaling

Upscaling is essential when attempting to make FOWTs economically viable. Replacing several smaller wind turbines with one larger means fewer sub-structures to manufacture, fewer turbines to install, less mooring, and less maintenance. Upscaling methods and industry trends are elaborated on in this section along with relevant standards and software.

5.1 Theoretical upscaling

The FOWT structure consists of three main parts; the turbine, the tower, and the floater. The turbine will be upscaled from a 15 MW turbine to a 25 MW turbine and the tower and floater will be upscaled to support the new turbine. The upscaling approach will be slightly different for the turbine compared to the platform. The turbine will be upscaled according to a scaling factor between the power ratings of the two turbines, $\sqrt{25/15}$, following the rules of similarity.

5.1.1 Similarity rules for wind turbines

Upscaling a wind turbine in accordance with the theory of similarity means that all geometric dimensions are multiplied with the same scaling factor. The geometry and aerodynamic effects on the turbine are assumed to be the same. The classical similarity laws are valid once neglecting the second-order aerodynamic effects, and when assuming linear-structural behavior (Sieros et al., 2012).

If the upscaled turbine is to have the same performance as the smaller turbine, the dimensionless coefficients for power C_P, thrust C_T, and torque moment C_M, will have to be the same (Gasch and Twele, 2011). This means that the flow conditions are required to be the same as well. From the theory of similarity, this can be achieved by maintaining the tip speed ratio, the blade profile, the number of blades, and the material used. By using the same blade profile, the lift and drag coefficients, C_L and C_D, are kept the same. This assumes a Reynolds number higher than the critical Re of $Re_{crit} = 200,000$ (Gasch and Twele, 2011).

The various performance characteristics of the wind turbine do not scale equally, as the proportionality with the radius differs. The equations for the wind turbine characteristics, as presented in Section 2.2 and 2.3, are summarized in Table 5.1 along with the proportionality to the radius R.

Table 5.1: Scaling properties.

Type	**Equation**	**Proportional**
Power	$P = \frac{1}{2}\rho_w C_P v_w^3 \pi r^2$	$\propto R^2$
Thrust	$Q = \frac{1}{2}\rho_w C_P v_w^3 \pi r^2$	$\propto R^2$
Torque	$Q = \frac{P}{\omega}$	$\propto R^3$
Mass	$m = \rho_{material} \forall$	$\propto R^3$
Rotational speed	$\omega = \frac{\lambda v_w}{R}$	$\propto R^{-1}$

As can be seen from Table 5.1, the weight scales with R^3 while the power scales with R^2. This suggests that the cost scales faster than the gain. Further, the aerodynamic forces scale with R^2, while the corresponding moments scale with R^3. The rotational speed decreases in proportion to the increase in blade length. This is of importance for blade stress and natural frequency.

At the blade root, the bending stress and tensile stress due to aerodynamic and centrifugal forces are independent of the change in blade length (Gasch and Twele, 2011). However, the bending

stress due to the increase in self-weight increases proportionally to the blade length. Figure 5.1 shows the bending moment at blade root due to self-weight for two different sizes. The bending moment is given in Equation 4.71, where the force is now the weight of the blade multiplied with the acceleration of gravity.

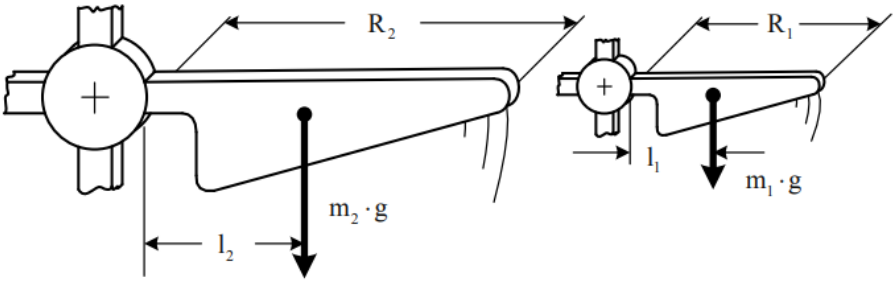

Figure 5.1: Bending moment due to weight (Gasch and Twele, 2011).

From the rules of similarity, the scaling factor is R_2/R_1. The upscaled weight of the blade in Figure 5.1, m_2 and length l_2, can hence be expressed as

$$m_2 = m_1(\frac{R_2}{R_1})^3 \tag{5.1}$$

and

$$l_2 = l_1(\frac{R_2}{R_1}). \tag{5.2}$$

The bending moment for the upscaled wind turbine becomes

$$M_2 = M_1(\frac{R_2}{R_1})^4. \tag{5.3}$$

The blade root cross-section is here rectangular, so the section modules Z_{ax} is given by

$$Z_{ax,2} = \frac{h_1 b_1^2}{6} (R_2/R_1)^3 = Z_{ax,1} (R_2/R_1)^3 \tag{5.4}$$

where h and b are the height and length of the rectangular cross-section. The ratio of bending stress to the scale factor becomes

$$\sigma_{B,2} = \frac{M_2}{Z_{ax,2}} = \frac{M_1}{Z_{ax,1}} (R_2/R_1) = \sigma_{B,1} (R_2/R_1). \tag{5.5}$$

The bending stress will increase linearly with blade length. This becomes an important factor in the application of the rules of similarity for very large wind turbines.

The rotational speed decreases in proportion to the increase in blade length. A slower rotor speed may require a larger gear ratio (Bachynski-Polic, 2021c). This implies a larger and usually heavier gearbox, adding to the already cubed weight increase of an upscaled turbine. Similarly to the rotor speed, the natural frequency ω_n of the blades also decreases in proportion to the increase in blade length (Gasch and Twele, 2011). Development to make the turbines lighter is becoming very important for large wind turbines (Gasch and Twele, 2011), and optimizing the turbine could be a topic for future work.

5.1.2 Floater scaling

It is possible to upscale the floater according to the same scaling factor as the turbine. Self-similar geometric upscaling of the semi-submersible is not limited by self-weight in the same way as the turbine. The increased weight and associated increase in volume generate a proportional increase in buoyancy force. The drawback of geometric upscaling is that the floater is likely to become larger than necessary. Upscaling based on scaling factor makes the design bigger without considering modifications which could improve stability and natural period while minimizing mass and hence lowering cost.

Rather than a strict geometric upscaling, the following key design parameters could stipulate the floater design:

- Stability
- Natural period
- Assembly procedure
- Overall dimension
- Mass
- Cost

The platform is required to have sufficient stability to operate safely. Modifications such as changing the distance between the pontoons can improve stability without making all other elements larger. Making such adjustments creates more leeway for adjusting the weight, which again helps tune the natural period.

The assembly procedure plays a part in terms of the required infrastructure and available water depth at yards. Large dimensions also put existing infrastructure to the test in terms of manufacturing, along with the fact that humans do not scale. However, one of the advantages of offshore turbines compared to land turbines is that offshore transport of large parts is more feasible than land transport.

The two last design parameters are very closely linked. An increase in mass results in an increase in cost. Hence, upscaling geometrically without attempting to achieve sufficient stability with a lower amount of mass, directly leads to a more expensive structure. An alternative in optimizing the design is thus to carry out a parametric study in order to minimize the steel mass of the platform while maintaining stability.

5.1.3 Tower design

The tower design can be upscaled geometrically without suffering major consequences from the increased weight. The challenges for the tower are, as already discussed, the flexibility of the structure. The vibrations may coincide with the 1P or 3P frequencies, depending on the stiff-soft ratio of the tower. However, the 1P frequency decreases as the diameter increases. This has been shown through work conducted by for example Tempel (2006) and Arany et al. (2016). Tempel (2006) calculated the frequency for a wind speed of 11.4 m/s and $\lambda = 8$ for three different rotor diameters, shown in Figure 5.2. For a land-based wind turbine, it could be an option to design the tower as to have a natural frequency below that of the 1P range, i.e. a soft-soft tower. However, this is not ideal for a FOWT due to the additional excitation force present from waves. Arany et al. (2016) compared typical wind and wave power spectral densities with the 1P and 3P frequencies of several commercial wind turbines of different capacities. The results are shown in Figure 5.3.

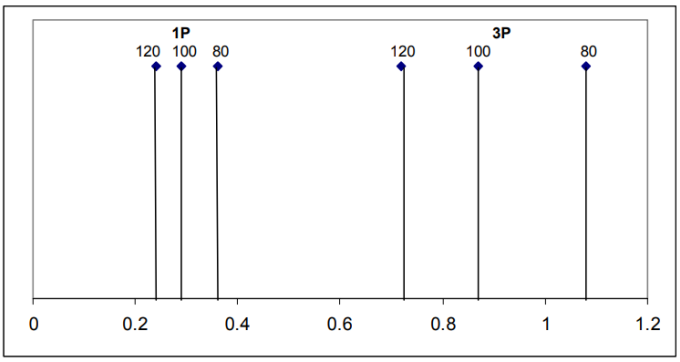

Figure 5.2: 1P and 3P for diameters of 80, 100, and 120 m (Tempel, 2006)).

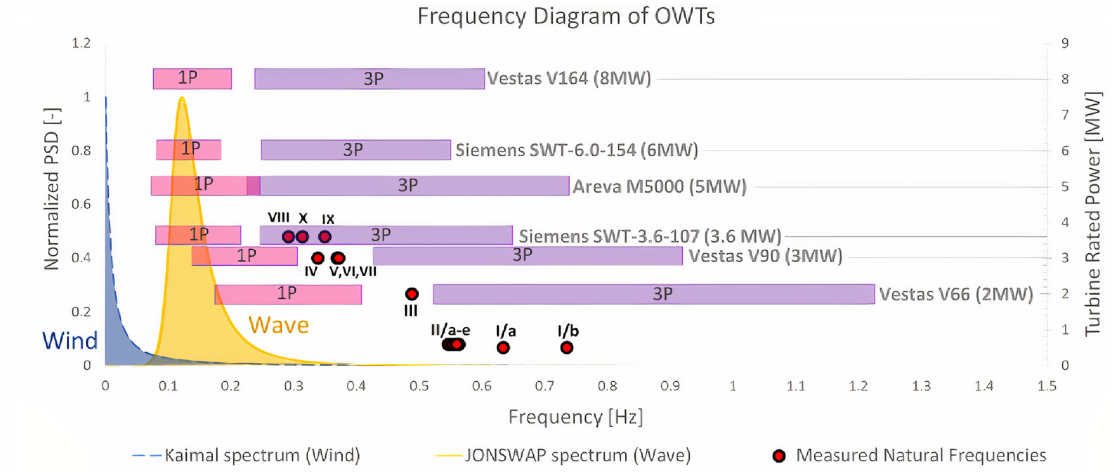

Figure 5.3: Comparison of wind and wave spectra with rotational speed (1P) and blade passing frequency (3P) (Arany et al., 2016)).

It is clear from Figure 5.3 that the natural frequencies of heavier turbines move closer to the wave excitation frequencies of waves and wind. Large FOWT are hence becoming more dynamically sensitive, and it is important to avoid resonance which may lead to increased fatigue damage through dynamic amplification. In general, the following conditions shall be fulfilled (DNV, 2021a):

$$\frac{f_R}{f_{0,n}} \leq 0.95 \text{ or } \quad \frac{f_R}{f_{0,n}} \geq 1.05$$

where f_R is the excitation frequency, in particular the rotating frequency range in the normal operating range. $f_{0,n}$ is the n^{th} natural frequency of the tower and the total complete system (DNV, 2021a).

5.2 Challenges of upscaling

The wind speed is assumed constant for the theoretical scaling. However, the increased height of the tower means a higher location in the wind shear. As presented in Figure 2.2, the wind velocity increases with height. The turbine is hence exposed to a higher wind velocity than its smaller counterpart. The higher velocity induce a higher load. In addition, Reynolds number might be different and hence affect other aspects of the turbine geometry.

For theoretical upscaling, it is shown that the mass increases faster than the power, and bending stress due to blade weight becomes a dominating factor for self-similar geometric upscale. Larger and heavier turbines pose construction challenges and require large foundations. Large foundations

require yards with a big enough area, and deep enough waters to launch the substructures. For locations not accessible by sea transport, transporting by land becomes challenging. Figure 5.4 shows the transport of the LM Wind Power wind turbine blade, measuring 88.4 meters. In 2016, this blade was the longest one in the world, and it required nine months of meticulous planning and coordination for the 218 km trip (LMWindPower, 2016). In 2019, LM Wind Power took it to the next level and transported a 107 m blade (Creig Richard, 2020). The 107 m blade was transported by sea from France to the ORE Catapult's facility in Blyth, UK (LMWindPower, 2019). However, the blades still need to be transported to and from the port if facilities are not located by the shore.

For the 107 m LM Wind Blade, the blade had to have its tip cut off to enable the doors to close at ORE Catapult's test center (Creig Richard, 2020). Larger turbines require larger test facilities, larger yards, and larger cranes. As mentioned, the human scale also remains unchanged.

Figure 5.4: Transport of a wind turbine blade in Denmark (LMWindPower, 2016).

Even though the mass theoretically increases faster than the power, it might still make economic sense to build larger turbines. If one large turbine can replace several smaller ones, it means less manufacturing, and fewer turbines to transport, install and maintain (IEA, 2019a). There will also be less mooring necessary and fewer power cables. The latter ones are becoming increasingly important as the FOWTs move towards deeper waters further offshore. Deep waters mean long mooring lines, and further offshore means long-distance power cables.

5.3 Real upscaling

In order to quantify the actual upscaling process, several studies have been conducted. It is also possible to examine the actual upscaling trend in the industry.

5.3.1 Scaling characteristics

Wind turbines are typically designed based on load cases which create the design-driving extreme or fatigue loads. These load cases do however tend to vary significantly because of design configuration differences and the influence of wind class. Regardless, examining the data can provide some information in terms of scaling trends. Sieros et al. (2012) conducted a study of the evolving trends in size, weight, and cost and found that the trend suggests an improved scaling behavior,

which is mostly attributed to the technology improvement. Some of the results from the study are presented in the following.

Trend lines derived for extreme loads and fatigue loads show that there is some deviation from the rules of similarity. Sieros et al. (2012) found that fatigue load exponents tent to exceed cubic scaling. Above rated wind speed, where most of the fatigue is accumulated, the self-weight of the blade introduces cyclic loading in fore-aft and side-side bending. The increasing effect of turbulence may also have an effect on the exponents' being greater than cubic. However, the reduction in RPM due to the constant tip speed assumption will reduce the fatigue loading (Sieros et al., 2012).

When considering the weight, Sieros et al. (2012) only considered newer turbines, with rotor diameters larger than 80 m. The reason is that when considering all turbines, it became difficult to distinguish between the effects of upscaling and those due to technology improvements accompanying the larger turbines. When only considering the larger turbines, the scaling exponent for weight increased in closer agreement with upscaling theory, as shown in Figure 5.5a. The effect of technology development can better be seen in Figure 5.5b for the increased weight of blades. As technology advances, new material types are used for the blades and the size correlation for each technology is closer to the theoretical prediction (Sieros et al., 2012). In Figure 5.5b, the three representing the highest mass are existing technology, while the two lowest ones are future projections based on the current trend.

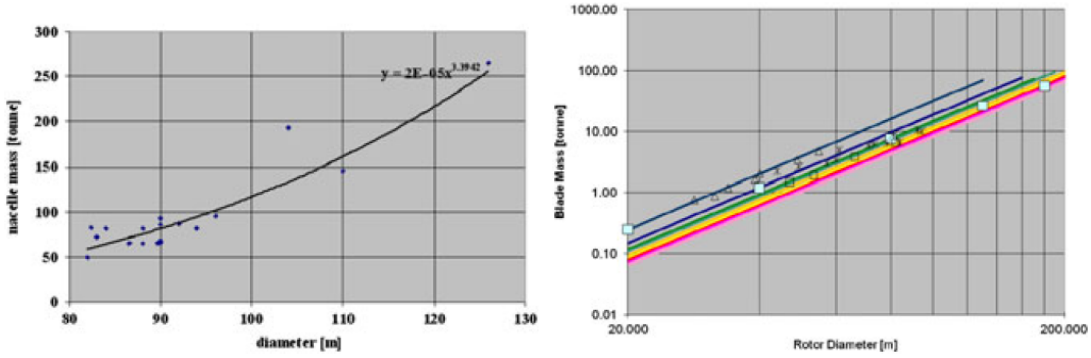

(a) Mass as a function of size for nacelle for wind turbines with D > 80 m.

(b) Blade mass as a function of size for different technologies (filled squares denote the combined size and technology improvement trend).

Figure 5.5: Upscaling trends (Sieros et al., 2012).

For the wind turbine tower, Sieros et al. (2012) considered constant stress upscaling rather than geometric upscaling, by introducing scaling functions $g_D(s)$ and $g_D(s)$. $g_D(s)$ quantifies the departure from geometric upscaling in diameter, while $g_t(s)$ is for thickness. The goal is to minimize the product of the two, i.e., minimize the weight while constraining stress. Sieros et al. (2012) used a constrained optimization algorithm with g_D and g_t as the optimization variable and the product $g_D(s)\ g_D(s)$ representing the extra weight needed in comparison to classical upscaling. Sieros et al. (2012) found that the extra weight term is always greater or equal ($s = 1$) to 1 and almost linearly increases with scale. The study by Sieros et al. (2012) proved that it is not possible to upscale without having a weight increase of $\geq s^3$. However, the conclusion was derived only considering normal stresses and assuming the limiting factor would be the buckling limit. Still, Sieros et al. (2012) states that the conclusion will not vary significantly as long as the combined loading can be expressed as a combination of terms similar to what was done in the study. Even though the relative magnitude of the terms will differ (e.g. weight-induced cyclic loading will have a bigger contribution in blade fatigue calculations (Sieros et al., 2012).

5.3.2 Industry trends

Upscaling a FOWT to 25 MW is no walk in the park. It puts today's knowledge to the test, but the industry seems optimistic. Already in 2011, the UpWind project, which was Europe's

largest European R&D wind energy project, concluded that a 20 MW turbine is feasible, but not yet cost-efficient (UpWind, 2011). Following the UpWind project, the FP7 project INNWIND.EU was initiated to develop innovation to make 10-20 MW offshore wind turbines design cost-efficient (INNWIND.EU, 2016).

As the industry moves towards larger wind turbines, larger reference wind turbines become available. Reference wind turbines provide open-access designs of complete wind turbine systems, with supporting models for simulation and design. It is hence possible to evaluate proposed designs before prototype development (NREL, 2020). In 2020, NREL released the International Energy Agency Wind Technology Collaboration Program 15-megawatt reference turbine, IEA Wind 15-MW for short. The turbine is illustrated in Figure 5.6. It provides an open-source model, features options for both fixed and floating turbine sub-structure, and can accommodate multiple software tools. It provides a public-domain tool for designing larger wind turbines (NREL, 2020).

Figure 5.6: Illustration of the IEA 15 MW reference turbine (Joshua Bauer, 2020).

Available reference wind turbines enable research like this report looking into 25 MW FOWT. Also, several other sources, like Ashuri et al. (2016) and Sartori et al. (2018) have investigated wind turbines as large as 20 MW. Ashuri et al. (2016) developed a 20 MW common research wind turbine available to the public to address the need for data available for very large wind turbines. The design objective was to minimize the levelized cost of energy and the research points toward the feasibility of a 20 MW wind turbine. It also provides a model with corresponding data for wind energy researchers to use in the upscaling wind turbines. While Sartori et al. (2018) provided a definition of a 20 MW turbine including aero-structural optimization of the rotor. It highlights directions for the development and optimization of very large rotors.

5.4 Standards

Upscaling the FOWT has to be done in accordance with the relevant standards and guidelines. The DNV-ST-0126 is the standard practice for support structure for wind turbines. This standard is mainly relevant for bottom fixed turbines. The DNV standard DNVGL-ST-0119 covers the structural design of floating wind turbine structures, so both the tower, the substructure, and the station keeping system (DNVGL, 2018b). Some aspects are overlapping, but in general the DNVGL-ST-0119 is the relevant standard for the FOWTs.

In 2020, DNV GL was asked by Norsk Industri (Norwegian Industry) to establish an overview

of rules, standards, guidelines, and certification requirements that are currently used for floating offshore wind, both in Norway and internationally. According to DNV, the common practice when it comes to the turbine is to use a type certified turbine. However, currently, the turbines are only type certified for bottom-fixed foundations. For a floating offshore wind turbine, a site and floater-specific assessment of the turbine is performed to ensure that the turbine is suitable for operation on the floating foundation (DNV, 2020).

The American Burau of Shipping (ABS) created a guide for building and classing floating offshore wind turbine installations, including the floating substructure and the station-keeping system (DNV, 2020).

The "Guidance Note for Classification and Certification of Floating Offshore Wind Turbines", published by BV, includes both technical requirements and recommendations for classification and certification. It is intended to cover floating platforms supporting single or multiple horizontal or vertical axis turbines. It does not cover top structure but considers the influence of top structure on the floating platform and mooring system (DNV, 2020).

The DNV standard DNVGL-RP-0286 provides guidance for modeling, load analysis, and model testing of floating offshore wind turbines. The loads and site conditions for wind turbines are outlined in DNVGL-ST-0437. There are also other standards from a long industry of land-based wind turbines, like the IEC 61400-1, which identifies three different classes of wind turbines to suit differing site wind conditions. The loads taken into account are the aerodynamic loads, gravitational loads, inertia loads, and operational loads (Burton et al., 2011). In 2019, the IEC developed a technical specification for floating wind turbines, the IEC TS 61400-3-2. The standard is a supplement to the first part and specifies additional requirements as the wind turbine is floating offshore.

The ABS published a guidance note named "Global performance analysis for floating wind offshore wind turbine installations", also updated in 2020. This guide provides suggested global performance analysis methodologies, modeling strategies, and numerical simulation approaches (DNV, 2020).

The ClassNK Guideline for Offshore Floating Wind Turbine Structures is based on the mentioned IEC 61400-1, which was published again in 2005. It is also based on the IEC 61400-3-1, which is the IEC 61400-3 "Wind Turbines - Part 3: Design requirements for offshore wind turbines". It also has some input from Rules for Survey and Construction of Steel Ships. The guideline covers, from DNV, "requirements for external conditions, loads, materials, structural design and welding, mooring, stability, equipment, machinery installations and electrical installations of the floating structure including the tower (DNV, 2020). The environmental loads follow DNV-RP-C205 "Environmental conditions and environmental loads".

The FOWT tower is required checked for buckling. The relevant standard for buckling depend on what part of the FOWT structure is checked for buckling. For buckling of plated structures and girders, the DNV-RP-C201 is recommended. For buckling strength of shells, DNVGL-RP-C202 is recommended. Shell structures in towers shall be checked for buckling in accordance with DNVGL-ST-0126 (DNV, 2021a).

5.5 Sofware

The modeling of the structure is done in parts through different software modules of the DNV Sesam software package. The software package is suited for hydrodynamic and structural analysis of marine structures (DNV, 2021b). The modules used are GeniE, HydroD and Sima. A simple flowchart of the modules is shown in Figure 5.7. The geometry of the platform hull is created in GeniE, this model is then exported to HydroD for hydrodynamic analyses to determine hydrodynamic coefficients. The platform is then exported into Sima, and equipped with the flexible tower and RNA. The software modules are explained in more detail in the following sections.

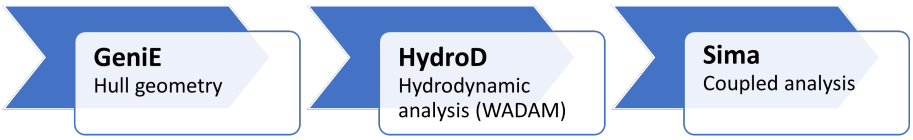

Figure 5.7: Sesam flowchart.

5.5.1 GeniE

GeniE is a program used for concept modeling of beams and stiffened plates and shells. There are different ways of modeling the structure depending on the goal of the modeling. In this case, the model is to be exported into hydroD to determine hydrodynamic coefficients. It is hence sufficient to create a panel model of the hull, without specifying material properties or the plate thickness. For symmetric models, only part of the structure needs to be modeled. The symmetry plane is specified once exported to HydroD.

Once modeled, the structure is meshed, i.e. the surface is divided into elements. The basic geometry of the model determines the mesh, but there are several ways to adjust the mesh according to own needs (DNV, 2021b). The option utilized here is setting a wanted mesh density by specifying the length of the element edge. The mesh density will be of importance when conducting structural or hydrodynamic analysis, as calculations are conducted on each element. A finer mesh will give a more accurate result, but also increase the computational time.

5.5.2 HydroD

The model is imported into HydroD, which is where the hydrodynamic analyses are performed. HydroD provides multiple stability and hydrodynamic analysis types. It can compute hydrostatic data like displaced volume, mass, center of buoyancy, and center of flotation. The actual hydrodynamic analysis is run in HydroD, but through Wadam. Wadam is a linear frequency domain theory (DNV, 2021b). The following information on Wadam is based on the Sesam user manual for Wadam by DNVGL (2017).

In Wadam there are three main model types: **hydro model**, **mass model**, and **structural model** (DNVGL, 2017).

Hydro model
The hydro model is used to calculate the hydrodynamic forces. It either consists of a panel model, a Morison model, or a composite model. For the panel model, the loads are calculated from potential theory. For the Morison model Morison's equation is used, and for composite, both are used. In terms of modeling the hydrodynamic loads in a coupled analysis, the potential flow model in combination with the panel method is the most common technique (A. Robertson et al., 2014). The panel model calculates hydrodynamic loads and responses from potential theory, which is described in Section 3.1. Loads on the structure can also be calculated using a Morison model. The specifics of how Wadam utilizes the Morison model are not described here, as only the panel model will be used.

Mass model
For floating structures, a mass model is used to notice the imbalance between buoyancy and self-weight in the equation of motion (DNVGL, 2017). In a structural model, hydrodynamic and hydrostatic loads are represented as finite element loads. For loads on beams, it uses the Morison model. Loads on the shell and solid elements are dependent on the wet surface similar to the panel model (DNVGL, 2017). Using the potential theory applied to a panel model, the mass, damping and restoring forces used in the equation of motion can be calculated. The hydrodynamic coefficients can then be loaded into Sima.

5.5.3 Sima

Sima is an efficient software when considering complex multi-body systems, including mooring analysis and marine operations. With the increased interest in FOWTs, the coupled analysis has been extended to include modeling of the offshore wind turbine blades, wind load models, wind turbine modeling (including control system), and blades and tower can be modeled as flexible (DNV, n.d.).

For analyses in Sima, wind can be included as a 3D wind field, 2D wind, or constant wind. The wind turbine blades can be modeled with aerodynamic properties following the BEM method, explained in Section 2.3. The control system allows for pitch control for blades, torque control, and power take-off, as well as an internal strategy with user-defined coefficients or a completely user-defined strategy. The motions of the marine unit can be both rigid and flexible. It is possible to utilize first and second-order wave loads, current loads, mooring systems and wind drag forces (Bachynski-Polic, 2021b). It is also possible with advanced structural modeling, like nonlinear Finite Element Method (FEM), mooring lines, power cables, and tower and blades.

In terms of a FOWT, the blades, turbine, and control system can either be specified in Sima, or be given by link to an external controller. The system can either be analyzed in the time domain or by a fully coupled method. The computations in Sima are based on the solver Simo and Riflex (DNV, 2021b).

5.5.4 Simo

Simo simulates the motions and station-keeping behavior of the complex system of a floating vessel and the suspended loads. Simo enables the following features, as outlined in the Simo theory manual by SINTEF Ocean (SINTEF, 2021b):

- Flexible modeling of multi-body system.
- Nonlinear time-domain simulation of wave-frequency and low-frequency forces.
- Environmental forces due to wind, waves, and current.
- Passive and active control forces.
- Interactive or batch simulation.

Simo uses linear wave potential theory, as described in Section 3.1. For sinusoidal motion, the equation of motion can be expressed as

$$\mathbf{M}\ddot{\mathbf{x}} + \mathbf{C}\dot{\mathbf{x}} + \mathbf{D}_1\dot{\mathbf{x}} + \mathbf{D}_2\mathbf{f}(\dot{\mathbf{x}}) + \mathbf{K}(\mathbf{x})\ \mathbf{x} = \mathbf{q}(t, \mathbf{x}, \dot{\mathbf{x}}) \tag{5.6}$$

$$\begin{aligned} \mathbf{M} &= \mathbf{m} + \mathbf{A}(\omega) \\ \mathbf{A}(\omega) &= \mathbf{A}_\infty + \mathbf{a}(\omega) \\ \mathbf{A}_\infty &= \mathbf{A}(\omega = \infty) \\ \mathbf{C}(\omega) &= \mathbf{C}_\infty + \mathbf{c}(\omega) \\ \mathbf{C}_\infty &= \mathbf{C}(\omega = \infty) \equiv 0 \end{aligned} \tag{5.7}$$

where

$\mathbf{M}$	frequency-dependent mass matrix
$\mathbf{m}$	body mass matrix

$\mathbf{A}$	frequency-dependent added-mass
$\mathbf{C}$	frequency-dependent potential damping matrix
D_1	linear damping matrix
D_2	quadratic damping matrix
$\mathbf{f}$	vector function where each element is given by $f_i = \dot{x}_i\|\dot{x}_i\|$
k_m	hydrostatic stiffness matrix
$\mathbf{x}$	position vector
$\mathbf{q}$	exciting force vector

The exciting forces on the right-hand side are given by

$$\boldsymbol{q}(t, \boldsymbol{x}, \dot{\boldsymbol{x}}) = \boldsymbol{q}_{WI} + \boldsymbol{q}_{WA}^{(1)} + \boldsymbol{q}_{WA}^{(2)} + \boldsymbol{q}_{CU} + \boldsymbol{q}_{\text{ext}} \tag{5.8}$$

where

$\boldsymbol{q}_{W1}$	wind drag force
$\boldsymbol{q}_{WA}^{(1)}$	first order wave excitation force
$\boldsymbol{q}_{WA}^{(2)}$	second order wave excitation force
$\boldsymbol{q}_{CU}$	current drag force
$\boldsymbol{q}_{ext}$	any other forces (wave drift damping, specified forces and forces from station-keeping and coupling elements, etc.)

Simo can solve the differential equation, Equation 5.6, in the time domain by use of the retardation function. Alternatively, the motions can be separated into a high-frequency part and a low-frequency part (SINTEF, 2021b). Simo considers both aerodynamic and hydrodynamic forces. The wind force is calculated based on the instantaneous wind and body velocities

$$q_j = C_{w,j}(\alpha)v^2 \tag{5.9}$$

where j represents the degree of freedom, C_w is the wind force coefficient for the instantaneous relative direction, v is the relative wind speed between body and wind, and α_w is the relative velocity direction in the local coordinate system (SINTEF, 2021b).

5.5.5 Riflex

Riflex conducts the analysis of flexible risers and other slender structures. The structural analysis is based on FEM. The most important features are, as listed in the riflex theory manual (SINTEF, 2021a):

- Unlimited rotations and translations in 3D space
- Beam and bar element based on small strain theory.
- Use of beam as well as bar elements in system modeling.
- Connector element for modeling of swivels, hinges, etc.
- Description of nonlinear material properties.

- Stiffness contribution from material properties as well as geometric stiffness, i.e. contribution of axial force to the transverse stiffness.
- General element assembly allowing for the description of arbitrary system topology, varying cross-sectional properties, arbitrary boundary conditions at supports, prescribed support displacements and specified external forces.

In riflex, the tower and turbine consist of beam elements. The calculations of beam defection are based on Bernoulli beam theory. However, instead of calculating beam displacement by direct integration of differential equations, Riflex calculates displacement through virtual work. The principle states that the work performed by the loads on the beam is identical to the internal virtual work, through the virtual deformation of the beam (Krenk and Høgsberg, 2013). The beam is hence considered to satisfy the equilibrium equations previously introduced, summarized as

$$\frac{dN}{dx} + n = 0, \quad \frac{dQ}{dx} + p = 0, \quad \frac{dM}{dx} - Q + m = 0 \tag{5.10}$$

where $m(x)$ is introduced as distributed moment load. The beam is subjected to a hypothetical displacement described by the virtual displacement $\delta u(x)$, $\delta w(x)$ and $\delta\theta(x)$. By integrating over the length of the beam the total virtual work is found. To achieve equilibrium, the external virtual work, δV_{ex}, shall be equal to the internal virtual work, δV_{ex}.

$$\delta V_{ex} = \delta V_{ex}. \tag{5.11}$$

The external virtual work is given by

$$\delta V_{\text{ex}} = [\delta u N + \delta w Q + \delta\theta M]_0^\ell + \int_0^\ell (\delta u n + \delta w p + \delta\theta m) dx. \tag{5.12}$$

whereas the internal virtual work, consisting of work associated with extension, shear, and bending, is given by

$$\delta V_{\text{in}} = \int_0^\ell (\delta\varepsilon N + \delta\gamma Q + \delta\kappa M) dx. \tag{5.13}$$

By the virtual work equation, it is possible to uniquely define the virtual strains that correspond to the internal forces. The kinematic relations follow the assumption of the existence of a virtual work equation. The virtual work equation determines the deformation and stiffness properties of the beam (Krenk and Høgsberg, 2013), and is the basis for beam calculations in the software used for coupled analysis.

5.6 Coupled analysis of FOWTs

Using sima, dynamic analyses can be carried out. Dynamic analyses should be carried out for FOWTs to evaluate dynamic responses at site-specific external conditions and operating conditions. For the final design, a coupled analysis is recommended (ABS, 2020).

In a fully coupled analysis, the total system of equations describing the rigid body model of the hull, the elastic model of the tower and turbine RNA, the slender body of the mooring lines, along with the control system are all solved simultaneously using a non-linear time-domain approach for dynamic analyses (ABS, 2020). However, time domain is a complex and computationally demanding analysis and is hence often combined with the frequency domain.

5.6.1 Time-domain analysis

Time-domain analysis typically includes motion analysis, air gap analysis, and mooring analysis. It numerically solves the equations of motions, under environmental and operational loads. The loads are calculated in response to the applied time series of wind and wave conditions. Time-domain analysis can capture the nonlinear and transient effects in the FOWT responses. It also allows modeling of the coupling effects between the FOWT subsystems and is hence the preferable approach for FOWT global analyses (ABS, 2020).

5.6.2 Frequency-domain analysis

In frequency-domain analysis, loads and responses are calculated in the frequency domain by solving equations of motion using methods of harmonic analysis or methods of Laplace and Fourier transformations (ABS, 2020). It typically includes wave load calculations, motion analysis, air gap analysis, and mooring analysis.

For wave frequency responses, it typically employs linear wave theory. Responses to wind dynamics and wave drift forces are evaluated through low-frequency motion analysis. For the FOWT dynamic responses, combined aerodynamic, hydrodynamic, and control systems in the frequency domain are preferably used (ABS, 2020). However, frequency-domain analysis can not capture nonlinear dynamic interactions between the subsystems of the FOWT. When using frequency domain analysis, the nonlinearity should be approximated using other methods. Further, this type of analysis does not consider transient responses or nonlinear load effects from aerodynamics and hydrodynamics. Due to these limitations, most available simulation software for FOWTs is based on time-domain analysis, while the frequency domain is used to calculate the hydrodynamic coefficients used as inputs in the time domain analyses. In the case of combined analysis, the mean and low-frequency responses are computed in the time domain, while wave frequency responses are solved in the frequency domain (ABS, 2020).

6 Upscaling the FOWTs

An introduction has now been given to the various aspects of the coupled aero-hydro-servo-elastic analysis, along with the methodology of upscaling and the relevant software. Now, this methodology is applied and the FOWTs are upscaled and tested in coupled analyses. As mentioned in the introduction, two reference platforms were upscaled. Both reference FOWT were upscaled as part of the project thesis. The upscaling was based on the work by Ph.D. candidate Serag Eldin Abdelmoteleb at NTNU. During the project thesis, both platforms were found to be useful alternatives as 25 MW platforms. This section presents both reference wind turbines, a summary of the upscaling procedure of the selected semi-submersible, and the accompanying 25 MW tower and turbine.

The two reference wind turbines are the INO WINDMOOR 12 MW platform, and the IEA 15 MW University of Maine (UMaine) VolturnUS-S reference floating offshore wind turbine semi-submersible. The main difference separating the two FOWTs is the design of the platform. Moreover, the first design represents a 12 MW turbine, while the latter represents a 15 MW turbine. Only the tower and turbine design for the 15 MW is presented as it was decided to use the largest tower and turbine as reference for the upscaled FOWT.

6.1 Reference platform 1: INO WINDMOOR 12 MW

The INO 12 MW FOWT development was started in early 2019 by Inocean, and the concept was chosen as the research candidate for the ongoing 4-year WINDMOOR project. The data presented in this section is based on the SINTEF report created by Carlos Eduardo Silva de Souza et al. (2021) as part of the WINDMOOR project. WINDMOOR is a competence building project with the main objective of "improving the understanding of loads governing the mooring system design of floating wind turbines" (Carlos Eduardo Silva de Souza et al., 2021). It describes the INO WINDMOOR 12 MW base case floating wind turbine, shown in Figure 6.1, and an aero-hydro-servo-elastic model.

The INO WINDMOOR concept design consists of a semi-submersible platform supporting a 12 MW wind turbine. The semi-submersible platform is jointly designed by Inocean and Equinor and is made of steel with three columns connected by pontoons and deck beams. The hull main dimensions and inertia properties are provided in Table 6.1. The radii of gyration refer to the hull COG.

Table 6.1: Sub-structure dimensions (Carlos Eduardo Silva de Souza et al., 2021).

Property	**Value**	**Unit**
Column diameter	15.0	m
Column height	31.0	m
Pontoon width	10.0	m
Pontoon height	4.0	m
Center-center distance	61.0	m
Deck beam width	3.5	m
Deck beam height	3.5	m
Total substructure mass	1,1974	t
Total substructure CG_x	-5.91	m
Total substructure CG_z	-9.7	m
Total substructure R_{xx}	23.66	m
Total substructure R_{yy}	18.63	m
Total substructure R_{zz}	28.10	m

Figure 6.1: INO WINDMOOR 12 MW FWT concept (Carlos Eduardo Silva de Souza et al., 2021).

The full FOWT properties are given in Table 6.2. The full FOWT includes the semi-submersible, the tower, turbine, and mooring lines. The distances in the table refer to the local coordinate system shown in Figure 6.2. The radii of gyration refer to the COG of the full FOWT, assuming the turbine's own COG at the tower center.

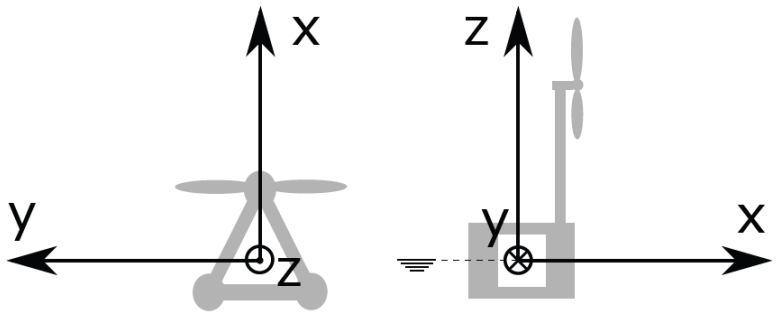

Figure 6.2: Coordinate system for INO WINDMOOR 12 MW (Carlos Eduardo Silva de Souza et al., 2021).

Table 6.2: INO WINDMOOR dimensions (Carlos Eduardo Silva de Souza et al., 2021).

Property	**Value**	**Unit**
Displacement	14176.1	t
Draft	15.5	m
CG_x^*	[-0.37 0.37]	m
CG_y^*	[-0.37 0.37]	m
CG_z	4.23	m
R_{xx}	43.67	m
R_{yy}	44.18	m
R_{zz}	30.26	m
Static heel angle at rated thrust	6.4	deg
Still water airgap to column top	15.5	m
Still water airgap to deck beam bottom	12.0	m
Still water airgap to blade tip	21.7	m

* CG_x and CG_y are dependant on the nacelle orientation.
For 0 deg orientation, $CG_x = 0.37$ m and $CG_y = 0$ m.
For 90 deg orientation, $CG_y = 0$ m and $CG_y = 0.37$ m.

6.2 Reference platform 2: IEA 15 MW UMaine VolturnUS-S

The second reference wind turbine is the UMaine VolturnUS-S. The specifications of the platform are based on the technical report *Definition of the UMaine VolturnUS-S Reference Platform Developed for the IEA Wind 15-Megawatt Offshore Reference Wind Turbine* by UMaine and National Renewable Energy Laboratory (NREL), prepared by Allen et al. (2020). The reference FOWT defined comprises of the semi-submersible, mooring, tower, and controller. All of which are tailored to the IEA15 MW turbine defined in *IEA Wind TCP Task 37: Definition of the IEA Wind 15-Megawatt Offshore Reference Wind Turbine* by Gaertner et al. (2020).

The reference floating offshore wind turbine system is intended to be distributed with the IEA-15-240-RWT to the wind energy community through the details specified in their report as well as OpenFAST and HAWC2 models through the Github repository (Gaertner et al., 2020). The general system properties are defined in Table 6.3. The wind turbine is shown in Figure 6.3.

Table 6.3: System properties (Allen et al., 2020).

Property	**Value**	**Unit**
Turbine Rating	15	MW
Hub Height	150	m
Excursion (Length, Width, Height)	90.1, 102.1, 290.0	m
Platform Type	Semi-submersible	-
Free-board	15	m
Draft	20	m^3
Total System Mass	20,093	t
Platform Mass	17,839	t
Tower Mass	1,263	t
RNA Mass	991	m
Water Depth	200	m
Mooring System	Three-line chain catenary	-

Figure 6.3: The UMaine VolturnUS-S reference platform and IEA 15 MW turbine (Allen et al., 2020).

The platform is a generic steel version of the UMaine patented concrete floating foundation technology, developed in collaboration with the U.S Department of Energy (Allen et al., 2020). The steel submersible comprises four columns, three radial and one central, with three lines of mooring. The tower is connected to the central column and places the nacelle at a hub height of 150 m above Still Water Line (SWL). The properties of the semi-submersible are provided in Table 6.4. The distance is in reference to the coordinate system as shown in Figure 6.4.

Table 6.4: Platform properties (Allen et al., 2020).

Property	**Value**	**Unit**
Column diameter	12.5	m
Center column diameter	10.0	m
Pontoon width	12.5	m
Pontoon height	7.0	m
Center-center distance	51.75	m
Hull Displacement	20,206	m^3
Hull Steel Mass	3,914	t
Tower Interface Mass	100	t
Ballast Mass (Fixed/Fluid)	2,540/11,300	t
Draft	20	m
Freeboard	15	m
CG_x	0	m
CG_y	0	m
CG_z from SWL	-14.94	m
Vertical center of buoyancy from SWL	-13.63	m
Roll Inertia about COG	1.251E+10	kg-m^2
Pitch Inertia about COG	1.251E+10	kg-m^2
Yaw Inertia about COG	2.367E+10	kg-m^2

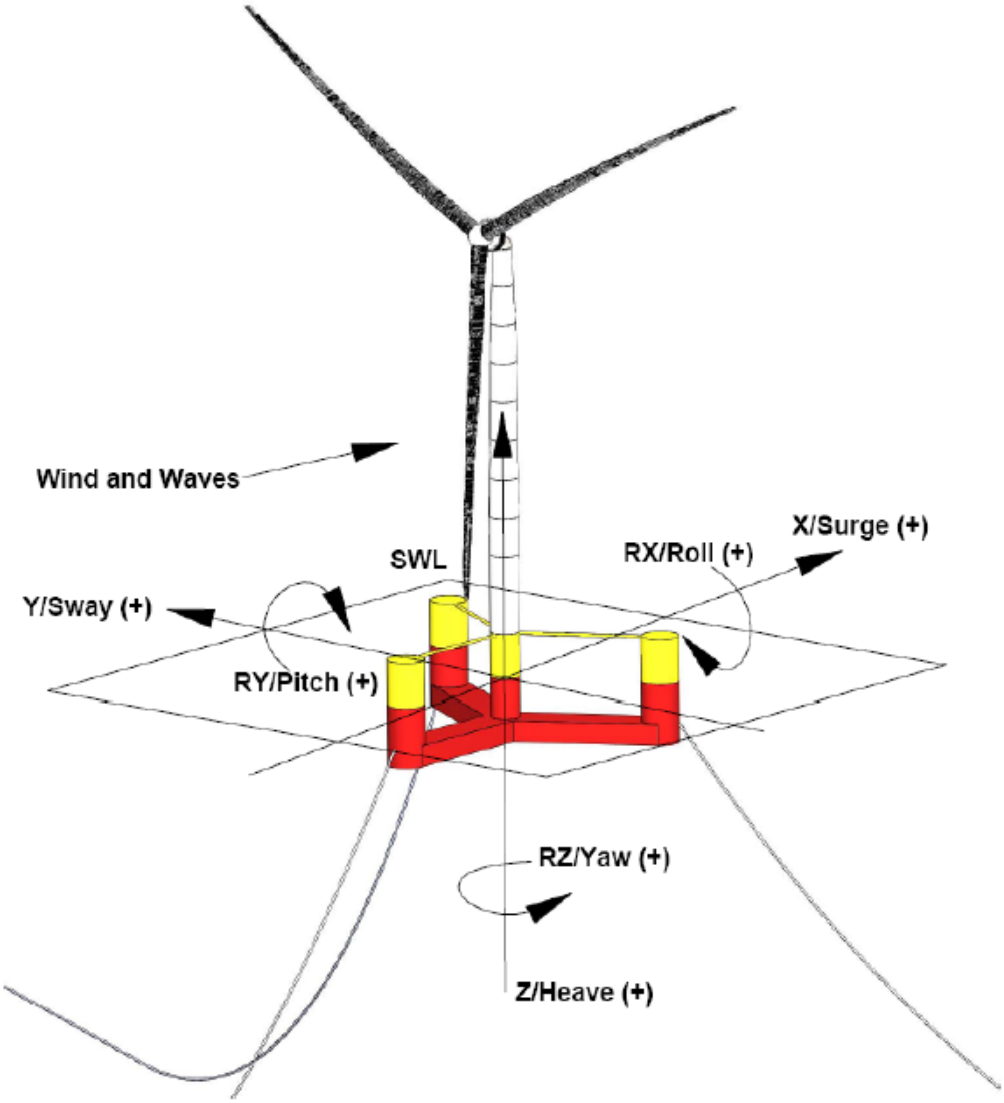

Figure 6.4: The UMaine VolturnUS-S coordinate system (Allen et al., 2020).

6.2.1 Tower

For upscaling purposes, the IEA UMaine VolturnUS-S turbine tower was used as a reference for both platforms. The tower properties are listed in Table 6.5, while the material properties are listed in Table 6.6.

Table 6.5: 15 MW tower properties (Allen et al., 2020).

Parameter	Value	Unit
Length	129.495	m
Mass	1263	Ton
Base outer diameter	10	m
Top outer diameter	6.5	m
1st Fore-Aft Bending Mode	0.496	Hz
1st Side-Side Bending Mode	0.483	Hz

Table 6.6: Material properties.

Parameter	**Symbol**	**Value**	**Unit**
Young's Modulus	E	2.1E10	Pascal (Pa)
Shear Modulus	G	7.93E10	Pa
Steel density	ρ	7850	kg/m^3

The data which is used to recreate the model is shown in Table 6.7. The table shows the length of the tower divided into 10 sections. Each of the segments has a top and bottom diameter. The properties in Table 6.7 are slightly different from what is specified in the report by (Allen et al., 2020), as the model has been recreated based on cross-sectional data from a modified tower input file from the github model.

Table 6.7: Sectional properties for 15 MW tower.

Height [m]	**Diameter [m]**	**Thickness [mm]**
15.000	10.000	82.996
27.991	9.964	82.995
27.992	9.964	82.995
40.983	9.967	82.996
40.984	9.967	82.996
53.974	9.927	82.995
53.975	9.927	30.000
66.965	9.528	30.000
66.966	9.528	28.000
79.956	9.149	28.000
79.957	9.149	26.000
92.948	8.945	26.000
92.949	8.945	22.967
105.939	8.735	22.966
105.940	8.735	19.977
118.930	8.405	19.976
118.931	8.405	18.002
131.921	7.321	18.004
131.922	7.321	21.004
144.495	6.500	21.007

The sectional properties in Table 6.7 show that the tower segments are shaped as truncated cones with a top and bottom diameter. The segments are approximately 13 m long and have a narrowing diameter but an almost constant thickness. The thickness instead reduces from one segment to the next. Figure 6.5 shows the structural properties of the 15 MW tower.

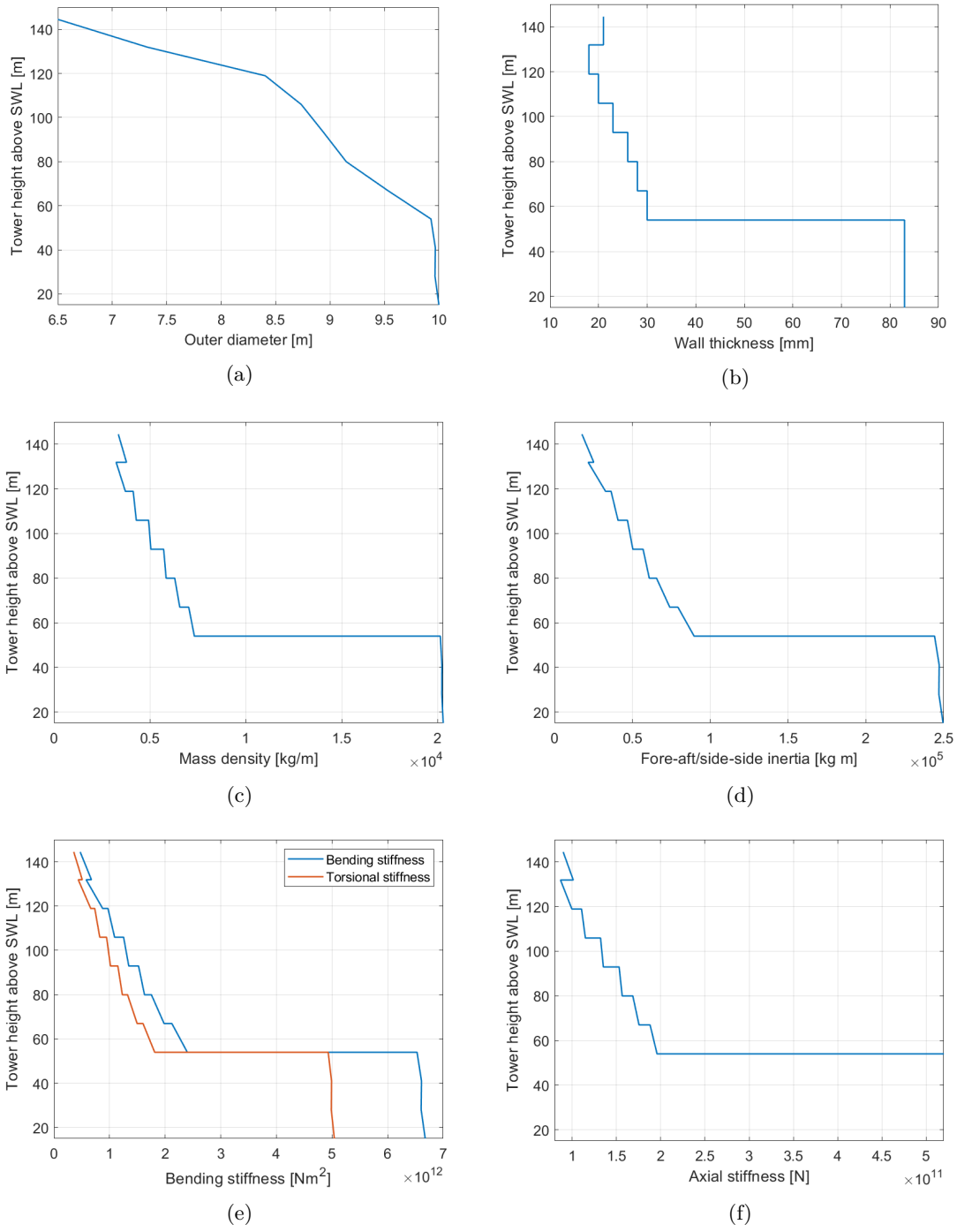

Figure 6.5: Tower structural properties vs. tower height above SWL

A noticeable aspect of the tower design is the abrupt change in thickness, Figure 6.5b. From 53.975 m height above SWL to 66.965 m, the thickness decreases from 82.995 mm to 30 mm. The influence of the thickness is seen in Figure 6.5c to 6.5f, as the mass density and stiffness properties are highly dependent on the thickness.

6.2.2 Turbine

The reference turbine is based on the IEA Wind TCP Task 37, *Definition of the IEA Wind 15-Megawatt Offshore Reference Wind Turbine* by Gaertner et al. (2020). The turbine was originally

designed for a fixed-bottom monopile support structure as shown in Figure 6.6. Upon being placed on a floating platform, the turbine was equipped with a float-specific controller tailored specifically to the 15 MW turbine. Key parameters for the turbine are listed in Table 6.8.

Table 6.8: Turbine key parameters (Gaertner et al., 2020).

Parameter	**Value**	**Unit**
Power rating	15	MW
Turbine class	IEC Class 1B	-
Specific rating	332	W/m^2
Rotor orientation	Upwind	-
Number of blades	3	-
Control	Variable speed, collective pitch	-
Cut-in wind speed	3	m/s
Rated wind speed	10.59	m/s
Cut-out wind speed	25	m/s
Design tip-speed ratio	90	-
Minimum rotor speed	5.0	RPM
Maximum rotor speed	7.56	RPM
Maximum tip speed	95	m/s
Rotor diameter	240	m
Hub height	150	m
Hub diameter	7.94	m
Hub height	11.35	m
Blade mass	65	t
Drive-train	Direct drive	-
RNA mass	1,017	t

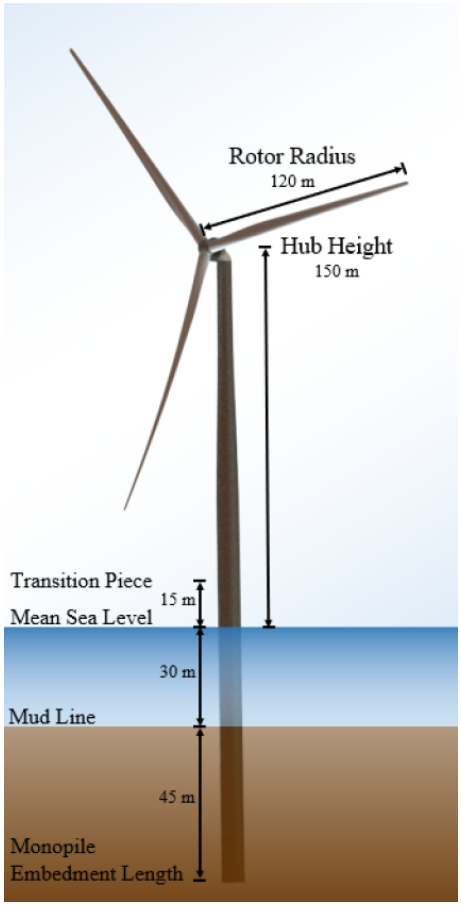

Figure 6.6: The IEA Wind 15-MW reference wind turbine (Gaertner et al., 2020).

6.2.3 Mooring

The mooring system for the IEA 15 MW FOWT consists of three 850 m long chain catenary lines, which properties are provided in Table 6.9. Each chain is connected at fairleads located at the outer columns of the platform, at a depth of 14 m below SWL. The anchors are spaced equally 12 degrees in the sure-sway plane, at 200 m depth and 837.6 m from the tower centerline. All three mooring lines use studless R3 chains with a nominal diameter of 185 mm.

Table 6.9: Mooring system properties (Allen et al., 2020).

Parameter	**Value**	**Unit**
Mooring system type	Chain catenary	-
Line type	R3 studless mooring chain	-
Line breaking strength	22,286	kN
Number of lines	3	-
Anchor depth	200	m
Fairlead depth	14	m
Anchor Radial Spacing	837.6	m
Fairlead Radial Spacing	58	m
Nominal Chain Diameter	185	mm
Dry Line Linear Density	685	kg/m
Extensional Stiffness	3270	MN
Line Unstretched Length	850	m
Fairlead Pretension	2,437	kN
Fairlead Angle from SWL	56.4	-

6.3 Upscaling INO WINDMOOR platform

When upscaling the INO WINDMOOR 12 MW platform, first the 12 MW design was recreated and validated against results in the SINTEF report by Carlos Eduardo Silva de Souza et al. (2021). This was done in order to confirm the baseline design and create comparison grounds for the upscaled model.

6.3.1 Creating the 12 MW model

A panel model of the platform was created in GeniE, Figure 6.7, following the coordinate system in Figure 6.2. The brackets which connect the top of the columns were not modeled as only submerged volume is of influence for the hydrostatic analysis.

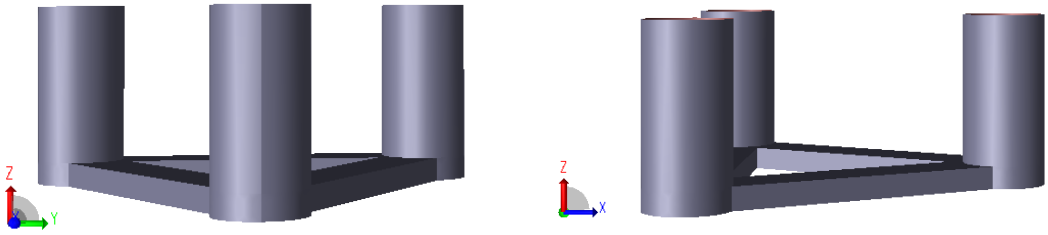

Figure 6.7: INO WINDMOOR 12 MW platform created in GeniE.

Carlos Eduardo Silva de Souza et al. (2021) carried out a panel size convergence study to determine the size of the panel elements needed for the results to converge. The study tested a panel size of 0.375 m, 0.750 m, and 1.500 m. The study showed that the results were converging as the number of panel elements was increased, but all panel sizes gave somewhat similar results. During the project thesis, a similar mesh study was conducted using mesh sizes of 0.75 m, 1 m, and 1.5 m respectively. A 0.375 m panel size was not run due to computational limitations. The number of elements for each mesh size is listed in Table 6.10. An illustration of the different mesh sizes is provided in Figure 6.8, which shows a close-up of the panel sizes of the three cases.

Table 6.10: Mesh parameters.

Mesh length [m]	No. of elements
0.75	7814
1.0	4457
1.5	2138

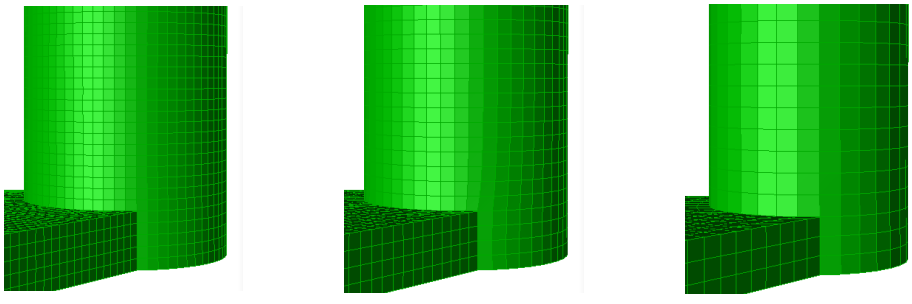

(a) Mesh size 0.75 m (b) Mesh size 1 m (c) Mesh size 1.5 m

Figure 6.8: INO WNDMOOR mesh size illustration.

The panel models were exported as T1.FEM files to HydroD for WADAM analyses. Figure 6.9

shows the model as visualized in HydroD with the water plane at z = 0. The analysis assumes a rigid single-body structure consisting of the platform, the tower, and the rotor-nacelle assembly combined. Only the substructure is modeled, as HydroD only requires the submerged area. However, the remaining structure is included by using the full displacement, COG, and radii of gyration.

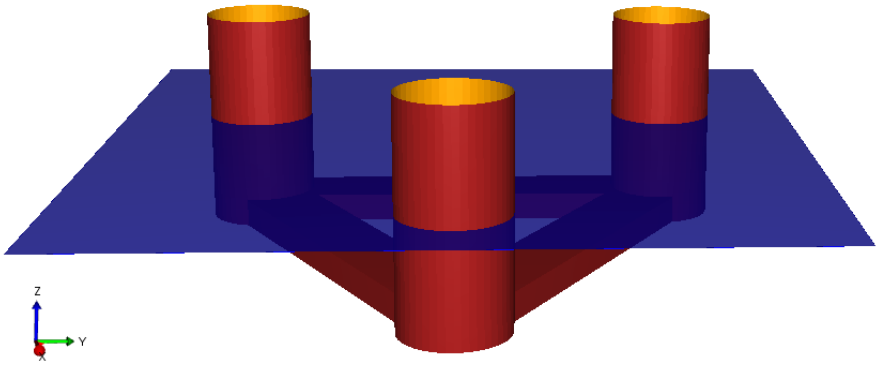

Figure 6.9: INO WINDMOOR 12 MW platform modeled in HydroD.

The model includes an additional 5% of critical heave damping, as well as 5% of critical damping in roll and 4% in pitch. An additional matrix was added to include the linear restoring coefficient from the mooring system. The values specified in Table 6.11 were added to account for surge, sway, and yaw.

Table 6.11: Restoring matrix.

Component	**Value**	**Unit**
Surge k_{11}	89800	N/m
Sway k_{22}	89800	N/m
Yaw k_{66}	121650000	N/m

The WADAM analysis was run for all panel sizes, and results were extracted using Matlab. Figure 6.10 show the Response Amplitude Operator (RAO)s for surge, pitch and surge due to pitch for the recreated model compared to the three mesh size SiNTED model.

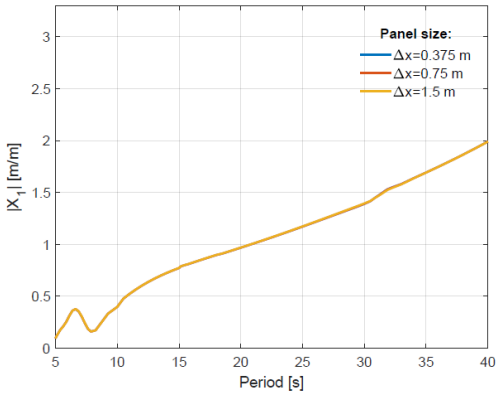

(a) SINTEF model

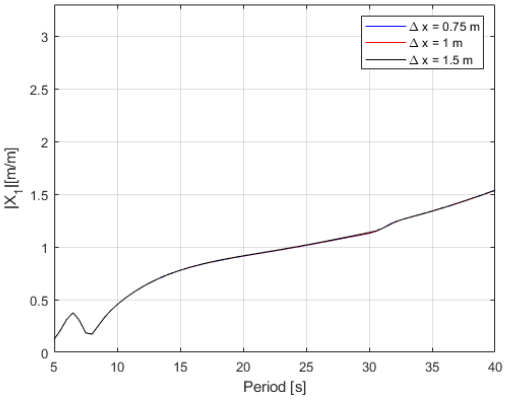

(b) INO 12 MW recreated model

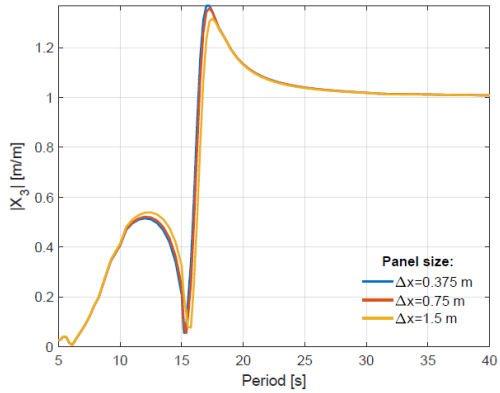

(c) SINTEF model

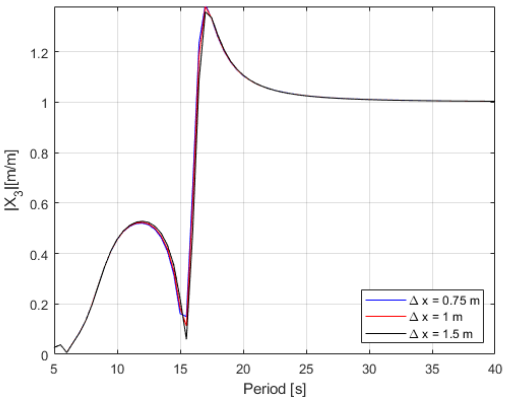

(d) INO 12 MW recreated model

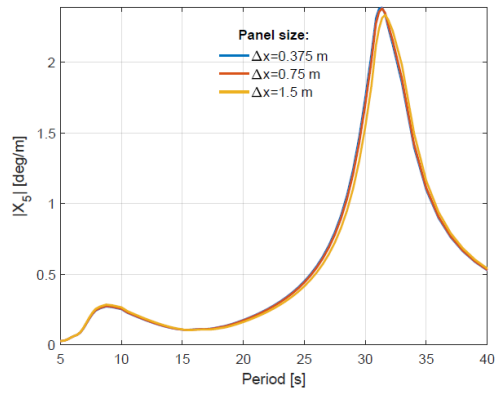

(e) SINTEF model

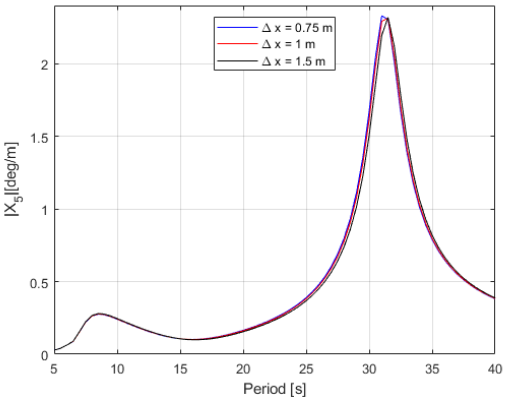

(f) INO 12 MW recreated model

Figure 6.10: Panel size sensitivity study.

The panel size sensitivity study concluded with a mesh size not having a large influence on the results from WADAM. It was also found to be little difference between the 0.375 m and 0.75 m panel sizes. A mesh size of 0.75 m was hence deemed sufficient. Further, the comparison between the SINTEF model RAO and the recreated model RAO showed that the recreated model were producing similar results. Results were also compared between added mass and damping for the SINTEF model and the recreated model, included in Appendix A. As for the RAOs, the results showed a good correspondence between the models. Some deviations were observed, possibly due to the difference in panel size or difference in time-step. For heave, the cancellation effect was observed at 6 s. The platform has a center-center distance between the columns of 61 m, with a length in the x-direction of approximately 52 m. The period corresponding to a wavelength of 61

m and 52 m is 6.25 and 5.8 s.

The model validation was deemed satisfactory. The model could then be upscaled to 25 MW, with the 12 MW as a borderline design. Upon upscaling, some assumptions and limitations were introduced.

6.3.2 Assumptions

As mentioned in Section 5.1.2, a strict geometric upscale is not necessarily the most cost-efficient alternative. When upscaling the platforms, Ph.D. candidate Serag Eldin Abdelmoteleb carried out a parametric study in order to minimize the steel mass of the platform. He found that the model with the least steel mass had unfavorable geometry. It had a large diameter instead of a large center-center distance. It also had large pontoon width to compensate for the increase in heave stiffness due to the larger column diameter (Abdelmoteleb, 2021). Design modifications were done to accommodate a more favorable design, following a set of preliminary assumptions set out by Abdelmoteleb (2021):

- The width of the pontoons has to be smaller than the diameter, D, of the column, but larger than D/2.
- Constant deck beam dimensions.
- Constant draft, free-board, and fair-lead position.
- Fixed ballast in after columns ($\rho = 2650 kg/m^3$).
- Seawater ballast in pontoons.
- Ballast adjusted to force the total COG of the turbine to coincide horizontally with the geometric center of the platform when the nacelle is yawed 90 degrees.
- Constant steel thickness.
- Constant vertical force (pretension).
- Constant surge offset under max thrust (18m).
- Natural periods in surge, heave, and pitch estimated using strip theory and 2D added mass coefficients.
- Fore-aft floating tower bending natural periods are calculated using FEM with beam elements.

The following constraints were applied to the parametric study to minimize steel mass (Abdelmoteleb, 2021):

- Mean pitch at rated wind speed below 15 degrees.
- Natural periods for rigid body motions larger than 20 s.
- Maximum hull dimensions 120 m.
- Stiff-stiff first bending natural frequency of the tower (on the floater).

6.3.3 Upscaled platform design

The platform parameters of the upscaled design were provided by Serag Eldin Abdelmoteleb and are listed in Table 6.12. The same procedure was followed for the 25 MW platform as for the 12 MW platform. A panel model was created and exported to HydroD. The total structure weight was achieved by adding the weight of the tower and turbine upscaled with a scaling factor. The whole-structure displacement was then tuned by the "fill from buoyancy" function in HydroD. This function assesses the draft achieved at the specified weight and finds the structure displacement and COG. Radii of gyration are calculated through that same function. A 5% of critical heave damping was included, along with 5% in roll and 4% in pitch.

Table 6.12: Baseline design INO WINDMOOR 25 MW.

Property	**Value**	**Unit**
Column diameter	20.93	m
Column height	42.30	m
Pontoon width	17.44	m
Pontoon height	2.89	m
Center-center distance	74.84	m
Whole structure displacement	35779667	kg
Draft	25.82	m
CG_x	0	m
CG_y	0	m
CG_z	7.95	m

Even though not a strict geometric upscale, it does serve as a validating guide to compare the upscaled model to the 12 MW results. The 25 MW platform is shown in comparison to the 12 MW platform in Figure 6.11. It should also be noted that the mesh size is different for the two models, as summarized in Table 6.13. The larger mesh size was due to the increased size of the model and computational limitations for the number of elements a 0.75 m mesh size would introduce.

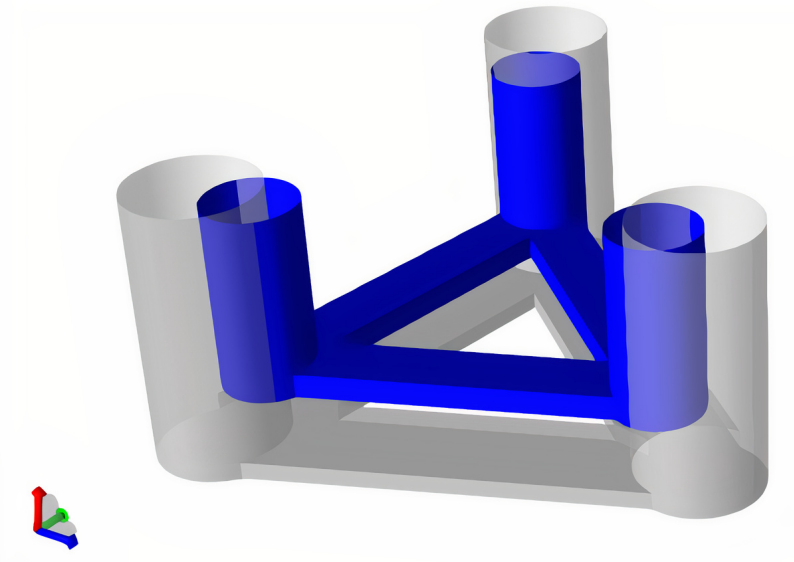

Figure 6.11: Size comparison of 12 MW and 25 MW platforms.

Table 6.13: Mesh parameters for the 25 MW and 12 MW platform.

Platform	Mesh length [m]	No. of elements
INO 25 MW	1.00	8969
INO 12 MW	0.75	7814

6.3.4 INO 12 MW and 25 MW comparison

Results from the hydrostatic analyses were compared between the upscaled 25 MW model and the original 12 MW model. Presented results show RAO, wave excitation force, added mass, and damping.

RAO
The results from the RAO are shown for the 25 MW and 12 MW for surge, heave, and pitch in Figure 6.12.

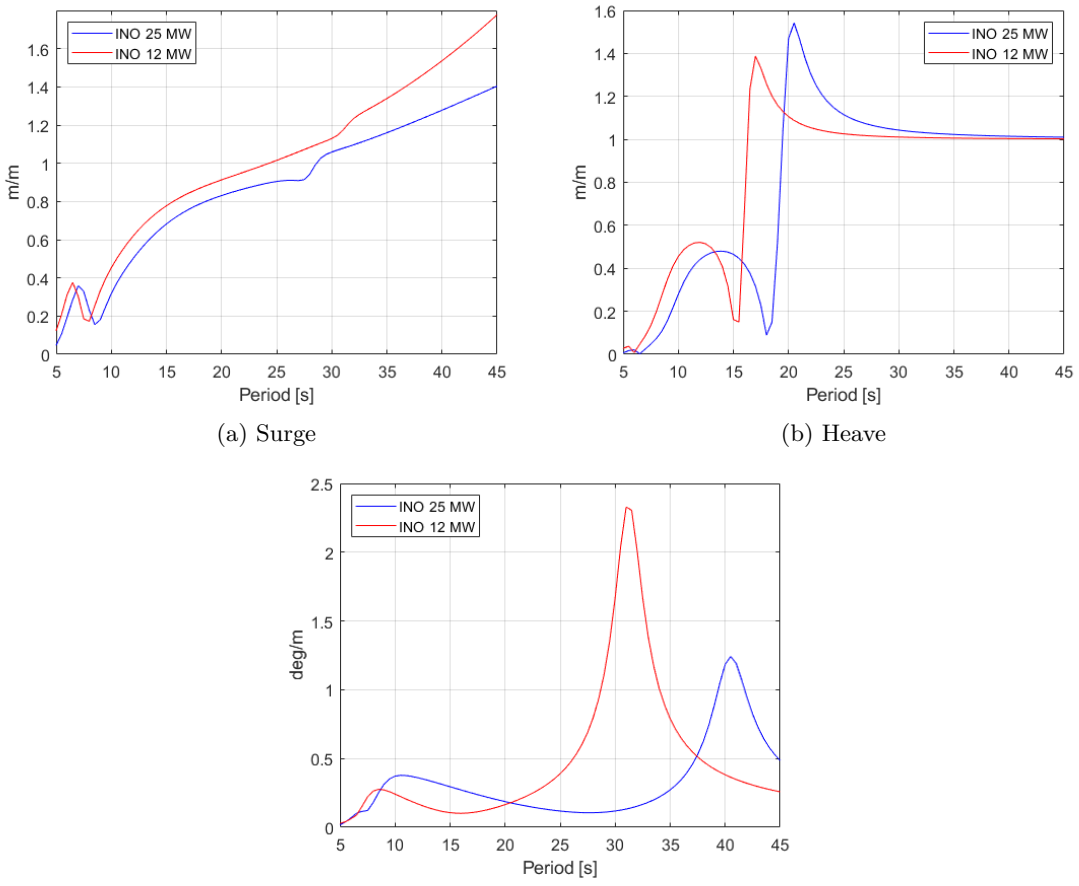

(a) Surge

(b) Heave

(c) Pitch

Figure 6.12: RAO.

The comparison of surge RAO in Figure 6.12a show little change in the first few seconds but is increasing in difference as the period increases. This is expected as the platform is significantly larger and the natural period in surge will be longer for the upscaled design. For heave, Figure 6.12b, the shape of the RAO is similar, but the natural period of heave is shifted to 19 seconds, and the increased area induces a larger motion. For pitch, the opposite is seen. Figure 6.12c show a longer natural period, but the peak is decreased.

Wave excitation force transfer function
The wave excitation is compared to that of the 12 MW turbine for the three same motions, surge, heave, and pitch. The results are scaled according to the volume of the structures.

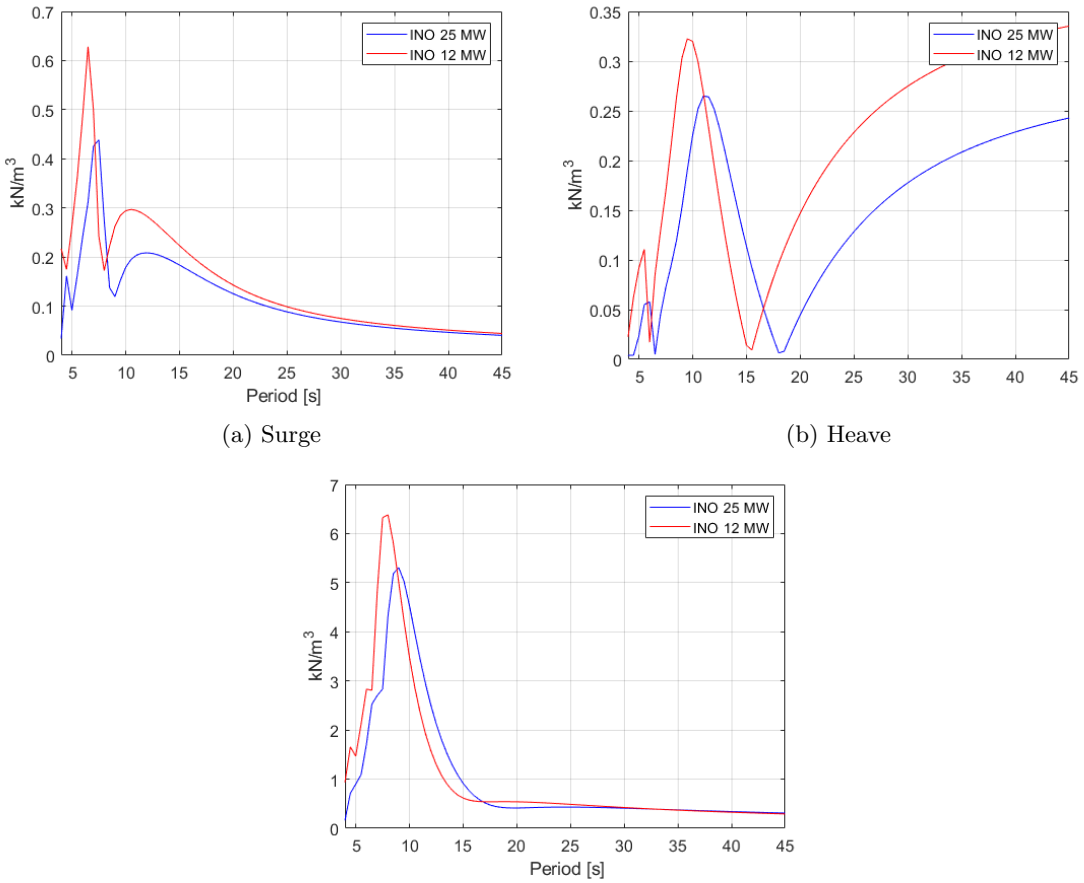

(a) Surge

(b) Heave

(c) Pitch

Figure 6.13: Wave excitation force transfer function.

The results show that the peak of the wave excitation is higher for the 12 MW case than for the 25 MW. As the results are scaled according to the volume, even if the 25 MW design experiences a higher force it is actually less affected than the smaller design.

Added mass coefficients

Results for added mass are shown for surge, heave, pitch, and surge due to pitch in Figure 6.14.

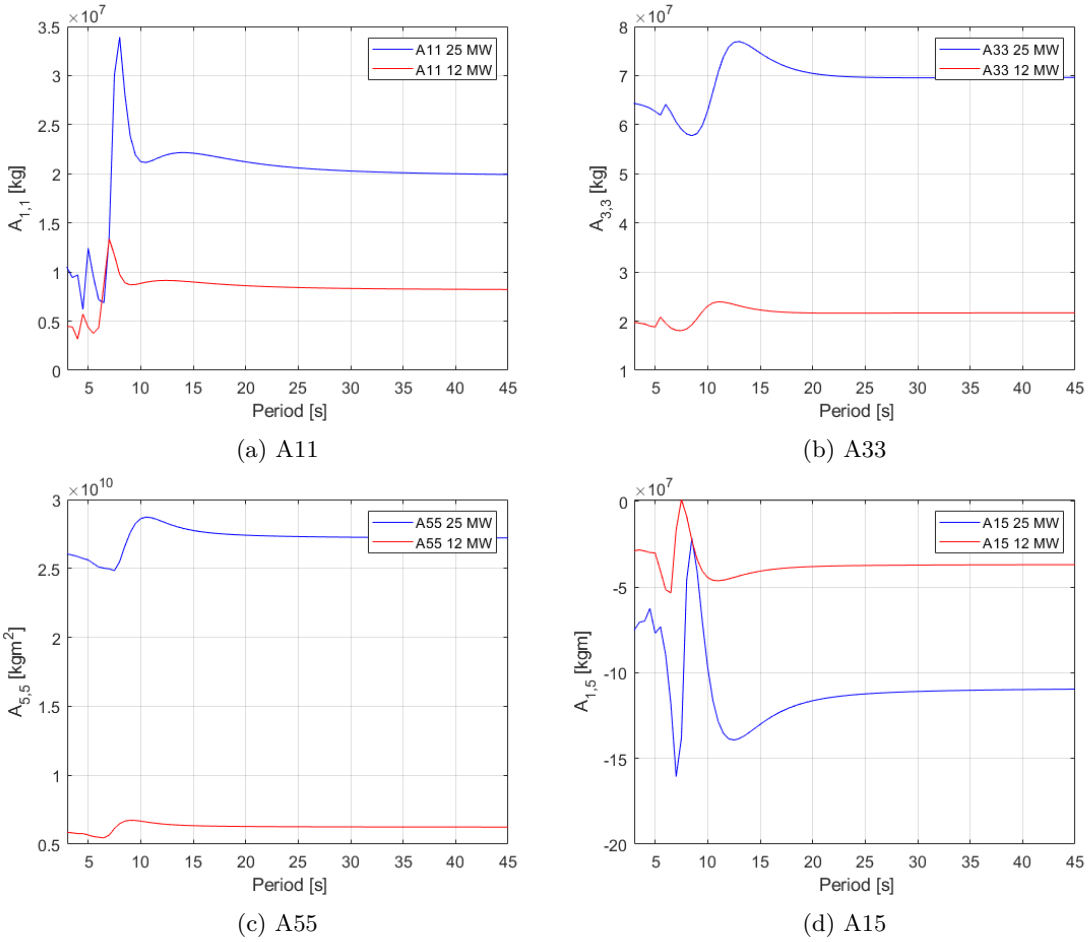

(a) A11 (b) A33

(c) A55 (d) A15

Figure 6.14: Added mass coefficients.

The results in Figure 6.14 show that the results depend largely on the mode of motion. Overall it can be seen that the 25 MW platform has a higher absolute value of added mass in all the motions. This is expected due to the increased total wet surface area.

Wave damping coefficients
The results for damping are shown for both models in Figure 6.15.

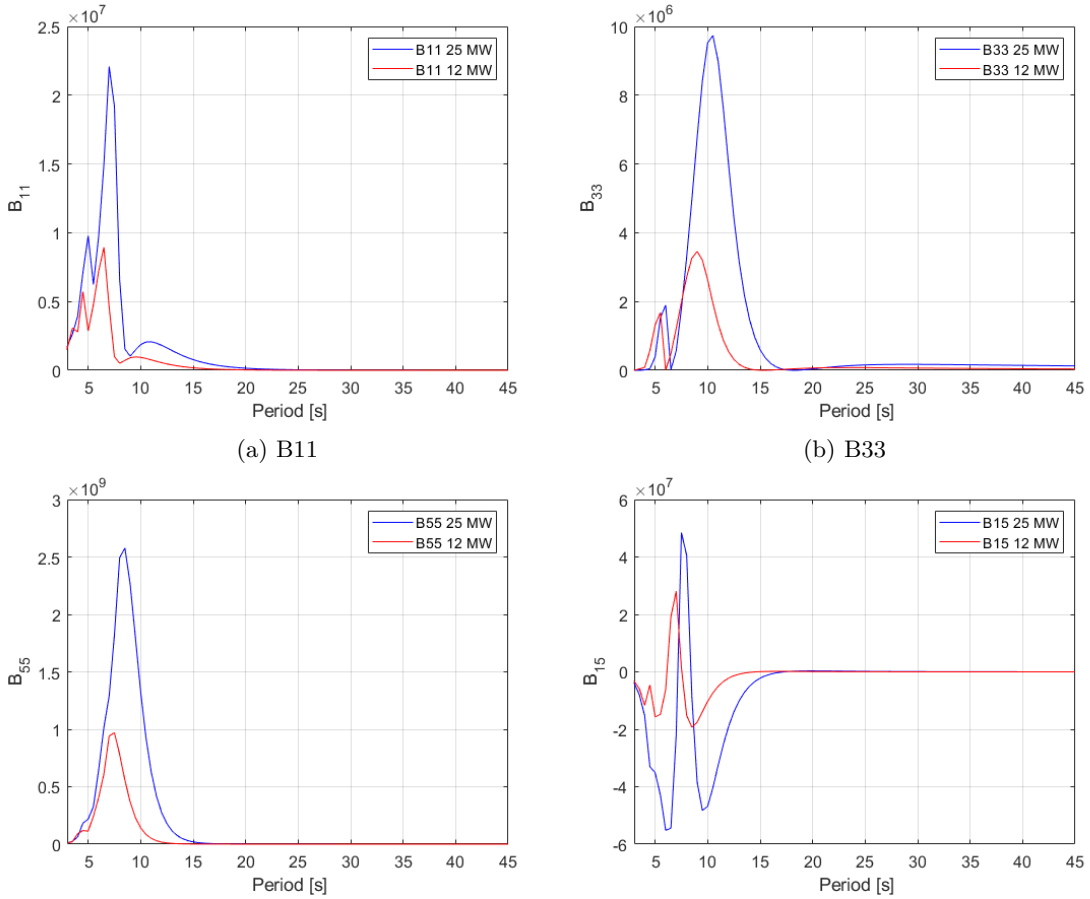

(a) B11 (b) B33

(c) B55 (d) B15

Figure 6.15: Wave damping coefficients.

The results in Figure 6.15 show that, unlike the added mass, the difference in potential damping is not as reliant on the modes of motion. The peaks and cancellations are shifted approximately 1.5 seconds for all motions. As mentioned, the 12 MW has a cancellation effect occurring at 6. s due to the length of the platform. For the 25 MW platform, which is larger, the cancellation period is 7.8 s. This corresponds well with the results, where the cancellation in heave for the 25 MW platform occurs at 8 s.

Overall, the comparison showed that the 25 MW platform was behaving similarly to the 12 MW and that the periods were reflecting the upscaled geometry.

6.4 Upscaling IEA UMaine VolturnUS-S

The previous sections presented the results of the INO 12 MW and 25 MW upscale models. Similar results were found for the IEA 15 MW and 25 MW models. The IEA 15 MW model was recreated as a panel model, exported to HydroD, and validated against the results in the report by Allen et al. (2020). The upscaled model was then created based on the parametric study by Abdelmoteleb (2021) and compared to the results obtained for the 15 MW model. The design for the upscaled 25 MW was not a strict geometric upscale, and some of the size ratios were changed to get a more steel-efficient platform. The resulting baseline design is presented in Table 6.14, and the platform size difference is illustrated in Figure 6.16.

The results from the hydrostatic analyses are not discussed here because the platform design was not chosen for further analyses in sima. The design chosen was instead the three-column design of the INO WINDMOOR, which results were more thoroughly summarized in the previous section. The INO WINDMOOR platform was chosen over the IEA UMaineUS-S platform for further analyses due to the industry interest in this type of FOWT platform design.

Table 6.14: 25 MW wind turbine properties.

Property	**Value**	**Unit**
Column diameter	14.91	m
Center column diameter	10.0	m
Pontoon width	14.91	m
Pontoon height	4.52	m
Center-center distance	61.73	m
Draft	25.82	m
Freeboard	15	m
Whole structure displacement	26818300.23	kg
CG_x	0.78	m
CG_y	0	m
CG_z	6.9	m

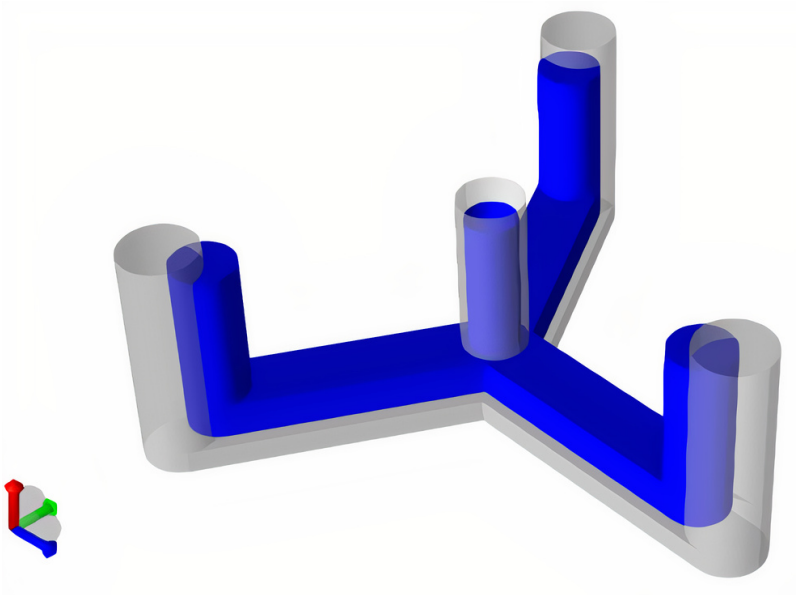

Figure 6.16: Size comparison of 15 MW and 25 MW platforms.

6.4.1 Tower

Though the INO WINDMOOR design was chosen for the platform, the IEA 15 MW UMaine VolturnUS-S design was still used for the tower design. The reason is that it was the largest tower available and the reference model contained cross-sectional data on the Github repository.

The tower is upscaled using the scaling factor $\sqrt{\frac{25}{15}}$. The upscaled properties for the 25 MW FOWT tower are listed in Table 6.15. The material properties are kept the same as for the 15 MW tower.

The 25 MW tower was divided into 10 segments. In order to enable more detailed tower modifications, the number of tower segments was doubled to 20. Each of the 10 segments was divided halfway using the average values between the top and bottom to specify the new value for the halfway point. The 20 sectional values are listed in Table 6.16.

Table 6.15: 25 MW tower properties.

Parameter	**25 MW**	**Unit**
Length	167.177	m
Mass	2,703	Ton
Base outer diameter	12.91	m
Top outer diameter	8.39	m

Table 6.16: Sectional properties for 25 MW tower.

Height [m]	**Diameter [m]**	**Thickness [mm]**
19.365	12.91	107.15
27.751	12.89	107.15
36.138	12.86	107.15
44.523	12.87	107.15
52.910	12.87	107.15
61.295	12.84	72.94
69.681	12.82	38.73
78.066	12.56	37.44
86.453	12.30	36.15
94.838	12.06	34.86
103.225	11.81	33.57
111.610	11.68	31.61
119.996	11.55	29.65
128.381	11.41	27.72
136.768	11.28	25.79
145.153	11.06	24.52
153.539	10.85	23.24
161.925	10.15	25.18
170.311	9.45	27.12
178.427	8.92	27.12
186.542	8.39	27.12

In contrast to the sectional properties specified for the 15 MW tower, which represented segments shaped like truncated cones, the segments for the 25 MW tower are shaped like cylinders with constant diameter and thickness. The reason is that sima simulates the tower as a number of constant area cylinders. The base diameter and thickness for each segment are hence used for the entire segment. This will cause a slightly larger volume than for a segment with a narrowing diameter. However, as the segments have been increased from 10 to 20, the resulting volume is actually lower than the original. The weight and volume of the tower are listed in Table 6.17 for the 15 MW tower, the strict upscaled value, and the resulting SIMA tower values.

Table 6.17: Tower mass comparison.

Model	**Volume [m^3]**	**Weight [t]**
15 MW	160.9	1,263
25 MW geometric upscale	346.2	2,717
25 MW SIMA model	331.1	2,599

Figure 6.17 shows the structural properties of the 25 MW tower alongside the 15 MW tower.

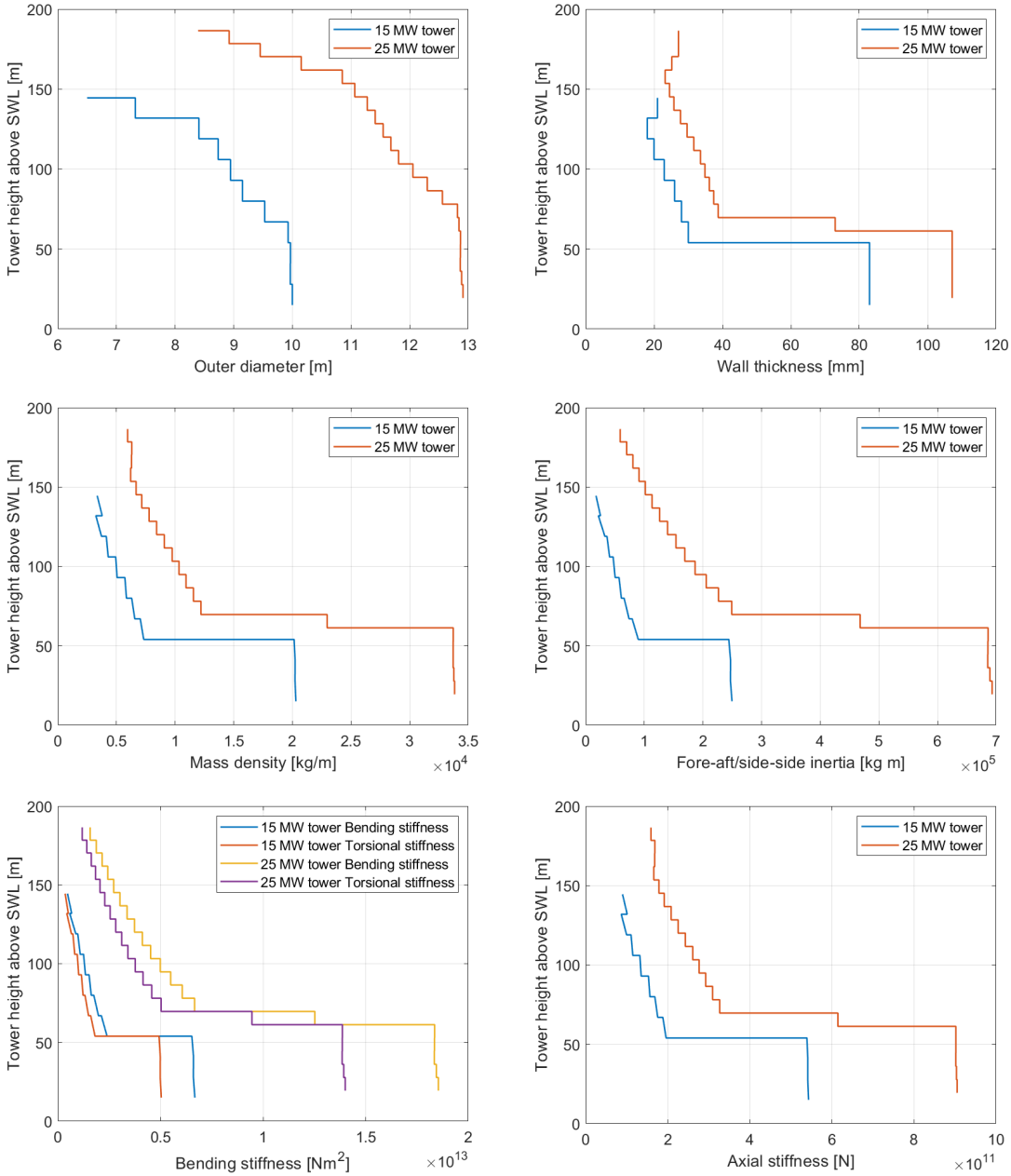

Figure 6.17: Tower structural properties vs. tower height above SWL

As the 25 MW is an (almost) strict geometric upscale of the 15 MW, the same thickness and accompanying stiffness change is seen throughout the plots in Figure 6.17.

Mode shape

The mode shapes are calculated using BModes, which is a finite-element code that provides dynamically coupled modes for a beam. In Figure 6.18 the first and second fore-aft mode is shown. As waves and wind will be applied in positive x-direction, the fore-aft bending is of most interest and hence side-side bending is not included here.

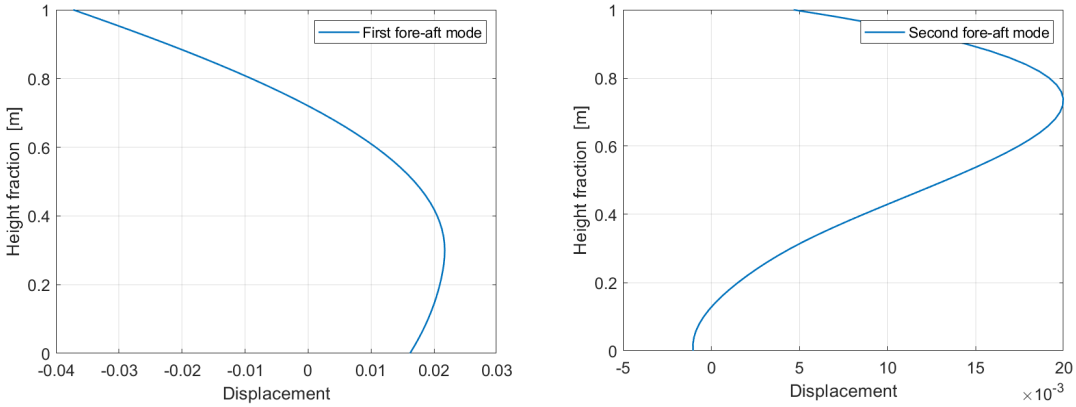

Figure 6.18: First and second mode shape fore-aft bending.

6.4.2 25 MW turbine

The upscaled sima model of the turbine is created by Erin Bachynski-Polić, professor at Institute of Marine Technology at NTNU. The upscaling follows the same scaling factor of $\sqrt{\frac{25}{15}}$. Similar to the tower, the blade is made up of several elements, each with its own specified cross-section. There are 49 segments making up each of the three 149.5 m long wind-turbine blades. Each of the segments has an assigned airfoil with defined aerodynamic characteristics. The turbine properties are provided in Table 6.18

Due to time constraints, the 25 MW turbine was at a preliminary stage when received, and has some limitations in regards to modeling. There is slight aeroelastic instability close to rated wind speed. For tests with wind, the turbine is hence required to run with stiff blades rather than flexible ones. This is accomplished by increasing the stiffness properties in the cross-sections with a factor of 10. This is likely to have an effect on the coupled motions between the blades and the rest of the structure in wind simulations. However, it is still possible to use the stiffer blades in the analyses and get comparable results.

Table 6.18: Turbine mass.

Coefficient	Value	Unit
Power rating	25	MW
Blade length	149.5	m
Blade weight	130	t
RNA mass	2,108	t

The controller for the upscaled wind turbine has a generator torque control mode in the above-rated conditions. The turbine has an active PI pitch control, but no yaw control. To avoid negative damping the controller includes a floating specific feedback mode, namely nacelle velocity feedback.

6.4.3 Mooring

The mooring system of the 15 MW platform is upscaled to match the 25 MW FOWT. However, the chain length is kept the same as for the 15 MW. The upscaled properties are listed in Table6.19.

In SIMA each mooring line is modeled as a solid bar element with the same cross-section for the entire length of the line. The equivalent diameter of the bar, OD, is found by

$$OD = \sqrt{\frac{4m}{\pi \rho_s}} = \begin{cases} 1.80d \text{ m} & \text{(studless)} \\ 1.89d \text{ m} & \text{(studlink)} \end{cases} \tag{6.1}$$

$$OD = 1.8 \cdot 238.65 = 430mm$$

Table 6.19: Mooring system properties for 25 MW.

Parameter	Value	Unit
Mooring system type	Chain catenary	-
Line type	R3 studless mooring chain	-
Anchor depth	200	m
Fairlead depth	14	m
Anchor Radial Spacing	837.6	m
Nominal Chain Diameter	238.65	mm
Dry Line Linear Density	1141.7	kg/m
Chain axial stiffness	54500	MN
Line Unstretched Length	850	m

Mooring line drag and added mass coefficients, listed in Table 6.20, were selected with reference to DNVGL-RP-C205 (DNV, 2014) and DNVGL-OS-E301 (DNVGL, 2018a). The coefficients are given relative to the volume equivalent diameter.

Table 6.20: Mooring line drag and added mass coefficients.

Coefficient	Value
Normal added mass	0.82
Tangential added mass	0.27
Normal drag	1.11
Tangential drag	0.20

6.5 SIMA model

The SIMA model of the FOWT is shown in Figure 6.19. The model features the upscaled three-column platform design, turbine tower, RNA, and mooring.

6.5.1 Platform body

The platform is included as a "body", with specifications imported from HydroD. As previously explained, HydroD includes the total mass of the system, including the tower and turbine. When assembling the SIMA model, the tower and turbine are mounted on top of the platform. The platform body is modeled with the option "gravity included", which means that sima finds equilibrium depending on the weight and buoyancy of the elements modeled. This means the weight of the tower and turbine are counted twice, and the FOWT would sink. To amend this issue, first, the platform is updated with its own mass coefficients and COG, as specified in Table 6.12. Secondly, a buoyancy force equaling the total mass force is then applied at the platform COB to achieve equilibrium. The FOWT hence assigns itself a correct draft depending on the amount of weight it registers and the submerged volume. The draft will hence change compared to the HydroD analyses, as the SIMA tower is slightly lighter than the strict geometric upscaled tower, as explained in Section 6.4.1.

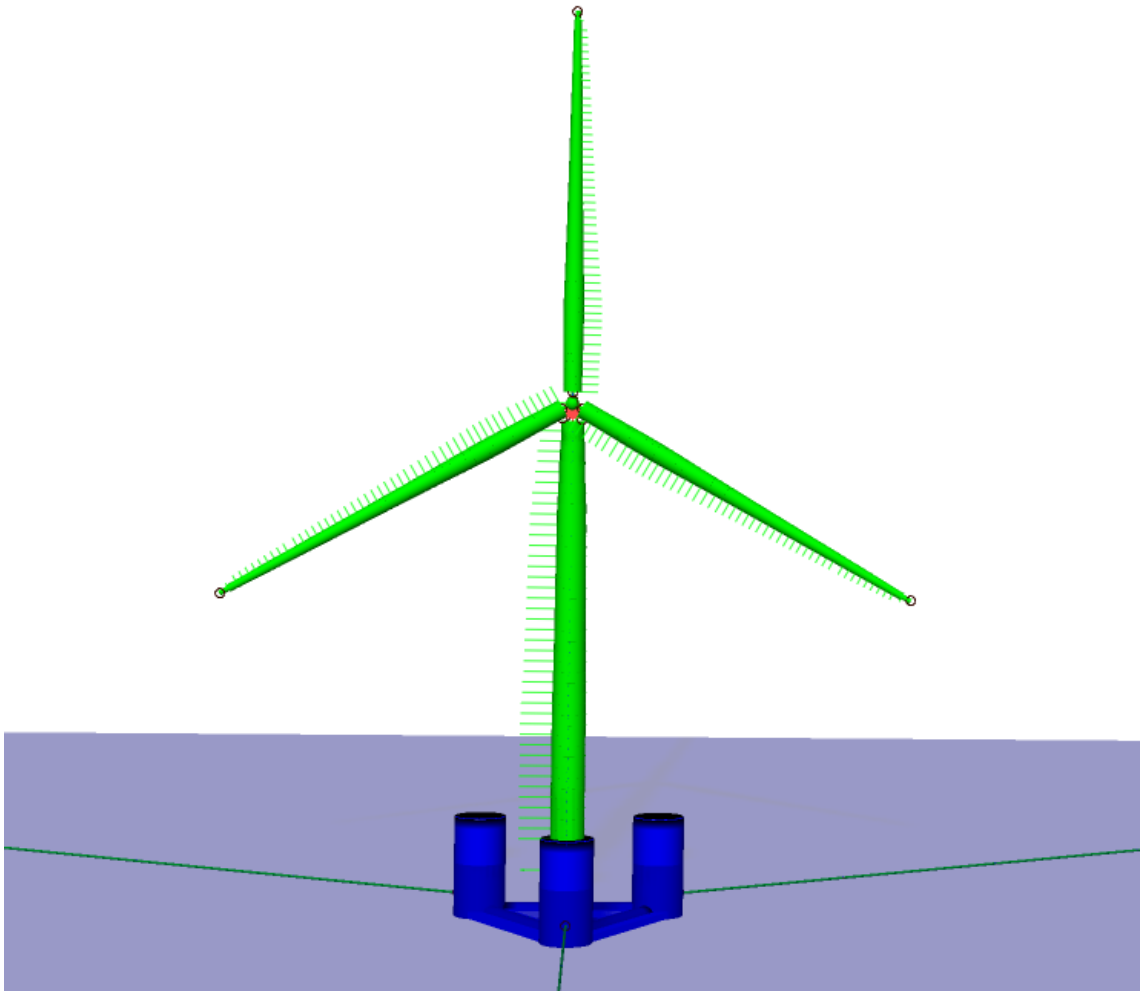

Figure 6.19: Sima model of the upscaled FOWT.

Hydrostatic stiffness is one of the properties imported from HydroD. Out of the imported hydrostatic stiffness values, C_{33} is correct. However, C_{44} and C_{55} should be modified such that only the parts related to the platform body are included. Due to symmetry, the moment of inertia is the same in the x-and y-direction, hence $C_{44} = C_{55}$, given by

$$C_{55} = \rho g I_{wp} + \rho g \nabla z_b - M g z_g \tag{6.2}$$

where I_{wp} is the moment of inertia about the water plane. With the "gravity included" option, the equation becomes just the first term, i.e.

$$C_{55} = \rho g I_{wp} \tag{6.3}$$

The hydrostatic coefficients are listed in Table 6.21.

Table 6.21: Hydrostatic coefficients.

Hydrostatic coefficient	**Value**	**Unit**
C_{33}	1.04e+07	N/m
C_{44}	9.94e+09	Nm
C_{55}	9.94e+09	Nm

When imported into SIMA, the body is technically a point mass with assigned properties. It is possible to assign a visualization of the platform model based on the HydroD output files. However, the waves can not "see" this model, as it is purely for visualization purposes. Hence, to enable hydrodynamic load calculations by Morison's equation it is necessary to define slender elements for the columns and pontoons. These are defined by specifying the volume and the start and stop coordinates.

The drag coefficient for the columns (Cd = 1.0) follows Appendix E of DNV-RP-C205 "Environmental conditions and environmental loads" (Case 14 of Table E-1). The drag coefficients are only used for hydrodynamic loads and not wind. Though the platform does have a freeboard that will be subjected to wind, the aerodynamic load on the platform is assumed negligible in comparison to the load on the tower and RNA.

It should be noted that the model in SIMA is rotated 180 degrees compared to the INO WINDMOOR 12 MW coordinate system specified in Figure 6.2.

6.5.2 Slender system

The tower and turbine are modeled as slender elements. For the tower, each of the 20 segments has an assigned cross-section with specified mass coefficient, external and internal area, gyration radius, and stiffness properties. The length of each segment is specified along a tower line which is subsequently connected to the platform and turbine through super-nodes.

The turbine blades consist of 49 segments, each with cross-sectional properties along with airfoil properties. The airfoil properties define the airfoil characteristics, the angle, C_D, C_L and C_M. The RNA is defined through a number of lines with point masses and rotational joints. The turbine will then rotate in accordance with the specified controller file.

7 Coupled analyses

With the wind turbine fully assembled in sima, it is now possible to conduct coupled analyses. Constant wind tests are run to assess the turbine performance. The maximum thrust force is used to check the tower for buckling. Decay tests are performed to assess the natural periods of the FOWT both without wind, at rated wind speed, and above rated wind speed. Tests in regular waves are also carried out to chec the RAOs. A set of simplified environmental conditions are defined for fatigue analysis of the tower.

7.1 Constant wind tests

The constant uniform wind tests are performed to check the performance of the FOWT and the controller. Wind speeds of 4 m/s to 24 m/s were used. Each wind speed was simulated for 600 s, with the exemption of the first wind speed which was simulated for an extra 400 s. The step wind file was generated in Matlab and is illustrated in Figure 7.1. The SIMA parameters for the constant wind simulation are provided in Table 7.1.

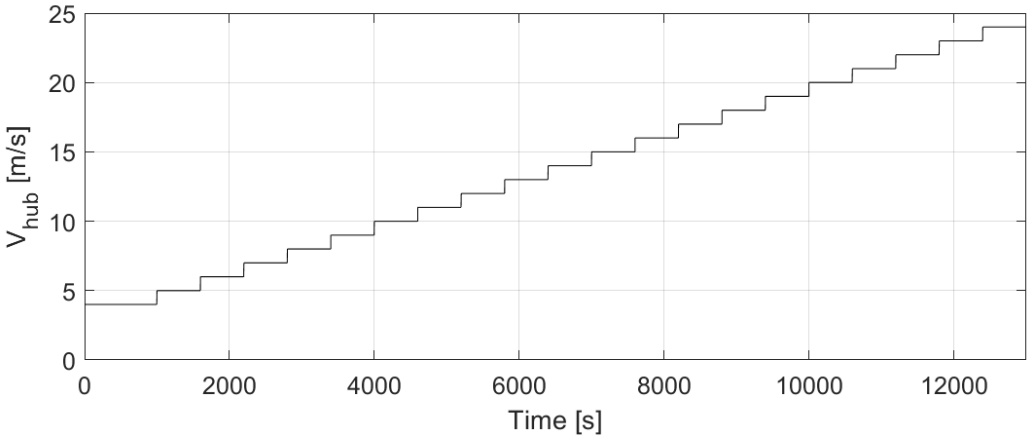

Figure 7.1: Wind step file for constant wind test.

Table 7.1: SIMA parameters for constant wind test.

Simulation length	13000 s
Simulation time step	0.005 s
Wave/body response time step	0.1 s
Turbine condition	Operational
Wind input	Constant
Wave conditions	Hs = 0.001 m, Tp = 20 s

Results from the constant wind test were processed and are presented in terms of mean rotor speed, mean thrust, mean torque, mean power, and mean blade pitch. Statistics were taken after the turbine and platform reached an approximate steady-state condition. The results were then averaged for each wind speed. The mean rotor speed, torque, and blade pitch are shown in Figure 7.2a, while the mean generator power and rotor thrust are shown in Figure 7.2b (NB double y-axis notation).

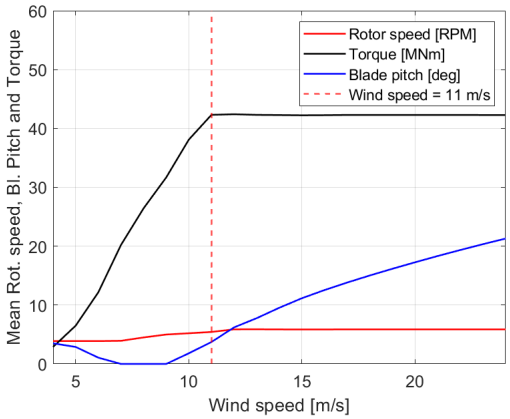

(a) Mean rotor speed, torque, and blade pitch

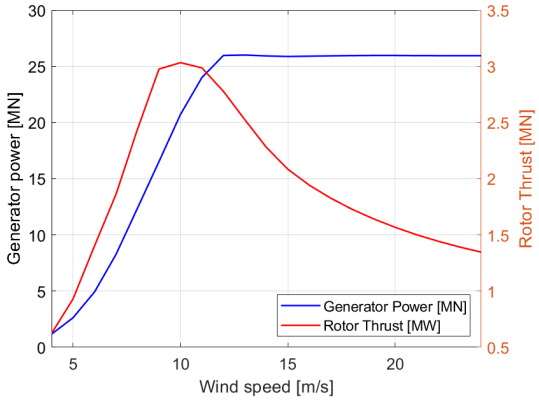

(b) Mean generator power and rotor thrust

Figure 7.2: Wind turbine performance curves.

From Figure 7.2a, the torque can be observed to increase until reaching a wind speed of 11 m/s. This is the rated wind speed. As the wind speed increases past 11 m/s the torque remains constant. The same can be said about the generator power in Figure 7.2b. Here, the rotor thrust, with the y-axis to the right, experiences a peak at approximately 3 MPa around rated wind speed, before decreasing as the blades pitch. The generator power is also observed to remain constant after rated wind speed. Both figures show a strong resemblance to the anticipated result, discussed in Section 4.2.

At cut-in wind speed, 4 m/s, the mean turbine rotational speed is 3.88 RPM. At the rated wind speed the rotational speed is 5.87 RPM. Beyond rated wind speed the wind turbine rotational speed is approximately constant. The rotational speed is divided by 60 to get the 1P frequency. Table 7.2 lists the minimum and maximum 1P frequency, along with the accompanying 3P frequencies.

Table 7.2: 1P and 3P frequency.

Frequency	Cut-in	Rated
RPM	3.88	5.87
1P	0.0646 [Hz]	0.0978 [Hz]
3P	0.1939 [Hz]	0.2935 [Hz]

7.2 Tower stability

The tower is checked for buckling under the weight of the RNA, and with applied thrust force. The structure is assumed to be fatigue-dominated, hence only simplified buckling checks are conducted. The results are used to assess if more exact calculations are necessary.

7.2.1 Buckling from a static load

The tower is here considered a beam with a point load equal to the weight of the RNA. As a conservative measure, the total weight of the tower is included in the point load. As outlined in Section 4.4.1, the tower is safe from global buckling if the applied load is less than the critical load P_c, given by Equation 4.69. The critical load is proportional to the moment of inertia, given by Equation 4.31. The moment of inertia depends on the diameter and thickness, which vary along the tower length. The diameter and thickness are taken as the values at 1/3 from tower base as an estimate for the averaged values for diameter and thickness. The input values for the global buckling check are listed in Table 7.3.

Table 7.3: Global buckling check parameters.

Parameter	Value	Unit
E-module	2.10+E11	Pa
Yield strength	250	MPa
Gravity acceleration	9.81	m/s^2
Diameter	12.8157	m
Thickness	0.0387	m
Tower height	167.18	m
RNA weight	2.1E+06	kg
Tower weight	2.6E+06	kg

For boundary conditions, the tower is assumed fixed at the base and free at tower top. The reference length is hence 2 times the length of the tower. The calculated values for moment of inertia, critical load, and mass load are listed in Table 7.4. The load from the RNA and tower mass is a permanent load and the load factor is taken as 1, according to table 5-1 in DNVGL-ST-0119 (DNVGL, 2018a).

Table 7.4: Global buckling check.

Parameter	Value	Unit
Load factor	1	-
Static load, P	53.11	MN
P_c	560	MN

As can be seen from Table 7.4

$$Pc >> P$$

confirming that the tower is safe from buckling under the static load of the upscaled RNA.

7.2.2 Applied thrust force

In operational conditions, the tower will be exposed to a bending moment due to the thrust force acting at the tower top. As an initial estimation, the maximum thrust force is taken as 3 MW following Figure 7.2b. This value is the mean maximum thrust force. There will be some variations but the mean is assumed sufficient for preliminary testing. The thrust force attaches point is taken at the tower top, hence the moment arm is equal to the tower height.

The static load from RNA and tower mass are included. The load is not strictly compressive anymore as the thrust force at the tower top results in a 0.75 m horizontal displacement of the tower top, calculated using Equation 4.74. As the tower top shifts, the weight of the RNA contributes to the bending moment at tower base. In addition, some of the tower mass will also contribute. As a conservative measure, the entire tower weight is taken as a mass with a moment arm of 0.75 m. There will also be some load on the wind turbine tower due to the wind acting on the base of the tower, but that is not included in this preliminary buckling check.

The calculated bending moments are listed in Table 7.5. The largest contribution is shown to be from the thrust force. The moment resistance is calculated using Equation 4.73. The stress at tower base is then found using Equation 4.72. The load factor for environmental loads is for ULS taken as 1.35 for consequence class 3 floating wind turbine structure, based on DNVGL (2018a). In reality, the safety factors are separated according to whether the load is permanent or operational. The RNA mass and tower mass are permanent loads, while the thrust is operational. However, the same safety factor is here used for both as an extra precaution to account for uncertainties in the simplified buckling check. A material factor of 1.15 is included in accordance with DNV following Eurocode 3 (DNVGL, 2016).

Table 7.5: Bending moments.

Parameter	Value	Unit
Moment from thrust force	501.5	MNm
Moment from RNA mass	15.2	MNm
Moment from tower weight	18.8	MNm
Load factor environmental loads	1.35	-
Moment with load factor	722.9	MNm
Moment resistance	13.68	m^3
Material factor	1.15	-
Stress, σ_b	52.9	MPa
Yield stress over material factor	217.4	MPa

The stress at tower base is seen to be much lower than the yield stress over the material factor

$$\sigma_b << \frac{f_y}{\gamma_m}$$

and the tower is safe from buckling. The safety margin is sufficiently large and further calculations are not deemed necessary.

7.3 Decay tests

Decay tests were performed to document the natural periods and damping of the FOWT both without wind, at rated wind speed, and above rated.

7.3.1 Simulation input

The initial displacement of the platform was achieved by applying a ramp force, followed by a constant force which was then released. The ramp force was applied after 50 s to allow the system to come to a steady-state. An example of the applied force for surge is shown in Figure 7.3. The force and moments for all motions are provided in Table 7.6. During the decay tests with no wind the turbine is parked and the blades are pitched 90 degrees.

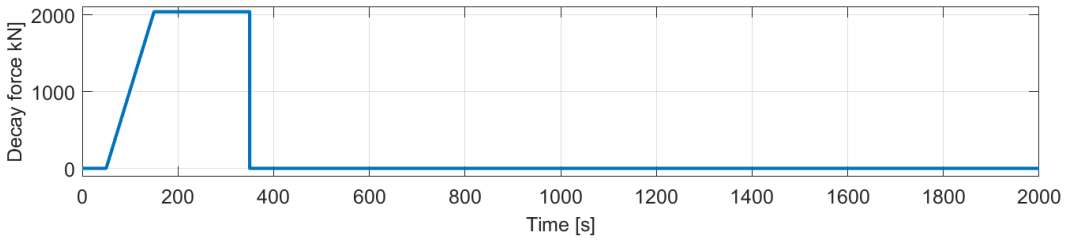

Figure 7.3: Example of applied force during surge decay.

7.3.2 Without wind

Motion decay was run in the absence of wind. The results from the decay tests were processed using Matlab with time series and motion history as input. Decay results are shown here for all six DOFs, taken after the force is released.

Surge
The surge period for the FOWT is shown in Figure 7.4. In surge there is low radiation of waves

Table 7.6: Forces and moments applied to the FOWT.

Motion	Force/Moments [kN/kNm]	Ramp duration [s]	Constant force duration[s]	Simulation length [s]
Surge	2040	100	200	2000
Sway	2040	100	200	2000
Heave	12000	50	200	1000
Roll	264000	100	200	1400
Pitch	264000	100	200	1400
Yaw	12000	100	200	1800

and damping is mainly due to viscous effects. The FOWT oscillates around zero value.

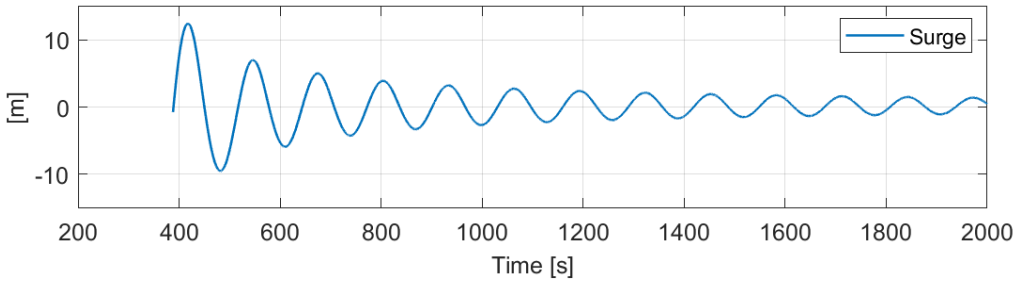

Figure 7.4: Decay in surge.

Sway
Results from sway decay are shown in Figure 7.5. They are similar to results from surge. Also here viscous damping dominates and there is low linear radiation damping. The motion is centered around zero.

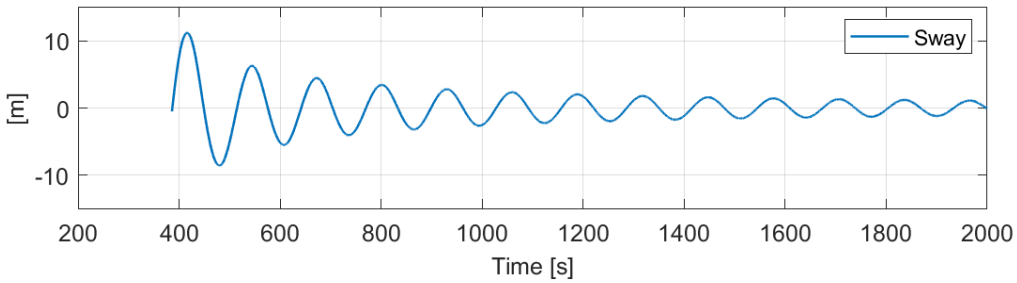

Figure 7.5: Decay in sway.

Heave
Heave decay is shown in Figure 7.6. As mentioned in Section 6.4.1, the tower is slightly lighter than the upscaled tower with truncated segments. Hence, the equilibrium position is slightly shifted and the heave surge motion oscillates around approximately 0.3 m. During heave motion there is radiation of waves, hence the semi-submersible experiences linear damping from radiation. There will also be slight viscous damping.

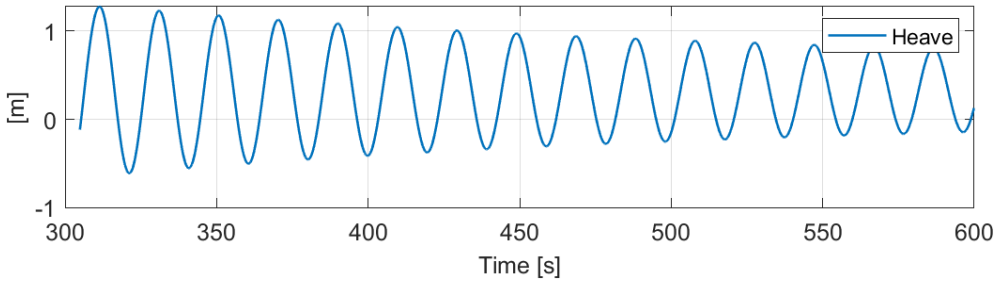

Figure 7.6: Decay in heave.

Roll

Figure 7.7 show the decay results for roll. Roll motion also causes wave radiation and hence experiences linear damping. It also experiences slight viscous damping from the body moving in a fluid.

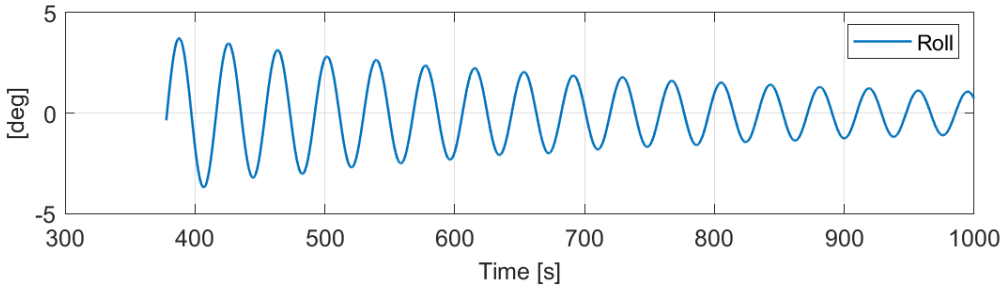

Figure 7.7: Decay in roll.

Pitch

Pitch decay is shown in Figure 7.8. For pitch motion, there is low viscous damping. Linear damping dominates.

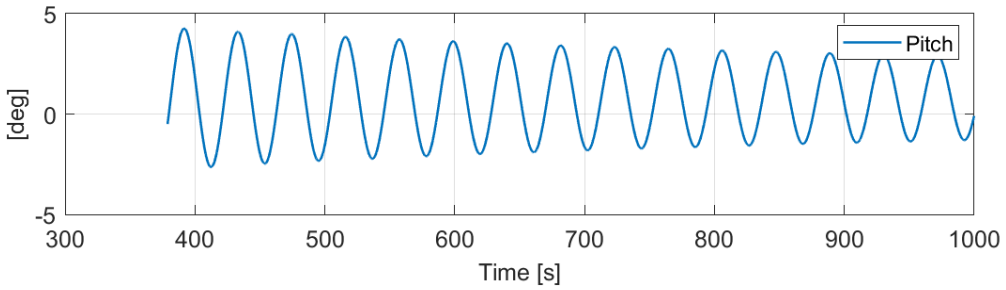

Figure 7.8: Decay in pitch.

Yaw

The last motion is yaw, shown in Figure 7.9. Yaw causes almost no linear radiation damping and hence the viscous damping is dominating. The motion is seen to oscillate around 180 degrees but represents the same scenario if it was oscillating around 0.

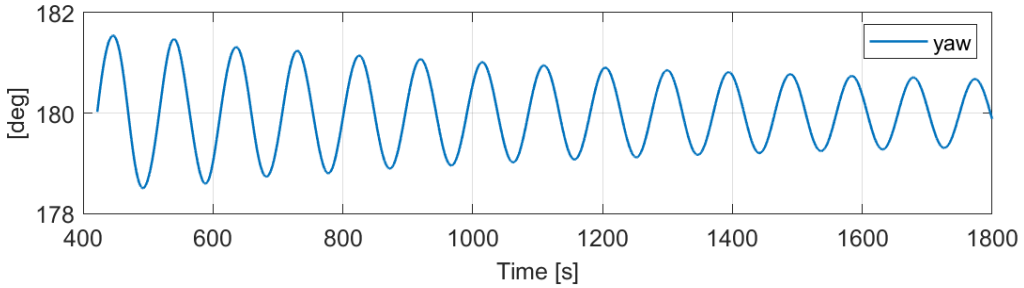

Figure 7.9: Decay in yaw.

The natural periods were calculated for all motions and are provided in Table 7.7.

Table 7.7: Natural periods from decay tests without wind.

Motion	**Natural periods** [s]
Surge	126.5
Sway	126.6
Heave	19.4
Roll	37.4
Pitch	40.8
Yaw	93.3

7.3.3 Decay with rated and above-rated wind

To assess the change in natural periods during rated and above-rated wind scenarios, the same decay tests are rerun with 11 and 25 m/s wind velocity. Figure 7.10 shows the comparison of decay in surge for the three cases.

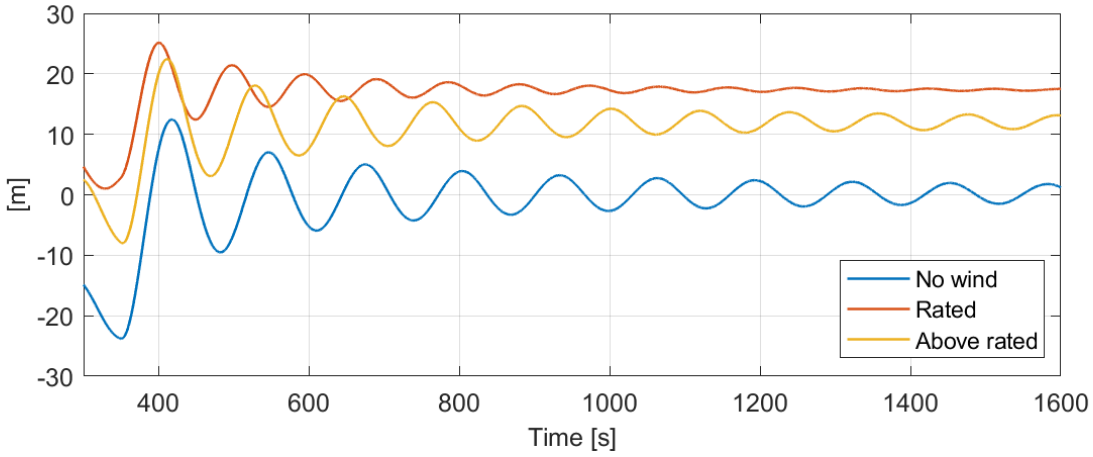

Figure 7.10: Surge decay no wind, rated and above rated.

In the absence of wind, the surge motion is oscillating around zero mean value. With wind, the FOWT oscillated at a non-zero value due to the wind displacing the platform. Figure 7.10 also shows that the motion settles quicker for the scenarios with wind, and quickest at rated wind speed where the thrust force is at its highest. Similar results can be seen for pitch motion in Figure 7.11. There are quick oscillations for the no-wind scenario, where the motion oscillates around a mean zero value. For rated and above rated the turbine is shifted to a negative degree as the thrust force is at its maximum. The natural period for pitch is lowest without wind, highest at rated, and in

between at above rated. This coincides with the anticipated results based on what was discussed in Section 4.1.4. These results emphasize the importance of coupled analyses as the relationship between motions and resonance shifts as quickly as the wind speed shifts. This is especially true for surge, sway, pitch, and yaw. Heave and roll are not as influenced by the rated and above rated wind speed, as shown by the natural periods listed in Table 7.8. It should be noted that it becomes more difficult to calculate the natural periods during rated and above rated as there are disturbances in the oscillations.

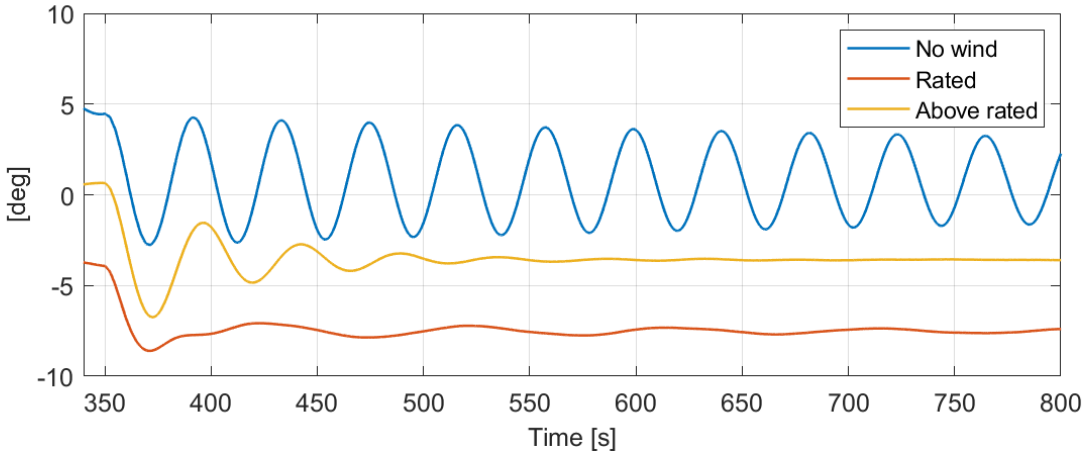

Figure 7.11: Pitch decay no wind, rated and above rated.

Table 7.8: Natural periods from decay tests.

Motion	No wind	Rated	Above rated
Surge	126.5	89.7	112.8
Sway	126.6	164.2	143.0
Heave	19.4	19.4	19.3
Roll	37.4	39.0	36.6
Pitch	40.8	51.3	46.7
Yaw	93.2	36.8	89.4

7.4 Tower bending

The time series of the tower base bending moment during pitch and roll decay are studied in addition to the motion time series. Based on the initial part of the decay, the first tower fore-aft and side-side bending natural periods are found. The frequency is compared to the 1P and 3P rotor frequencies. The tower bending moment can be seen at the initial part of the pitch and roll decay as illustrated in Figure 7.12 for pitch decay.

From the oscillation peaks shown in the right part of Figure 7.12, the natural period of the first fore-aft bending moment at tower base is found to be 2.33 s. The same approach is taken for the side-side bending in roll decay, where the natural period is found to be 2.15 s. The associated frequency in hz is 0.4211 and 0.4225. The frequency is shown in Figure 7.13, compared to the 1P and 3P. The frequency of the tower is seen to be in the stiff-stiff range.

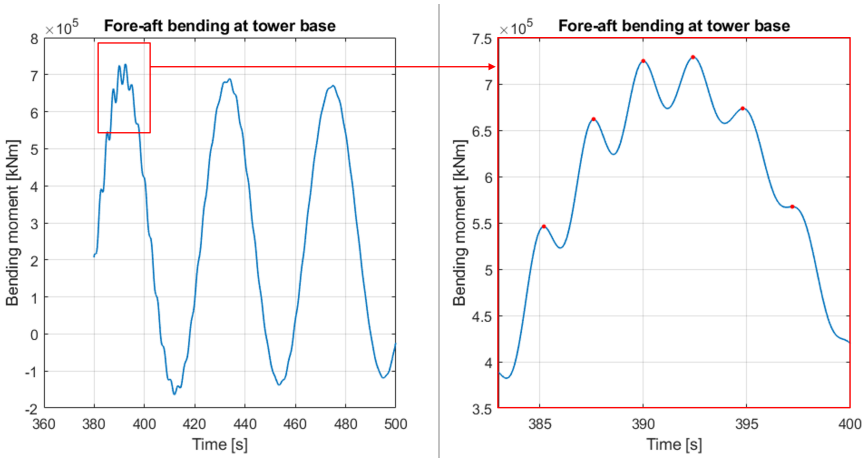

Figure 7.12: Fore-aft bending moment at tower base for pitch decay.

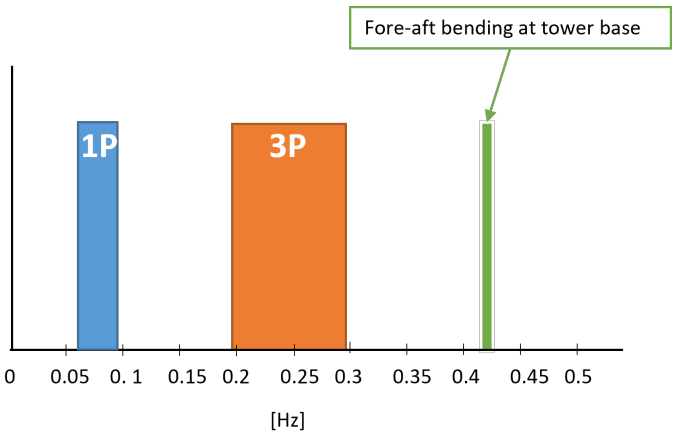

Figure 7.13: Fore-aft bending moment at tower base compared to 1P and 3P.

The bending frequency of the tower also complies with the DNV-ST-0126 requirement of $f_R/f_{0,n} \leq 0.95$.

7.5 Regular waves

As explained in Section 3, regular waves are sinusoidal with constant wave amplitude and period. The FOWT are tested in regular waves with a wave height of 1 m. Periods range from 4 to 50 s with a step length of 0.5 s. The waves are run for a number of periods equaling a simulation length of approximately 4000 s. Simulation input is listed in Table 7.9. The turbine is parked and no wind is applied. The wave direction is 0, i.e., the waves travel along the x-axis in a positive direction.

The results for global platform motion are extracted for surge, heave, and pitch. The results are processed and presented as RAOs in Figure 7.14a, 7.14b and 7.14c respectively.

Table 7.9: Simulation input regular waves.

Parameter	Input	Unit
Wave amplitude	0.5	m
Wave direction	0.0	m
Wave phase	0.0	m
Wave period	4-50	s
Wind velocity	0.01	m/s
Time step	0.01	s
Simulation length	4000	s

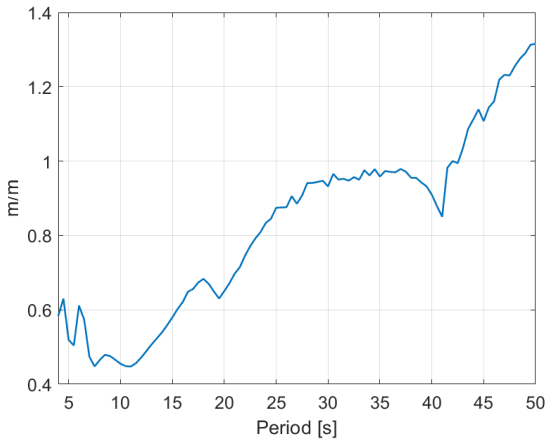

(a) RAO in surge

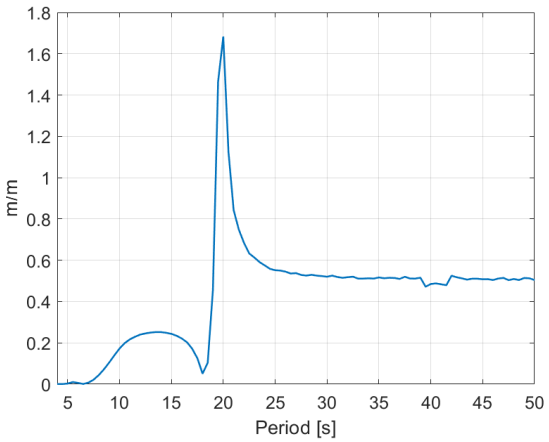

(b) RAO in heave

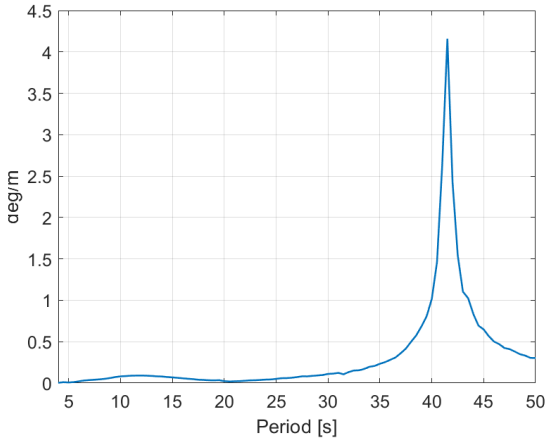

(c) RAO in pitch

Figure 7.14: RAO

From Figure 7.14b and 7.14c, the peak is seen to coincide with the natural period in heave and pitch, as expected. The peaks are higher than what was seen from the initial HydroD results from the model validation, Figure 6.10. However, the hydrostatic analysis in HydroD was run with additional stiffness in heave and pitch. The difference in results is hence assumed to be due to the difference in stiffness. The RAO in surge shows some coupling between the natural period in heave and pitch. The results from the regular wave test showed that the natural periods found through the decay tests coincide with experimental results.

7.6 Fatigue study

Fatigue is assumed to be the design-limiting factor for the upscaled tower. A fatigue study is hence conducted to assess if the tower can sustain the environmental and operational loads for the duration of its lifetime. 20 years for design fatigue life is normally used as a minimum for a structural component, regardless of whether the true service life is less than 20 years (DNVGL, 2018b). The fatigue analysis is carried out in the time domain using Rainflow counting. The fatigue damage on the tower is calculated using the SN-curve as explained in Section 4.4.2.

7.6.1 Simulation input

Fatigue is calculated based on the stress and bending moment experienced by the tower during different environmental conditions. For this fatigue analysis, a set of simplified environmental conditions is defined based on a generic site defined in the EU-founded LIFES50+ project by Krieger et al. (2015). The site is partly based on the publicly available information on site conditions in the Gulf of Main area in the USA (Krieger et al., 2015).

The environmental conditions consist of seven different wind/wave combinations, each with three different wave periods and probability of occurrence. The waves follow a 3-parameter Jonswap and are generated in SIMA. The wind files are generated using TurbSim in accordance with the Kaimal spectral model, and properties are provided in Table 7.10. The turbulence is class C, following the IEC 61400-3 standard (IEC, 2019). The turbulent wind is simulated as a box of wind that is pushed towards the turbine, with the size of the "wind-box" given by the grid width and height.

The wind velocities are the same as in the LIFES50+ project. It should be noted that these wind velocities are, per that generic location, velocities at 119 m, which is the hub height of the LIFES50+ turbine. If the upscaled FOWT were placed at the same location, the wind velocity would be slightly higher due to a different position in the wind shear profile, as discussed in Section 2. However, as no specific site is chosen for the upscaled turbine, these wind velocities are used. The environmental conditions are listed in Table 7.11.

Table 7.10: Turbulent wind.

Parameter	**Value**	**Unit**
Time step	0.05	s
Hub height	192	m
Grid height	350	m
Grid width	350	m
Vertical grid-point matrix dimensions	47	-
Horizontal grid-point matrix dimensions	47	-
Surface roughness length	0.03	m

Kvittem and Moan (2015) conducted a comprehensive fatigue assessment of a semi-submersible FOWT and found that important fatigue effects seemed to be captured by one-hour simulations. Hence, each of the 21 environmental conditions is run for one hour and fatigue damage is multiplied with time and probability to find 20-year damage from axial stress and bending moments. The shear stress is neglected. Moreover, the turbine is facing perfectly upwind (no yaw error), and the direction of the waves is aligned with the direction of the wind. It is hence deemed sufficient for the purpose of this study, to take a point on the outer radius as an example for fatigue evaluation (Xu et al., 2019). Further, only loads during normal production are considered. This approach is considered sufficient for a preliminary assessment of the tower designs. For future work, idling, start-up, and shutdown cases could be included (Krieger et al., 2015).

Table 7.11: Environmental conditions for fatigue analyses (Krieger et al., 2015).

Condition number	V_{hub} **[m/s]**	H_s**[m]**	**Tp [s]**	P [%]
1	5	1.38	5	3.45
2	5	1.38	7	6.89
3	5	1.38	11	3.45
4	7.1	1.67	5	5.99
5	7.1	1.67	8	11.98
6	7.1	1.67	11	5.99
7	10.3	2.2	5	6.41
8	10.3	2.2	8	12.83
9	10.3	2.2	11	6.41
10	13.9	3.04	7	5.12
11	13.9	3.04	9.5	10.24
12	13.9	3.04	12	5.12
13	17.9	4.29	7.5	2.90
14	17.9	4.29	10	5.81
15	17.9	4.29	13	2.90
16	22.1	6.2	10	0.94
17	22.1	6.2	12.5	1.88
18	22.1	6.2	15	0.94
19	25	8.31	10	0.19
20	25	8.31	12	0.37
21	25	8.31	14	0.19

7.6.2 Calculation parameters

For the fatigue study, each condition is run with six seeds. The analysis is thus based on a total of 126 one-hour simulations featuring different environmental conditions. Axial forces and bending moments are stored for each of the 20 tower segments, allowing for a detailed fatigue assessment of the entire tower length. The forces and moments stored from the simulations are output from riflex in the local riflex coordinate system. For the tower, the transformation to the calculation coordinate system, illustrated in Figure 7.15, is given by

- Nx = DOF 1 Axial force from RIFLEX
- My = $-1*$ DOF 3 Mom. about local y-axis, from RIFLEX
- Mz = DOF 5 Mom. about local z-axis from RIFLEX

These are used as inputs in the equation for nominal stress for a location as per Equation 4.79.

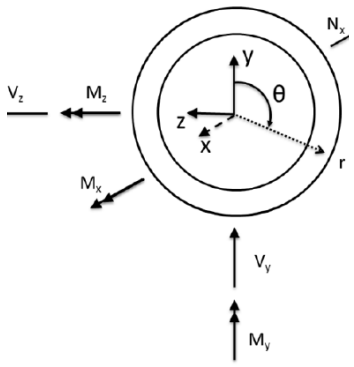

Figure 7.15: Coordinate system for tower base fatigue damage calculation (Xu et al., 2019).

The safety class for the FOWT is set to normal based on recommendations from DNVGL (2018b). The load factor, γ_F, for FLS is 1.0 for all load categories (DNVGL, 2018a). The parameters for the SN curve are listed in Table 7.12 based on data from DNV (2010). For simplicity, a stress concentration factor of 1 is assumed.

Table 7.12: SN parameters (DNV, 2010).

$N \leq 10 * 7$ cycles		$N > 10^7$ cycles		Fatigue limit at	k	t_{ref}
m	$log\bar{a}$	m	$log\bar{a}$	10^7 cycles		(for the given cross section)
3	12.164	5.0	15.606	52.63 MPa	0.20	25 mm

The fatigue damage is calculated using Matlab. The axial force and bending moments are extracted at the base of each segment, except for segment 20 in which the moment is extracted at the top. Due to damage calculation at each segment, it is possible to show the fatigue as a function of tower height.

7.6.3 Fatigue results

Upon averaging the six seeds per condition, there are 21 fatigue results for each of the 20 segments. The results are first presented as a function of tower height to identify the critical tower segments. As seen in Table 7.11, each of the seven wind velocities has three different scenarios of probability. The condition with the highest probability for each of the wind velocities is shown as a function of tower height in Figure 7.16. Due to the higher probability, it is likely that one of these conditions will contribute to the most accumulated fatigue damage over 20 years.

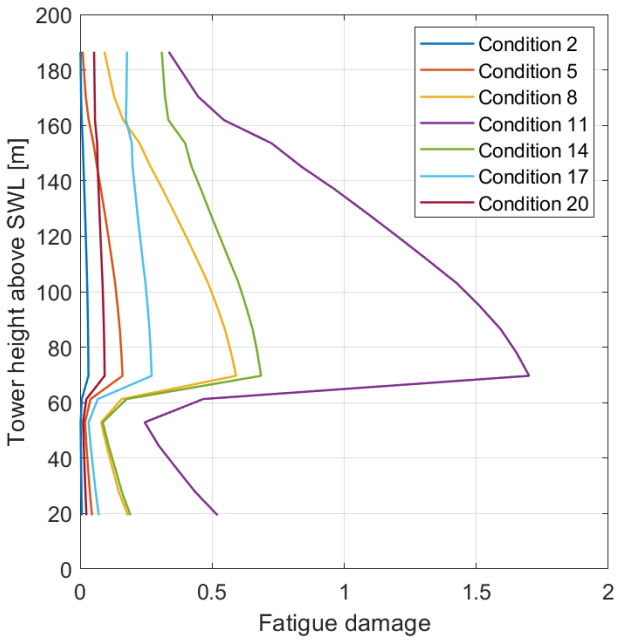

Figure 7.16: Fatigue damage as a function of tower height.

From Figure 7.16 it is clear that the tower experiences the highest amount of fatigue at approximately 70 m above SWL. This location is the start of tower segment 7 where there is an abrupt decrease in thickness, as previously discussed, see Figure 6.17 and Table 6.16. The thickness reduced by 63.85% from one segment to the next, causing an equal percentage decrease in cross-sectional area. When compared with the mode shape of the tower from Figure 6.18, the profile is seen to have large curvature at that location.

Out of the conditions in Figure 7.16, condition 11 is the one causing the largest amount of fatigue damage. Condition 11 alone is > 1, implying failure even before all conditions are summarized. When summarizing, fatigue is seen to be larger than 1 for all segments except segment 5. The damage is largest for segment 7, with D = 6.97. Accumulated 20-year damage for all conditions is shown in Figure 7.17 as a function of tower height. The 20-year fatigue damage for all conditions and all segments are included in Appendix B.1. When calculating the fraction of total fatigue damage for each condition, condition 11 is responsible for 25-20% of the damage, depending on the location along with the tower. The damage fraction for each segment per condition is provided in Appendix B.2.

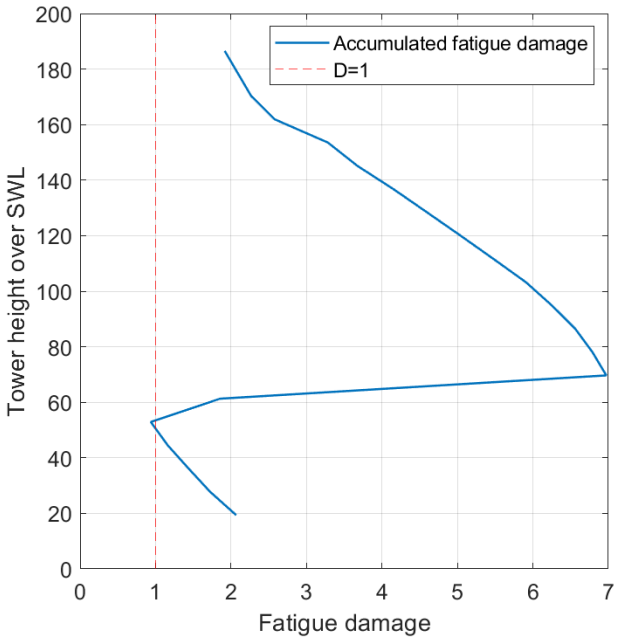

Figure 7.17: 20 years accumulated fatigue damage.

For visualizing the fatigue damage for all 21 conditions, the fatigue damage is plotted for a few key segments, based on the results from Figure 7.16. The selected segments are tower base, segments 5 and 7, and tower top. The segments and properties are summarized in Table 7.13. The resulting scatter plot is shown in Figure 7.18 as a function of wind speed for the four locations.

Table 7.13: Segment description.

Segment number	**Tower height above SWL [m]**	**Diameter [m]**	**Thickness [mm]**
1 (tower base)	19.365	12.9	107.2
5	52.909	12.9	107.2
7	69.681	12.8	38.73
20 (tower top)	186.54	8.4	27.12

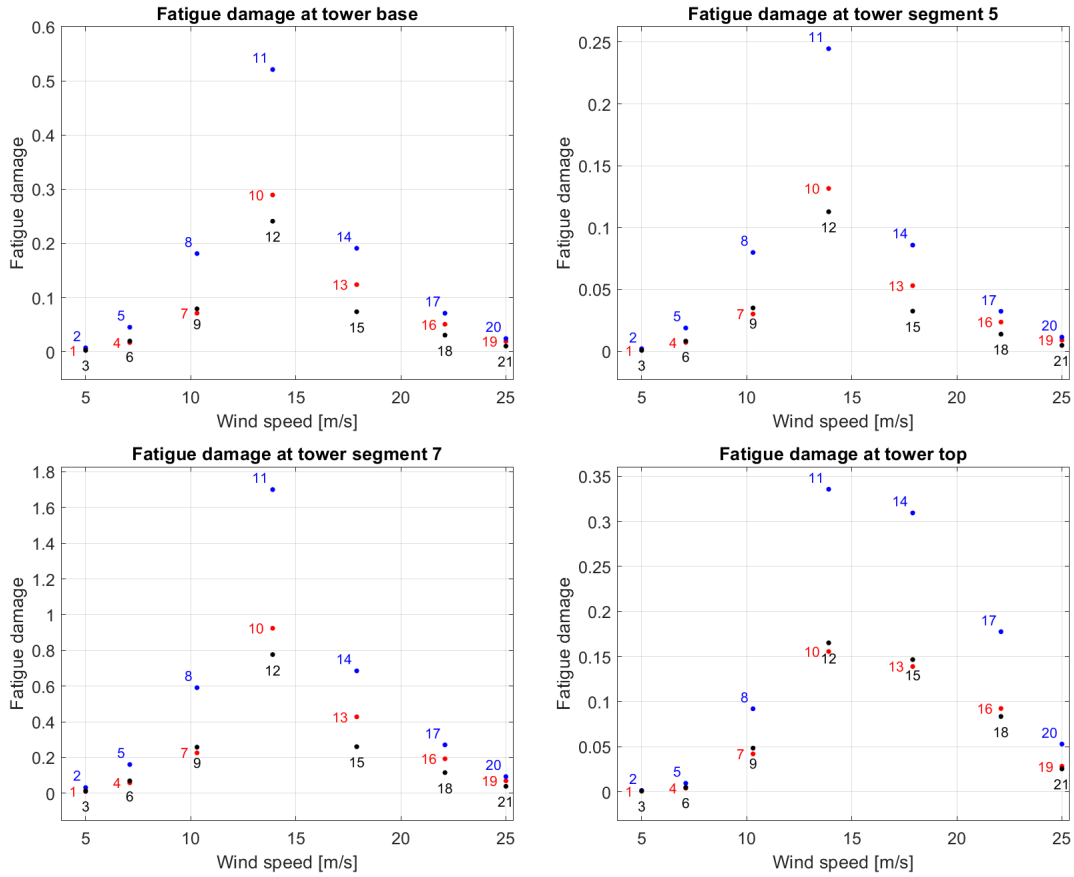

Figure 7.18: Fatigue damage as a function of wind speed.

The overview of all conditions in Figure 7.18 confirm that condition 11 is the one causing the largest fatigue damage. Following condition 11 is condition 10 and 12 for the tower base, segment 5, and segment 7. For tower top on the other hand, the second most critical condition is conditions 14 and 17, corresponding to higher wind velocities.

Condition 11 has a high probability. In addition, it has a wind velocity of 12.9 m/s, a wave height of 3.04 m, and a wave period of 9.5 s. As discussed in Section 5.1.3, large wind turbines are subject to a rotational frequency located in the wave frequency range. The rotational speed of the 25 MW turbine is 10 to 15 seconds. This leaves only a 0.5 s gap between the wave period of the second most probable environmental condition of all 21 conditions, and the 1P frequency range.

Further, in the case of aligned waves and wind traveling along the positive x-axis, the fore-aft bending moment contributes significantly to fatigue. Fore-aft bending moment is largely dependent on pitch motion. The natural period of pitch motion will depend on the specific condition and will hence be alternating along with the different conditions. Spectral analysis for pitch motion for all 21 environmental conditions is shown in Figure 7.19 for two of the six seeds. A peak can be observed at around 0.02 Hz, which is inside the window of pitch natural period of 40.8 s to 51.3 s. To avoid resonance it could be an option to consider frequency skipping by the control system (Tempel, 2006). Spectral analysis for all motions are included in Appendix E.

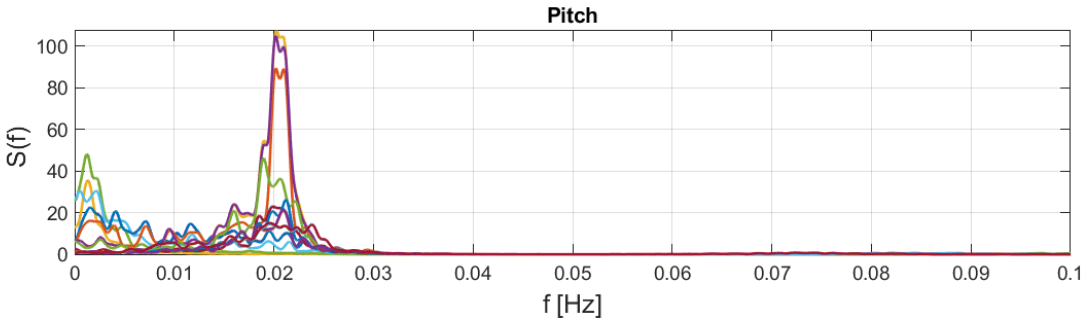

Figure 7.19: Spectral analysis pitch motion.

Figure 7.20 shows the spectral analysis of bending moment for base, segment 7, and tower top.

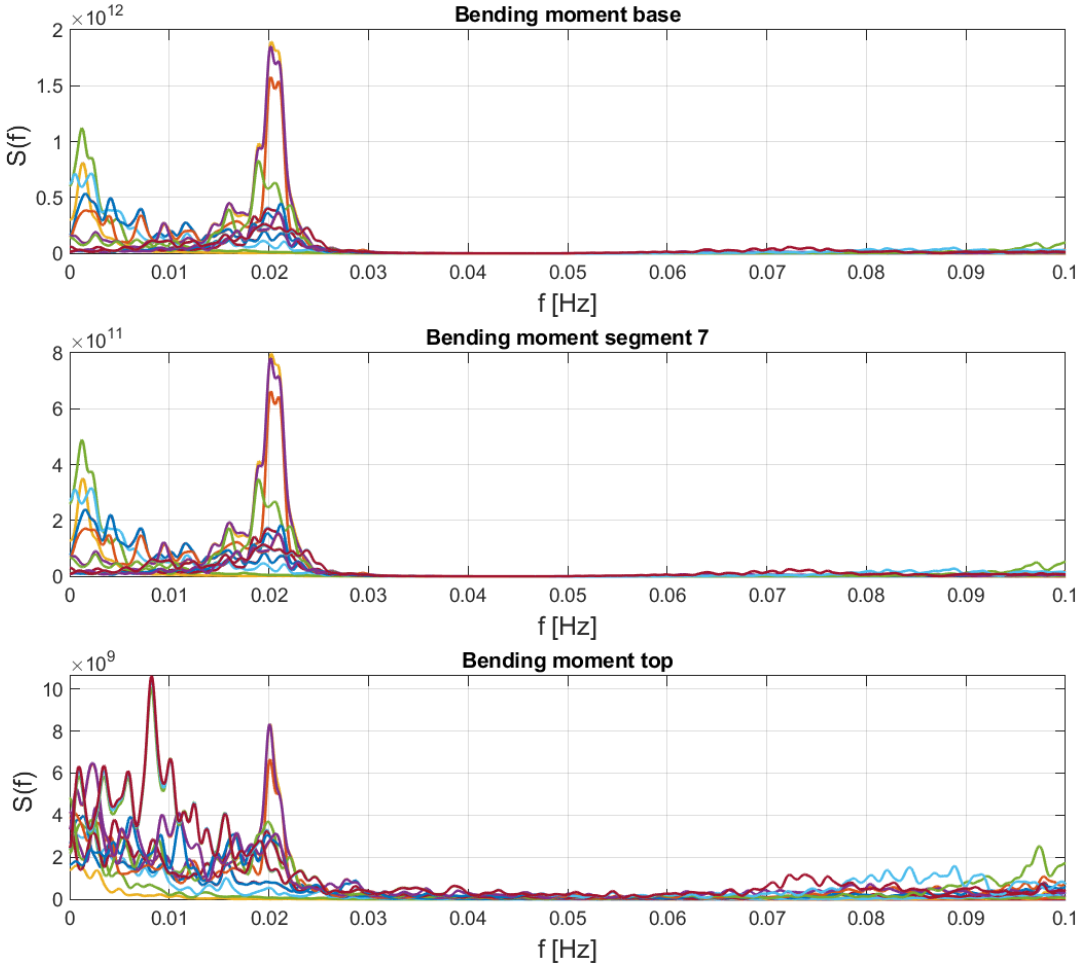

Figure 7.20: Spectral analysis bending moment.

It is clear from Figure 7.20 that bending moment at base and tower top coincide with pitch motion. For tower top, there is also a peak at pitch natural frequency, but the largest peak is located at 0.0081, corresponding to a period of 123.5 s. This is closer to the natural period of surge, as shown in Figure 7.21. It can also be observed that there is more energy at a very low frequency, which suggests loads from wind gusts.

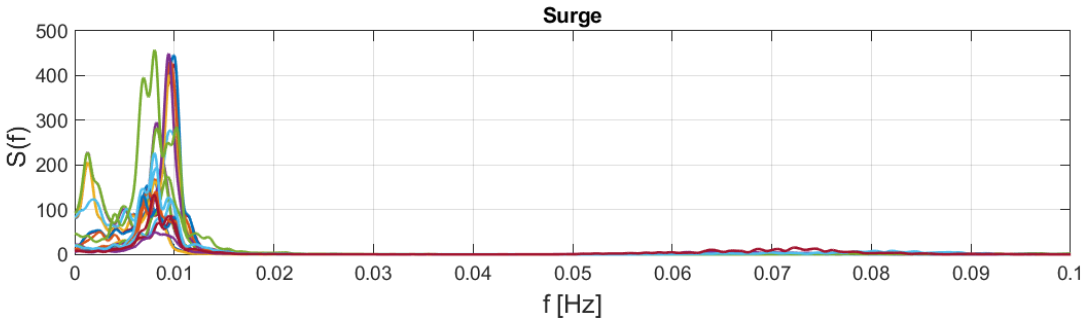

Figure 7.21: Spectral analysis surge

Global motions of the semi-submersible have an impact on the various bending loads experienced by the tower. The tower experiences large bending loads and hence large stresses and large fatigue loads with the current design.

8 Tower design modification

This section examines the trends in the tower natural frequency, mode shapes, and fatigue damage for design modifications. The rest of the system design is kept constant, the only changes made are to the tower diameter and thickness. Two alternate designs are developed, and each is evaluated in regard to the natural frequency, mode shape, and fatigue.

8.1 Design 2

The first proposed tower design hereon referred to as **Design 2**, attempts to amend the large thickness variation of the original tower. The previous design was found to have a very large fatigue damage accumulation as the thickness decreased. Providing a steady decrease in thickness is thought to decrease the large fatigue damage differences. In addition, the diameter is increased in order to create a larger resisting bending moment in an attempt to lower the fatigue damage.

8.1.1 Tower properties

The tower diameter is increased along the entire tower length with a factor of 1.2. The resisting moment can simplified be said to increase with diameter square while increasing linearly with thickness. It is hence more beneficial to increase diameter rather than thickness, and a small increase in diameter provides a large increase in the resisting moment. The steady decrease in thickness is hence accomplished by reducing base thickness rather than increasing top thickness. The new tower segments are provided in Table 8.1. The material properties, i.e., steel density, Young's modulus, and shear modulus are all kept constant.

Table 8.1: Sectional properties for tower design 2.

Height [m]	**Diameter [m]**	**Thickness [mm]**
19.365	15.492	80.360
27.751	15.464	75.003
36.138	15.436	69.645
44.523	15.438	64.288
52.910	15.441	58.931
61.295	15.410	51.057
69.681	15.379	44.539
78.066	15.070	41.183
86.453	14.761	37.955
94.838	14.467	34.857
103.225	14.174	33.566
111.610	14.016	31.608
119.996	13.858	29.650
128.381	13.695	27.720
136.768	13.532	25.790
145.153	13.277	24.516
153.539	13.021	23.241
161.925	12.181	25.179
170.311	11.342	27.116
178.427	10.706	27.118
186.542	10.070	27.120

The difference in tower properties only stems from the difference in diameter and thickness. The design 2 properties are shown compared to the design 1 properties in Figure 8.1.

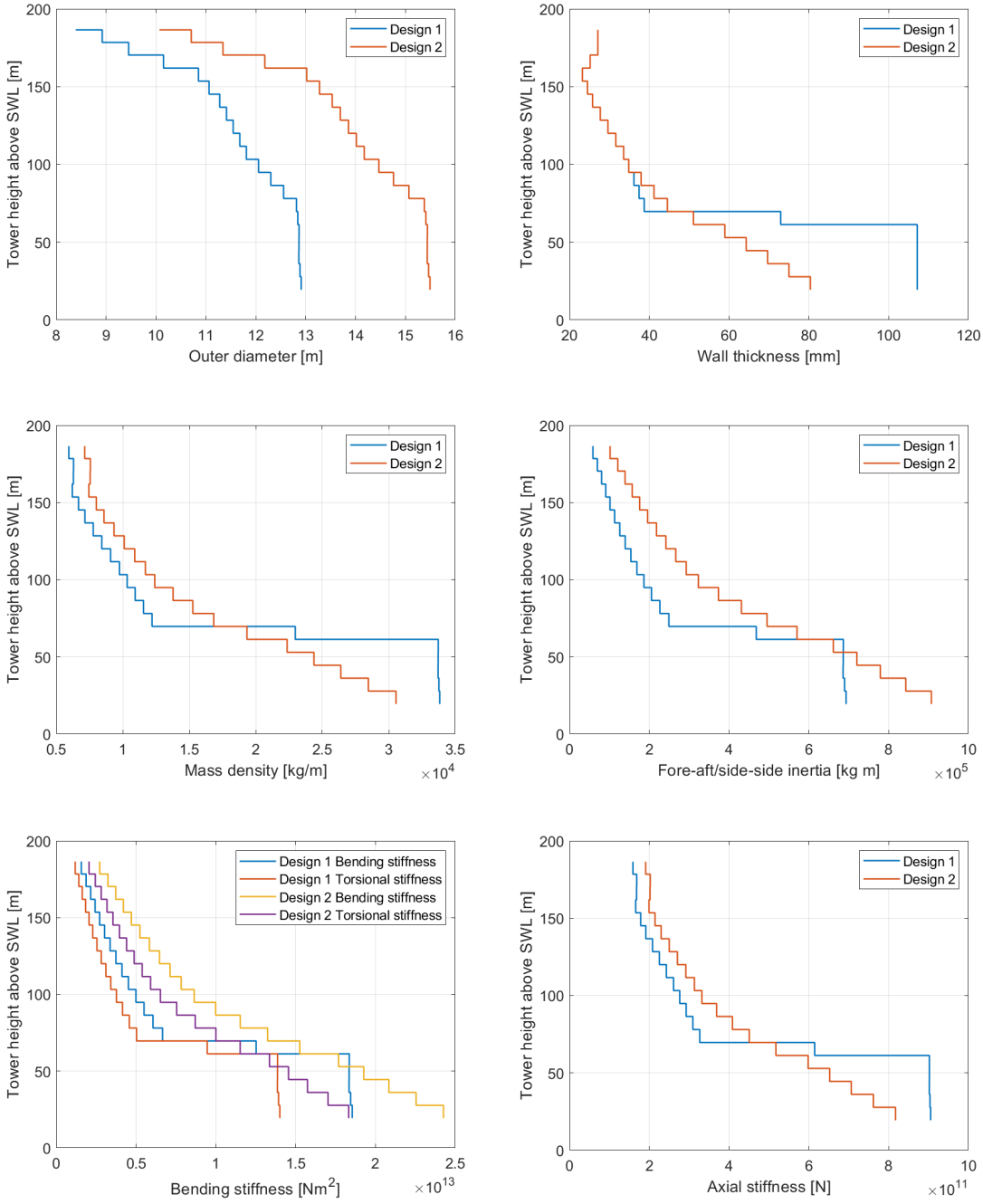

Figure 8.1: Comparison of tower properties design 1 and 2.

8.1.2 Natural frequencies

Design 2 is tested similarly as the first design. As the wind turbine is not altered, it is unlikely that the wind turbine properties will change. Nevertheless, the constant wind test is re-run to confirm that there is no change in turbine characteristics. A comparison between the original design and the new design showed a difference in 1P and 3P frequencies of less than 0.1%. This difference is negligible, and the new design is compared to the same 1P and 3P frequencies as the original design.

Even though the tower design has a larger diameter and increased stiffness, the amount of steel is less than the original tower. The reduction of steel mass equals a reduced tower weight of 4%.

Decreasing weight will influence natural periods in terms of the lesser draft, and shifting of COG and COB. However, a 4% weight reduction does not result in a notable difference, as shown in Table 8.2. However, a notable difference is seen in tower fore-aft and side-side bending.

Table 8.2: Natural periods, comparison between design 1 and 2.

Motion	**Design 1** [s]	**Design 2** [s]	**Difference** [%]
Surge	126.5	126.0	-0.36%
Sway	126.6	126.4	-0.15%
Heave	19.4	19.4	-0.11%
Roll	37.4	39.9	1.25%
Pitch	40.8	41.3	1.13%
Yaw	93.2	92.9	-1.11%
Tower fore-aft bending	2.33	1.843	-29.1
Tower side-side bending	2.15	1.8	-31.5

Surge, sway, heave, and yaw all experienced an inconsequential decrease. Though small, the reduction in these motions is due to the reduction in viscous damping caused by the reduced draft. For pitch and roll, the decreased weight causes a raised COG, and hence a slower rotational translation.

The largest percentage difference between the two designs is found for the tower fore-aft and side-side bending. As shown in Figure 8.1, design 2 is significantly stiffer than the first design. This will subsequently cause a reduction in tower bending period. For tower fore-aft bending this reduction is 29.1%, while for side-side bending the reduction is 31.5%. The tower will hence move further from the rotational frequencies and more into the stiff-stiff range.

8.1.3 Mode shapes

The compared plots for the fore-aft mode shape are shown in Figure 8.2.

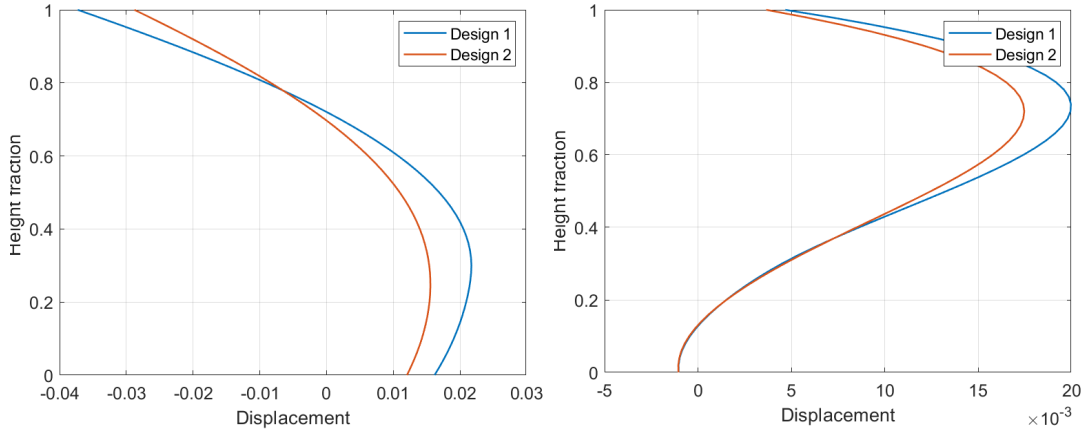

(a) First fore-aft bending

(b) Second fore-aft bending

Figure 8.2: First and second mode shape fore-aft bending.

The increased stiffness in design 2 is also visible in the mode shapes. The first fore-aft bending mode, Figure 8.2a, show less curvature for the lower part of the mode. It has also less displacement at the top. The second fore-aft bending mode, Figure 8.2b, is almost identical for the lower par, but is significantly stiffer in the second bend. Same results were found for side-side bending.

8.1.4 Fatigue analysis

The same environmental conditions are run for tower design 2. The calculated fatigue is shown in Figure 8.3a as a function of tower height for the same seven most probable conditions. Figure 8.3b shows the accumulated fatigue of design 2 compared to design 1.

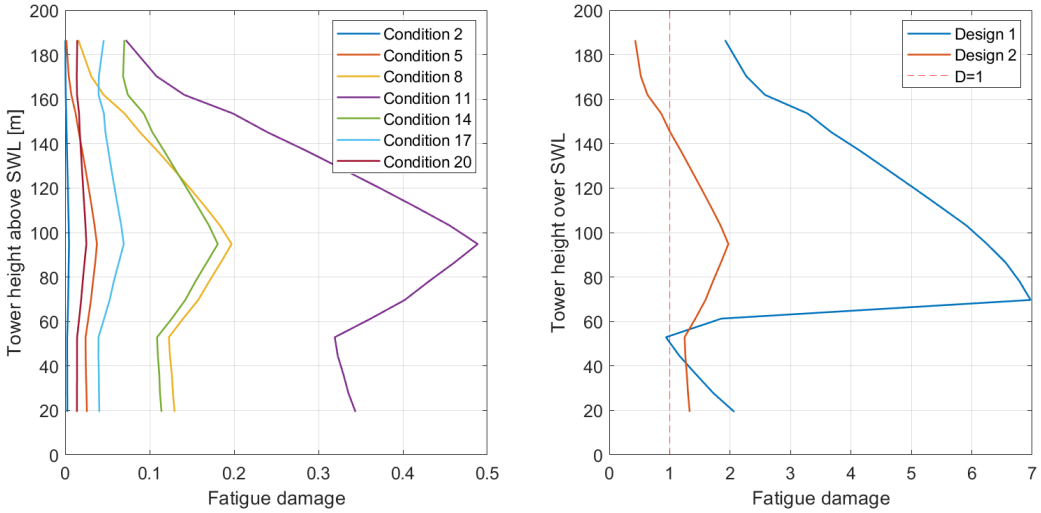

(a) Fatigue damage as a function of tower height.

(b) Accumulated damage over 20 years.

The location of the most fatigue damage has for design 2 shifted to segment 10. The amount of fatigue damage is also significantly lowered. Condition 11 is now not already responsible for fatigue failure. However, upon accumulating the 20 years for all conditions the tower does still experience fatigue failure. It is nevertheless a significant decrease in overall fatigue damage compared to design 1, as seen from Figure 8.3b. The top four segments are now outside harm's way, but the remainder of the segments still experience fatigue failure. The results from Figure 8.3b do however show a more even distribution of fatigue damage along the tower length.

Segment 10 is now the most fatigue-damaged segment. Hence, segment 7 is swapped for segment 10 in the plots showing fatigue as a function of wind speed. The distribution of the conditions in Figure 8.4 resembles the one for design 1 in Figure 7.18. The difference is related to the decrease in fatigue damage.

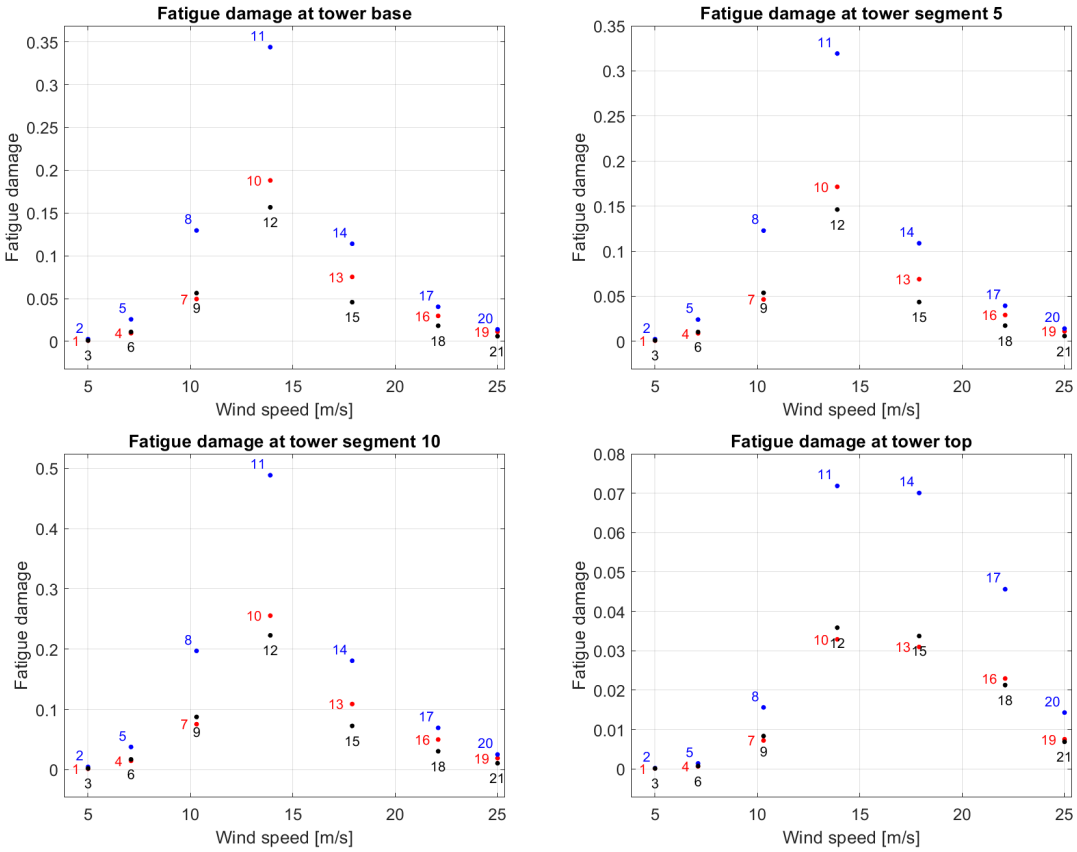

Figure 8.4: Fatigue damage as a function of wind speed.

The larger diameter and decreased thickness has caused the highest recorded fatigue damage to go from 1.7 for segment 7 design 1, to 0.489 for segment 10 design 2, both for condition 11. However, the fraction of fatigue damage is approximately the same, reading in at 24% from condition 11 at segment 7, to 25% from condition 11 at segment 10. The full overview of fatigue damage can be viewed in Appendix C.1 and C.2.

As the natural periods for motions are approximately the same, there is little difference in the relationship between pitch and surge motion and bending moment at base and tower top, shown in Figure 8.5 and 8.6.

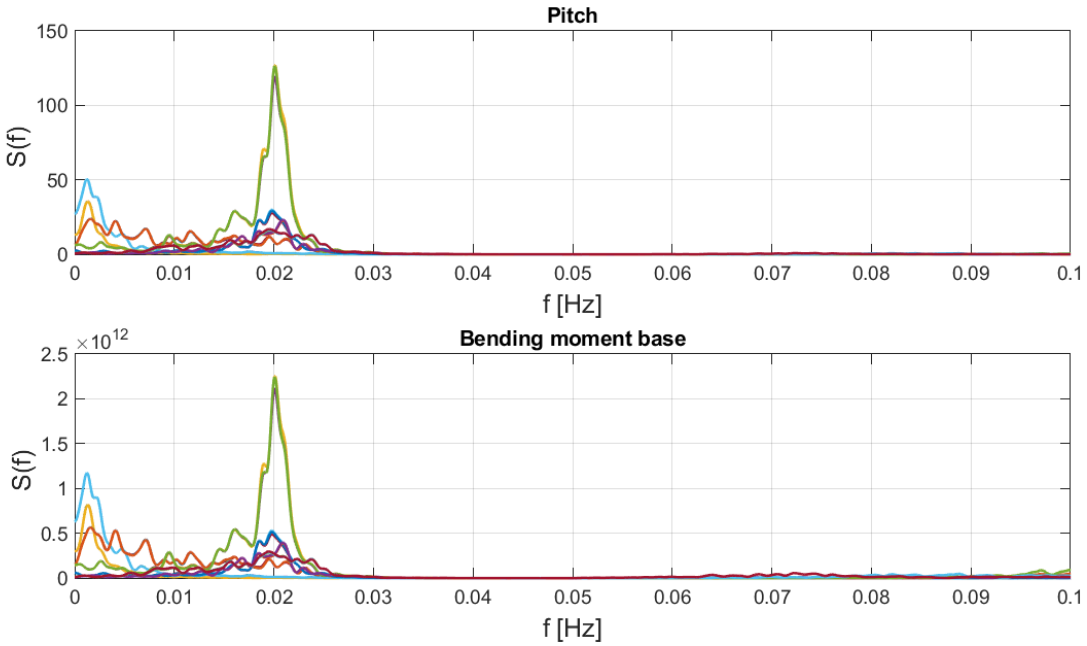

Figure 8.5: Spectral analysis pitch and bending moment design 2.

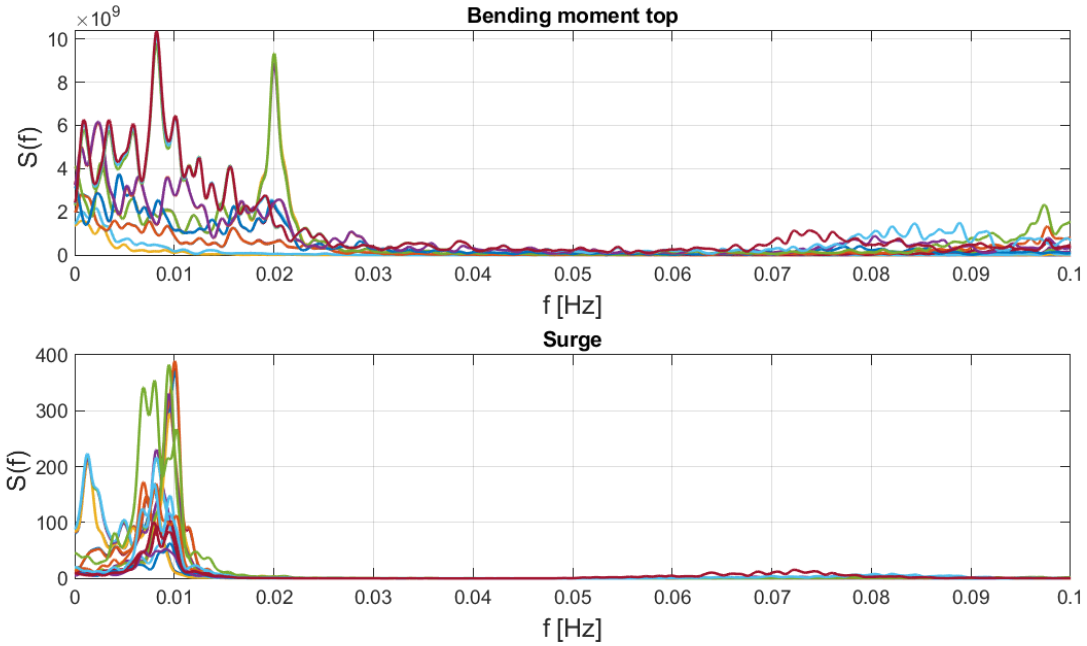

Figure 8.6: Spectral analysis bending moment tower top and surge.

8.2 Design 3

For design 3, the diameter is changed while the thickness is kept constant. The change in diameter is selected in an attempt of getting closer to $D = 1$ for fatigue damage. Design 2 was significantly more fatigue resistant than design 1, but still experienced fatigue failure. The tower modifications of design 3 are based on a stress decreasing approach using the relationship between the diameter, moment resistance, and fatigue damage of design 2.

8.2.1 Tower properties

The accumulated fatigue damage for design 2, as shown graphically in Figure 8.3b, can be said to share a relationship with a necessary increase in diameter by a power of 5. The reason is that the fatigue damage approximately follows the stress concentration cubed, and the moment resistance can be said to follow the medium diameter squared. If only changing the diameter, the necessary factor to multiply the diameter with is the 5th root of the fatigue damage. For all segments exposed to fatigue failure, this factor becomes > 1. For segment 16 to 20, the factor is < 1. The factor found from the fatigue damage relationship is multiplied by the tower diameter from design 2. The resulting design 3 tower segment properties are provided in Table 8.3.

Table 8.3: Sectional properties for tower design 3.

Height [m]	**Diameter [m]**	**Thickness [mm]**
19.365	15.492	80.360
27.751	15.464	75.003
36.138	15.436	69.645
44.523	15.438	64.288
52.910	15.441	58.931
61.295	15.410	51.057
69.681	15.379	44.539
78.066	15.070	41.183
86.453	14.761	37.955
94.838	14.467	34.857
103.225	14.174	33.566
111.610	14.016	31.608
119.996	13.858	29.650
128.381	13.695	27.720
136.768	13.532	25.790
145.153	13.277	24.516
153.539	13.021	23.241
161.925	12.181	25.179
170.311	11.342	27.116
178.427	10.706	27.118
186.542	10.070	27.120

The tower properties are shown compared to design 1 and 2 in Figure 8.7. The plot showing thickness is excluded, as the thickness is the same for design 2 and 3. Instead, the bending stiffness and torsional stiffness are separated into two plots, to easier distinguish the three designs.

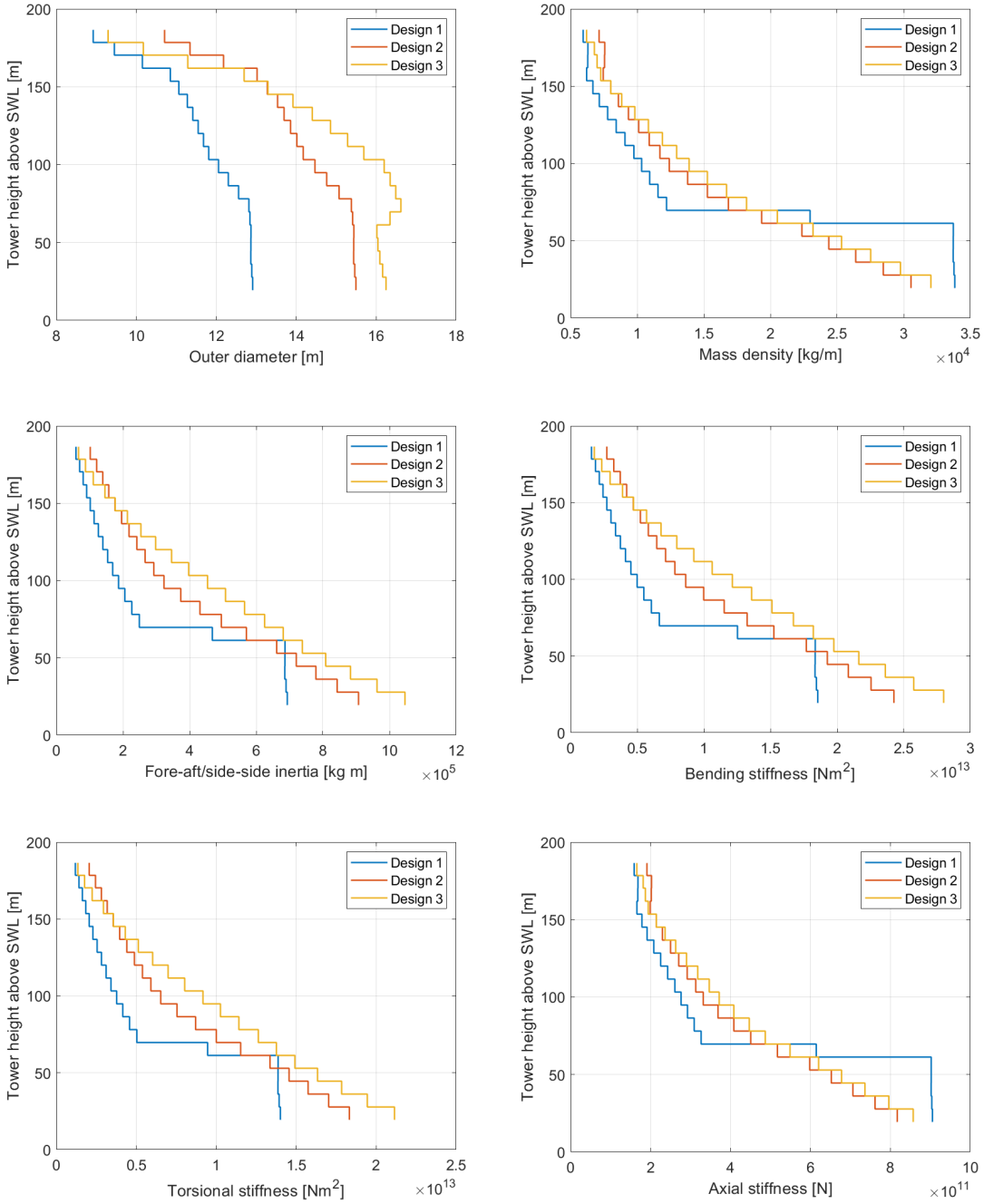

Figure 8.7: Comparison of tower properties design 1,2 and 3.

In the diameter comparison of Figure 8.7 it is shown that the diameter is increased the most at the location where the fatigue was largest. The stiffness is increased for all parts of the tower except the top, where the diameter was decreased.

8.2.2 Natural frequencies

With the increased diameter, the weight of design 3 is 5 % heavier than design 2, and 1% heavier than design 1. The platform will hence be floating with approximately the same draft as it did initially. The natural periods for global motions are hence roughly the same, as shown in Table 8.4.

Table 8.4: Natural periods, comparison between design 1, 2 and 3.

Motion	**Design 1** [s]	**Design 2** [s]	**Design 3** [s]
Surge	126.5	126.0	127.0
Sway	126.6	126.4	126.7
Heave	19.4	19.4	19.2
Roll	37.4	39.9	38.8
Pitch	40.8	41.3	41.5
Yaw	93.2	92.9	92.2
Tower fore-aft bending	2.33	1.843	1.81
Tower side-side bending	2.15	1.8	1.83

8.2.3 Mode shapes

The mode shapes of design 3 are compared to design 1 and 2 in Figure 8.8.

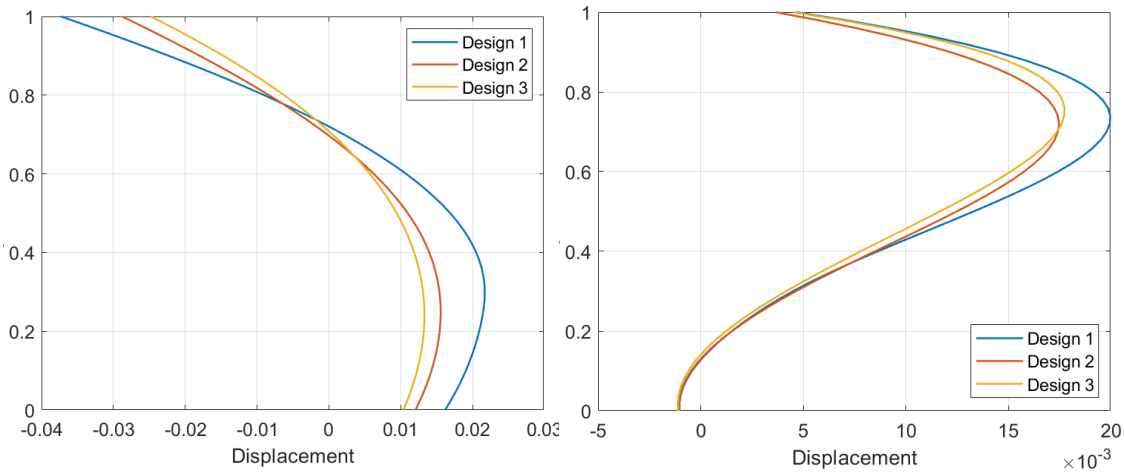

(a) First fore-aft bending

(b) Second fore-aft bending

Figure 8.8: First and second mode shape fore-aft bending.

The difference between the mode shapes of design 2 and 3 are less pronounced than between design 1 and 2. For the first mode shape, Figure 8.8a, the curvature is further reduced, confirming the increased stiffness of the tower. For the second fore-aft mode shape, Figure 8.8b, the reduced tower tow diameter is visible through a slight increase in the curvature of the figure.

8.2.4 Fatigue analysis

Before re-running the analyses for design 3, a preliminary test is conducted. Using the same recorded stress and bending moments from the simulations run on design 2, the fatigue is re-calculated using design 3 diameter. The direct change in fatigue damage due to diameter increase can hence be observed. Further, making this preliminary assessment of design 3 fatigue is an interesting opportunity to see the difference in fatigue which directly stems from the impact of the changed diameter on the simulations. The coupled effect in the aero-hydro-servo-elastic analysis might yield different results as the geometry is updated.

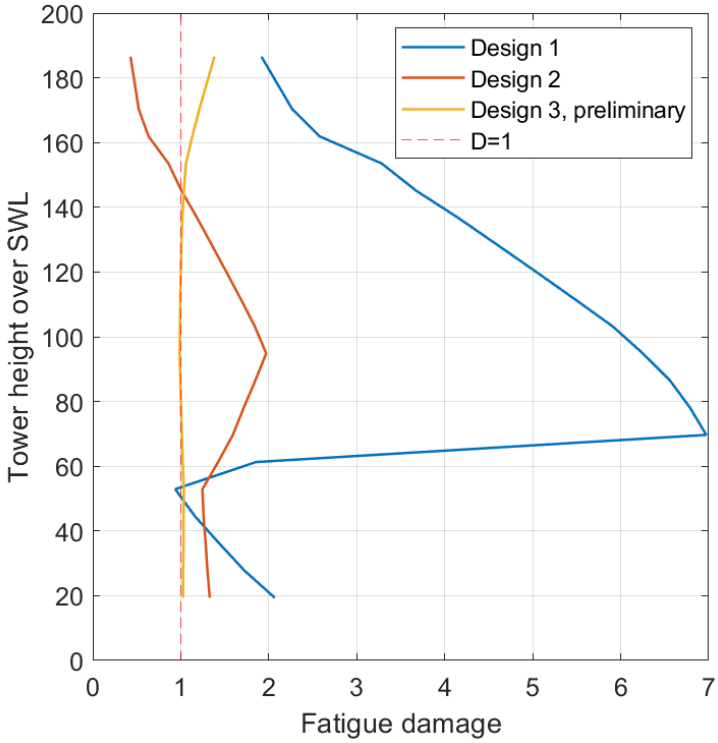

Figure 8.9: Comparison of accumulated damage over 20 years.

The preliminary results for design 3 show a good correspondence with the line representing $D = 1$. The modification in accordance with the fatigue damage hence provides a good method of getting a fatigue-resistant design. The exception is the part of the tower where the diameter was decreased.

It becomes possible to see the influence of the diameter on the coupled analyses when re-running the simulations with updated geometry. As was shown in Table 8.4 and Figure 8.8, there is little difference in natural periods for design 2 and 3, but the tower is stiffer. The resulting difference in results is hence not likely due to change in the natural period but rather changed stiffness and possibly other coupled effects of the increased diameter. The fatigue as a function of tower height is shown in Figure 8.10a for the seven most probable conditions.

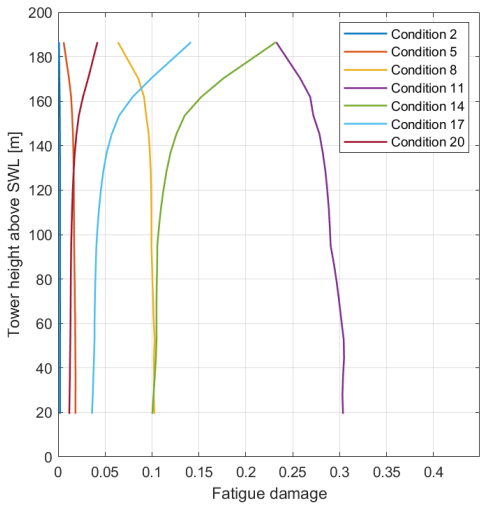

(a) Fatigue damage as a function of tower height.

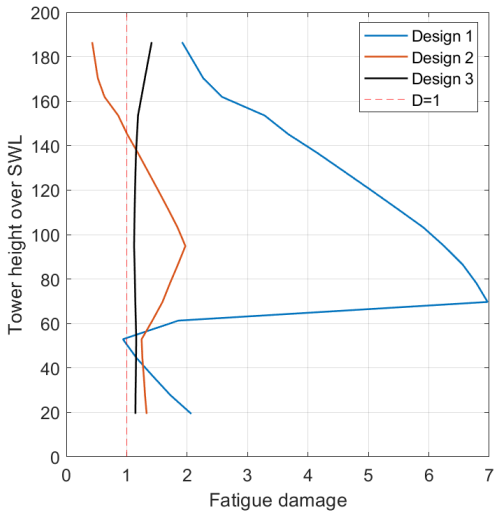

(b) Accumulated damage over 20 years.

From Figure 8.10a the fatigue damage is observed to be constant for the lower 3/4 of the tower length, as suggested by the preliminary calculation. However, the tower top shows both a lower- and higher fatigue damage than tower base, depending on the condition.

Condition 11, which is the most damaging condition, is seen to give lower tower top fatigue compared to tower base. For condition 14 on the other hand, there is significantly more fatigue damage for tower top compared to tower base. Nonetheless, though condition 11 has three times the fatigue damage at tower base compared to condition 14, they both contribute with the same amount of tower top fatigue damage. When accumulating the damage, the fatigue damage of the lower half of the tower would likely be straight, while the top depends on the number of conditions yielding either higher or lower tower top fatigue compared to tower base. If similarity to the preliminary calculations the accumulated fatigue damage will reach 1 for the mid-to-lower part of the tower. However, as seen in Figure 8.10b, the accumulated damage is seen to be a little higher than $D = 1$.

The fatigue damage of design 3 shows an even fatigue damage distribution along with the tower, except for slightly higher fatigue at tower top. The fatigue damage is closer to $D = 1$ than the other two designs, with fatigue damage $D \approx 1.15$ at < 150 m tower height. Compared to the preliminary design, the fatigue damage is consistently higher, as shown in Figure 8.9

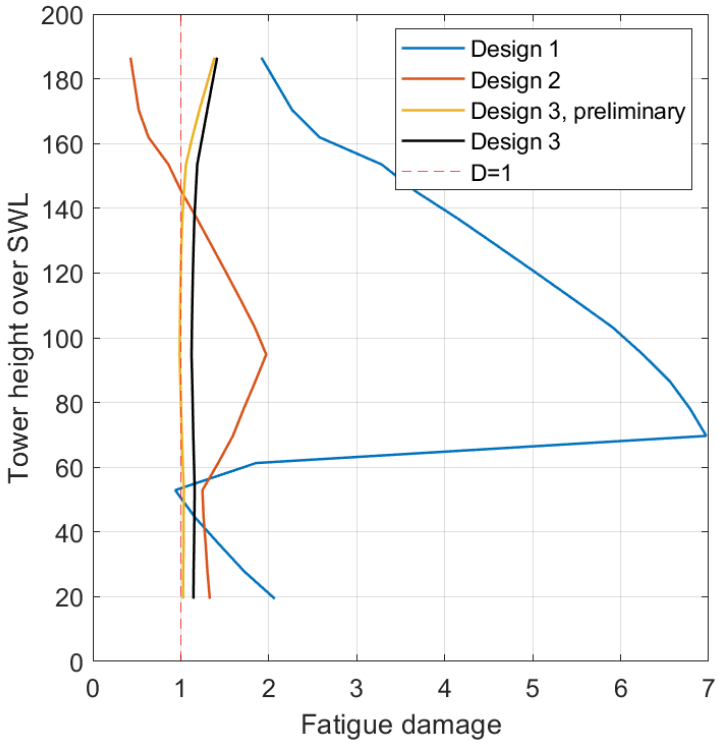

Figure 8.11: Comparison of accumulated damage over 20 years.

The compared results in Figure 8.9 show that other than the strict stress-to-moment resistance relationship, the tower design has influenced the amount of fatigue generated in the simulations. The fatigue damage, which is approximately 1 for the preliminary version of design 3, is consistently higher after simulations are rerun with the new geometry.

The main differences between design 2 and 3 is the increased weight and the increased diameter. The increased diameter might cause slightly higher fatigue damage due to the larger area. However, the area was significantly increased from design 1 to 2, and still experienced a significant reduction of fatigue damage. It can seem like there is a coupling of effects that causes the fatigue damage to be higher for design 3 after the simulation is rerun. However, it is likely that a few more similar modifications would result in a design with accumulated damage equal to 1. However, a

1.15 fatigue damage is considered a decent decrease from that of design 1. A detailed overview of fatigue damage for all segments and conditions, along fraction of total damage for design 3 is included in Appendix D.1 and D.2.

Location-specific plots for fatigue damage as a function of wind velocity are shown in Figure 8.12 for tower base and tower top. There is no practical purpose in showing either segment 7 nor 10, as fatigue damage is almost identical to tower base.

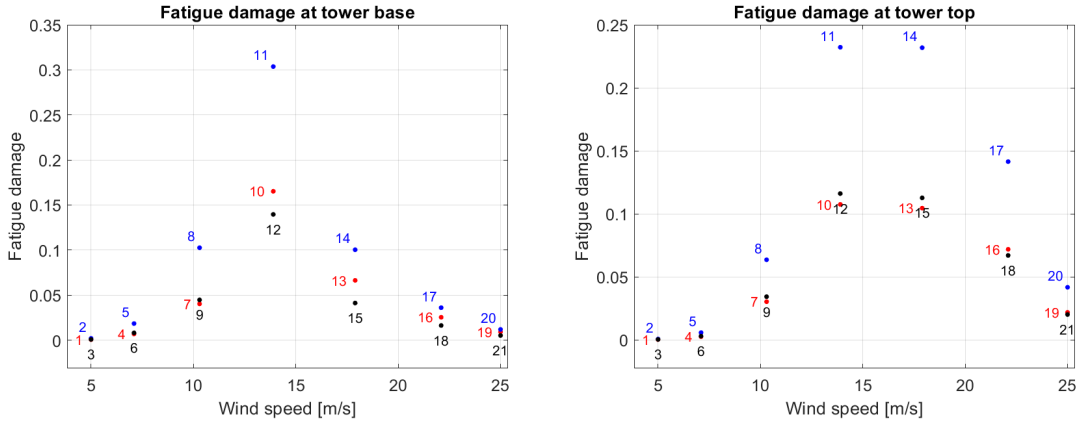

Figure 8.12: Fatigue damage as a function of wind speed.

Tower base shows the same distribution of fatigue damage per condition as for design 1 and 2. However, tower top has now equal damage contribution from conditions 11 and 14. This was also seen in the fatigue damage as a function of tower height in Figure 8.10a.

With approximately the same natural periods and tower bending frequency, there is little reason to anticipate large differences in the comparison of spectral analyses. However, for the sake of totality Figure 8.13 and 8.14 shows the spectral analysis of bending moment for pitch compared to tower base bending, and tower top compared to surge.

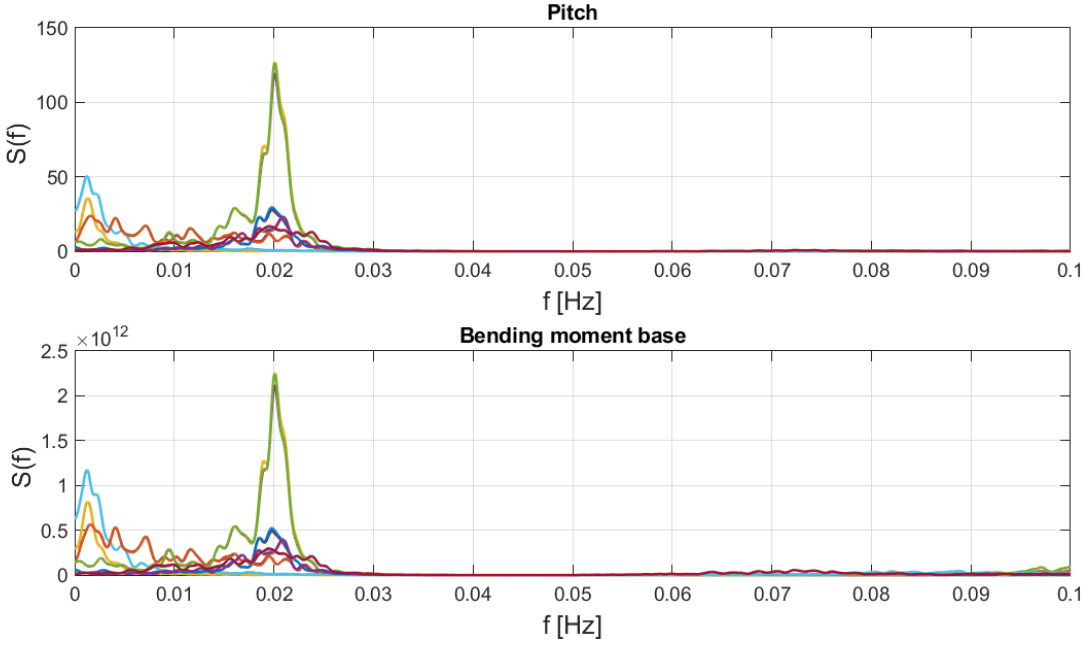

Figure 8.13: Spectral analysis pitch and tower base bending moment.

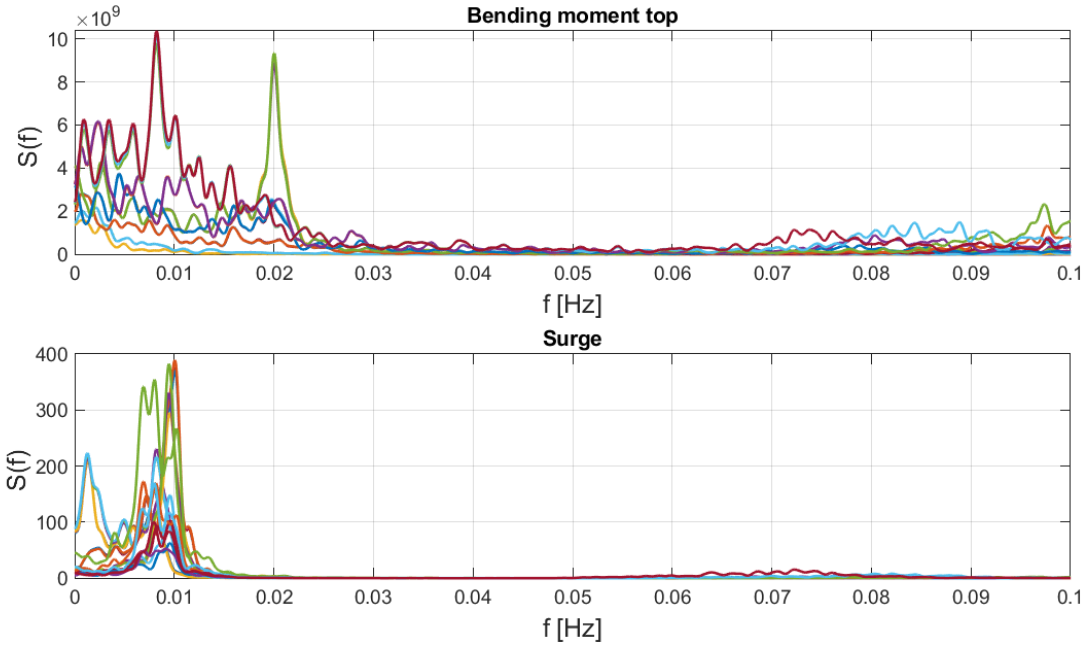

Figure 8.14: Spectral analysis tower top bending moment and surge.

8.2.5 Buckling remarks

Using the same simplified buckling check as for design 1, the diameter and thickness of design 3 increase the critical load from 560 MN to 1405.9 MN. While the bending stress at tower base reduces from 52.8 MPa to 42.4 MPa due to the increased moment resistance.

Even though the tower has a high capacity for global buckling, the large D/t ratio increases the risk of local buckling. A FOWT is typically an ALS-dominated structure. When increasing the diameter and reducing the thickness the structure can be pushed towards ULS and ALS due to the increased risk of local buckling. It is called ”local buckling“, as it is buckling of thin elements of a column section, typically in a series of waves. However, in contrast to a jacket structure where the failure of one element is mitigated by load distribution to the other elements, a wind turbine tower exposed to local buckling is likely to experience total failure. Local buckling can happen without indications, whereas fatigue-induced cracks are more likely to be discovered before reaching critical failure. The D/t ratio should hence be carefully considered to avoid making the structure ULS dominated.

In the case of design 3, if taking a rough estimate, the critical buckling stress can be given by Poisson's ratio $\nu = 0.3$, times Young's modulus times thickness over the radius. By using the same 1/3 along with the tower length value, the critical buckling stress is calculated to be 337 MPa. This value is indeed higher than the yield stress of 250 MPa. It may therefore seem like local buckling does become an issue for design 3. More thorough calculations for further work are hence necessary to get an accurate estimation of the local buckling strength of the tower.

If design 4 had been created, it would have been convenient to increase the thickness rather than the diameter when attempting to reach fatigue damage of D = 1. As seen from previous results, a small increase in weight has not had large effects on the natural period of the system. Making the tower slightly thicker might hence be just what is needed to reach D = 1, but also reaching a safe space from local buckling.

9 Conclusion and further work

This section presents the conclusion of the master thesis, namely on the development of the FOWT numerical model and the tower modifications carried out. It also suggests recommendations for future work.

9.1 Conclusion

A 25 MW FOWT was successfully upscaled based on the INO WINDMOOR 12 MW platform and the IEA 15 MW UMaine VolturnUS-S tower and turbine. A numerical model was created and aero-hydro-servo-elastic analyses conducted. Through turbine performance tests it was observed that the 25 MW turbine has a rated wind speed of 11 m/s, a maximum thrust force of 3 MN, and a mean generator power of 26 MN. It was further found that the 1P frequency band is located in the wave frequency range, which is found to be a one of the main challenges of large FOWTs. Simplified buckling checks showed that the upscaled tower design was stable in terms of global buckling under the load of RNA and maximum thrust. The natural periods of the system was found through decay tests. Decay tests with rated wind and above rated confirmed correct coupled behavior of the FOWT in terms of the effect of wind on an operating turbine during decay. The natural period of the tower showed it to be in the stiff-stiff range. Regular wave tests confirm the natural period found from decay. The fatigue study showed that the upscaled tower experienced fatigue failure at multiple segments.

The tower design was modified by changing the diameter and thickness. It was fund that changing diameter and thickness had little effect on natural periods for global motions, as the difference in weight was small. The natural period for tower bending was decreased as the diameter and thickness modifications made the tower stiffer. The same was seen in mode shapes, where the curvature was less profound for the stiffer tower designs.

The first design experienced failure due to fatigue, before the 20-year mark. For design 2, the increased diameter resulted in a much better fatigue capacity and fatigue damage distribution. The tower did however still fail before reaching 20 years. Design 3 was changed according to the relationship between diameter and fatigue damage. It gave the most fatigue resistant design, with constant fatigue damage along 3/4 of the tower length, close to $D = 1$. The tower did still experience failure from fatigue before 20 years but the design was very close to surviving. However, due to the increased diameter and decreased thickness, design 3 also became exposed to local buckling.

It is concluded that a strict geometric upscale does not survive a lifespan of 20 years. Design 3 is almost at the stage of giving a FOWT system that can be operational for 20 years. It is shown that when upscaling, design and moment resistance is of high importance. Design 1 and 3 have approximately the same amount of steel, but a different distribution of it and hence a significant difference in fatigue resistance. A smarter distribution of the steel has proven to give a better utilization of the material, without causing large influences on other coupled aspects of the system.

9.2 Further work

There are several aspects of this master thesis that could be elaborated on in future work, notably regarding an accurate reflection of realistic model behavior and simulation considerations.

9.2.1 Model

In terms of the model itself, it was mentioned that the turbine was at a preliminary stage and hence the wind turbine blades were not modeled as flexible. With a longer time aspect, the turbine could be amended such that there is a more realistic interrelation between the flexible blades and the rest of the structure. Further, the platform was modeled as rigid. It would be beneficial for

future work to model the platform is flexible. Depending on the ratio of the wave frequency to the natural frequency of the platform, the stresses experienced by the platform might be higher than those found when the elastic behavior is neglected Faltinsen, 1990. The aerodynamic loads on the platform are also neglected from the study due to their impact being assumed small compared to the aerodynamic loads on the tower. For future work, it could give more accurate results to include also these loads.

The FOWT is equipped with a mooring system consisting of chains bigger than what is on the market today. The chains are a direct upscale of the mooring chains of the 15 MW system, which already is on the borderline of what is commercially available. It is also uncertain if a mooring system consisting of only chains is the best alternative for such a large FOWT. A mooring analysis could be carried out, assessing the design of very large mooring chains, and comparing different alternative mooring systems using e.g. polyester rope. Moreover, the mooring chains have not been modeled with marine growth. The mooring bar would represent a larger volume if marine growth was accounted for, and should be included in future work. Corrosion has also not been included, and could be included in further work.

9.2.2 Simulations

For the simulations, there are several recommendations. Firstly, all simulations have during this master thesis been run in the absence of current, both wind-generated and tidal. It is understandable that for very large chains, there is a likely increase in drag forces on the lines. The current may also affect the coupled dynamic behavior of the turbine. Also, loads from snow and ice could potentially be included. This might follow site-specific tests in locations where ice loads are likely.

Speaking of site-specific, a wind turbine is rarely installed alone but rather as part of a wind farm. If a commercial wind farm consisting of 25 MW turbines would be developed, additional considerations would be needed Krieger et al., 2015. Simulations could possibly include the interference effect between wind turbines in a wind farm.

9.2.3 Fatigue

Following the LIFES50+ project, a sensitivity study should be carried out in order to prove that the fatigue assessment is conservative for the design. The fatigue analysis has investigated loads caused by aligned wind and waves. The sensitivity study should investigate the relative importance of the misalignment in the analysis and orientation of the wind turbine with respect to the platform. If it is found to be not conservative for some parts of the system then it is recommended that a contingency factor be applied to take the uncertainty into account Krieger et al., 2015.

The fatigue analysis is also only considering a point along the circumference of the tower. In the case of a more thorough fatigue analysis, it could be recommended to include several points. Further, fatigue has only been calculated for the operational state, for future work, idling, start-up, and shutdown cases could be included. The control system could also be equipped with frequency skipping to assess the possibility of skipping 1P-wave frequency resonance.

Bibliography

A. Robertson, J. Jonkman et al. (2014). 'Offshore Code Comparison Collaboration Continuation Within IEA Wind Task 30: Phase II Results Regarding a Floating Semisubmersible Wind System Preprint'. In: *33rd International Conference on Ocean,Offshore and Arctic Engineering*. National Rneble Energy Laboratory. URL: https://www.nrel.gov/docs/fy14osti/61154.pdf.

Abdelmoteleb, Serag Eldin (2021). *Upscale substructure V0*. Powerpoint.

ABS (2004). *Guide for buckling and ultimate strength assessment for offshore structures*.

— (2020). *Guidance notes on global performance analysis for floating offshore wind turbines*. Tech. rep.

ACP (2021). *ACP 61400-1-202xWind Energy Generation Systems – Part1: Design requirements – ModifiedAdoption of IEC 61400-1*. Tech. rep. The American Clean Power Association. URL: https://cleanpower.org/wp-content/uploads/2021/05/ACP-61400-1-202x_Draft.pdf.

Allen, Christopher et al. (2020). *Definition of the UMaine VolturnUS-S Reference Platform Developed for the IEA Wind 15-Megawatt Offshore Reference Wind Turbine*. Tech. rep. NREL/TP-5000-76773. Golden: National Renewable Energy Laboratory.

Arany, Laszlo et al. (Apr. 2016). 'Closed form solution of Eigen frequency of monopile supported offshore wind turbines in deeper waters incorporating stiffness of substructure and SSI'. In: *Soil Dynamics and Earthquake Engineering* 83, pp. 18–32. DOI: 10.1016/j.soildyn.2015.12.011.

Ashuri, T. et al. (Mar. 2016). 'Aeroservoelastic design definition of a 20 MW common research wind turbine model'. In: *Wind Energy* 19.11, pp. 2071–2087. DOI: 10.1002/we.1970.

Atcheson, Mairead and Andrew Garrad (2016). 'Floating Offshore Wind Energy'. In: ed. by Joao Cruz and Mairead Atcheson. Springer International Publishing. Chap. Looking back. DOI: 10.1007/978-3-319-29398-1.

Bachynski, Erin E. and Lene Eliassen (2018). 'The effects of coherent structures on the global response of floating offshore wind turbines'. In: *Wind Energy* 22.2, pp. 219–238. DOI: 10.1002/we.2280.

Bachynski-Polic, Erin (2021a). 'Basic Aerodynamics for Wind Turbines'. In: *Lecture notes NTNU*.

— (2021b). 'Coupled Analysis'. In: *Lecture notes NTNU*.

— (2021c). 'Scaling and experimental methods for offshore wind turbines'. In: *Lecture slides NTNU*.

Bachynski-Polić, Erin (2021). *Basic Concepts in Wind Turbine Control (Lecture notes)*. Tech. rep. Norwegian University of Science and Technology.

Barthelmie, R. J. and L. E. Jensen (May 2010). 'Evaluation of wind farm efficiency and wind turbine wakes at the Nysted offshore wind farm'. In: *Wind Energy* 13.6, pp. 573–586. DOI: 10.1002/we.408.

Benitz, M.A., M.A. Lackner and D.P. Schmidt (Apr. 2015). 'Hydrodynamics of offshore structures with specific focus on wind energy applications'. In: *Renewable and Sustainable Energy Reviews* 44, pp. 692–716. DOI: 10.1016/j.rser.2015.01.021.

Berge, Stig and Sigmund Kyrre Aas (2017). *Compendium. Fatigue and Fracture Design of Marine Structures*. Third revised. Norwegian University of Science, Technology. Faculty of Engineering Science and Technology.

Brorsen, Michael (2007). *Non-linear Waves*. English. DCE Lecture notes 9. Denmark: Department of Civil Engineering, Aalborg University.

Burton, Tony et al. (2011). *Wind Energy Handbook*. Chichester, West Sussex: Wiley. ISBN: 9780470699751.

Chakrabarti, Subrata (2005). *Handbook of offshore engineering*. Amsterdam London: Elsevier. ISBN: 9780080443812.

Chandrasekaran, Srinivasan (2015). *Dynamic Analysis and Design of Offshore Structures*. Vol. 5. Springer India. ISBN: 978-81-322-2276-7. DOI: 10.1007/978-81-322-2277-4.

Devinant, Ph., T. Laverne and J. Hureau (June 2002). 'Experimental study of wind-turbine airfoil aerodynamics in high turbulence'. In: *Journal of Wind Engineering and Industrial Aerodynamics* 90.6, pp. 689–707. DOI: 10.1016/s0167-6105(02)00162-9.

DNV (2010). 'DNV-RP-C203 Fatigue design of offshore steel structures'. In: *Recommended practice*.

— (Mar. 2014). *DNV-RP-C205 Environmental conditions and environmental loads*. URL: https://rules.dnv.com/docs/pdf/dnvpm/codes/docs/2014-04/RP-C205.pdf.

— (2019). 'Energy Transition Outlook 2019: A global and regional forecast to 2050'. In.

DNV (2020). *Overview of offshore wind standards and regulations in selected countries*. Tech. rep. URL: https://www.norskindustri.no/siteassets/dokumenter/rapporter-og-brosjyrer/leveransemodeller-havvind/dnv-gl-report_overview-of-offshore-wind-standard-and-certification-requirements_final_11.12.2020_signed.pdf.
— (2021a). 'DNV-ST-0126 Support structures for wind turbines'. In: *Standard*.
— (2021b). *Sesam. Software suite for hydrodynamic and structural analysis of renewable, offshore and maritime structures*. Tech. rep. URL: https://www.dnv.com/Images/Sesam-Feature-Description_tcm8-58834.pdf.
— (2021c). 'Technology Progress Report'. In: *Energy Transition Outlook 2021*.
— (n.d.). *Marine operations and mooring analysis software - Sima*. URL: https://www.dnv.com/services/marine-operations-and-mooring-analysis-software-sima-2324.
DNVGL (2016). 'DNVGL-OS-C101 Design of offshore steel structures, genral - LRFD method'. In: *Offshore standards*.
— (2017). 'WADAM Wave Analysis by Diffraction and Morison theory'. In: *Sesam user manual*.
— (2018a). *DNVGL-OS-E301 Position mooring*.
— (2018b). *DNVGL-ST-0119 Floating wind turbine structures*. Standard. URL: https://rules.dnv.com/docs/pdf/DNV/ST/2018-07/DNVGL-ST-0119.pdf.
Eliassen, Lene and Erin E. Bachynski (2017). 'The Effect of Turbulence Model on the Response of a Large Floating Wind Turbine'. In: *Volume 10: Ocean Renewable Energy*. American Society of Mechanical Engineers. DOI: 10.1115/omae2017-61179.
Equinor (2021a). 'Hywind Scotland remains the UK's best performing offshore wind farm'. In: URL: https://www.equinor.com/en/news/20210323-hywind-scotland-uk-best-performing-offshore-wind-farm.html (visited on 16/11/2021).
— (2021b). *Hywind Tampen facts*. URL: https://www.equinor.com/no/what-we-do/hywind-tampen.html (visited on 16/11/2021).
Faltinsen, O. M. (1990). *Sea loads on ships and offshore structures*. Cambridge New York: Cambridge University Press. ISBN: 0521372852.
Gaertner, Evan et al. (Mar. 2020). *Definition of the IEA 15-Megawatt Offshore Reference Wind*. Tech. rep. NREL/TP-5000-75698. National Renewable Energy Laboratory.
Gasch, Robert and Jochen Twele (Nov. 2011). *Wind Power Plants*. Springer Berlin Heidelberg. 568 pp. ISBN: 3642229379.
Global.Wind.Atlas (2021). URL: https://globalwindatlas.info/download/high-resolution-maps/OFFSHORE.
Greco, Marilena (2019). 'TMR4215: Sea Loads. Lecture Notes'. In: Department of Marine Technology, NTNU.
GWEC (2021). 'Global Wind Report 2021'. In.
Hanley, Steve (2021). 'Vestas Unveils World's Most Powerful Offshore Wind Turbine'. In: URL: https://cleantechnica.com/2021/02/12/vestas-unveils-worlds-most-powerful-offshore-wind-turbine/.
Hansen, Martin (2008). *Aerodynamics of wind turbines*. Sterling, VA: Earthscan. ISBN: 9781844074389.
Holthuijsen, Leo H. (2007). *Waves in Oceanic and Coastal Waters*. Cambridge University Press. DOI: 10.1017/CBO9780511618536.
IEA (2019a). 'Offshore Wind Outlook 2019'. In: *World Energy Outlook*. URL: https://iea.blob.core.windows.net/assets/495ab264-4ddf-4b68-b9c0-514295ff40a7/Offshore_Wind_Outlook_2019.pdf.
— (2019b). 'World Energy Outlook'. In: URL: https://iea.blob.core.windows.net/assets/98909c1b-aabc-4797-9926-35307b418cdb/WEO2019-free.pdf (visited on 14/09/2021).
IEC (2019). *IEC 61400-3-1 Wind energy generation systems. design requirements for fixed offshore wind turbines*. Geneva: International Electrotechnical Commission (IEC). ISBN: 9782832266007.
INNWIND.EU (2016). *About INNWIND.EU*. URL: http://www.innwind.eu/about-innwind.
IRENA (2019a). *Future of wind: Deployment, investment, technology, grid integration and socio-economic aspects (A Global Energy Transformation paper)*. Tech. rep. International Renewable Energy Agency, Abu Dabi. URL: https://www.irena.org/-/media/Files/IRENA/Agency/Publication/2019/Oct/IRENA_Future_of_wind_2019.pdf.
— (2019b). *Offshore Renewables: An action agenda for deployment*. Tech. rep. The International Renewable Energy Agency, Abu Dhabi.
Jonkman, J. M. (2008). 'Influence of Control on the PitchDamping of a Floating WindTurbine'. In: National Renewable Energy Labotratory.

Joshua Bauer, NREL (2020). 'New Reference Turbine Gives Offshore Wind an Upward Draft'. In: URL: https://www.nrel.gov/news/program/2020/reference-turbine-gives-offshore-wind-updraft.html.

Joshua Bauser, NREL (2020). 'NREL Floats New Offshore Wind Cost Optimization Vision'. In: URL: https://www.nrel.gov/news/program/2020/nrel-floats-new-offshore-wind-cost-optimization-tool.html.

Kelley, N. D. and B. J. Jonkman (2007). *Overview of the TurbSim Stochastic Inflow Turbulence Simulator*. Tech. rep. National Renewable Energy Laboratory. URL: https://www.nrel.gov/wind/nwtc/assets/pdfs/turbsimoverview.pdf.

Krenk, Steen and Jan Høgsberg (2013). *Statics and Mechanics of Structures*. Springer Netherlands. DOI: 10.1007/978-94-007-6113-1.

Krieger, Antonia et al. (2015). 'Deliverable D7.2 Design Basis'. In: *Qualification of innovative floating substructures for 10MW wind turbines and water depths greater than 50m*.

Kvittem, Marit I. and Torgeir Moan (Jan. 2015). 'Time domain analysis procedures for fatigue assessment of a semi-submersible wind turbine'. In: *Marine Structures* 40, pp. 38–59. DOI: 10.1016/j.marstruc.2014.10.009.

Larsen, Carl M. and Erin E. Bachynski (1990). *Marine Dynamics*. Cambridge New York: Cambridge University Press. ISBN: 0521372852.

Lee, Yung-Li, Mark E. Barkey and Hong-Tae Kang (Aug. 2011). *Metal Fatigue Analysis Handbook: Practical Problem-Solving Techniques for Computer-Aided Engineering*. Butterworth Hainemann. 580 pp. ISBN: 0123852048. URL: https://www.ebook.de/de/product/16113771/yung_li_lee_mark_e_barkey_hong_tae_kang_metal_fatigue_analysis_handbook_practical_problem_solving_techniques_for_computer_aided_engineering.html.

Leimeister, Mareike et al. (Sept. 2016). 'Design optimization and upscaling of a semi-submersible floating platform'. In.

Li, Liang et al. (May 2019). 'Dynamic and structural performances of offshore floating wind turbines in turbulent wind flow'. In: *Ocean Engineering* 179, pp. 92–103. DOI: 10.1016/j.oceaneng.2019.03.028.

LMWindPower (2016). 'World's longest wind turbine blade successfully completes its first journey'. In: URL: https://www.lmwindpower.com/en/stories-and-press/stories/news-from-lm-places/transport-of-longest-blade-in-the-world (visited on 12/12/2021).

— (2019). 'World's largest wind turbine blade sets sail!' In: URL: https://www.lmwindpower.com/en/stories-and-press/stories/news-from-lm-places/107-worlds-largest-wind-turbine-blade-sets-sail (visited on 12/12/2021).

Mann, Jakob (1998). 'Wind field simulation'. In: *Probabilistic Engineering Mechanics* 13.4, pp. 269–282. DOI: 10.1016/s0266-8920(97)00036-2.

Manwell, James F., Jon G. McGowan and Anthony L. Rogers (Jan. 2010). *Wind Energy Explained*. Wiley John + Sons. 704 pp. ISBN: 0470015004. URL: https://www.ebook.de/de/product/6597132/james_f_manwell_jon_g_mcgowan_anthony_l_rogers_wind_energy_explained.html.

Mendes, Rafael C. F. et al. (2020). 'A Computational Fluid Dynamics Investigation on the Axial Induction Factor of a Small Horizontal Axis Wind Turbine'. In: *Journal of Energy Resources Technology* 143.4. DOI: 10.1115/1.4048081.

Myrtvedt, Maylinn Haaskjold, Astrid Nybø and Finn Gunnar Nielsen (2020). 'The dynamic response of offshore wind turbines and their sensitivity to wind field models'. In: *Journal of Physics: Conference Series* 1669, p. 012013. DOI: 10.1088/1742-6596/1669/1/012013.

Newman, J. Nicholas (1992). 'Panel methods in marine hydrodynamics'. In: *11th Australasian Fluid Mechanics Conference*.

NREL (2020). 'New Reference Turbine Gives Offshore Wind an Upward Draft'. In: URL: https://www.nrel.gov/news/program/2020/reference-turbine-gives-offshore-wind-updraft.html.

Nybø, Astrid et al. (2020). 'Evaluation of different wind fields for the investigation of the dynamic response of offshore wind turbines'. In: 23.9, pp. 1810–1830. DOI: 10.1002/we.2518.

O. A. Bauchau, J. I. Craig (Aug. 2009). *Structural Analysis: With Applications to Aerospace Structures*. SPRINGER PG. 943 pp. ISBN: 9048125154.

Öchsner, Andreas (June 2021). *Classical Beam Theories of Structural Mechanics*. Springer International Publishing. 200 pp. ISBN: 3030760340. URL: https://www.ebook.de/de/product/40504331/andreas_oechsner_classical_beam_theories_of_structural_mechanics.html.

Open Ocean (2017). 'Vindeby (1991-2017): decommission of the world's first offshore wind farm'. In: URL: http://www.openocean.fr/en/news/2017/03/21/vindeby-1991-2017-decommission-of-the-worlds-first-offshore-wind-farm/.

Radowitz, Bernd and Darius Snieckus (2019). 'Spain grants Equinor ok for world's biggest floating wind farm'. In: *Recharge: Global news and intellegence for the Energy Transition*. URL: https://www.rechargenews.com/wind/spain-grants-equinor-ok-for-worlds-biggest-floating-wind-farm/2-1-615375.

Richard, Craig (2021). 'Plans for 1GW-plus offshore wind farm with 20MW turbines'. In: *Windpower monthly*. URL: https://www.windpowermonthly.com/article/1715905/plans-1gw-plus-offshore-wind-farm-20mw-turbines.

Richard, Creig (2020). 'World's longest wind turbine blade gets engineers' approval'. In: *Windpower monthly*. URL: https://www.windpowermonthly.com/article/1699714/worlds-longest-wind-turbine-blade-gets-engineers-approval (visited on 12/12/2021).

Robertson, A. et al. (Sept. 2014). *Definition of the Semisubmersible Floating System for Phase II of OC4*. Tech. rep. DOI: 10.2172/1155123.

Sartori, L et al. (June 2018). 'Preliminary design and optimization of a 20MW reference wind turbine'. In: *Journal of Physics: Conference Series* 1037, p. 042003. DOI: 10.1088/1742-6596/1037/4/042003.

Sieros, G. et al. (2012). 'Upscaling wind turbines: theoretical and practical aspects and their impact on the cost of energy'. In: *Wind Energy* 15.1, pp. 3–17. DOI: 10.1002/we.527.

SINTEF (2021a). *RIFLEX 4.20.2 Theory Manual*.

— (2021b). *SIMO 3.20.2 Theory Manual*.

Souza, Carlos Eduardo S. and Erin E. Bachynski (May 2019). 'Changes in surge and pitch decay periods of floating wind turbines for varying wind speed'. In: *Ocean Engineering* 180, pp. 223–237. DOI: 10.1016/j.oceaneng.2019.02.075.

Souza, Carlos Eduardo Silva de et al. (2021). *Definition of the INOWINDMOOR 12 MWbase case floating wind turbine*. Tech. rep. 1.2. SINTEF. URL: https://ntnuopen.ntnu.no/ntnu-xmlui/handle/11250/2772738.

Tempel, Jan van der (2006). 'Design of support structures for offshore wind turbines'. PhD thesis. Delft, the Netherlands. ISBN: 9076468117.

UpWind (2011). 'Design limits and solutions for very large wind turbines'. In: URL: http://www.ewea.org/fileadmin/files/library/publications/reports/UpWind_Report.pdf.

Veen, G. J. van der, I. J. Couchman and R. O. Bowyer (June 2012). 'Control of floating wind turbines'. In: *2012 American Control Conference (ACC)*. IEEE. DOI: 10.1109/acc.2012.6315120.

Voutsinas, Spyros G. (2010). 'Structural dynamics of wind turbines'. In: *Wind Power Generation and Wind Turbine Design*. WIT Press, pp. 121–151. DOI: 10.2495/978-1-84564-205-1/04.

Xu, Kun et al. (Oct. 2019). 'Effect of wave nonlinearity on fatigue damage and extreme responses of a semi-submersible floating wind turbine'. In: *Applied Ocean Research* 91, p. 101879. DOI: 10.1016/j.apor.2019.101879.

A INO 12 MW validation

A.1 Added mass

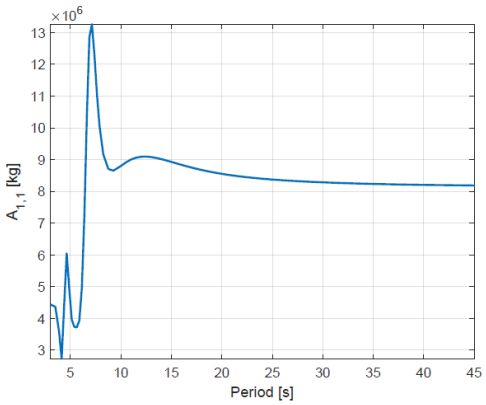

(a) SINTEF model

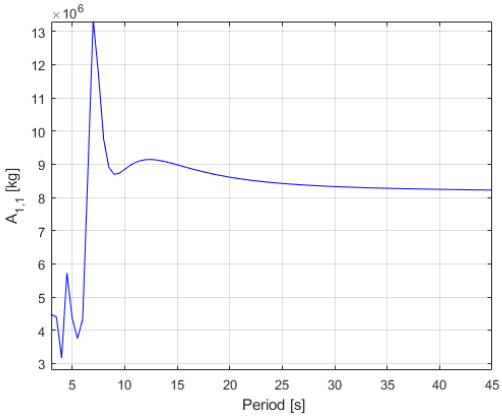

(b) Recreated model

Figure A.1: Added mass coefficients in surge.

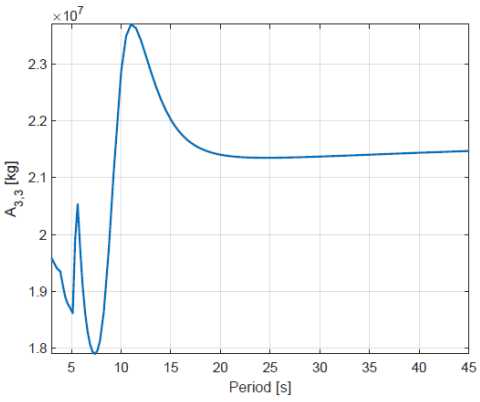

(a) SINTEF model

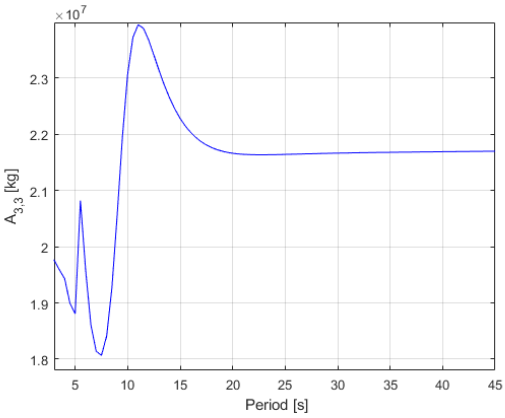

(b) Recreated model

Figure A.2: Added mass coefficients in heave.

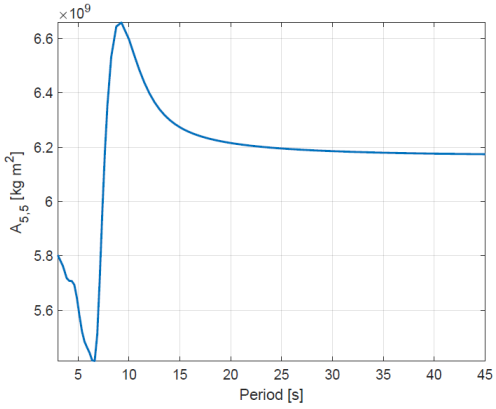

(a) SINTEF model

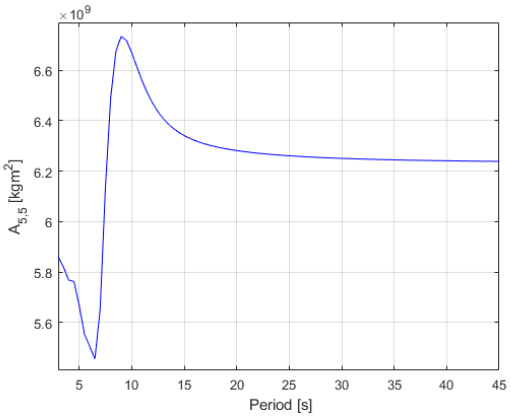

(b) Recreated model

Figure A.3: Added mass coefficients in pitch.

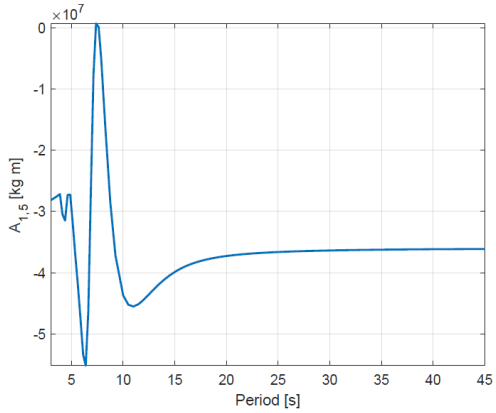

(a) SINTEF model

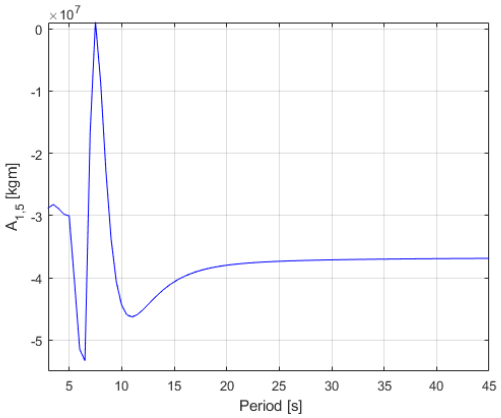

(b) Recreated model

Figure A.4: Added mass coefficients in surge due to pitch.

A.2 Damping

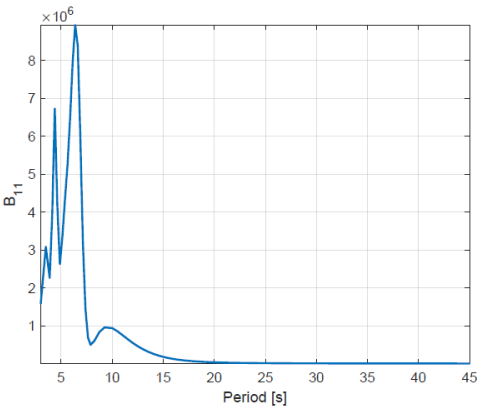

(a) SINTEF model

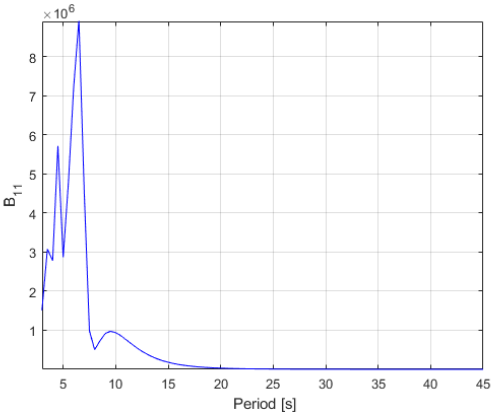

(b) Recreated model

Figure A.5: Damping coefficients in surge.

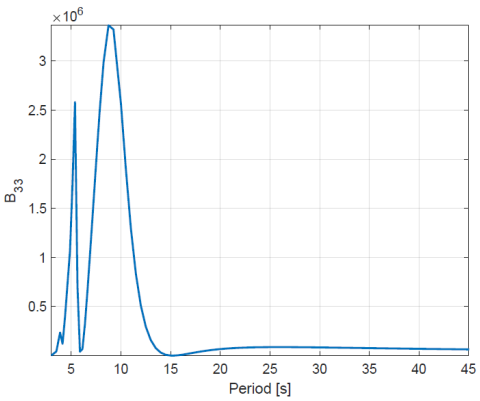

(a) SINTEF model

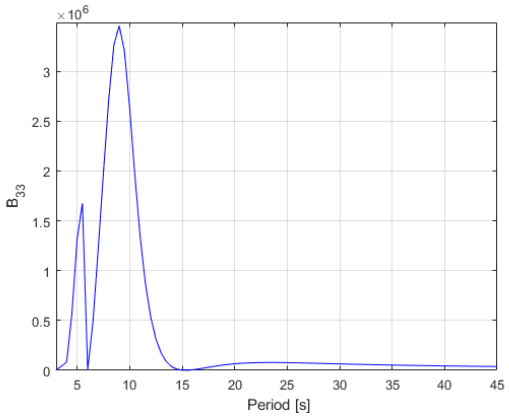

(b) Recreated model

Figure A.6: Damping coefficients in heave.

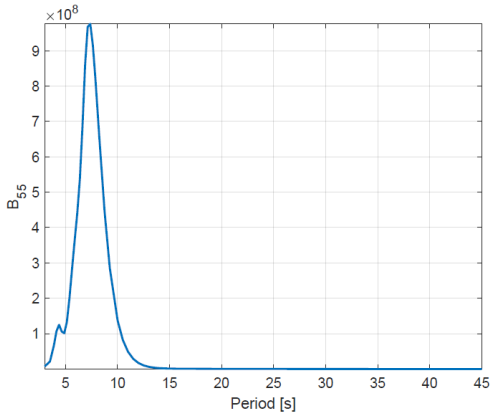

(a) SINTEF model

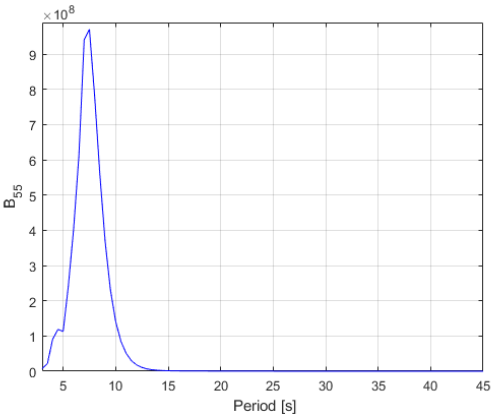

(b) Recreated model

Figure A.7: Damping coefficients in pitch.

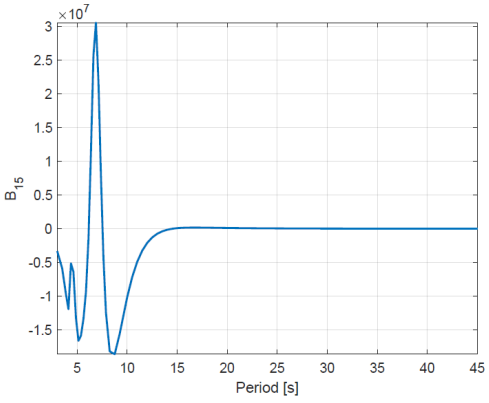

(a) SINTEF B15

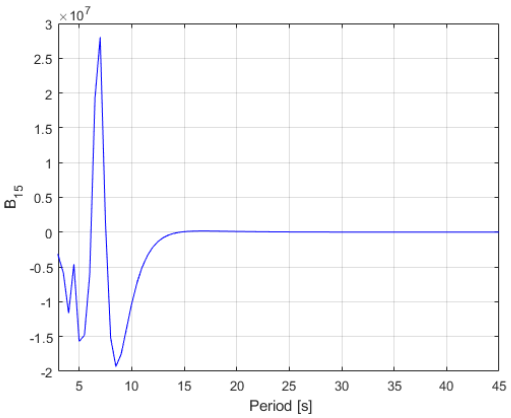

(b) Recreated model

Figure A.8: Damping coefficients in surge due to pitch.

B Fatigue damage design 1

B.1 20 year fatigue damage

Design1: 20 year fatigue damage

Condition	base	seg 2	seg 3	seg 4	seg 5	seg 6	seg 7	seg 8	seg 9	seg 10	seg 11	seg 12	seg 13	seg 14	seg 15	seg 16	seg 17	seg 18	seg 19	top
1	0.002	0.002	0.001	0.001	0.001	0.002	0.010	0.010	0.010	0.009	0.009	0.008	0.007	0.006	0.005	0.004	0.004	0.002	0.001	0.001
2	0.007	0.005	0.004	0.003	0.002	0.007	0.032	0.031	0.030	0.029	0.027	0.024	0.022	0.019	0.016	0.013	0.010	0.006	0.004	0.002
3	0.003	0.002	0.001	0.001	0.001	0.003	0.013	0.012	0.012	0.012	0.011	0.010	0.009	0.008	0.007	0.006	0.005	0.003	0.002	0.001
4	0.017	0.014	0.012	0.009	0.007	0.015	0.058	0.057	0.055	0.052	0.049	0.045	0.040	0.036	0.030	0.025	0.020	0.013	0.009	0.004
5	0.045	0.037	0.030	0.024	0.019	0.040	0.161	0.156	0.150	0.142	0.132	0.120	0.107	0.093	0.079	0.064	0.051	0.033	0.022	0.010
6	0.020	0.016	0.013	0.010	0.008	0.018	0.069	0.068	0.066	0.062	0.058	0.053	0.048	0.042	0.037	0.030	0.024	0.016	0.011	0.005
7	0.071	0.059	0.049	0.038	0.030	0.061	0.226	0.219	0.211	0.200	0.187	0.171	0.156	0.139	0.123	0.106	0.091	0.067	0.055	0.042
8	0.181	0.147	0.123	0.100	0.080	0.157	0.591	0.572	0.548	0.518	0.484	0.443	0.401	0.358	0.314	0.266	0.225	0.163	0.129	0.092
9	0.079	0.065	0.054	0.043	0.035	0.069	0.258	0.251	0.241	0.229	0.216	0.198	0.181	0.163	0.145	0.125	0.107	0.080	0.065	0.048
10	0.289	0.242	0.201	0.163	0.132	0.253	0.924	0.894	0.858	0.811	0.760	0.697	0.633	0.568	0.501	0.430	0.368	0.272	0.217	0.156
11	0.521	0.436	0.366	0.298	0.245	0.466	1.700	1.652	1.593	1.513	1.424	1.314	1.201	1.085	0.966	0.837	0.725	0.544	0.447	0.336
12	0.241	0.202	0.171	0.136	0.113	0.215	0.776	0.755	0.729	0.693	0.653	0.603	0.553	0.502	0.449	0.392	0.342	0.260	0.217	0.165
13	0.124	0.102	0.084	0.068	0.053	0.108	0.428	0.415	0.399	0.379	0.358	0.331	0.305	0.279	0.254	0.227	0.207	0.167	0.153	0.139
14	0.191	0.158	0.134	0.108	0.086	0.176	0.685	0.671	0.653	0.628	0.600	0.564	0.528	0.492	0.458	0.422	0.398	0.334	0.321	0.309
15	0.074	0.063	0.051	0.041	0.032	0.068	0.261	0.256	0.251	0.242	0.233	0.221	0.209	0.198	0.187	0.176	0.171	0.148	0.147	0.147
16	0.051	0.043	0.036	0.029	0.024	0.049	0.193	0.190	0.185	0.179	0.172	0.162	0.153	0.143	0.134	0.125	0.118	0.100	0.097	0.092
17	0.071	0.059	0.049	0.040	0.032	0.067	0.271	0.267	0.263	0.256	0.248	0.237	0.227	0.217	0.208	0.199	0.196	0.174	0.175	0.178
18	0.030	0.026	0.021	0.017	0.014	0.029	0.116	0.114	0.112	0.109	0.106	0.102	0.098	0.094	0.091	0.088	0.088	0.079	0.081	0.084
19	0.019	0.016	0.013	0.011	0.009	0.018	0.069	0.068	0.067	0.064	0.061	0.058	0.054	0.051	0.047	0.043	0.040	0.034	0.031	0.028
20	0.024	0.020	0.017	0.014	0.011	0.024	0.093	0.092	0.090	0.088	0.085	0.081	0.077	0.074	0.070	0.066	0.065	0.056	0.055	0.053
21	0.010	0.009	0.007	0.006	0.005	0.010	0.039	0.039	0.038	0.037	0.036	0.034	0.033	0.032	0.030	0.029	0.029	0.026	0.026	0.025
Accumulated fatigue damage during 20 years																				
All	2.068	1.724	1.438	1.161	0.937	1.854	6.973	6.789	6.561	6.252	5.908	5.478	5.042	4.598	4.152	3.674	3.283	2.576	2.267	1.916

B.2 Fraction of total fatigue damage 20 years

Design 1: Fraction of total fatigue damage for 20 years

Condition	base	seg 2	seg 3	seg 4	seg 5	seg 6	seg 7	seg 8	seg 9	seg 10	seg 11	seg 12	seg 13	seg 14	seg 15	seg 16	seg 17	seg 18	seg 19	top
1	0%	0%	0%	0%	0%	0%	0%	0%	0%	0%	0%	0%	0%	0%	0%	0%	0%	0%	0%	0%
2	0%	0%	0%	0%	0%	0%	0%	0%	0%	0%	0%	0%	0%	0%	0%	0%	0%	0%	0%	0%
3	0%	0%	0%	0%	0%	0%	0%	0%	0%	0%	0%	0%	0%	0%	0%	0%	0%	0%	0%	0%
4	1%	1%	1%	1%	1%	1%	1%	1%	1%	1%	1%	1%	1%	1%	1%	1%	1%	1%	0%	0%
5	2%	2%	2%	2%	2%	2%	2%	2%	2%	2%	2%	2%	2%	2%	2%	2%	2%	1%	1%	0%
6	1%	1%	1%	1%	1%	1%	1%	1%	1%	1%	1%	1%	1%	1%	1%	1%	1%	1%	0%	0%
7	3%	3%	3%	3%	3%	3%	3%	3%	3%	3%	3%	3%	3%	3%	3%	3%	3%	3%	2%	2%
8	9%	9%	9%	9%	9%	8%	8%	8%	8%	8%	8%	8%	8%	8%	8%	7%	7%	6%	6%	5%
9	4%	4%	4%	4%	4%	4%	4%	4%	4%	4%	4%	4%	4%	4%	3%	3%	3%	3%	3%	3%
10	14%	14%	14%	14%	14%	14%	13%	13%	13%	13%	13%	13%	13%	12%	12%	12%	11%	11%	10%	8%
11	25%	25%	25%	26%	26%	25%	24%	24%	24%	24%	24%	24%	24%	24%	23%	23%	22%	21%	20%	18%
12	12%	12%	12%	12%	12%	12%	11%	11%	11%	11%	11%	11%	11%	11%	11%	11%	10%	10%	10%	9%
13	6%	6%	6%	6%	6%	6%	6%	6%	6%	6%	6%	6%	6%	6%	6%	6%	6%	6%	7%	7%
14	9%	9%	9%	9%	9%	9%	10%	10%	10%	10%	10%	10%	10%	11%	11%	11%	12%	13%	14%	16%
15	4%	4%	4%	4%	3%	4%	4%	4%	4%	4%	4%	4%	4%	4%	5%	5%	5%	6%	6%	8%
16	2%	2%	3%	3%	3%	3%	3%	3%	3%	3%	3%	3%	3%	3%	3%	3%	4%	4%	4%	5%
17	3%	3%	3%	3%	3%	4%	4%	4%	4%	4%	4%	4%	4%	5%	5%	5%	6%	7%	8%	9%
18	1%	1%	1%	1%	1%	2%	2%	2%	2%	2%	2%	2%	2%	2%	2%	2%	3%	3%	4%	4%
19	1%	1%	1%	1%	1%	1%	1%	1%	1%	1%	1%	1%	1%	1%	1%	1%	1%	1%	1%	1%
20	1%	1%	1%	1%	1%	1%	1%	1%	1%	1%	1%	1%	2%	2%	2%	2%	2%	2%	2%	3%
21	0%	0%	0%	1%	1%	1%	1%	1%	1%	1%	1%	1%	1%	1%	1%	1%	1%	1%	1%	1%
sum	100%	100%	100%	100%	100%	100%	100%	100%	100%	100%	100%	100%	100%	100%	100%	100%	100%	100%	100%	100%

C Fatigue damage design 2

C.1 20 year fatigue damage

Design 2: 20 year fatigue damage

Condition	base	seg 2	seg 3	seg 4	seg 5	seg 6	seg 7	seg 8	seg 9	seg 10	seg 11	seg 12	seg 13	seg 14	seg 15	seg 16	seg 17	seg 18	seg 19	top
1	0.001	0.001	0.001	0.001	0.001	0.001	0.001	0.001	0.001	0.001	0.001	0.001	0.001	0.001	0.001	0.001	0.000	0.000	0.000	0.000
2	0.003	0.003	0.002	0.002	0.002	0.003	0.004	0.004	0.004	0.005	0.004	0.004	0.003	0.003	0.002	0.002	0.001	0.001	0.000	0.000
3	0.001	0.001	0.001	0.001	0.001	0.001	0.001	0.002	0.002	0.002	0.002	0.002	0.001	0.001	0.001	0.001	0.001	0.000	0.000	0.000
4	0.010	0.009	0.009	0.009	0.009	0.010	0.012	0.013	0.014	0.015	0.014	0.012	0.011	0.010	0.008	0.007	0.005	0.003	0.002	0.001
5	0.026	0.025	0.025	0.024	0.024	0.027	0.031	0.033	0.036	0.038	0.035	0.031	0.028	0.024	0.020	0.016	0.012	0.007	0.004	0.001
6	0.011	0.011	0.011	0.010	0.010	0.012	0.014	0.015	0.016	0.017	0.016	0.014	0.013	0.011	0.009	0.008	0.006	0.004	0.002	0.001
7	0.049	0.049	0.048	0.047	0.046	0.054	0.060	0.065	0.070	0.075	0.070	0.064	0.057	0.050	0.043	0.035	0.028	0.019	0.013	0.007
8	0.130	0.128	0.126	0.124	0.123	0.140	0.158	0.171	0.184	0.197	0.183	0.166	0.148	0.129	0.109	0.088	0.070	0.046	0.031	0.016
9	0.056	0.056	0.055	0.054	0.054	0.062	0.069	0.075	0.081	0.087	0.082	0.074	0.067	0.059	0.050	0.041	0.034	0.022	0.016	0.008
10	0.188	0.183	0.179	0.174	0.171	0.194	0.214	0.228	0.243	0.256	0.236	0.214	0.191	0.168	0.144	0.120	0.098	0.069	0.052	0.033
11	0.344	0.335	0.330	0.323	0.319	0.362	0.402	0.431	0.461	0.489	0.455	0.415	0.373	0.329	0.286	0.239	0.199	0.141	0.108	0.072
12	0.157	0.153	0.150	0.148	0.146	0.166	0.184	0.197	0.210	0.223	0.208	0.190	0.171	0.151	0.132	0.112	0.093	0.067	0.053	0.036
13	0.075	0.073	0.072	0.070	0.069	0.079	0.088	0.095	0.102	0.109	0.101	0.091	0.082	0.073	0.064	0.055	0.048	0.036	0.032	0.031
14	0.114	0.112	0.111	0.110	0.109	0.126	0.142	0.154	0.168	0.181	0.170	0.157	0.144	0.130	0.117	0.103	0.093	0.074	0.069	0.070
15	0.046	0.045	0.044	0.044	0.044	0.050	0.057	0.062	0.067	0.073	0.069	0.064	0.059	0.054	0.050	0.045	0.041	0.034	0.032	0.034
16	0.030	0.030	0.030	0.029	0.029	0.034	0.039	0.042	0.046	0.050	0.047	0.044	0.041	0.037	0.034	0.031	0.028	0.023	0.022	0.023
17	0.040	0.040	0.040	0.039	0.039	0.046	0.053	0.058	0.063	0.069	0.066	0.062	0.059	0.055	0.051	0.048	0.046	0.040	0.040	0.046
18	0.018	0.018	0.018	0.017	0.017	0.020	0.023	0.025	0.028	0.030	0.029	0.028	0.026	0.024	0.023	0.021	0.021	0.018	0.018	0.021
19	0.011	0.011	0.011	0.011	0.011	0.013	0.015	0.016	0.018	0.019	0.018	0.017	0.015	0.014	0.013	0.011	0.010	0.008	0.008	0.008
20	0.014	0.014	0.014	0.014	0.014	0.017	0.019	0.021	0.023	0.025	0.024	0.023	0.021	0.020	0.019	0.017	0.016	0.014	0.014	0.014
21	0.006	0.006	0.006	0.006	0.006	0.007	0.008	0.009	0.010	0.011	0.010	0.010	0.009	0.009	0.008	0.008	0.007	0.006	0.006	0.007
Accumulated fatigue damage during 20 years																				
All	1.329	1.303	1.283	1.259	1.246	1.424	1.592	1.715	1.846	1.971	1.841	1.682	1.519	1.352	1.184	1.007	0.859	0.633	0.522	0.428

C.2 Fraction of total fatigue damage 20 years

Design 2: Fraction of total fatigue damage for 20 years

Condition	base	seg 2	seg 3	seg 4	seg 5	seg 6	seg 7	seg 8	seg 9	seg 10	seg 11	seg 12	seg 13	seg 14	seg 15	seg 16	seg 17	seg 18	seg 19	top
1	0%	0%	0%	0%	0%	0%	0%	0%	0%	0%	0%	0%	0%	0%	0%	0%	0%	0%	0%	0%
2	0%	0%	0%	0%	0%	0%	0%	0%	0%	0%	0%	0%	0%	0%	0%	0%	0%	0%	0%	0%
3	0%	0%	0%	0%	0%	0%	0%	0%	0%	0%	0%	0%	0%	0%	0%	0%	0%	0%	0%	0%
4	1%	1%	1%	1%	1%	1%	1%	1%	1%	1%	1%	1%	1%	1%	1%	1%	1%	0%	0%	0%
5	2%	2%	2%	2%	2%	2%	2%	2%	2%	2%	2%	2%	2%	2%	2%	2%	1%	1%	1%	0%
6	1%	1%	1%	1%	1%	1%	1%	1%	1%	1%	1%	1%	1%	1%	1%	1%	1%	1%	0%	0%
7	4%	4%	4%	4%	4%	4%	4%	4%	4%	4%	4%	4%	4%	4%	4%	3%	3%	3%	3%	2%
8	10%	10%	10%	10%	10%	10%	10%	10%	10%	10%	10%	10%	10%	10%	9%	9%	8%	7%	6%	4%
9	4%	4%	4%	4%	4%	4%	4%	4%	4%	4%	4%	4%	4%	4%	4%	4%	4%	4%	3%	2%
10	14%	14%	14%	14%	14%	14%	13%	13%	13%	13%	13%	13%	13%	12%	12%	12%	11%	11%	10%	8%
11	26%	26%	26%	26%	26%	25%	25%	25%	25%	25%	25%	25%	25%	24%	24%	24%	23%	22%	21%	17%
12	12%	12%	12%	12%	12%	12%	12%	11%	11%	11%	11%	11%	11%	11%	11%	11%	11%	11%	10%	8%
13	6%	6%	6%	6%	6%	6%	6%	6%	6%	6%	5%	5%	5%	5%	5%	5%	6%	6%	6%	7%
14	9%	9%	9%	9%	9%	9%	9%	9%	9%	9%	9%	9%	9%	10%	10%	10%	11%	12%	13%	16%
15	3%	3%	3%	3%	3%	4%	4%	4%	4%	4%	4%	4%	4%	4%	4%	4%	5%	5%	6%	8%
16	2%	2%	2%	2%	2%	2%	2%	2%	3%	3%	3%	3%	3%	3%	3%	3%	3%	4%	4%	5%
17	3%	3%	3%	3%	3%	3%	3%	3%	3%	4%	4%	4%	4%	4%	4%	5%	5%	6%	8%	11%
18	1%	1%	1%	1%	1%	1%	1%	1%	2%	2%	2%	2%	2%	2%	2%	2%	2%	3%	3%	5%
19	1%	1%	1%	1%	1%	1%	1%	1%	1%	1%	1%	1%	1%	1%	1%	1%	1%	1%	1%	2%
20	1%	1%	1%	1%	1%	1%	1%	1%	1%	1%	1%	1%	1%	1%	2%	2%	2%	2%	3%	3%
21	0%	0%	0%	0%	0%	0%	1%	1%	1%	1%	1%	1%	1%	1%	1%	1%	1%	1%	1%	2%
sum	100%	100%	100%	100%	100%	100%	100%	100%	100%	100%	100%	100%	100%	100%	100%	100%	100%	100%	100%	100%

D Fatigue damage design 3

D.1 20 year fatigue damage

Design 3: 20 year fatigue damage

Condition	base	seg 2	seg 3	seg 4	seg 5	seg 6	seg 7	seg 8	seg 9	seg 10	seg 11	seg 12	seg 13	seg 14	seg 15	seg 16	seg 17	seg 18	seg 19	top
1	0.001	0.001	0.001	0.001	0.001	0.001	0.001	0.001	0.001	0.001	0.001	0.001	0.001	0.001	0.001	0.001	0.001	0.001	0.001	0.000
2	0.002	0.002	0.002	0.002	0.002	0.002	0.002	0.002	0.002	0.002	0.002	0.002	0.002	0.002	0.002	0.002	0.002	0.002	0.001	0.001
3	0.001	0.001	0.001	0.001	0.001	0.001	0.001	0.001	0.001	0.001	0.001	0.001	0.001	0.001	0.001	0.001	0.001	0.001	0.001	0.000
4	0.007	0.007	0.007	0.007	0.007	0.007	0.007	0.007	0.007	0.007	0.007	0.007	0.007	0.007	0.006	0.006	0.006	0.006	0.005	0.003
5	0.018	0.018	0.019	0.018	0.018	0.018	0.018	0.018	0.017	0.017	0.017	0.017	0.017	0.017	0.016	0.016	0.015	0.014	0.011	0.006
6	0.008	0.008	0.008	0.008	0.008	0.008	0.008	0.008	0.008	0.008	0.008	0.008	0.008	0.008	0.008	0.007	0.007	0.007	0.006	0.003
7	0.040	0.040	0.041	0.041	0.041	0.041	0.040	0.040	0.040	0.040	0.040	0.040	0.040	0.040	0.040	0.040	0.039	0.039	0.037	0.030
8	0.103	0.102	0.102	0.102	0.103	0.102	0.101	0.101	0.100	0.099	0.099	0.099	0.099	0.099	0.098	0.096	0.094	0.091	0.085	0.064
9	0.045	0.045	0.045	0.045	0.046	0.046	0.045	0.045	0.045	0.045	0.045	0.045	0.045	0.046	0.046	0.046	0.045	0.045	0.043	0.034
10	0.165	0.164	0.163	0.163	0.162	0.160	0.157	0.155	0.153	0.150	0.149	0.148	0.146	0.144	0.142	0.139	0.134	0.130	0.122	0.108
11	0.304	0.303	0.304	0.305	0.304	0.302	0.300	0.297	0.294	0.290	0.290	0.288	0.287	0.285	0.282	0.279	0.272	0.269	0.258	0.232
12	0.140	0.139	0.140	0.139	0.139	0.138	0.137	0.136	0.135	0.133	0.133	0.133	0.133	0.132	0.131	0.130	0.128	0.127	0.124	0.116
13	0.066	0.066	0.066	0.066	0.066	0.066	0.065	0.064	0.064	0.063	0.063	0.063	0.064	0.064	0.065	0.067	0.069	0.075	0.083	0.105
14	0.100	0.102	0.103	0.104	0.105	0.105	0.105	0.105	0.106	0.106	0.107	0.109	0.112	0.115	0.120	0.126	0.135	0.153	0.176	0.232
15	0.041	0.042	0.042	0.042	0.043	0.043	0.043	0.043	0.043	0.044	0.044	0.046	0.047	0.049	0.051	0.055	0.060	0.070	0.083	0.113
16	0.025	0.026	0.026	0.027	0.027	0.027	0.027	0.028	0.028	0.028	0.029	0.030	0.031	0.032	0.034	0.036	0.040	0.046	0.055	0.072
17	0.036	0.037	0.038	0.038	0.039	0.039	0.039	0.040	0.040	0.041	0.042	0.044	0.046	0.048	0.052	0.057	0.065	0.079	0.099	0.142
18	0.016	0.016	0.017	0.017	0.017	0.017	0.017	0.018	0.018	0.018	0.019	0.020	0.021	0.022	0.024	0.026	0.030	0.036	0.046	0.067
19	0.009	0.009	0.010	0.010	0.010	0.010	0.010	0.010	0.010	0.010	0.010	0.011	0.011	0.011	0.012	0.013	0.014	0.016	0.018	0.022
20	0.012	0.012	0.012	0.013	0.013	0.013	0.013	0.013	0.014	0.014	0.014	0.015	0.016	0.016	0.018	0.019	0.022	0.026	0.032	0.042
21	0.005	0.005	0.005	0.005	0.006	0.006	0.006	0.006	0.006	0.006	0.006	0.006	0.007	0.007	0.008	0.009	0.010	0.012	0.015	0.020
Accumulated fatigue damage during 20 years																				
All	1.144	1.146	1.151	1.154	1.158	1.150	1.142	1.136	1.130	1.122	1.126	1.131	1.137	1.145	1.154	1.170	1.187	1.244	1.300	1.413

D.2 Fraction of total fatigue damage 20 years

Design 3: Fraction of total fatigue damage for 20 years

Condition	base	seg 2	seg 3	seg 4	seg 5	seg 6	seg 7	seg 8	seg 9	seg 10	seg 11	seg 12	seg 13	seg 14	seg 15	seg 16	seg 17	seg 18	seg 19	top
1	0%	0%	0%	0%	0%	0%	0%	0%	0%	0%	0%	0%	0%	0%	0%	0%	0%	0%	0%	0%
2	0%	0%	0%	0%	0%	0%	0%	0%	0%	0%	0%	0%	0%	0%	0%	0%	0%	0%	0%	0%
3	0%	0%	0%	0%	0%	0%	0%	0%	0%	0%	0%	0%	0%	0%	0%	0%	0%	0%	0%	0%
4	1%	1%	1%	1%	1%	1%	1%	1%	1%	1%	1%	1%	1%	1%	1%	1%	1%	0%	0%	0%
5	2%	2%	2%	2%	2%	2%	2%	2%	2%	2%	2%	1%	1%	1%	1%	1%	1%	1%	1%	0%
6	1%	1%	1%	1%	1%	1%	1%	1%	1%	1%	1%	1%	1%	1%	1%	1%	1%	1%	0%	0%
7	4%	4%	4%	4%	4%	4%	4%	4%	4%	4%	4%	4%	4%	3%	3%	3%	3%	3%	3%	2%
8	9%	9%	9%	9%	9%	9%	9%	9%	9%	9%	9%	9%	9%	9%	8%	8%	8%	7%	7%	5%
9	4%	4%	4%	4%	4%	4%	4%	4%	4%	4%	4%	4%	4%	4%	4%	4%	4%	4%	3%	2%
10	14%	14%	14%	14%	14%	14%	14%	14%	14%	13%	13%	13%	13%	13%	12%	12%	11%	10%	9%	8%
11	27%	26%	26%	26%	26%	26%	26%	26%	26%	26%	26%	25%	25%	25%	24%	24%	23%	22%	20%	16%
12	12%	12%	12%	12%	12%	12%	12%	12%	12%	12%	12%	12%	12%	12%	11%	11%	11%	10%	10%	8%
13	6%	6%	6%	6%	6%	6%	6%	6%	6%	6%	6%	6%	6%	6%	6%	6%	6%	6%	6%	7%
14	9%	9%	9%	9%	9%	9%	9%	9%	9%	9%	10%	10%	10%	10%	10%	11%	11%	12%	14%	16%
15	4%	4%	4%	4%	4%	4%	4%	4%	4%	4%	4%	4%	4%	4%	4%	5%	5%	6%	6%	8%
16	2%	2%	2%	2%	2%	2%	2%	2%	2%	3%	3%	3%	3%	3%	3%	3%	3%	4%	4%	5%
17	3%	3%	3%	3%	3%	3%	3%	3%	4%	4%	4%	4%	4%	4%	4%	5%	5%	6%	8%	10%
18	1%	1%	1%	1%	1%	1%	2%	2%	2%	2%	2%	2%	2%	2%	2%	2%	3%	3%	4%	5%
19	1%	1%	1%	1%	1%	1%	1%	1%	1%	1%	1%	1%	1%	1%	1%	1%	1%	1%	1%	2%
20	1%	1%	1%	1%	1%	1%	1%	1%	1%	1%	1%	1%	1%	1%	2%	2%	2%	2%	2%	3%
21	0%	0%	0%	0%	0%	0%	0%	1%	1%	1%	1%	1%	1%	1%	1%	1%	1%	1%	1%	1%
sum	100%	100%	100%	100%	100%	100%	100%	100%	100%	100%	100%	100%	100%	100%	100%	100%	100%	100%	100%	100%

E Spectral analysis

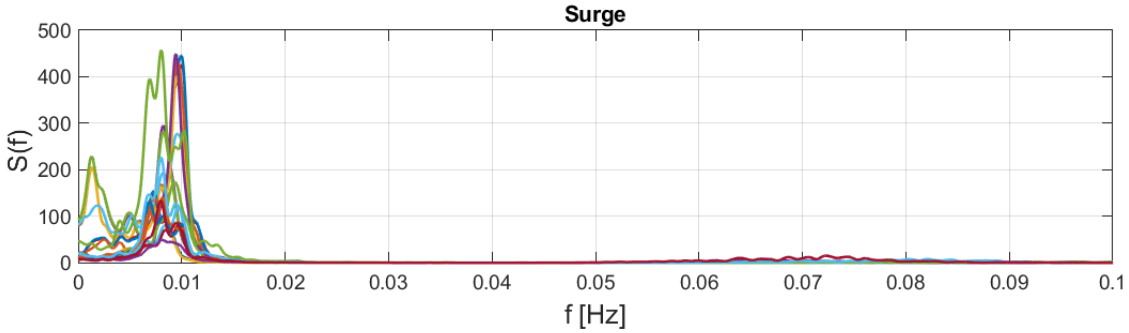

Figure E.1: Spectral analysis in surge.

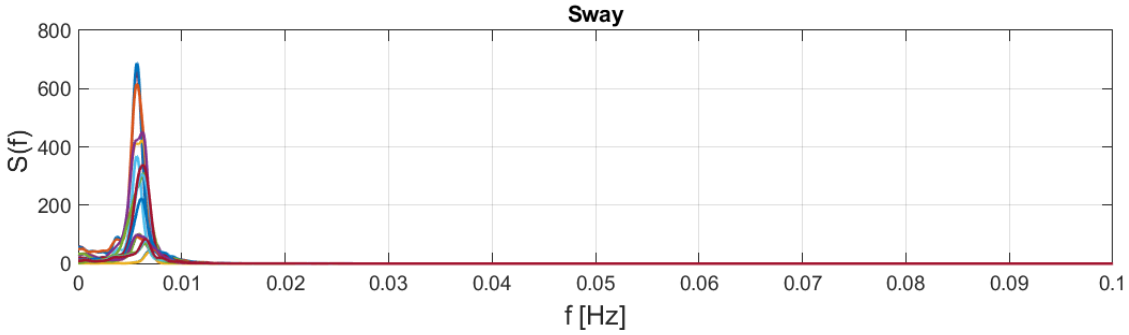

Figure E.2: Spectral analysis in sway.

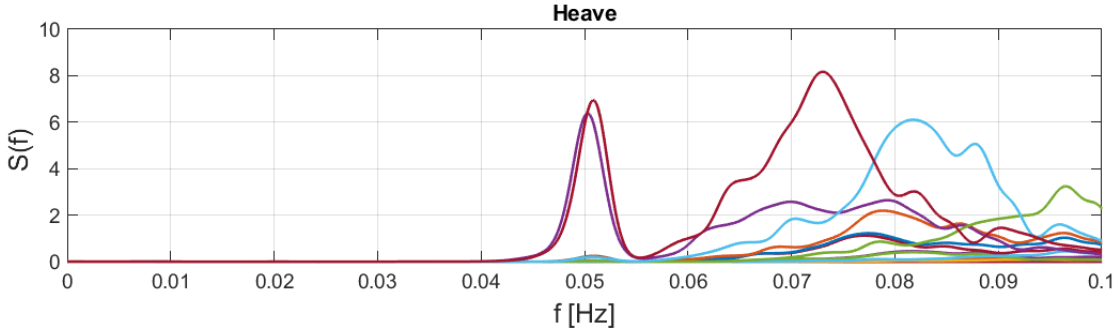

Figure E.3: Spectral analysis in heave.

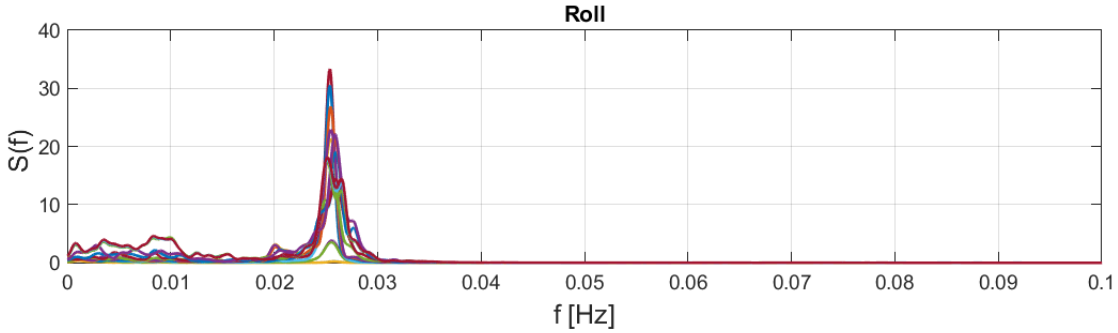

Figure E.4: Spectral analysis in roll.

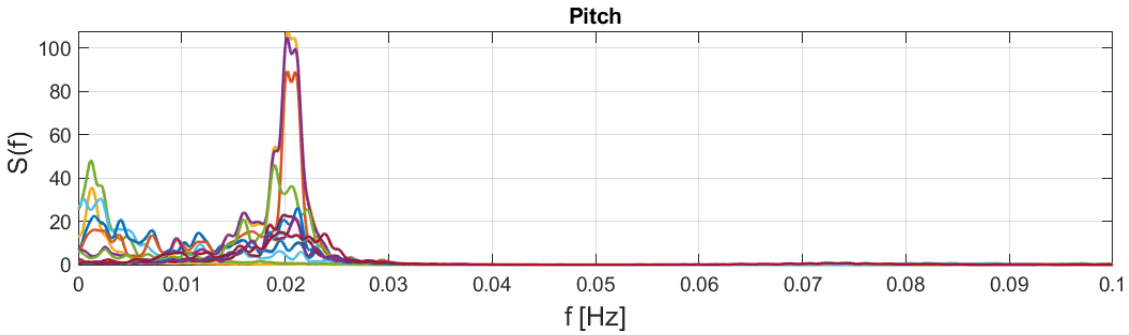

Figure E.5: Spectral analysis in pitch.

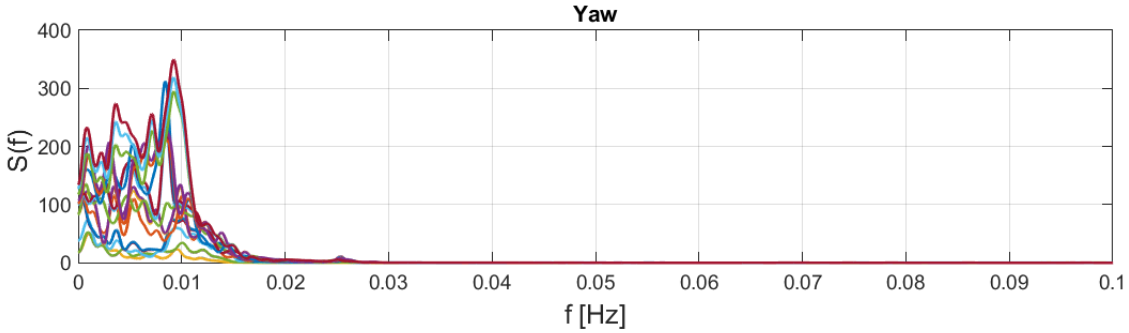

Figure E.6: Spectral analysis in yaw.

Rikke Olsen Fredheim

Tower design for very large floating wind turbines

NTNU
Norwegian University of
Science and Technology